MULTIWAVELENGTH INVESTIGATION OF CORE-COLLAPSE SUPERNOVAE

THESIS

Submitted for the degree of

DOCTOR OF PHILOSOPHY

in PHYSICS

to

The Kumaun University

By

Subhash Bose

Aryabhatta Research Institute of observational sciencES (ARIES)

Manora Peak, Nainital 263002, India

August 2015

DECLARATION

I hereby declare that the work presented in this thesis is a result of the investigation carried out by me at the Aryabhatta Research Institute of observational sciencES (ARIES), Nainital, under the supervision of Dr. Brijesh Kumar (Scientist E, ARIES, Manora Peak, Nainital) and Co-Supervision of Prof. H. C. Chandola (Department of Physics, Kumaun University, Nainital). This thesis has not been submitted for the award of any degree, diploma, associateship or fellowship of any University or Institute.

Place : Nainital
Date :

Subhash Bose
ARIES, Manora Peak
Nainital, India
email@subhashbose.com
Mob: +919917737629

CERTIFICATE FROM THE SUPERVISORS

This is to certify that

The synopsis of the thesis entitled **"Multiwavelength investigation of Core-Collapse Supernovae"** for the award of the degree of Doctor of Philosophy in Physics was approved by the Kumaun University, Nainital (Letter no.: Research/ Physics/43/2013, dated: 27-12-2013).

This thesis embodies the work of Mr. Subhash Bose himself.

Mr. Subhash Bose worked under our joint supervisions for this thesis as a Research Fellow at the Aryabhatta Research Institute of observational sciencES (ARIES), Nainital. He has put in more than 200 days of attendance at ARIES, Nainital during this period.

This thesis has not been submitted before for the award of any degree, diploma, associateship or fellowship of any University or Institute.

Dr. Brijesh Kumar
(Supervisor)
ARIES,
Manora Peak, Nainital
brij@aries.res.in
Mob: +917351440011

Prof. H. C. Chandola
(Co-Supervisor)
Department of Physics
Kumaun University, Nainital
chandolaharish@gmail.com
Mob: +919412986369

Head & convener
RDC Physics Deptt.
Kumaun University, Nainital

To,

My Family

Acknowledgments

Finally the milestone moment has come which myself and all my well wishers have been eagerly waiting for. At this very moment I take the opportunity to express my gratitude towards everyone who has supported and encouraged me, without which this bound volume would have been impossible. Firstly I express my heartiest thanks my thesis advisor Dr. Brijesh Kumar, who has been a true mentor for me. He has given me full freedom to work comfortably, develop my own skills and take my own decision, but at the same time he has been also a constant motivation. Thank you Sir, for exploring my potential and guiding me in right direction during the entire course of my Ph.D. Sometime you have shown more trust on my capability than I had on myself, which has pushed me beyond my pseudo-boundaries. My sincere thanks also goes to my co-supervisor Prof. H. C. Chandola for his invaluable support and cooperation. I am highly indebted to Dr. Kuntal Misra for her immense support during my Ph.D. She has been extremely cooperative and has often went out of her way to help me in both academic and non-academic matters. It was a great pleasure to work with her and have useful scientific discussions which has been very fruitful during my research. I also express my sincere gratitude to Profs. Shibaji Banerjee and Suparna Roychoudhuri who have been a great motivation during my M.Sc. course and have important role in shaping my academic career.

I thank Drs. Biman J. Medhi, Hum Chand, Indranil Chatyopadhay, Maheshwar G., Jeewan C. Pandey, Sneh Lata, Saurabh Sharma, Amitesh Omar, Shashi B. Pandey, Santosh Joshi, Manish Naja and Yogesh Joshi for their help and discussions in various academic and scientific matter. I am also thankful to the entire supernova research group - Rupak, Brajesh and Mridweeka, with whom I spent several hours at the telescope building and enjoyed working collaboratively with them. I also acknowledge all those research scholars at ARIES who have cooperated in intense observations as required for supernovae follow-up. I highly appreciate their understanding, sharing and wise utilization of telescope time which have made much of these observations possible.

My sincere thanks to my collaborators, Drs. P. J. Brown, S. Chakraborti, K. Matsumoto, A. Pastorello, M. L. Pumo, A. Ray, D. Sand, F. Sutaria, S. Valenti and

L. Zampieri for their kind support and valuable suggestions which helped immensely in enriching the scientific content of this research work.

I am highly indebted to ARIES, where I perused my Ph.D. and utilized its observations facilities. I also thankfully acknowledge the grant provided by DST-SERB to partially support my international travel as a part of my research work.

I acknowledge the support and cooperation of engineers and support staff whose efforts have made possible to run various facilities at ARIES. I would like to thank Pradeep Chakraborty, T. S. Kumar, Abhishek Sharma, Mohit Joshi, Hemant, Naveen, Pawan, Arjun, Prashant, A. K. Singh, Shashank and S. Giri who have been helpful and supportive when I approached them with various issues during my stay at ARIES. I specially thank Computer and Library section for always being cooperative during the time of my Ph.D. I also acknowledge the accounts section for their supportive nature and prompt settlement of financial matters. Technical staff and observing assistants of 104cm and 130cm telescope have been always helpful and active in addressing any issue arising with these facilities. My deep appreciation also goes to the gentle and humble security personnels of ARIES for their sincerity and honesty.

I cherished the company of helpful seniors – Manash, Ramkesh, Rupak, Sumana, Eswar, Akash, Jessy, Neelam, Rajesh, Brajesh who were always ready to extend their helping hands and I often sought their advices in various matters. I also thank research scholars at ARIES – Narendra, Devesh, Ravi, Tapaswini, Haritma, Prashanth Mohan, Manoj, Archana, Raman whose presence have made a enjoyable atmosphere during the years of my Ph.D. I also got to see the joining of some junior batches who provided a wonderful friendly ambiance – Abhishek, Neha, Subhajeet, Aabha, Aditi, Arti, Parveen, Mridweeka, Mukesh, and also the current junior most batch – Anjasha, Ashwini, Ekta, Kuldeep, Nabhdeep, Pankaj, Piyali, Raya, Sapna, Vineet. I specially thank my fellow batch mates – Jai, Piyush and Pradeep, with whom I enjoyed several good moments.

My heartfelt thanks to Hema, Krishna, Rajiv and Sumit for being more a friend than a senior and providing the friendly and enjoyable environment. I cherished the odd hour irrelevant yet fun-filled chats with Sumit and Krishna. I enjoyed Rajiv's company in our regular dinner parties in Nainital for all these years. I highly appreciate the company and support which I received from Hema and I thank her

for always standing by me. Oh.. and talking about friends, I can not miss Jimmy, our most loved and pampered dog in ARIES hostel. Her unconditional affection and innocence has always made me happy even during the most tiring and work loaded days. She knows how to be happy even at the slightest thing and also to make others feel special by her joyous gesture.

Lastly, but most importantly, I express my utmost gratitude to my family for supporting me in every stage of my life and in every possible way. My mother and elder sister have always stood beside me and encouraged to continue my higher studies and research, without even a slightest complain for not being with them for these full five years. I sincerely thank Mr. Ashok for always being there and my little nephew Apratim for bringing so much joy when I visit home. I thank my father who made me love science, answered my endless queries, encouraged my quests and boosted my interest towards physics. He taught me honesty and sincerity, without which this thesis could not be possible.

Subhash Bose

Preface

Core-Collapse supernovae (SNe) are extremely energetic cosmic explosions which mark end stages of evolution in massive stars ($> 8M_{\odot}$). At the end of nuclear burning phase in the core, these stars collapse under self gravity and the resulting gravitational energy release in the form of energetic shock wave and neutrinos is responsible to disrupt the entire dying star. The observed properties of these events show wide diversity in their light curves and spectra, which are primarily governed by their progenitor properties and history of pre-SN stellar evolution. Due to high intrinsic brightness, SNe are attractive probe to study environment and various properties at extragalactic distances. SNe are recognized as independent extragalactic distance indicators.

This thesis entitled "Multiwavelength Investigation of Core-Collpase Supernovae" embodies work on five SNe viz. SNe 2012aw, 2013ab, 2013ej, 2013hj and 2014G observed primarily from Indian facilities along with complementary data from various international facilities and data archives. Extensive analysis as well as theoretical modeling of light curves and spectra of SNe have been performed to constrain progenitor properties (e.g. mass and radius), explosion parameters (e.g. energies) and also to probe circumstellar environment to infer their pre-SN evolution which the progenitor might have undergone. This thesis also revisits the complex diversity of type II SNe and examines distinguishable characteristic of various subtypes. Extensive study has also been done to explore the potential of type II SNe as distance estimators by applying expanding photosphere method.

Chapter 1 provides a general introduction to supernovae. This chapter presents a brief review of our present understanding of explosion mechanisms, their underlying physics and current issues involved in this subject. Various observable parameters are discussed and connected those with properties and parameters of explosion, progenitor and environment. An elaborate outline and motivation of the thesis is also given in §1.10 of the chapter. Chapter 2 describes the observational resources along with the technical description of instruments and observational facilities which have been used in the thesis. Introduction to data acquisition and reduction techniques

in optical photometry, spectroscopy and polarimetry are presented in this chapter. A brief description of *Swift* UVOT archival data and its analysis is also presented.

Chapter 3 is dedicated on Expanding photosphere method (EPM). This being a redshift independent technique of distance estimation, it has great importance in astronomical and cosmological perspective. We applied EPM collectively on a sample of eight SNe to reliably estimate distances to their host galaxies. The comparative study of two dilution factors revealed that the corresponding EPM distances differ by 30 – 50% and Dessart & Hillier (2005a) prescription for dilution factor is significantly better suited than Hamuy et al. (2001) for EPM applications. In this study, we introduced the following two improvements in addition to existing EPM methodology – (1) using photospheric velocities estimated by SYNOW modeling observed spectra and (2) using the semi-deconvolution of filter response while fitting the observed broadband fluxes to estimate θ and T. Reddening or $E(B-V)$ being one of the quantity with most uncertainty, we examined its implication on EPM estimated results and showed that EPM is weakly dependent on $E(B-V)$. Our study not only revealed the potential of EPM as an excellent distance estimator, but also very useful in determination of explosion epoch of SNe. Among the SNe sample on which EPM has been implemented, three of them (SNe 2004et, 2005cs and 2012aw) have fairly precise determined explosion epoch from observational non-detection. The EPM estimated explosion epochs for all these SNe are found to be very consistent and within ~ 2 days of the observationally constrained values. This study also showed that dilution factor prescription are only applicable to data in early phases of SNe, i.e, when limited to < 50 days. We also note that SYNOW estimated photospheric velocities can be more reliable than velocities estimated by directly locating the absorption troughs, especially when spectra are of poor signal to noise ratio or contamination from neighboring spectral lines are dominant.

Chapter 4 presents densely-sampled $UBVRI/griz$ photometric and low-resolution ($6-10$Å) optical spectroscopic observations from 4 to 270 days after explosion of a newly discovered type II SN 2012aw in a nearby ($\sim$9.9 Mpc) galaxy M95. The light-curve characteristics of apparent magnitudes, colors, bolometric luminosity and the presence and evolution of prominent spectral features are found to have striking

similarity with the archetypal IIP SNe 1999em, 1999gi and 2004et. The early time observations of SN 2012aw clearly detect minima in the light-curve of V, R and I bands near 37 days after explosion and this we suggest to be an observational evidence for emergence of recombination phase. The mid-plateau M_V magnitude (-16.67 ± 0.04) lies in between the bright (~ -18) and subluminous (~ -15) IIP SNe. The mass of nickel is 0.06 ± 0.01 $M_\odot$. The SYNOW modelling of spectra indicate that the value and evolution of photospheric velocity is similar to SN 2004et, but about $\sim$600 km s^{-1} higher than that of SNe 1999em and 1999gi at comparable epochs. This trend is more apparent in the line velocities of Hα and Hβ. A comparison of ejecta velocity properties with that of existing radiation-hydrodynamical simulations indicate that the energy of explosion lies in the range 1-2$\times10^{51}$ ergs; a further comparison of nebular phase [O I] doublet luminosity with SNe 2004et and 1987A indicate that the mass of progenitor star is about 14-15 $M_\odot$. The presence of high-velocity absorption features in the mid-to-late plateau and possibly in early phase spectra show signs of interaction between ejecta and the circumstellar matter; being consistent with its early-time detection at X-ray and radio wavebands.

Chapter 5 presents densely-sampled ultraviolet/optical photometric and low-resolution optical spectroscopic observations of the type IIP supernova 2013ab in the nearby ($\sim$24 Mpc) galaxy NGC 5669, from 2 to 190d after explosion. Continuous photometric observations, with the cadence of typically a day to one week, were acquired with the 1-2m class telescopes in the LCOGT network, ARIES telescopes in India and various other telescopes around the globe. The light curve and spectra suggest that the SN is a normal type IIP event with a plateau duration of $\sim$ 80 days with mid plateau absolute visual magnitude of -16.7, although with a steeper decline during the plateau (0.92 mag 100 d^{-1} in V band) relative to other archetypal SNe of similar brightness. The velocity profile of SN 2013ab shows striking resemblance with those of SNe 1999em and 2012aw. Following the Rabinak & Waxman (2011) prescription, the initial temperature evolution of the SN emission allows us to estimate the progenitor radius to be $\sim$ 800 $R_\odot$, indicating that the SN originated from a red supergiant star. The distance to the SN host galaxy is estimated to be 24.3 Mpc from expanding photosphere method (EPM). From our observations,

we estimate that 0.064 $M_\odot$ of ^{56}Ni was synthesized in the explosion. General relativistic, radiation hydrodynamical modeling of the SN infers an explosion energy of 0.35×10^{51} erg, a progenitor mass (at the time of explosion) of ~ 9 $M_\odot$ and an initial radius of ~ 600 $R_\odot$.

Chapter 6 presents optical photometric and spectroscopic observations of supernova 2013ej. It is one of the brightest type II supernovae exploded in a nearby ($\sim$ 10 Mpc) galaxy NGC 628. The light curve characteristics are similar to type II SNe, but with a relatively shorter ($\sim$ 85 day) and steeper ($\sim$ 1.7 mag (100 d)$^{-1}$ in V) plateau phase. The SN shows a large drop of 2.4 mag in V band brightness during plateau to nebular transition. The absolute ultraviolet (UV) light curves are identical to SN 2012aw, showing a similar UV plateau trend extending up to 85 days. The radioactive ^{56}Ni mass estimated from the tail luminosity is $0.02M_\odot$ which is significantly lower than typical type IIP SNe. The characteristics of spectral features and evolution of line velocities indicate that SN 2013ej is a type II event. However, light curve characteristics and some spectroscopic features provide strong support in classifying it as a type IIL event. A detailed SYNOW modelling of spectra indicates the presence of some high velocity components in Hα and Hβ profiles, implying possible ejecta-CSM interaction. The nebular phase spectrum shows an unusual notch in the Hα emission which may indicate bipolar distribution of ^{56}Ni. Modelling of the bolometric light curve yields a progenitor mass of $\sim 14M_\odot$ and a radius of $\sim 450R_\odot$, with a total explosion energy of $\sim 2.3 \times 10^{51}$ erg.

Chapter 7 presents broadband photometric and polarimetric observations of two type II SNe 2013hj and 2014G. SN 2014G is a spectroscopically classified type IIL event, which we also confirm photometrically as its light curve show characteristic features (plateau slope of 2.55 mag (100 d)$^{-1}$ in V-band and duration of $\sim$ 77d) of a generic IIL SN. On the other hand SN 2013hj also shows high plateau decline rate of 1.5 mag (100 d)$^{-1}$ in V-band, similar to SNe IIL, but marginally lower than SNe IIL template light curves. Our high cadence photometric observations of SNe 2013hj and 2014G enables us to cover all characteristic phases up to radioactive tail of optical light curves. Broadband polarimetric observations reveal significant polarization in SN 2013hj with subtle enhancement as SN evolves towards plateau end, however the

polarization angle remains constant throughout the evolution. This characteristic is consistent with the idea that the evolving SN with recombining hydrogen envelope is slowly revealing more asymmetric central region of explosion. Modelling of bolometric light curve yields a progenitor mass of $\sim 11M_{\odot}$ with a radius of $\sim 700R_{\odot}$ for SN 2013hj, while for SN 2014G model estimated progenitor mass is $\sim 9M_{\odot}$ with a radius of $\sim 630R_{\odot}$, both having a typical energy budget of $\sim 2 \times 10^{51}$ erg.

In summary, this thesis includes detailed investigation of two type IIP SNe 2012aw and 2013ab and three fast declining type II SNe 2013ej, 2013hj and 2014G. The thesis also includes statistical study on applicability of type II SNe as extragalactic distance indicators. SN 2012aw is found to have remarkable similarity to archetypal IIP event and the good quality of data presented in this thesis have helped in detection of first conclusive evidence of emergence of recombination phase and also revealed signature of interaction with CSM. For SN 2013ab, a densely sampled observational data from plateau to nebular phase for a normal type IIP event ever, is obtained. SN 2013ej has been throughly examined and revealed detection for CSM interaction which is further connected to atypical flattening of H I velocity profile. The photometric and polarimetric observations of two fast declining / IIL SNe 2013hj and 2014G indicates that the prototypical IIL SN like SN 2014G is very rare in its own whereas SN 2013hj is found to lie at an intermediate position of wide SNe II diversity. In view of diverse nature of type II events this thesis tests applicability of distance determination using EPM on total of nine type IIP SNe and the estimated distances are found to be consistent with other extragalactic distance indicators.

List of Publications

Publications in refereed journal

1. Supernova 2012aw a high-energy clone of archetypal Type IIP SN 1999em
   Subhash Bose, *Brijesh Kumar, Firoza Sutaria, Brajesh Kumar, Rupak Roy, V. K. Bhatt, S. B. Pandey, H. C. Chandola, Ram Sagar, Kuntal Misra and Sayan Chakraborti*, (2013), Monthly Notices of the Royal Astronomical Society (MNRAS), *Volume 433, Issue 3, p.1871-1891.*

2. Distance determination to eight galaxies using expanding photosphere method
   Subhash Bose *and Brijesh Kumar*, (2014), The Astrophysical Journal (ApJ), *Volume 782, Issue 2, article id. 98, 12 pp.*

3. SN 2013ab: a normal Type IIP supernova in NGC 5669
   Subhash Bose, *Stefano Valenti, Kuntal Misra, Maria Letizia Pumo, Luca Zampieri, David Sand, Brijesh Kumar, Andrea Pastorello, Firoza Sutaria, Thomas J. Maccarone, Brajesh Kumar, M. L. Graham, D. Andrew Howell, Paolo Ochner, H. C. Chandola and Shashi B. Pandey*, (2015), Monthly Notices of the Royal Astronomical Society (MNRAS), *450, 2373-2392.*

4. SN 2013ej: A Type IIL Supernova with Weak Signs of Interaction
   Subhash Bose, *Firoza Sutaria, Brijesh Kumar, Chetna Duggal, Kuntal Misra, Peter J. Brown, Mridweeka Singh, Vikram Dwarkadas, Donald G. York, Sayan Chakraborti, H. C. Chandola, Julie Dahlstrom, Alak Ray and Margarita Safonova*, (2015), The Astrophysical Journal (ApJ), *806, 160.*

5. Photometric and polarimetric observations of fast declining Type II SNe 2013hj and 2014G
   Subhash Bose, *Brijesh Kumar, Kuntal Misra, Katsura Matsumoto, Brajesh Kumar, Mridweeka Singh, Daiki Fukushima, Miho Kawabata*, (2015), Under review in Monthly Notices of the Royal Astronomical Society (MNRAS)

6. Light curve and spectral evolution of the Type IIb supernova 2011fu
Brajesh Kumar, S. B. Pandey, D. K. Sahu, J. Vinko, A. S. Moskvitin, G. C. Anupama, V. K. Bhatt, A. Ordasi, V. V. Sokolov, T. N. Sokolova, V. N. Komarova, Brijesh Kumar, **Subhash Bose***, Rupak Roy, Ram Sagar*, (2013), Monthly Notices of the Royal Astronomical Society (MNRAS), *Volume 431, Issue 1, p.308-321.*

7. Electron Cooling in a Young Radio Supernova: SN 2012aw
Naveen Yadav, Alak Ray, Sayan Chakraborti, Christopher Stockdale, Poonam Chandra, Randall Smith, Rupak Roy, **Subhash Bose***, Vikram Dwarkadas, Firoza Sutaria, and David Pooley*, (2014), The Astrophysical Journal (ApJ), *Volume 782, Issue 1, article id. 30, 10 pp.*

Conference Proceedings

1. Distance determination to six nearby galaxies using type IIP supernovae
Subhash Bose*, Brijesh Kumar*, (2014), Supernova Environmental Impacts, Proceedings of the International Astronomical Union, IAU Symposium, *Volume 296, pp. 90-94.*

2. Optical observations of supernova 2012aw
Subhash Bose*, Brijesh Kumar, Firoza Sutaria, Rupak Roy, Brajesh Kumar, Vijay K. Bhatt, Sayan Chakraborti*, (2014), Supernova Environmental Impacts, Proceedings of the International Astronomical Union, IAU Symposium, *Volume 296, pp. 334-335.*

3. Radio Observations Of A Nearby Type IIP SN 2012aw
Naveen Yadav, Alak Ray, Sayan Chakraborti, Christopher Stockdale, Poonam Chandra, Randall Smith, Rupak Roy, Vikram Dwarkadas, Firoza Sutaria, Dave Pooley, Brijesh Kumar, **Subhash Bose**, (2014), Supernova Environmental Impacts, Proceedings of the International Astronomical Union, IAU Symposium, *Volume 296, pp. 112-115.*

4. The optical photometric and spectroscopic investigation of Type IIP supernova 2012A
   Rupak Roy, Firoza Sutaria, **Subhash Bose***, Sean Johnson, Vikram Dwarkadas, Brian York, Brijesh Kumar, Brajesh Kumar, Vijay K. Bhatt, Sayan Chakraborti, Don York, Adam Ritchey, Gabrielle Saurage, Mary Beth Kaiser*, (2014), Supernova Environmental Impacts, Proceedings of the International Astronomical Union, IAU Symposium, *Volume 296, pp. 116-120.*

5. Evolution of the Type IIb SN 2011fu
   S. B. Pandey, Brajesh Kumar, D. K. Sahu, J. Vinko, A. S. Moskvitin, G. C. Anupama, V. K. Bhatt, A. Ordasi, A. Nagy, V. V. Sokolov, T. N. Sokolova, V. N. Komarova, Brijesh Kumar, **Subhash Bose***, Rupak Roy, Ram Sagar*, (2014), Supernova Environmental Impacts, Proceedings of the International Astronomical Union, IAU Symposium, *Volume 296, pp. 336-337*

6. Core-Collapse supernovae and its progenitors
   Subhash Bose*, Brijesh Kumar and Kuntal Misra*, (2015), in RETCO II, ASI Conference Series (ASInC), *in press*

Conference Abstracts

1. Optical study of Type IIb supernovae 2011dh and 2012P
   Subhash Bose*, Brijesh Kumar, Firoza Sutaria, Brajesh Kumar, Rupak Roy, Vijay K. Bhatt*, (2013), in 31st ASI Meeting, ASI Conference Series (ASInC), *Vol. 9, pp 134, Edited by Pushpa Khare & C. H. Ishwara-Chandra.*

2. Photometric and spectroscopic follow-up of Type IIn SN 2010jl
   Rupak Roy, Firoza Sutaria, **Subhash Bose***, and Brijesh Kumar*, (2013), in 31st ASI Meeting, ASI Conference Series (ASInC), *Vol. 9, pp 86, Edited by Pushpa Khare & C. H. Ishwara-Chandra.*

Notations and Abbreviations

The most commonly used notations and abbreviations which have been used in this thesis are listed below for a for a quick reference. All these notations and abbreviations have also been explained on their first appearance in the thesis. If a symbol has been used in a different connection than listed here, it has been explained at the appropriate place.

Notations

Å	Angstrom
α, RA	right ascension
A_V	extinction in the visual magnitude
$'$, arcmin	arc minute
$''$, arcsec	arc second
cm	centimeter
d	day
D	Distance
$^\circ$, deg	degree
δ, Dec	declination
$E(B-V)$	colour excesses in $(B-V)$
eV	Electron Volt
foe	10^{51} erg
H_0	Hubble constant
hr	Hour
hrs	Hours
$J2000$	epoch of observation with reference year 2000
km	Kilometer
kpc	kiloparsec
λ	wavelength
λ_{eff}	Effective wavelength of a filter
$M_\odot$	mass of the Sun
M_V	absolute visual magnitude

mag	Magnitude
Mpc	Mega parsec
m	meter
mm	milli meter
μm	micro meter
milliarcsec	milli arcsecond
min	Minutes
Myr	million Years
nm	nanometer
$\Omega_{\rm m}$	Matter density of the Universe
Ω_{Λ}	Vacuum energy density of the Universe
pc	parsec (unit of distance)
R_V	ratio of total to selective extinction at visible band
§	Section
s, sec	second (unit of time)
τ	optical depth
$v_{\rm ph}$	Photospheric velocity of supernova
X	air mass
yr	year
yrs	years
z	Redshift

Abbreviations

AIMPOL	ARIES IMaging POLarimeter
ARIES	Aryabhatta Research Institute of observational SciencES
Alt	Altitude
Az	Azimuth
CBET	Central Bureau for Electronic Telegrams
CCD	Charge Coupled Device
CCSNe	Core-collapse supernovae

CRTS	Catalina Real-Time Transient Surveys
CSM	Circumstellar Medium
CSS	Catalina Sky Survey
DAOPHOT	Domanian Astrophysical Observatory PHOTometry
DFOT	Devasthal fast optical telescope
EPM	Expanding photosphere method
Fig.	Figure
FITS	Flexible Image Transport System
FOV	Field of view
FWHM	Full Width at Half Maximum
HEASARC	High Energy Astrophysics Science Archive Research Center
HCT	Himalayan Chandra Telescope
HFOSC	Hanle Faint Object Spectrograph and Camera
HST	Hubble Space Telescope
IAO	Indian Astronomical Observatory
IAU	International Astronomical Union
IAUC	International Astronomical Union Circular
IFOSC	IUCAA Faint Object Spectrograph and Camera
IGO	IUCAA Girawali Observatory
IIA	Indian Institute of Astrophysics
IR	Infra-Red
IRAF	Image Reduction and Analysis Facility
ISM	Interstellar Matter/Medium
IUCAA	Inter University Center for Astronomy and Astrophysics
LCOGT	Las Cumbres Observatory Global Telescope
LOSS	Lick Observatory Supernova Search
LTE	Local thermodynamic equilibrium
MCG	Morphological Catalogue of Galaxies
NED	NASA Extragalactic Database
MIDAS	Munich Image and Data Analysis System

NASA	National Aeronautics and Space Administration
NGC	New General Catalogue
NOAO	National Optical Astronomy Observatories
PGC	Principal Galaxies Catalogue
PSF	Point Spread Function
PTF	Palomar Transient Factory
QE	Quantum Efficiency
SED	Spectral Energy Distribution
SN	Supernova
SNe	Supernovae
SNR	Signal to noise ratio
ST	Sampurnanand Telescope
UT	Universal Time
UTC	Universal Time Coordinated
UV	Ultraviolet
UVOT	Ultra-Violet Optical Telescope
ZAMS	Zero Age Main Sequence

Contents

List of Figures

LIST OF FIGURES

List of Tables

LIST OF TABLES

Chapter 1

Introduction

Some class of stars die off extreme violently producing one of the most energetic explosions of the cosmos, these are called "Supernovae". They release an enormous amount of energy in form of energetic particles and radiation in almost all wavelengths: X-rays, gamma rays, infrared, ultraviolet, radio waves, cosmic rays and neutrinos. The radiative energy alone, which is just a minor fraction of total energy output, is sufficient enough to outshine the brightness of entire host galaxy. Supernovae are responsible for enrichment of heavy elements in the present universe. Big bang nucleosynthesis produced primarily hydrogen, helium in small fractions and some lithium, in the primordial universe. Heavier elements only up to iron are produced in stellar nucleosynthesis in massive stars. All elements heavier than iron are produced in explosive nucleosynthesis during shock breakout. As supernova explodes, all these synthesized material produced during stellar life or in supernova explosion, are dispersed away in the interstellar medium. Thus it would be appropriate to say that, supernovae provides the key elemental ingredients to the universe, for the formation of planetary systems and originating life on it. It also triggers the formation of next generation stars which provides the necessary heat for sustaining all life forms on Earth.

In a typical spiral galaxy like our Milk Way, it is expected to host approximately one or two supernovae in a century. Once such an event would occur, it would be a spectacular bright celestial object visible through unaided eye. However, the actual

brightness will depend on several parameters like distance and position in the galaxy leading to dust obscuration. The last supernova observed in our galaxy was in year 1604, the Kepler's Supernova, which was as bright as Jupiter. Possibly the best candidate to explode into a supernova in near future (in astronomical time scales) is the star 'Betelgeuse' in constellation of Orion. It is a red supergiant or radius ~ 1000 times to that of our Sun. Once Betelgeuse explode, it will be much brighter than any star in the sky, and possibly as bright as a half moon.

1.1 Historical observations

Astronomy being the oldest natural science studies since prehistoric times, when isolated studies were rarely recorded or communicated to rest of the world. Supernovae due to its transient nature, drew explicit attention of ancient astronomers. The earliest supernova recorded and partially documented in human history is SN 185. Chinese astronomers in 185 AD, identified this 'new star' in between constellations Circinus and Centaurus, which they described as the 'guest star' (Zhao et al., 2006). In 1006 AD another guest star appeared which was extensively observed by Arabic and Chinese astronomers (Winkler et al., 2003). Its estimated peak brightness was -7.5 visual magnitude, which was the brightest celestial event recorded till date. The widely observed supernova whose remnants gave rise to the famous Crab Nebula, exploded in the year 1054 reaching a peak visual magnitude of -4 and was observed for two years. Tycho Brahe on November 1572, noticed a 'new and unusual' (Burnham's Celestial Handbook 1978) star in the constellation Cassiopeia. Tycho initially found it as bright as Jupiter, which in couple of weeks turned similar to the brightness of Venus. He continued his observations as this new star fades and changes colour from bright bluish white to faint red, totally fading away from visibility after 16 months. The last observed galactic event was in 1604, which is also known as Kepler's supernova, named after Johannes Kepler for his contribution in extensive systematic observations which he carried out for 18 months.

During this period of last 400 years although we did not witness any Galactic supernova, this is because of thick interstellar dusts specially along line of sight

through galactic disk, which might be optically obscuring any such event. There are couple of young supernova remnants discovered which have been identified lately. One is Cassiopeia A, which was detected in 1947 as one of the strongest radio source even though it was optically never observed at the time of explosion, which is estimated to be in the year 1680. The second one is the youngest supernova remnant in our galaxy, G1.9+0.3 in Sagittarius constellation. The estimated year of explosion is around 1868, similar to Cassiopeia A, precursor supernova for G1.9+0.3 was also not observed at the time of explosion.

Since the invention of optical telescopes, the first supernova observed was a 7 magnitude event in 1885 in the Andromeda "nebula", which was otherwise not observable by naked eye. By the beginning of 19th century, with increasing number of such detected transients along with follow-up systematic studies, astronomers start to realize the unusual nature and large distances of these events, which they now designated a generic term 'nova'. In 1917, George W. Ritchey estimated distance to Andromeda nebula and realized the extragalactic origin of 1885 event, which led him to conclude the vast amount of energy being released in the process. Walter Baade and Fritz Zwicky pioneered detailed study and observation of this new class of objects. With the information of distance, they estimated the radiation energy output from a typical explosion is equivalent to the energy released by Sun during tens of millions of years. Having the idea of the tremendous energetics of these events, Baade and Zwicky first coined the name 'Supernova' in the year 1931. Following to the newly naming of these objects, Baade & Zwicky (1934) made a great leap by predicting that collapse of massive stars turn into neutron stars, releasing huge amount of energetic cosmic rays.

1.2 Triggering mechanisms in supernovae

As early as 1960s Hoyle & Fowler proposed two basic scenarios of stellar deaths on the basis of triggering mechanism of explosions.

1. *Thermonuclear supernovae:* thermonuclear runaway *or* detonation *or* deflagration of a white-dwarf progenitor.

2. *Core-Collapse supernovae:* explosion triggered by gravitational collapse of a dying star.

1.2.1 Thermonuclear Supernovae

Thermonuclear SNe are believed to occur form explosion of degenerate compact objects called white dwarfs. White dwarfs are common fate of lower mass stars ($< 8M_{\odot}$) which does not have enough mass to collapse and undergo supernova explosion. These stars at the end of main sequence phase, swells up to become redgiants, eventually shedding outer layer into planetary nebulae, leaving behind a compact carbon-oxygen degenerate cores called white dwarfs. Core up to $\sim 1.4M_{\odot}$, which is also known as Chandrasekhar mass limit, is supported by electron degeneracy pressure against gravity. In single degenerate scenario (Whelan & Iben, 1973), a white dwarf remaining from a died star in a binary system, may able to accrete matter from companion star which have swollen to become a giant and filled up the Roche-lobe to begin mass transfer. After accreting enough matter to reach the critical mass of $1.4M_{\odot}$, electron degeneracy is no more able to sustain the gravitational pressure, initiating a new chain of nuclear reaction, causing the entire white dwarf to disintegrate and explode into type Ia supernova. Due to uniformity of triggering mechanism and constant threshold mass of explosion, the energetics of all thermonuclear events are expected to be similar. Thus, having constant and large luminosity across all such event, it is used as an excellent standard candle for distance measurement. Another proposed mechanism for thermonuclear supernova is the double degenerate scenario (Iben & Tutukov, 1984; Webbink, 1984), in which explosion is triggered by merging of in-spiral binary white dwarfs. Such a mechanism is capable of explaining some of the subluminous Ia SNe observed. Although, there is no unambiguous proof for any of these two scenarios, the single degenerate scenario seems more favorable for most type Ia SNe observed.

1.2.2 Core-Collapse Supernovae

Core-Collapse supernovae (CCSNe) originate from massive stars ($> 8M_{\odot}$) when they undergo gravitational collapse at the end of stellar life cycle. Unlike lower mass stars which end up into degenerate C-O core being unable to reach temperature for carbon fusion, these massive stars undergo a series of further nuclear fusion reactions until Fe core is formed. Detailed stellar evolutionary and nucleosynthesis models have been built by many groups (Woosley, 1988; Woosley et al., 2002). In Table. 1.1 various nuclear burning phases and stages of core collapse for a massive star is shown along with theoretical estimates of core temperature, density and duration of corresponding stages are tabulated.

Nuclear burning: During main sequence stage, H fuses in the core to form He nuclei until the hydrogen there is used up. Helium burning sets in when the core contracts, which fuses to forms carbon. Simultaneously H burning also begins at the surrounding layers and star swells up to form giant. At the end of He burning, C-O core is formed, which is reignited when core further contracts and temperature reaches more than 5×10^8 K if the core mass is $M_{\mathrm{CO-core}} > 1.06$ $M_{\odot}$. This critical core mass is achieved only by stars of initial mass approximately > 8 $M_{\odot}$. Following carbon exhaustion in the center, the core is now mostly composed of O, Ne and Mg. On further contraction carbon burning in shell continues. In stars $\lesssim 11$ $M_{\odot}$, O-Ne-Mg core becomes degenerate and further nuclear burning is halted, where supernova explosion occur when core reaches Chandrasekhar limit by addition of ashes from shell burning. On the other hand, for stars with masses more than 11 $M_{\odot}$ contraction continues to reach core temperature of 1.5×10^9 K when Ne is burned into O and Mg by a combination of photo-disintegration and α-capture. On further rise in temperature to 2.0×10^9 K, O burning also sets in the core to form Si. Similar to previous burning stages, O burning also continues in shell as core continue to contract. Following this, Si burning starts, as core temperature exceeds 3×10^9 K, giving rise to iron group elements (Fe, Cr). No further fusion reaction takes place as Fe has most stable nucleus. After each subsequent core and shell burning stages the outer burning shells have

Table 1.1: Evolutionary stages of a $25M_{\odot}$ star and theoretical estimates of core temperature, density and duration of the stage.

Stage	Core temperature (K)	Core density (kg m^{-3})	Duration of stage
Hydrogen fusion	4×10^7	5×10^3	7×10^6 years
Helium fusion	2×10^8	7×10^5	7×10^5 years
Carbon fusion	6×10^8	2×10^8	600 years
Neon fusion	1.2×10^9	4×10^9	1 year
Oxygen fusion	1.5×10^9	1×10^{10}	6 months
Silicon fusion	2.7×10^9	3×10^{10}	1 day
Core collapse	5.4×10^9	3×10^{12}	0.25 second
Core bounce	2.3×10^{10}	4×10^{15}	few milliseconds
Explosion	$\sim 10^9$	varies	10 seconds

advanced outward. Eventually forming an onion shell structure of different layers consisting of heavier nuclei at increasing depth with inert Fe core at the center. The sequence of processes following this stage is schematically represented in Fig.1.1.

Overcoming electron degeneracy: At the end of nuclear burning stages, the central core temperature is 4×10^9 K and its composition is governed by *nuclear statistical equilibrium* where the most abundant nuclei are those with the lowest binding energy, i.e. mainly Fe isotopes. Predominately due to neutrino cooling, the core start to become degenerate. However at extreme temperature and density electrons are relativistic and is unable to withhold the contraction even if the core is degenerate. A state of dynamical instability is reached continuing rapid collapse.

Neutronization and photo-disintegration: At very high density inverse β-decay occurs when electrons are captured into unstable heavier nuclei in the core. On capturing electron, proton gets converted to neutrons releasing electron neutrino and the reaction goes as follows

$$e^- + p \rightarrow n + \nu_e \quad ; \quad e^- + (\mathrm{A}, \mathrm{Z}) \rightarrow \nu_e + (\mathrm{A}, \mathrm{Z}-1). \tag{1.1}$$

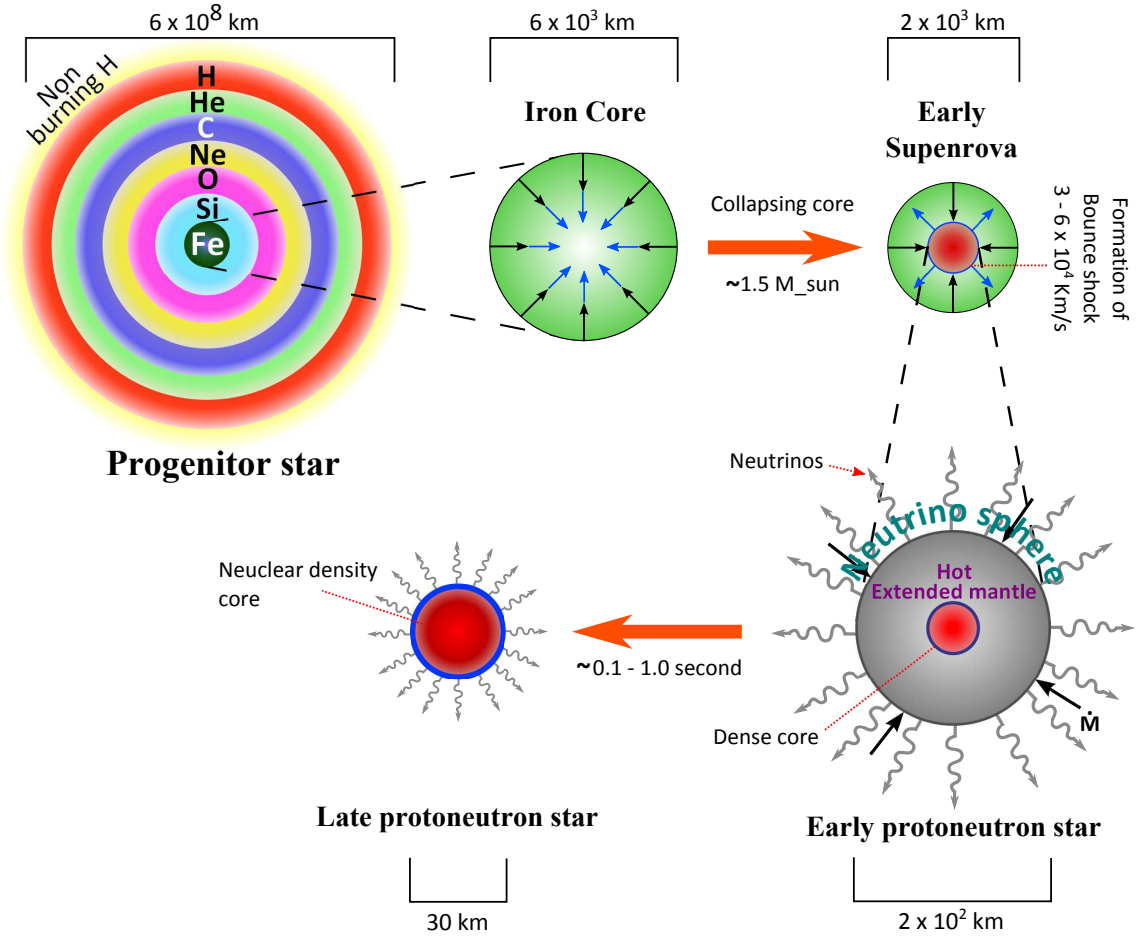

Figure 1.1: Schematic representation of sequence of undergoing processes in core-collapse supernovae. The straight arrows represent motion of mass while curly arrows represents neutrinos. The figure is reproduced from Burrows (2000).

The core continues to become neutron rich, a process also known as 'neutronization', as a result of which electron pressure decreases in the core which facilitates the collapse. In a significantly degenerate core further collapse is aided by the fact, that on electron capture average mass per free electron get increased, reducing the Chandrasekhar mass ($M_{\rm Ch}$). For a Fe dominated core $M_{\rm Ch}$ can be be as low as 1.26 $M_\odot$. In a massive contracting core photo-disintegration also plays a important role when temperature reaches $\sim 10^{10}$ K. Predominant Fe disintegrates into α particles and neutrons absorbing energy

of the order of 2 MeV per nucleon,

$$^{56}\mathrm{Fe} + \gamma \rightarrow 13\ ^{4}\mathrm{He} + 4\mathrm{n} \tag{1.2}$$

thereby decreasing radiation pressure which assists the collapse. This relation represents a statistical equilibrium where the balance is dependent on temperature.

Collapse and Core bounce: The process of collapse is extremely rapid ~ 10 msec and during this time density is $\sim 10^{10}$ g cm^{-3}. Electron capture continues enriching the core with neutrons, eventually turning the core into a stellar mass nucleus of neutrons approaching to a nuclear density of $\sim 10^{14}$ g cm^{-3}. With ongoing collapse the neutron rich core becomes degenerate and instantaneously becomes stiff and incompressible. Here the core collapse halts suddenly when its radius is ≈ 20 km. The gravitational energy released during the collapse of core alone is $\sim 10^{53}$ erg, which is several orders larger than the energy necessary to disrupt the envelope ($\sim 10^{50}$ erg). With the impact of in falling matter, the hardened core get further compressed by $\sim 50\%$ when it bounces back to preserve the neutron degeneracy, which is termed as *core bounce*. The acoustically detached free falling outer part of the core violently collides with the bounced core making a supersonic impact and generating a shock wave (or *bounce shock*) propagating outward. This marks the initiation of the explosion. Stirling Colgate and Montgomery Johnson in 1960 first proposed this modern model of CCSNe and stated that the bounce shock is sufficiently energetic to continue moving outward like a sonic boom ultimately disrupting the envelope as a so-called *prompt explosion*.

Failure of prompt explosion: A couple of issue were found to arise which prevents the explosion to occur. The post shock temperature is so high that complete phtodisintegration of constituent nuclei start to occur in ^{56}Fe dominated in-falling outer core, consuming huge amount of energy (9 MeV/nucleon) from the shock. The total energy absorbed in this process is so huge, that it is potentially equivalent to the all energy which the star has emitted during its

entire life in form of nuclear fusion. Moreover, the intense and energetic neutrino emission from the electron capture with free protons behind the shock will carry away largest fraction of the energy produced in collapse, which can easily escape from low density outer core. Due to these combined loss of energy from the shock front, the shock stalls before reaching the surface. Thus the prompt mechanism fails to stop the collapse and explode the star, rather the shock front retreats and star collapses into black hole.

Neutrino triggered delayed explosion: In 1965 Colgate & White put forth a model invoking heating due to neutrinos to trigger explosion. The principle idea behind the model is that, when the iron core collapses on the proto-neutron star energetic neutrinos are emitted when in turn heats the in-falling material and converts it into sufficient kinetic energy to reverse the implosion into explosion. However the biggest issue is to realize an apparently improbable scenario under which a noninteracting particle like neutrino, which can pass light years of lead without interacting, will interact and deposit energy within a collapsing core of size only few hundreds of kilometers. For this it is essential to understand the nature of these generated neutrinos and physical condition prevailing in the core. Neutrinos produced prior to collapse have typical energies just of the order of electron's thermal energy, whereas those produced during the collapse through electron capture have energies of the order of Fermi energy of relativistic electrons. Mean free path of neutrinos l_ν within a collapsing core with assumed typical energy, can be represented as,

$$l_\nu = 2 \times 10^{25} \frac{1}{\mu_e A} \left(\frac{\rho}{\mu_e} \right)^{-5/3} \text{ cm}. \tag{1.3}$$

This turns out to be $l_\nu \approx 10^7$ cm, which is of the order of the dimension of a collapsing core, while putting other parameters typical for a in-falling core ($\mu_2 \approx 2$, $A \approx 100$ and $\rho/\mu_e \approx 4 \times 10^9$ g cm^{-3}). Thus collapsing core become opaque to neutrinos, which can now only escape through multiple *neutral-current* scattering. Neutral-current scattering is a form neutrino interaction with nuclei and unbound nucleons under high density condition. Towards

the end of core collapse when the density is even higher, diffusion velocity of neutrons is smaller than in-fall velocity, thus neutrinos are effectively trapped within the core. This sphere within which neutrinos are trapped is termed as *neutrinosphere* which is effectively the newly formed proto-neutron star. With increasing density of trapped neutrinos within the core causes them degenerate and slowing down neutronization, which only continues with the diffused escape of neutrinos. Therefore the process of neutronization is delayed to several seconds, while the collapse only takes few tens of millisecond (and thats the timescale for prompt explosion). Neutrinos diffusing through the dense outer core deposits energy and heats up the region, some of which gets converted to kinetic energy reviving the previously stalled shock wave. This mechanism, however delayed, is energetic enough to overcome the ram pressure of imploding outer layers finally disrupting the star into supernova explosion. In 1982, James Wilson ran computer simulation for a relatively longer period of time, in contrary to previous unsuccessful attempts where explosion was expected quick and so the simulation was allowed to run only for few tens of millisecond after the bounce. His simulation also apparently frizzles momentarily, but evolved into successful explosion for the first time, but only half a second after bounce.

1.3 Brief summary of modern understanding and challenges in CCSNe research

One primary objective which always remained a major goal in theoretical understanding is to constrain the type of progenitors which can produce Fe or O-Mg-Ne core, collapsing which will give rise to such a catastrophe. Numerous work have been done along this line to theorize the undergoing processes (see, e.g. Eldridge & Tout, 2004; Heger et al., 2003; Woosley et al., 2002), but require observational validations to establish the theory. With the advent of modern computational resources, intense simulation studies have been done to understand the mechanism undergoing to convert the gravitational energy from collapse of $\sim 1.4 M_{\odot}$ metallic

core into a shock dominated explosion. The imploding envelope bouncing from the newly formed proto neutron star (NS) in unable to inject enough energy in form of shock which can explode the star (Janka et al., 2007; Woosley & Weaver, 1986). Collapsing core while forming NS releases large amount of neutrinos in all three flavors carrying away a total energy $\sim 10^{53}$ ergs. Even a deposition of small fraction of this neutrino energy is capable to drive the explosion (Janka et al., 2007). This proposed idea of core-collapse explosion has been verified from neutrinos detected at the time of SN 1987A explosion (Hirata et al., 1987). A total of 24 antineutrinos were detected by 3 detectors across the globe within a duration of less than 13 seconds.

SN 1987A which exploded in our Galactic neighborhood, Large Magellanic Cloud, initiated a new era of supernova astrophysics. Most of our present understanding is entirely theoretical and strictly require observational validation. Since the beginning of modern astronomy with advanced telescopes and detectors, researchers are prepared for long awaited Galactic core-collapse event to observe micro properties of supernova. Strong neutrino burst and gravitational wave are expected to be detected from such an event. It would be an opportunity to test existing theoretical predictions and constrain model for stellar evolution, explosion mechanism and elemental nucleosynthesis. In CCSNe, around 10^{51} ergs (1 foe) is in the form of kinetic energy, which is around 1% of the energy carried away by neutrinos, whereas all the energy radiated in form of light only sums up to 1 – 10% of kinetic energy. These SNe exhibits wide variation of physical properties, energetics, chemical composition and environmental properties, whose variation is much more diverse than type Ia counterparts.

With the use of powerful ground and space based telescopes, large archives of high resolution images haves been built for all nearby galaxies, which are searched for direct identification of progenitors after a SN is discovered. Massive progenitors identified from the pre-explosion images at the precise location of the SN, offers unique opportunity to study the star and its environment before it exploded and also to test predictions from theoretical models. The archive of high resolution HST images have major contribution in direct detection of progenitors. Nearby galaxies,

within 30 Mpc, have well resolved images of stellar populations. By late 1990s, researchers started looking for nearby SN to be discovered and get resolved pre-explosion images of the SN location from well prepared archives of HST and other high resolution ground bases facilities (Van Dyk et al., 1999). The first discovery of stellar progenitor in pre-SN image was for IIP SN 2003gd (Smartt et al., 2004; Van Dyk et al., 2003), which was revealed to be a Red supergiant (RSG) as was predicted from theoretical models. Along with the requirement of deep high resolution, it is found to be very essential to perform extremely accurate alignment and astrometry ($<$ 30 milli-arcsec) to avoid any mis-identification. Following SN 2003gd, a series of identification was carried out for all feasible SNe. Smartt et al. (2009) studied a sample of 20 such identifications of IIP progenitor and their carefully estimated mass distribution is used to perform maximum likelihood analysis to fit Salpeter initial mass function, estimating lower mass limit of $8.5 \pm 1.5 M_{\odot}$ and upper mass limit $16.5 \pm 1.5 M_{\odot}$. Smartt (2015) further extended the study to a total of 45 nearby SNe and their detected progenitors, however the estimated limits remains the same. The lack of high mass RSG progenitors having masses between 17 – 30 $M_{\odot}$ posses interesting and serious implications, which let us revisit the present understanding of core-collapse mechanisms.

SNe environment and location in host galaxies provide important clues to masses of stellar population and hence nature of their explosion. CCSNe are associated to HI regions in arms of spiral galaxies where star formation takes place and hence massive progenitors as expected. However no preference has been found for type Ibc SNe association with HI regions as compared to Type II (Van Dyk, 1992; Van Dyk et al., 1996), on the other hand thermonuclear SNe are found in all types of galaxies including spirals and ellipticals.

1.4 Supernova classifications

SNe are broadly classified as Type I and Type II, based on the presence of Hydrogen Blamer lines in their spectra (Minkowski, 1941), which directly indicate hydrogen abundance in the explosion. SNe I does not show any prominent H lines,

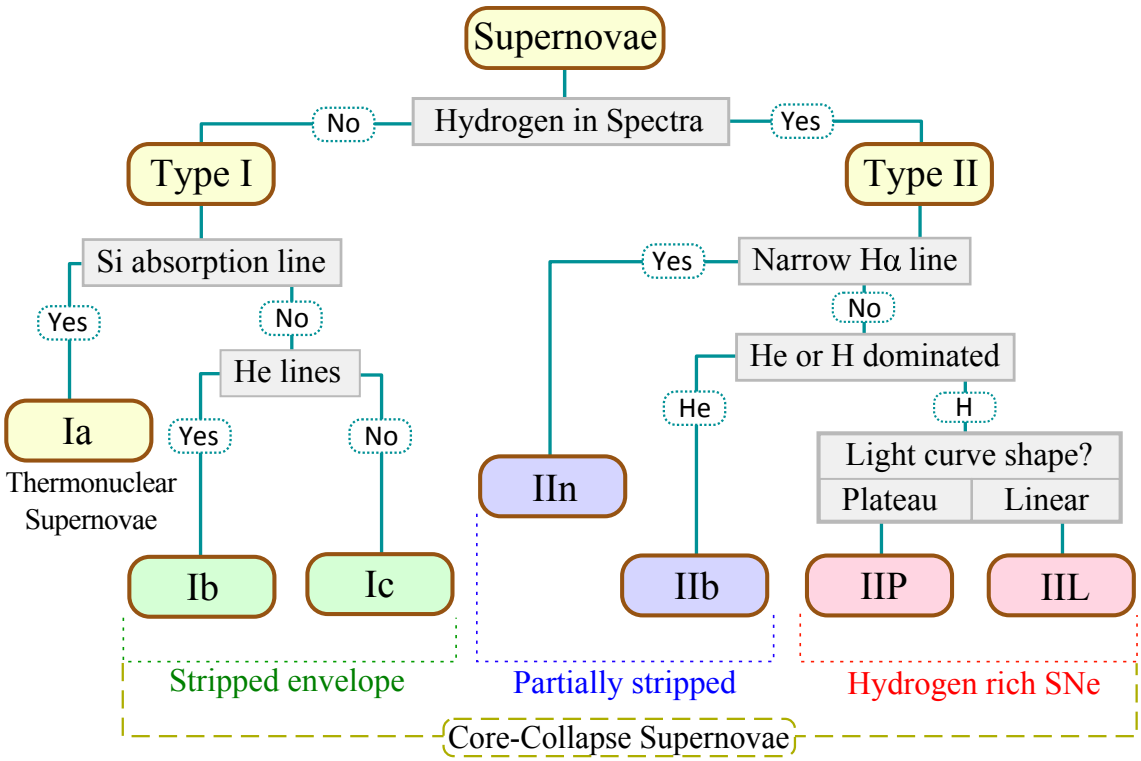

Figure 1.2: Supernovae classification scheme.

whereas SNe II show strong Balmer lines throughout the spectral evolution. With ever increasing pool of SNe data, astronomers start to realize the vast diversity in characteristics among each of these SNe. Detailed taxonomy scheme was developed (Filippenko, 1997) which is pictorially presented in Fig. 1.2. Most of these subclasses are based on spectral features identified during early phases. As already discussed, thermonuclear explosions obeys a uniform triggering mechanism resulting into a unique set of properties, thus it form only a single subclass of SNe, which is Type Ia. As it is obvious, their white-dwarf progenitors lacks hydrogen, so no Balmer lines are observed and thus they comes under Type I. On the other hand CCSNe originate from progenitor of various masses, metallicity and environments, which decides the evolutionary path they follows. As a consequence, these explosions show vast diversity in observed proprieties and constitutes all other (except Ia) subclasses in the taxonomy scheme. Thus, CCSNe observed properties, both light curve and spectral, are closely related to pre-SN evolution which they undergo.

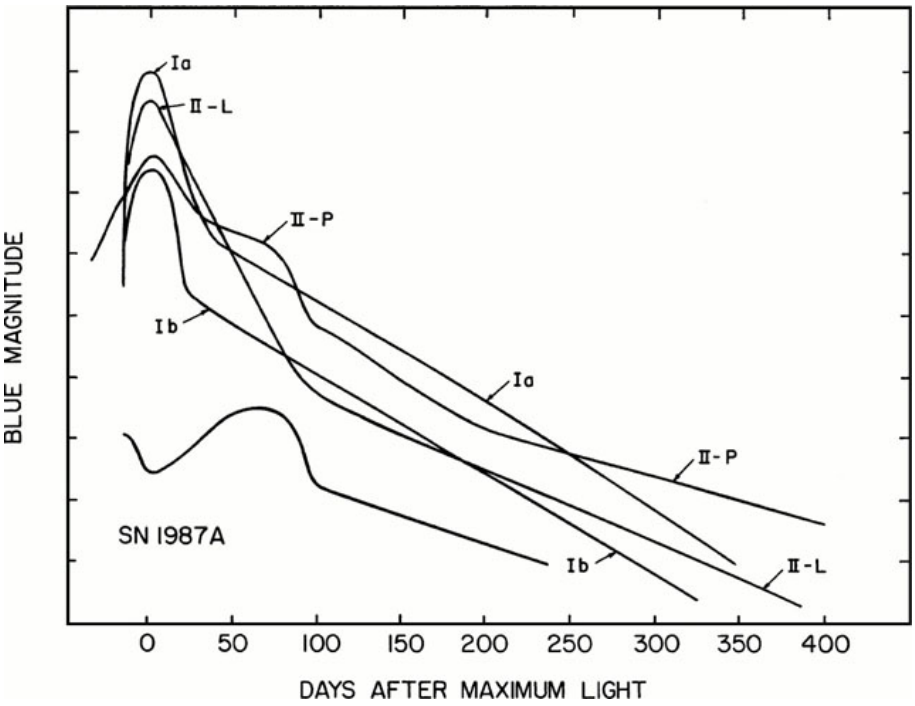

Figure 1.3: The blue band light curve templates for various SNe types (adopted from Filippenko 1997).

The light curve and spectral characteristics, properties of progenitors and their environment are briefly described in Table 1.2 for comparison. Although each of these SNe subtypes have characteristic and distinguishable optical light curve (see Fig. 1.3), SN spectra are used for preliminary but robust classification of these event are at early age. SN spectra start to unveil a wealth of information at very young age, when photometric observations are not even sufficient to form any distinguishable part of the light curve. The criteria of classification for most of these sub-classes are based on spectral features, except for Type IIP and IIL, which have distinguishable light curve decline rates during first $\sim$ 90 days. Fig. 1.4 shows canonical spectra for SNe Type II, Type I and their subtypes. Spectra at three different phases of SN are shown in the figure – (i) spectra taken during maximum light are used for classification, (ii) spectra of a 3 week old SN shows evolved metallic line features and (iii) year old nebular phase spectra shows various metallic emission lines.

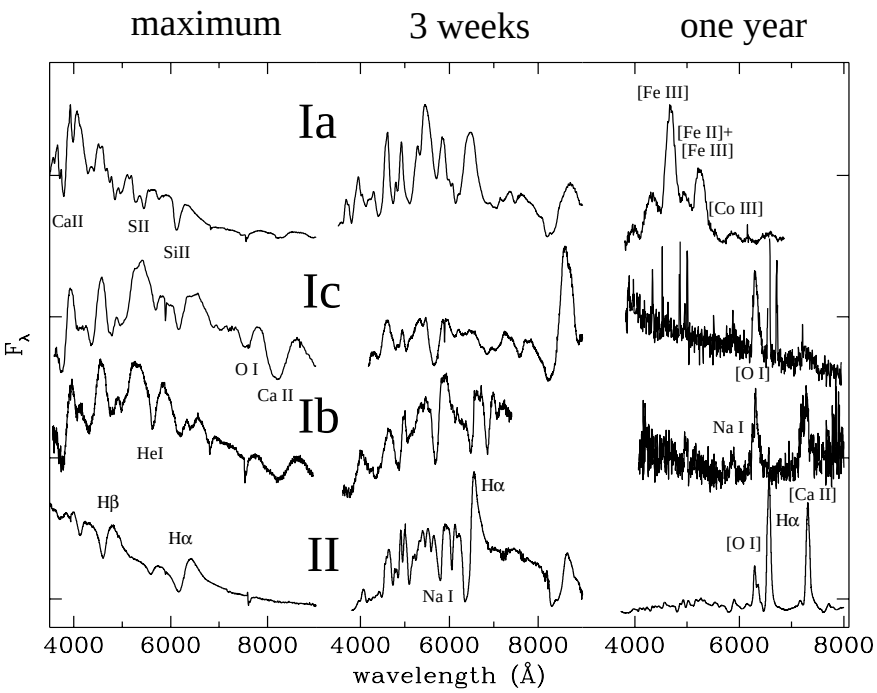

Figure 1.4: Spectra for various SN types shows at three different phases – during maximum light, at a age of 3 weeks and one year (adopted from Turatto 2003).

Table 1.2: Various supernova classes and their characteristic properties.

SN Type	Charecteristics	Progenitor & its environment
Ia	**1)** H lines are not present in the spectrum.	**1)** White dwarf accreting matter from its companion in a binary system.
	2) Strong Si 6150 Å absorption line are visible during maxima.	**2)** Merger of two white dwarfs.
	3) Late time spectrum is dominated by Fe group elements.	**3)** Found in all type of galaxies and never associated with H II regions.
Ib	**1)** No H lines in spectrum	**1)** Core collapse of massive stars ($>$ $30M_\odot$) with H envelope stripped, either due to wind or roche-lobe overflow in a binary system.
	2) No Si lines in the spectrum	
	3) Strong He 5700 Å absorption line can be observed.	**2)** Massive Wolf-Rayet stars are the probable progenitors.

Table 1.2 - continued.

SN Type	Charecteristics	Progenitor & its environment
	4) O I & Ca II lines are present in the nebular spectra.	**3)** Generally associated with star forming regions.
Ic	**1)** No H lines in spectrum **2)** Nither Si nor He lines are present in the spectrum. **3)** Strong absorption lines of O I & Ca II are present in the spectra.	**1)** Core-collapse of massive stars, which have stripped off both their H and He envelopes. **2)** Massive Wolf-Rayet stars are the probable progenitors. **3)** Always associated with star forming regions.
IIn	**1)** H lines are present in spectra. **2)** Spectra are dominated by narrow emission lines **3)** Light curve rising part is relatively faster, luminous peak brightness with a very slowly light curve decline. **4)** Strong ejecta-CSM interaction signatures found in observations.	**1)** Massive LBV or WR stars ($\gtrsim$40 $M_\odot$), with huge H-envelope. **2)** Core-collapse SNe. **3)** Submerged in/ CSM material shredded off by progenitor during pre-SN evolution. **4)** Always associated with the star forming region of the host galaxy.
IIb	**1)** H lines are found in the early spectrum, but gradually disappears at late epochs. **2)** He lines similar to type Ib, start to appear after reaching peak brightness **3)** O I, Ca II lines are visible during late phases of spectra.	**1)** Probably the progenitor has lost a major fraction of H envelope during pre-SN evolution. **2)** Core-collapse is the basic triggering mechanism.
IIP	**1)** Characteristic P-Cygni profiles of H is visible through out the spectral evolution. **2)** O I, Ca II are present in nebular phase.	**1)** Progenitors are red supergiants having extended H envelope. **2)** Core-collapse triggers explosion. **3)** Direct observational evidences found to show masses $8 - 17M_\odot$.

Table 1.2 - continued.

SN Type	Charecteristics	Progenitor & its environment
	3) Light curve shows a prolonged plateau of $\sim 80 - 100$ days.	**4)** Generally explosions are found in relatively clean CSM environment in spiral arms of host.
IIL	**1)** Featureless early spectrum with slight impression of Hα emission. **2)** Very similar to IIP SNe. **3)** Light curve shows a fast and linear uninterrupted decline after maximum until end of photospheric phase. **4)** Hα and Hβ velocities are higher and its profile of temporal evolution is flatter as compared to IIP counterpart	**1)** Probably more massive RSG progenitors than IIP's but less thinner H envelope. **2)** Some fraction of H lost during pre-SN evolution. **3)** Like all SNe II core-collapse is the triggering mechanism. **4)** Associated with star forming regions.

Some of these SN subtypes, does not have very distinguishable spectral characteristics at very early times, often leading to misclassification, which are re-identified when SN is more evolved. For examples, SNe IIb shows H I lines in early spectra like any Type II, but mostly after attaining peak light they start to show Type Ib characteristics, i.e. lack of H and presence of He lines in spectra. Another misleading SN Type is IIL, which is purely based on light curve characteristics, i.e. fast decline of light curve distinguishes these from Type IIP, otherwise their early spectra are very similar to type IIP. To minimize such error and to have a robust and unified algorithm for SN classification based on early spectrum, software tools like GELATO (Harutyunyan et al., 2008) and SNID (Blondin & Tonry, 2007) have been developed which perform cross-correlation matching of a given spectrum with its growing database of well classified SN spectra and finds the best match spectrum along with its SN Type and age.

Over time with growing body of observational data, several authors have revisited many aspects of historical classification schemes to understand its possible

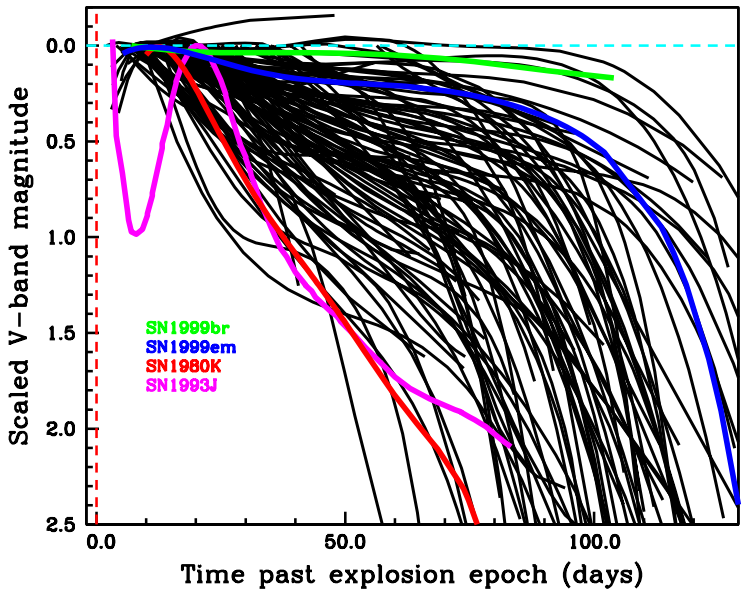

Figure 1.5: Continuum of 116 SNe II V-band light curves normalized to peak magnitudes, as presented by Anderson et al. (2014b). Some archetypal SNe 1999em, 1999br (Type IIP), 1993j (Type IIb) and 1980K (Type IIL) are also shown on the light curve continuum.

implications. Arcavi et al. (2012) analyses a sample of 15 SNe II and reported to find three distinct classes of events based on light curve decline rates, viz. plateau, slow declining and rapid declining, which they related to SN Type IIP, IIL and IIb respectively. This possessed serious implication on their origin, which might reflect their very distinct progenitor systems. Anderson et al. (2014b) extended a similar study on a large sample of 116 SNe II, where they found a continuum distribution light curve properties (see Fig. 1.5) and clearly disapproving any bimodality to classify into distinct subclasses. This implies they all are originating from physically similar progenitors, but with variable amount of H envelope, which is responsible for varying light curve slope, where a thin H envelope would result into a fast decline. From the study they also found an interesting anti-correlation between plateau slope and its duration, which is also evident from Fig. 1.5. Faran et al. (2014) also attempt

to reestablish SNe II taxonomy on basis of light curve decline rate. They proposed that a decline of 0.5 mag during first 50 day of light curve would qualify the SN as type IIL. However such a rigid criteria would classify more than 50% of all SNe II presented in sample of Anderson et al. (2014b), which is a significantly large fraction. Faran et al. (2014) also presented templates of SNe IIP and IIL light curves from well classified SNe sample. Although it is evident that these SNe do not form distinct subclasses in term of progenitor properties, but following the historical classification scheme (Barbon et al., 1979) based on template light curves would imply variable amount of H envelope in the explosion. However, it must be remembered that a number of SNe (e.g. SN 2013hj) would also fall in an intermediate position in broad continuum of SNe II diversity.

1.5 SNe spectra

SNe spectra and its evolution provide a vast amount of information about the explosion. Identification of spectral lines reveal the presence of various atomic lines and provide clues about their composition and abundances. These information coupled with temporal variation are useful to test various pre- and post-SN evolutionary models to constrain progenitor properties. Spectra act as a direct probe to examine the line emitting region above the evolving SN photosphere. Characteristic line profiles and their evolution also tell us about the kinematics of associated line forming region for corresponding ions.

A SN spectra during photospheric phase is strongly dominated by 'P-Cygni' profile from various atomic lines which are indicators of expansion. Formation of P-Cygni profile is schematically represented in Fig. 1.6. A thermal continuum is produced in the hotter and deeper photosphere. Absorption lines are formed at the cooler envelope above photosphere but only from the region along the line of sight which is moving towards the observer at the velocity of expansion. While the superimposed emission counterpart is produced by scattering of light from the entire spherical envelope. Thus, summing up all the emission components from the entire envelope would result into broadened emission profile at rest position.

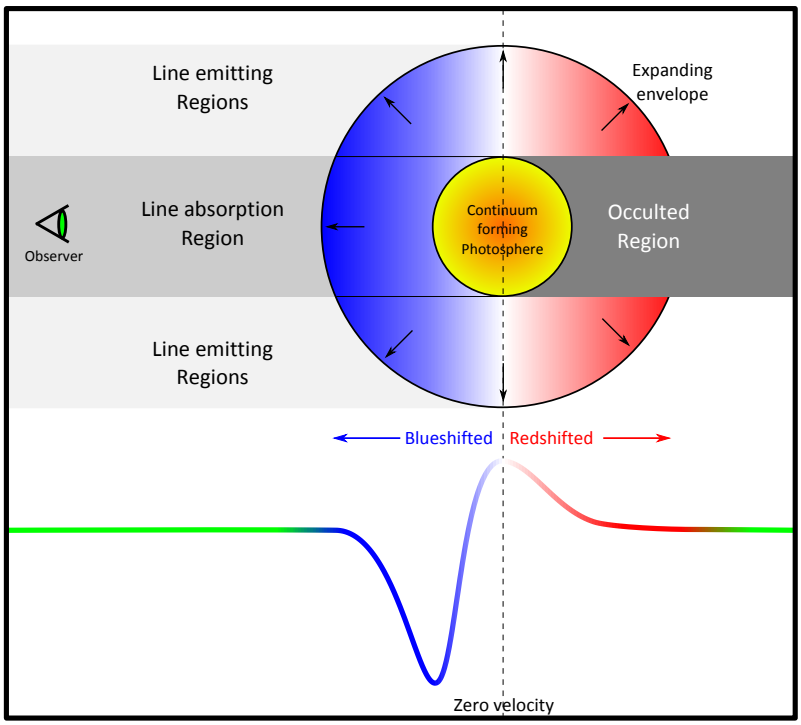

Figure 1.6: Formation of P-Cygni profile as viewed form the direction of observer. In the envelope and spectrum, the red and blue colors indicate the red and blue shifted component with respect to rest wavelength in white (or zero velocity dotted line). The green parts in the spectrum represent continuum.

The resultant of the superimposition of this emission with blueshifted absorption counterpart is the P-Cygni profile. In a realistic SN atmosphere the situation is bit more complex. The optically thick photosphere partially occults the receding part of the envelope and also the photons from rest of the receding hemisphere have to suffer some extinction as it traverse through the foreground envelope of considerable optical depth. As a result of this biasing, emission profiles are found to somewhat blueshifted. Therefore, the resultant P-Cygni profile will have a absorption minima blueshifted by the expansion velocity along with a emission counterpart, which is also somewhat blueshifted but is tied with density structure of ejecta (Anderson et al., 2014a).

As a SN evolves rapidly with decreasing parameters like – effective temperate, velocity of photospheric layer and optical depth of envelope; line profile changes and

accordingly SN spectra evolve. Due to expansion and recombination of envelope, the optically thick photosphere recedes inwards progressively revealing deeper layer within the ejecta having lower expansion velocity. Thus, studying the time evolution of spectra we can get detailed structural and kinematic information of the ejecta up to the core. However, as the supernova evolve number of atomic species with all associated lines starts showing up and crowding the spectra. Heavy blending of lines occurs and thus it would require detailed spectral synthesis models to recover information from spectra.

During early stage shortly after the explosion, CCSNe spectra shows featureless blue continuum as the almost entire ejecta is optically thick and have not got enough time to rarefy. Within few days broad and extended P-Cygni profiles for the most abundant H and He species start to appear in the spectrum[1]. Within few weeks other metallic lines of Fe II, Na I, Ca II, Sc II in form of P-Cygni start to dominate the spectra. In type IIP/L He lines disappear by this time and H lines continues to remain visible throughout the evolution. At even later stage, a couple of months old SN also show traces of Ba II, Ti II and sometimes Si II, whereas the existing metallic lines continue to become stronger. Subsequently as the ejecta becomes transparent and supernova enters nebular phase (age $> 150-200$ days), the spectrum is dominated by Hα, Na I emission and forbidden emission lines of O I, Ca II, Fe II and Mg I. Further detailed review of SNe spectra are presented by several authors, e.g. Filippenko (1997); Turatto (2003); Turatto et al. (2003).

Sometimes atypical features are found on careful inspection of spectra, revealing information about unusual circumstance or phenomenon which SN has undergone. A symmetric or double peaked Hα emission in nebular phase spectra indicate asymmetric or bipolar distribution of ^{56}Ni within ejecta but with a spherical H envelope (Chugai, 2006; Chugai et al., 2005). Such asymmetric feature has been reported by number of authors in several SNe, e.g. SN 1999em; Leonard et al. (2002c), SN 2004dj; Chugai et al. (2005) and SN 2013ej Bose et al. (2015b). Signatures of ejecta-CSM interaction is often detectable in Hα and Hβ line profiles with a superimposi-

[1]Here a generalized description of CCSNe spectral evolution is presented, actual presence and strength of of various atomic lines are associated with the class of SN, for example in SNe I hydrogen will not be a dominant component.

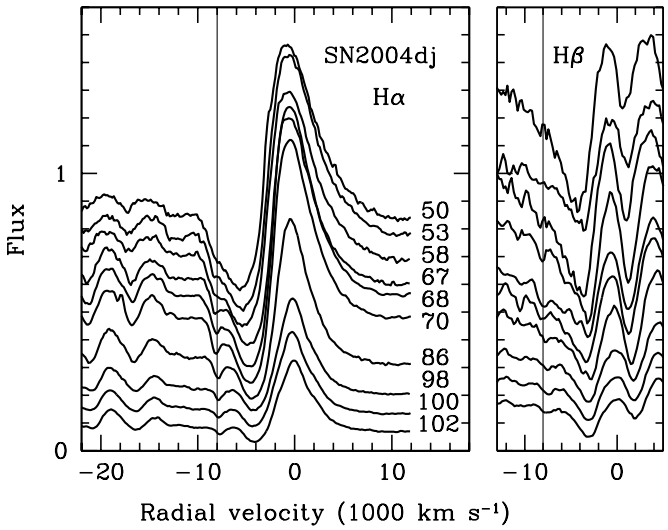

Figure 1.7: Signature of ejecta-CSM interaction as high velocity features in Hα and Hβ profiles. The spectral evolution is for type IIP SN 2004dj (Chugai et al., 2007).

tion of high velocity (HV) features. Such HV features are visible as superimposition on the blue wing of SN P-Cygni, e.g. SNe 1999em, 2004dj (Chugai et al., 2007), SN 2009bw (Inserra et al., 2012b), SN 2012aw (Bose et al., 2013), or weakly blended HV feature recovered on careful analysis as in SN 2013ej (Bose et al., 2015b). Fig. 1.7 shows spectral evolution of Hα and Hβ for SN 2014dj. The visible HV features are marked with vertical lines, which shows that these HV features start to appear after mid-photospheric phase and continue to evolve stronger but remain unchanged in position. Chugai et al. (2007) argued that SN ejecta can interact with the cooler dense shell of CMS material, which might have originated from the pre-SN mass loss in the form of stellar winds. Their analysis showed that such an interaction can lead to the detection of HV absorption features on bluer wings of Balmer lines due to enhanced excitation of the outer layers of unshocked ejecta.

SNe light traveling through large distances collect information about each of the intervening medium and their spectrum would exhibit all those information in form of various spectral features. All the medium which will leave their impression in the spectrum includes – the SN circumstellar medium, intergalactic medium, interstellar medium of host galaxy as well as Milky way and also the Earth's atmosphere if

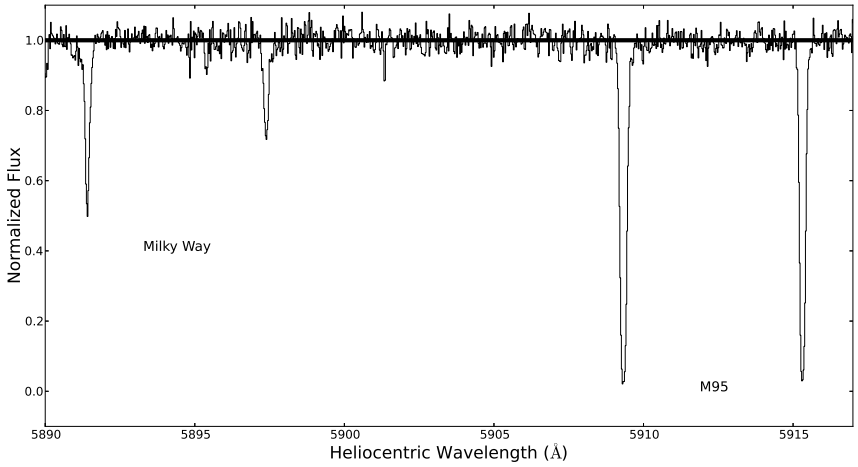

Figure 1.8: A high resolution spectrum of type IIP SN 2012aw showing resolved Na I D doublet (D1 λ5896 Å and D2 λ5890 Å) one for the Milky way and other at the redshifted position of host galaxy (M95). Equivalent width of these narrow lines are estimator of host galaxy and Milk Way extinction. Spectra taken from Van Dyk et al. (2012).

observed thorough ground based telescopes. One immensely important application of such a feature is to determine line of sight extinction, which itself a very important parameter in SN studies. The dust in ISM of host galaxy and Milky Way will produce narrow absorption features of Na I D doublet (D1 λ5889.95 Å and D2 λ5895.92 Å) at respective redsifted positions of each medium. A high-resolution spectrum of SN 2012aw is shown in Fig. 1.8 with resolved Na I D1 and D2 lines for both Milky Way and host galaxy. The equivalent width of Na I D absorption feature is found to be correlated with the reddening $E(B-V)$ estimated from the tail of SN Ia colour curves (Barbon et al., 1990; Poznanski et al., 2012b; Turatto et al., 2003). Therefore, using the correlation it is possible to independently estimate line-of-sight reddening components due to host galaxy and Milky Way.

Nebular phase spectra is also an important probe to investigate dust formation during late phases. A late nebular phase SN spectrum may show a blueshifted asymmetry in Hα emission profile indicating dust formation. The skewness of the profile is a result of preferential attenuation of red wings due to formation of dust in the ejecta. The indication of dust formation is seen in SN 1999em after 500d

(Elmhamdi et al., 2003b), SN 2004et after 320d (Maguire et al., 2010; Sahu et al., 2006) and in SN 2006bp at a much earlier age (350d) (Quimby et al., 2007).

1.5.1 SYNOW – a parametrized spectrum synthesis model

SYNOW (Branch et al., 2002; Fisher et al., 1999, 1997) is a highly parameterized spectrum synthesis model with pure resonant scattering line profile formation, used for direct analysis of observed SN spectrum. There are detailed non-LTE radiative transfer spectral synthesis models available like CMFGEN (Dessart & Hillier, 2005c) and PHOENIX (Baron et al., 2004), but LTE code like SYNOW is widely used as it offers quick and low computational resource intensive execution to produce resonant scattering line profiles. SYNOW assumes simple LTE model atmospheres having a sharp photosphere emitting a blackbody continuum and a spherically symmetric SN expanding homologously; the line formation is due to pure resonant scattering and radiative transfer is solved by employing the Sobolev approximation (Jeffery & Branch, 1990; Sobolev, 1957). The optical depth τ profile is a function of velocity (which is assumed to be scaled along the radial distance of a layer) either as – (i) power law; $(v/v_{phot})^{-n}$ or (ii) exponential; $exp\left[-\frac{v-v_{phot}}{v_e}\right]$ or (iii) Gaussian; $exp\left[-\frac{(v-v_{phot})^2}{2\sigma^2}\right]$, where n, v_e and σ are respective profile fitting parameters. A reference line profile for a given ion species is calculated for its τ value and rest of the lines are computed from Boltzmann statistics. The model input parameters are photospheric velocity v_{phot}, a series of ionic species with their corresponding τ values, radial distribution in terms of velocity ranges, optical depth profile and profile parameters and excitation temperature of ions.

One important aspect of SYNOW modelling is the concept of 'detachment' of an ion. When the minimum velocity of a line-forming layer is higher than that of the photospheric layer, the ion is said to be detached, which results into flat topped emission and blueshifted absorption counterpart of the line profile in synthetic spectra produced by SYNOW. In a realistic scenario this becomes important for H I lines as they are essentially formed at much higher velocities than photospheric velocities. Therefore, only the detached scenario for H I reliably fits the blueshifted absorption trough in the observed spectra. In Fig. 1.9 (**Left**) a synthetic Hα profile is shown

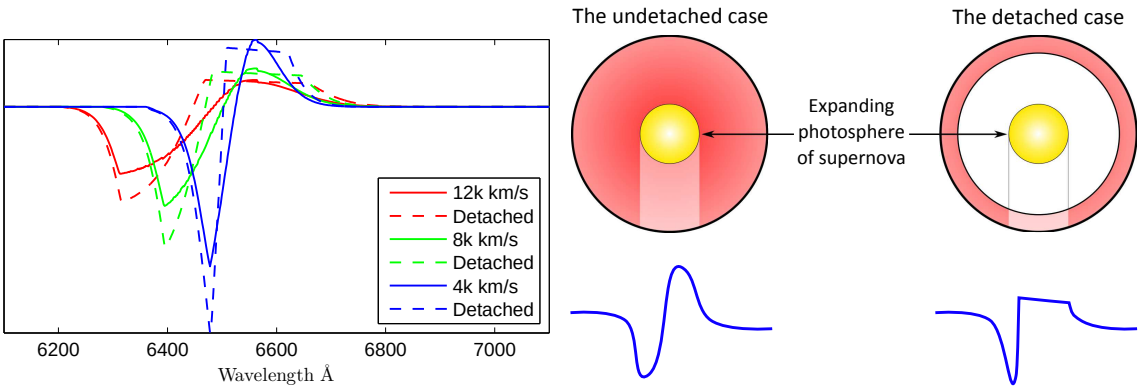

Figure 1.9: **Left:** SYNOW generated synthetic, continuum normalized Hα profile at three different velocities but keeping same τ. Profiles with dotted lines are for same velocity and τ but detached by 1k km s^{-1} from photosphere. **Right:** Line profile formation scenario when line forming layer (shell) is detached and at higher velocity than photosphere.

by changing velocity (4k, 8k and 12k km s^{-1}) of line forming layer (but constant τ and undetached) to demonstrate the variation of the P-Cygni profile. Now, keeping the same configuration but layers are detached from photosphere by 1000 km s^{-1} resulting into flat topped emission with deeper and narrower absorption, however the position of minima remains unaltered. The physical scenario of detachment is schematically shown in Fig. 1.9 (**Right**), when the forming layer is physically connected with the photosphere a complete P-Cygni profile is produced, now when the layer is detached from photosphere and the line forming layer is confined in a shell as assumed in SYNOW, a flat topped emission with narrow absorption will form, which will further vary with the extent of detachment.

A synthesized spectrum is shown in Fig. 1.10 which is generated to fit late plateau observed spectrum of a type IIP SN 2013ab. In this example, the set of atomic species used to generate the spectrum are H I, He I; Fe II; Ti II; Sc II; Ca II;Ba II; Na I; Si II; O I and N I which facilitated the identification of all atomic lines and subtle features in observed spectrum. Due to LTE approximation SYNOW can not reproduce the underlying continuum of the SN spectrum during late phases. Also due to several simplified assumptions involved in the model, it is not useful to determine physical parameters like chemical abundances and true optical depths. However,

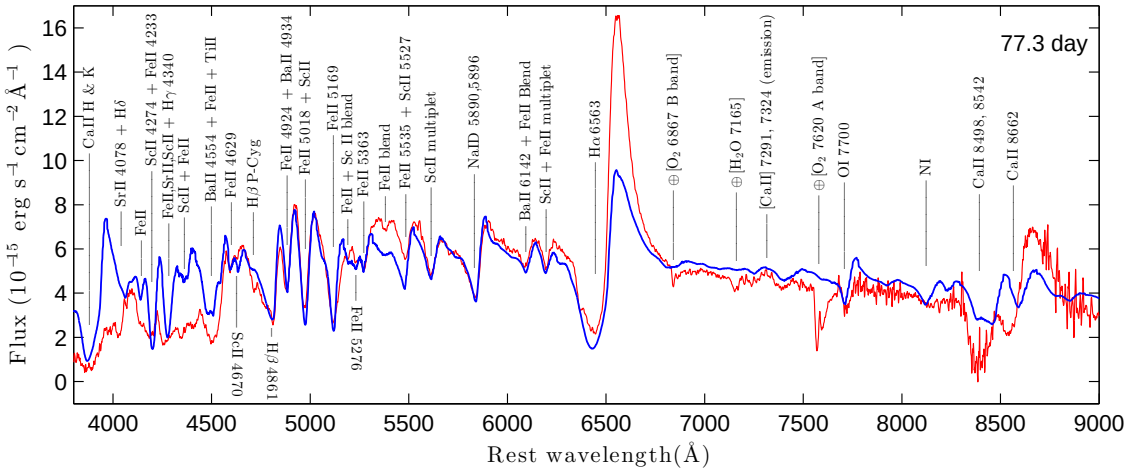

Figure 1.10: A synthetic spectrum (blue) generated from SYNOW model is fitted on a spectrum of SN 2013ab (red) observed at 77d with all identified spectral features marked.

SYNOW employs all the necessary physical mechanisms which is adequate to reliably reproduce P-Cygni profiles and so it is sufficient enough for line identification in observed spectrum and to estimate line velocities by fitting with synthetic spectrum. Utilizing the capability of SYNOW to synthesize spectrum by simultaneously using various atomic species, we can carefully reproduce heavily blended line and subtle features as seen in SN spectrum. This improves the reliability to model the entire line blended profile and accurately estimate their velocities.

1.6 Polarization in CCSNe

One of the common notion in simplified SN studies, is to assume spherically symmetric explosion with stratified layers of various elements. However for a realistic SN the situation is bit more complex. There are evidences for a number of SNe explosions with significant departure from spherical asymmetry. Shapiro & Sutherland (1982) first proposed polarimetry as a tool to probe the explosion geometry, which over the time has proved to be a unique probe for studies. Analyzing the polarized light from a supernova can reveal the shape and distribution of matter ejected in the explosion. A hot and ionized SN atmosphere, specially for CCSNe, is dominated by free

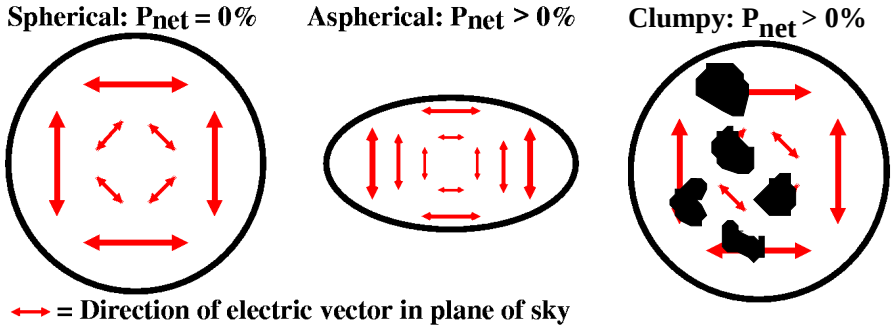

Figure 1.11: Schematic representation of electric vector components in spherical, aspherical and clumpy SN envelope. In case of spherical envelope net zero polarization is observed while for a aspherical or clumpy envelope net non-zero polarization is observed. (Image: Leonard 2007)

electron which are responsible for strong scattering. For a perfectly spherical electron scattering atmosphere, directional components of all the electric vector would exactly cancel yielding a net zero polarization. However any asymmetry pertaining to scattering atmosphere would result into some residual electric vector yielding a net non zero observed polarization. Fig. 1.11 shoes schematic representation of electric vector cancellation in spherical, aspherical and clumpy SN envelope. A clumpy ejecta would also give rise to net non-zero polarization even if the envelope is overall symmetric. The uneven distribution of clumps will result to non-uniform blockage of light yielding a net polarization. The amount of polarization observed depends on the degree of asphericity, density profile of atmosphere and also viewing angles. A polarization of 1% is expected for a asphericity of roughly 20% in the envelope (Leonard & Filippenko, 2005).

CCSNe are often found to show significant degree of polarization in optical and IR bands (Leonard & Filippenko, 2001; Leonard et al., 2001; Pereyra et al., 2006; Wang et al., 2002a; Wang & Wheeler, 1996). SNe with hydrogen envelope stripped (Type Ib/c) or partially stripped (Type IIb or IIn) exhibit higher level of polarizations as compared to SNe with intact H envelope like in SNe IIP, which is typically about $0.5 - 0.8\%$ polarization. The thick H envelope suppresses the observed asymmetry, whereas probing deeper towards the central part of the explosion more polarization is observed implying higher degree of asymmetry in electron scattering

atmosphere (Leonard & Filippenko, 2005). However, in SNe IIP polarization enhancement is observed towards the end of plateau as SN starts to enter the nebular phase, where the hydrogen recombination is close to completion, and with decreasing opacity the inner asymmetric core is being revealed (e.g. SN 2004dj; Leonard et al., 2006). Besides asphericity in electron scattering atmosphere or presence of foreground clumps, some amount of polarization may also originate from scattering by dust environment (Wang & Wheeler, 1996), asymmetric distribution of radioactive ^{56}Ni (Chugai, 2006) or asymmetric ionization of outer envelope due to shock originated in CSM interaction.

The first broadband polarimetric observation was done for SN 1987A (Barrett, 1988) demonstrating significant polarization and its time evolution. Late time *HST* observations of spatiality resolved ejecta revealed elongation in a direction consistent to the polarization angle inferred from polarimetry (Wang et al., 2002b), which validated our understanding to use polarimetry as a probe for SN explosion geometry. SNe 1999em and 2004dj are extremely well studies and observed spectropolarimetrically, which presented detailed insight of these explosions (Leonard et al., 2001, 2006). While spectropolarimetry has advantage of wavelength resolved polarization information, on the other hand broadband polarimetry is useful to extract overall polarimetric information without the requirement of bight SN or powerful observational resources and is sufficient to infer the asymmetry of explosion.

1.7 Model of SNe II light curve

By performing theoretical modeling to reproduce observable quantities we can fetch information about the progenitor properties and parameters of explosion. Detailed hydrodynamical models have been built be several groups (e.g. Bersten et al., 2011; Falk & Arnett, 1977; Pumo & Zampieri, 2011; Utrobin, 2007) to accurately analyze observed light curves of SNe along with spectroscopic information to estimate progenitor and explosion properties. Although there are certain discrepancies in derived parameters from object to object, but the overall results are consistent to the accepted paradigm of SN explosions and also to that estimated from direct detection

of progenitors for handful nearby SNe. However application of simple numerical or analytical models (Arnett, 1980, 1982; Arnett & Fu, 1989; Chatzopoulos et al., 2012; Popov, 1993; Zampieri et al., 2003) can also be useful to get preliminary yet reliable estimates of the parameters without running resource intensive and time consuming hydrodynamical codes. Here we describe one such simple semi-analytical model originally formulated by Arnett & Fu (1989) which laid the foundation of more complicated hydrodynamical models of present time.

Soon after the shock breakout, the SN envelope is set into homologous expansion and its evolution is governed by first law of thermodynamics:

$$\frac{dE}{dt} + P\frac{dV}{dt} = \epsilon - \frac{\partial L}{\partial m} \tag{1.4}$$

where $E = aT^4V$ is the radiation energy per unit mass, $P = aT^4/3$ is the isotropic radiation pressure, the specific volume $V = 1/\rho$ and ϵ is the entire energy production per unit mass of the ejecta. Under photon diffusion approximation,

$$\frac{\partial L}{\partial m} = \frac{1}{4\pi r^2 \rho}\frac{\partial L}{\partial r} = -\frac{a}{r^2\rho}\frac{\partial}{\partial r}\left(\frac{cr^2}{3\kappa\rho}\frac{\partial T^4}{\partial r}\right) \tag{1.5}$$

In order to separate spatial and temporal components, a co-moving dimensionless radius x is defines as,

$$x = \frac{r}{R(t)} \tag{1.6}$$

where r is physical radius of any particular layer and $R(t)$ is the outer radius of the expanding envelope. The radial mass distribution is assumed to have exponential profile and thus the density structure is given as,

$$\rho(x,t) = \rho(0,0)e^{-\alpha x}\left(\frac{R_0}{R(t)}\right)^3 \tag{1.7}$$

where R_0 is the initial radius and the exponent α, is a small value.

After the shock breaks out, the ejecta is fully ionized which is predominantly hydrogen and its temperature is well above the recombination temperature T_{rec}. As the ejecta cools down, hydrogen start to recombine and recombination front

of co-moving radius x_i starts to recede which separates the ionized and recombined hydrogen. Matter confined withing this recombination sphere is dominated by Thomson-scattering and so the opacity κ_t is high enough for photon diffusion and thermalization to take place. Whereas ejecta above this layer is mostly neutral and transparent to optical photons. Thus, κ can be represented as a step function at the recombination front, under reasonable approximation for Roseland mean opacity at low density.

$$\kappa(x,t) = \begin{cases} \kappa_t & \text{if } \; x \leq x_i \; ; \quad T(x) \geq T_{rec} \\ 0 & \text{if } \; x > x_i \; ; \quad T(x) < T_{rec} \end{cases} \tag{1.8}$$

Assuming a strictly adiabatic expansion, $T \propto R(t)^{-1}$ and thus temperature can be represented as a function of space and time,

$$T^4(x,t) = \psi(x)\phi(t)T(0,0)^4 \left(\frac{R_0}{R(t)}\right)^4 \tag{1.9}$$

where $\phi(t)$ is the temporal dependence of temperature other than the cooling due to the expansion itself. The function $\psi(x)$ is the radial component of temperature which remains unchanged during the evolution.

Putting all relevant quantities in Eq. 1.4 and following the assumptions made by Arnett (1982); Arnett & Fu (1989), the temporal and spatial component can be separated as eigen value solution. The temporal component is described as ordinary differential equation:

$$\frac{d\phi(t)}{dz} = \frac{R(t)}{R_0 x_i^3}\left[p_1\zeta(t) - p_2 x_i \phi(t) - 2\tau_{Ni}x_i^2\phi(t)\frac{R_0}{R(t)}\frac{dx_i}{dt}\right] \tag{1.10}$$

where substituted variables are

$$z = t/\tau_{Ni} \tag{1.11}$$

$$p_1 = \frac{\tau_{Ni}\epsilon_{Ni}M^0_{Ni}}{E^0_{Th}} \tag{1.12}$$

$$p_2 = \frac{\tau_{Ni}}{\tau_d} \tag{1.13}$$

$\tau_d = 3\kappa\rho(0,0)R_0^2/\pi c^2$ is the diffusion timescale of photons within the ionized ejecta.

M^0_{Ni} and $E^0_{Th} = 4\pi R_0^3 a T^4(0,0) \int_0^1 \psi(x) x^2 dx$ are the mass of synthesized radioactive nickel and initial thermal energy respectively. The total explosion energy E_0 for the supernova is the sum of E^0_{Th} and E^0_{Kt}, where $E^0_{Kt} = 2\pi R_0^3 v_{sc}^2 \int_0^1 x^4 \rho(x,0) dx$ is the initial kinetic energy.

$\zeta(t)$ is the total radioactive energy production rate from decay chain of unit mass of ^{56}Ni, normalized to energy production rate of ^{56}Ni nuclide, which is defined as,

$$\zeta(t) = X_{Ni} + \frac{\epsilon_{Co}}{\epsilon_{Ni}} X_{Co} \tag{1.14}$$

and mass fractions for respective radioactive nuclides vary as,

$$\frac{dX_{Ni}}{dz} = -X_{Ni} \tag{1.15}$$

$$\frac{dX_{Co}}{dz} = -X_{Co}\frac{\tau_{Ni}}{\tau_{Co}} + X_{Ni} \tag{1.16}$$

$$\tag{1.17}$$

The spatial component of temperature profile, $\psi(x)$ for uniform density with "radiative zero" solution given by Arnett (1980)

$$\psi(x) = \frac{sin(\pi x)}{\pi x} \tag{1.18}$$

The total luminosity is the sum of the radioactive heat diffusing out from ionized sphere of radius x_i and the rate of energy released from the recombination taking place at the inward moving recombination front.

$$L(t) = x_i \frac{\phi(t) E^0_{Th}}{\tau_d} \left(1 - e^{-A_g/t^2}\right) + 4\pi r_i^2 Q \rho(x_i, t) R(t) \frac{dx_i}{dt} \tag{1.19}$$

here, dx_i/dt is the inward velocity of co-moving recombination front and the term $[1 - exp(-A_g/t^2)]$, takes into account of gamma-ray leakage from the ejecta. The factor A_g is the effectiveness of gamma ray trapping (see e.g., Chatzopoulos et al., 2012; Clocchiatti & Wheeler, 1997), where large A_g means full trapping of gamma rays. The second term of this relation, accounts for the energy release from the recombination of envelope mass (Bose et al., 2015b). Q is the recombination energy

released from per unit mass of the ejecta.

1.8 Remnants of core collapse explosion

The fate of massive stars are essentially governed by its mass, composition and history of mass loss. Massive stars after building up large iron core exceeding Chandrasekhar mass, collapses to form a neutron star (NS) or a black hole (BH), ending their stellar life into type II or Ib/c SNe. During the collapse a star shrinks by a factor of $\sim 10^6$ times by volume, fraction of which turns into a compact remnant of nuclear density, while rest of the matter is dispersed in the SN explosion. A progenitors of main-sequence mass less than $\sim 20-25 M_\odot$ and solar metallicity would leave behind a NS while more massive stars forms BH. In a even more massive star, the core probably collapses into BH which continue to accrete in falling matter matter without even triggering a explosion, these are also dubbed as a 'failed-supernova' (Woosley, 1993). In such stars even if the explosion occur fall back of matter onto the NS would ultimately turn into a BH.

A small difference in initial mass may result into large variation of explosion characteristics (Janka, 2012). Stellar evolutionary models are employed and a star with a certain set of initial parameters is let to evolve unit it explodes into a SN (Eldridge & Tout, 2004; Heger et al., 2003). The produced remnants are mapped to the initial parameters and resulting explosion types. In Fig. 1.12 the obtained map (Heger et al., 2003) is represented relating the nature of explosion (top panel) to the compact remnant (bottom panel) left behind along with the variation of metallicity and initial stellar mass. Various shaded and coloured areas are marked for corresponding explosion and remnant types in both the panels. Under most of the circumstance, progenitors with low mass ($< 25 M_\odot$) and high-mass with high-metallicity produces NS. The regions marked for BH remnant has two distinct portions, one of which represents direct formation of BH, while the other corresponds to BH formation through fall back of matter on momentarily formed NS. In the directed BH formation regime no 'normal' (non-jet-powered) SN occur since no SN shock is launched, which represents the probable failed SN scenario. On the other hand, according

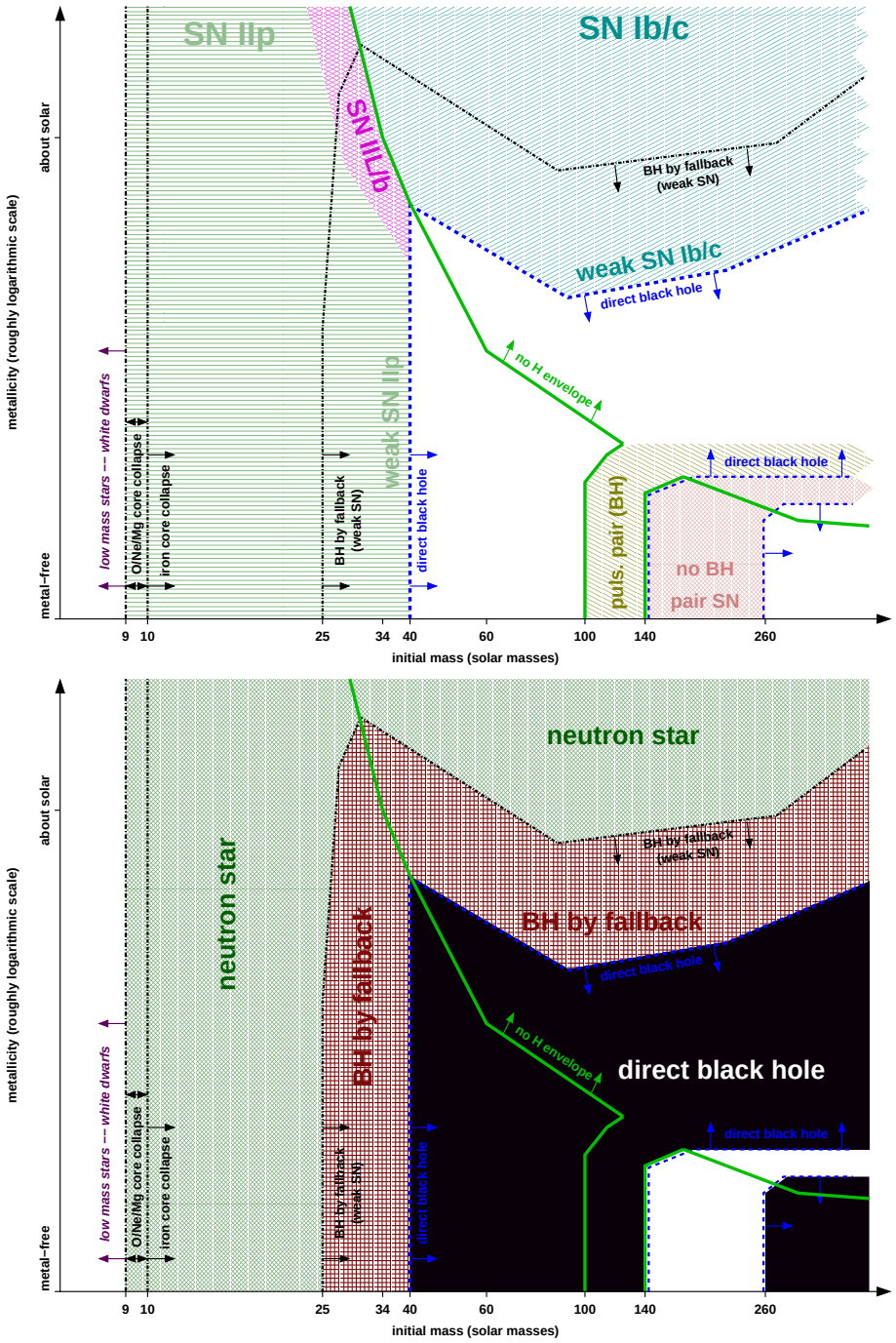

Figure 1.12: Mapping of various SNe subtypes (top panel) to expected compact remnants (bottom panel) from their single non-rotating progenitors of different initial mass and metallicity (Heger et al., 2003).

to the model BH formation through fall back on NS would give rise to explosion but apparently weak. The thick green solid line separates progenitors with stripped (SNe Ib/c) or intact H envelope (SNe II). In the figure (top panel) the direct BH formation region (black) is interrupted by a strip of pair-instability supernovae that leaves no remnant (white).

The compact remnants formed in explosion is only of few solar masses of stellar material. While the rest of the material (unless BH formed) from the massive star is dispersed in the ISM in form of 'supernova remnants' (SNR). The transition from SN to SNR is not very well defined and takes few tens of years. SNR are extended structures which consist of ejected materials expanding since explosion. Ejecta is highly supersonic (Mach no. > 1000) and sweeps the ISM producing strong shocks which heats up the plasma to high temperatures ($\sim 10^6$K). Over time shock continues to slows down by dissipating energy expanding for hundreds of thousands of years and extending up to several parsecs. A evolved SNR may include ejected stellar debris, a shocked ISM and swept-up material, a central NS or BH, a synchrotron nebula around the NS created by the pulsar wind, may also produce thermal X-ray emission from the hot interior and optical filaments formed from ejected stellar material. Spectroscopic studies of SNR allows us to relate it to the type of SNe explosion and also pre-SN evolution. The famous SNR, Crab Nebula which is supposedly the remnant from historical SN 1054 is a likely outcome of type IIP SN. The filaments of SNR G292.0+1.8 are observed to be O-rich and H-poor indicating its precursor is a SN IIL/b or Ib/c category (Gaensler & Wallace, 2003). This is the only Galactic remnant to show all possible SNR components together, which we discussed above. Another interesting and young SNR is Cas A which is also H-poor and suggesting a Wolf-Rayet progenitor of mass < 60M$_\odot$(Fesen & Becker, 1991; Garcia-Segura et al., 1996). However, according to (Young et al., 2006), observations of Cas A can also be explained by a $M < 25$M$_\odot$ progenitor which has lost H envelope through binary interaction.

1.9 EPM – Type II supernovae as distance indicators

Supernovae due to high intrinsic brightness are excellent tool to probe the universe at large distances and early times. This makes high redshift SNe immensely important for cosmological studies Due to the homogeneity in explosion and triggering mechanism of type Ia SNe, these objects are excellent standard candles for distance estimation owing to almost constant peak luminosity. Using these SNe as a tool two independent research groups, Supernova Cosmology Project (Perlmutter et al., 1999) and the High-z Supernova Search Team (Riess et al., 1998) simultaneously arrived to the conclusion of accelerating expansion universe.

However, CCSNe due to wide variation in peak luminosity they are unsuitable as direct standard candles. Type IIP SNe have been detected out to $z = 0.6$ and are more abundant at higher redshifts (Hopkins & Beacom, 2006). Extensive studies have been carried out and various methodologies have been developed to use type II SNe as distance estimators. Hamuy & Pinto (2002) found correlation between plateau luminosity and photospheric velocity, following which they established standard candle method (SCM) using SNe IIP. Olivares et al. (2010) successfully applied SCM to 37 nearby SNe with relative precision of 12 – 14 %. Another method which was developed in early 2000 was the Spectral-fitting Expanding Atmosphere Method (SEAM, Baron et al., 2004, 1995; Dessart & Hillier, 2006), which employs full non-LTE spectral synthesis codes like PHOENIX or CMFGEN, to model observed SNe spectra to estimate distance. This method require executing computing resource intensive codes to synthesize and fit observed spectra, which makes it often not suitable to use on larger sample of SNe.

Another method which was developed back in nineteen seventies, is Expanding Photosphere Method (EPM, Kirshner & Kwan, 1974; Schmidt et al., 1992a), whose fundamental concept forms the heart of SEAM as well. EPM is fundamentally a geometrical technique in which angular radius θ of a SN is compared with the physical radius R to derive its distance D. Obviously, SN angular radius is not spatially resolvable, it is estimated by assuming a spherically symmetric photosphere radiat-

ing as a 'diluted' blackbody. Whereas, the physical size is estimated by assuming homologous spherical expansion of photosphere, whose velocity is estimated from spectra. Both the assumptions of symmetric photosphere and homologous expansion are reasonably good for a real SN, however the assumption of diluted blackbody does require cautious treatment for EPM application.

Angular radius would be geometrically related to physical radius as $\theta = R/D$. Thus, for a spherically symmetric SN photosphere under homologous expansion with velocity $v_{\rm ph}$ at a given time t, physical radius can be approximated as,

$$R = v_{\rm ph}(t - t_0) \tag{1.20}$$

and so the geometric relation can be written as,

$$t = D\left(\frac{\theta}{v_{\rm ph}}\right) + t_0 \tag{1.21}$$

where t_0 is the time of beginning of expansion, i.e. explosion epoch. Here we neglect possible deceleration due to gravity as gravitational binding energy ($U \sim 10^{49}$ erg) is few orders lower than kinetic energy of expansion ($E_{\rm Kt} \sim 10^{51}$ erg) (Jones et al., 2009). Also the initial radius of progenitor ($R_0 \sim 10^5$ km) is not considered as it becomes negligible within a day due to high expansion velocity ($\sim 10,000\,{\rm km\,s^{-1}}$). The Eq. 1.21 here form a linear relation between $\theta/v_{\rm ph}$ vs. t, where D and t_0 determined as slope and time intercept. For known t_0 each value of $\theta/v_{\rm ph}$ gives unique solution for D. Otherwise, in case of unknown precise explosion epoch, which is true for most SNe, distance and explosion epoch both can be simultaneously determined from the method.

Determination of photospheric expansion velocity $v_{\rm ph}$ is a non trivial issue, as it requires special attention while selecting a line as a representative of $v_{\rm ph}$. Photosphere is defined as the surface where optical depth becomes 2/3, implying low probability for a photon to get further scattered above this layer. No spectral line does uniquely represent represents the photospheric layer. However it has been found that weak Fe II ($\lambda\lambda$ 4924, 5018, 5169) lines form close to photosphere and are best estimators of photospheric layer during plateau phase (Leonard et al., 2002b;

Schmidt et al., 1992a). During early phases ($< 10 - 15$ days) these lines are too weak or absent, at those phase photosphere resides at much outer layer, so He I or Hβ may be used as a proxy for photospheric layer (Dessart & Hillier, 2006; Jones et al., 2009). Several attempts have been made to improve determination of $v_{\rm ph}$ for EPM application.

Angular radius θ is determined by fitting a blackbody function on observed fluxes f_λ^{obs}. However, as already mentioned that SN atmosphere is not a true LTE, instead it behaves like a blackbody diluted by a factor of ξ^2 (Leonard et al., 2002b; Wagoner, 1981). As a result of flux dilution, the apparent angular radii would represent thermalization layer which would be deeper than true photosphere, and so the ξ is defined as,

$$\xi = \frac{R_{\rm therm}}{R_{\rm ph}} \tag{1.22}$$

The determination of factor ξ is non trivial and require accurate SN atmosphere models. It is computed by taking the ratio of luminosity from SN atmosphere model and blackbody function,

$$\xi = \sqrt{\frac{L_\lambda^{\rm model}}{4\pi^2 R^2 B_\lambda(T_c)}} \tag{1.23}$$

Therefore, the relation to fit on observed flux to obtain θ goes as follows,

$$f_\lambda^{obs} = \xi_\lambda^2 \theta^2 \pi B_\lambda(T_c) 10^{-0.4 A_\lambda} \tag{1.24}$$

where $B_\lambda(T_c)$ is Planck function at temperature T_c and A_λ is the total extinction. ξ is required to be computed by for all filter combinations in use, e.g. $\{BV\}$, $\{BVI\}$ and $\{VI\}$. Generally R band is omitted from calculation as flux from this filter is highly contaminated from Hα emission. Two set of independent dilution factor prescriptions have been presented by (Eastman et al., 1996) and Dessart & Hillier (2005a). Subsequent studies (e.g. Bose & Kumar, 2014a; Jones et al., 2009) have proved that EPM analysis using these two prescriptions have widely different result differing by 40 – 50%, where the newer Dessart & Hillier (2005a) prescription yield significantly better results and is consistent to other redshift independent distance

estimates.

1.10 Motivation and outline of the thesis

CCSNe originate from massive stars with vast diversity of properties in terms of initial mass, physical dimension and chemical composition, and so the observable parameters of these explosions are also very diverse. History of pre-SN evolution and circumstellar environment also plays an important role in diversifying their properties. The amount of hydrogen intact at the time of explosion governs key features of evolution and any possible interaction of ejecta with CSM would morph observed properties. Thus it becomes important to carefully observe and analyze such diverse class of events where each of the event exhibit distinct set of properties revealing information about the explosion mechanism and circumstances. As already discusses in this chapter, one of the prevailing issue in SNe IIP understanding is the lack of observational detection of high mass ($> 17M_{\odot}$) progenitors (Smartt, 2015; Smartt et al., 2009). One among the many possible explanation is that higher mass stars may turn into IIL or IIn types of events (Smartt, 2009), which can be confirmed only from more observation to these less frequent type of events. We aim to characterize a number of new CCSNe by using optical photometric, spectroscopic and polarimetric observations.

This thesis utilizes extensive observational data collected primarily from Indian telescope facilities viz. 104cm ST and 130cm DFOT at ARIES, 2mIGO at IUCAA and 2mHCT at IIA. Complementary data were also collected from several international network of telescopes and *Swift* UVOT observations. Our primary goal is to understand various mechanisms involved in the explosions and how they govern observable parameters. We analyze the observational data and perform theoretical modeling (light curve and spectral) to constrain progenitor properties (e.g. mass and radius), explosion parameters (e.g. energies) and also to probe circumstellar environment to infer their pre-SN evolution which the progenitor might have undergone. We also identify and investigate various peculiarities they exhibit in their observed light curves and spectra, which are crucial to improve our understanding

of these event.

Most of the SN classification were defined in the years of 80 – 90s, when detections and observations of these events were pretty limited. At the present era with number automated SN discovery programs and increases number of observational facilities, these taxonomy schemes need to be revisited and revalidated. For example, the historical classification of SNe IIL (Barbon et al., 1979; Filippenko, 1997) is defined to show fast and linear decline in light curve until reaching nebular phase, whereas the type IIP counterpart is supposed to have a constant or plateau in light curves for a prolonged duration. Over the time, rarity of SN events have been realized which qualify the definition of SNe IIL. Based of the pool of data collected over several decades of observations, it is now believed that all SNe IIL would show a break in slope at the end of photospheric phase before entering tail phase. Moreover, a perfect plateau is also not evident in most type II SNe, rather light curve properties form a continuum among IIP–IIL–IIb subclasses (Anderson et al., 2014b). In this thesis we also aim to address such issues in historical taxonomy scheme by observing and investigating SNe having characteristics of prototypical type IIP, IIL and also intermediate class in SNe II diversity. We also try to identify and explain various distinguishable features among these class of events.

Another vital component of this thesis is to utilize type II SNe as a distance estimator, which has immense cosmological as well as astronomical importance. SNe due to high intrinsic brightness are always an attractive probe for extragalactic distance measurements, however SNe II require an approach which is entirely different than standard candle methods. We intend to implement Expanding photosphere method (EPM) to estimate distances to host galaxies of several type II SNe, which are observed as a part of this thesis or data available in public archives. We would also validate EPM for its reliable application, explore various sources of uncertainties and introduce possible improvements in the existing methodology.

The thesis is organized into following eight chapters.

Chapter 1: Basic introduction to supernovae is given in this chapter. We review our present understanding of these explosions mechanism, their underlying

physics and current issues involved in this subject. We also discuss on observable parameters and connect those with various properties and parameters related to explosion, their progenitor and environment.

Chapter 2: This chapter describes the observational resources which have been uses in the thesis. Introduction to data acquisition and reduction techniques in optical photometry, spectroscopy and polarimetry are presented. A brief description of *Swift* UVOT archival data and its analysis are also presented.

Chapter 3: In this chapter we apply the Expanding photosphere method (EPM) on a sample of eight events to test its reliability as a distance estimator. We explore various sources of uncertainties involved and compare two sets of available dilution factors, which is a crucial component of this method. We also introduce some improvements to the the existing methodology. The derived EPM distances for the host galaxies are compared with that estimated from other redshift independent methods, and which is found to be fairly consistent.

Chapter 4: Photometry and spectroscopy of bright SN 2012aw is presented in this chapter. The optical light curve is found identical to archetypal IIP SN 1999em in terms of shape and absolute magnitude values. The dense and high SNR photometric observation enabled us to reliably detect the emergence of recombination phase in *VRI*-band for the first time. Complete characterization of the event is presented along with comparative estimation of progenitor and explosion properties. Detailed spectroscopic modelling is performed to estimate line velocities and identify spectral features, which also revealed signatures of ejecta-CSM interaction.

Chapter 5: High cadence optical photometry, spectroscopy and ultraviolet observations of SN 2013ab are presented in this chapter. Such extensive observations facilitated us to completely characterize the object, apply EPM, perform detailed spectroscopic and light curve modeling to estimate various physical parameters. This entire observational data set and accurately determined physical properties of the SN shall be counted in the golden sample of well studies archetypal events.

Chapter 6: In this chapter we present optical observation of SN 2013ej, which is one of the brightest SN of the year 2013. The light curve properties reveal it to be a rare type IIL class of events. Ejecta-CSM interaction signatures are identified from spectroscopic modelling during photospheric phase. This indicate towards the prevalence of interaction in IIL SNe and its possible reason is also explained. The flattening of H I velocity profile found for this SN is also explained which we connect with interaction signatures. We also report asymmetry in nebular phase Hα emission indicating bipolar distribution of ^{56}Ni. Semi-analytical light curve modelling is performed to estimate physical parameters of explosion.

Chapter 7: Extensive photometric observations and few epochs of polarimetry of SNe 2013hj and 2014G are presented in this chapter. Light curve properties found in SN 2013hj indicate it to be a fast declining type II event, in an intermediate position between IIL and IIP class. on the other hand light curve properties exhibited by of SN 2014G is a perfect example of SNe IIL. We execute semi-analytical light curve model to estimate progenitor properties and explosion parameters. Evolution of polarimetric parameters reveal some asymmetry in SN 2013hj which enhances as SN evolve but remains unchanged in orientation.

Chapter 8: In this final chapter we summarize the results which we obtained and discussed in this thesis. Along the line of this research contribution, we also discus the scope of future work which can be perused.

Chapter 2

Observations and data reduction

During last few decades a large number of systematic survey has been initiated to detect transients. Number of bright supernovae are discovered by amateur astronomers and are reported to community through ATELs and CBATs. Dedicated survey programs have been setup to discover, classify and follow-up new supernovae. Some of the systematic surveys like ASAS-SN (All-Sky Automated Survey for Supernovae), CRTS (Catalina Real-Time Transient Survey), PTF (Palomar transient factory), which has been upgraded to iPTF (intermediate Palomar Transient Factory), MASTER (Mobile Astronomical System of the TElescope-Robots), ROTSE (Robotic Optical Transient Search Experiment) and OGLE (Optical Gravitational Lensing Experiment) are actively contributing in discovery of large number of SNe.

Since SN are non periodic transients by nature it is essential to initiate observations soon after explosion and continue dense follow-up to cover all phases of SN evolution describing different undergoing physics. As a part of this thesis project we initiate systematic follow-up soon after the report of transient detection, sometimes even before spectroscopic confirmation. The major Indian facilities which have been used are 1.04m and 1.30m ARIES telescopes, 2.0m Himalayan Chandra telescope and 2.0m IUCAA Girawali telescope. Other international facilities from which data have been used in this thesis are (i) 2.0m Faulkes Telescope South (FTS), Siding Spring, Australia; (ii) 2.0m Faulkes Telescope North (FTN), Haleakala in Maui; (iii) twelve 1m class telescopes, all operated as part of Las Cumbres Observatory

Global Telescope (LCOGT) network; (iv) 1.22 m Galileo Telescope, Italy; (v) 3.5 m ARC telescope at Apache Point Observatory, U.S; and (vi) 0.5m telescope at Osaka Kyoiku University, Japan. Additionally, data for ultraviolet observations were also collected from archive for Ultraviolet optical telescope (UVOT) on board *Swift* satellite. In case of requirement for large sample of data for the purpose of comparative or statistical study, data is obtained from published literature whose sources are mentioned at appropriate places in the thesis.

2.1 Optical photometry

Photometric observations and reduction techniques in optical wave bands are discussed in this section.

2.1.1 Ground based telescopes for optical photometry

Indian observatories provide a geographical advantage in transient follow up as they lies in the wide $\sim 180^{\circ}$ longitudinal gap between Canary Islands and East cost of Australia. Three telescopes which have been used primarily for optical observations in photometric mode are Sampurnanand Telescope (ST), Devsathal Fast Optical Telescope (DFOT) and Himalayan Chnadra Telescope (HCT). All three telescopes are situated in Northern India, HCT being operated by Indian Institute of Astronomy (IIA) in Hanle, Ladakh, while ST and DFOT are operated by Aryabhatta Research Institute of observational sciencES (ARIES) in district of Nainital and are situated at an aerial distance of only 22 km apart. IUCAA Girawali observatory (IGO) is although capable for optical imaging, however in this thesis we mainly used it for spectroscopy which we shall discuss in §2.3. The parameters of these telescopes are listed in Table 2.1 and their pictures are shown in Fig. 2.1.

2.1.2 CCD detectors

Charge Coupled Device (CCD) has revolutionized modern astronomy and are essential component of telescope systems. CCDs are mounted at the focus of a telescope

Figure 2.1: (a) 1.04m ARIES Sampurnanand telescope (ST) at ARIES, Nainital; (b) 2.0m IIA Himalayan Chandra telescope (HCT) at Hanle; (c) 1.3m ARIES Devasthal Fast Optical Telescope (DFOT) at Devasthal, Nainital and (d) 2.0m IUCAA Girawali observatory (IGO) at Pune.

Table 2.1: Telescope and CCD parameters of the Indian facilities used

Telescope	**ST**	**DFOT**	**HCT**	**IGO**
Site	Nainital	Devasthal	Hanle	Pune
Latitude	29° 22′ N	29° 22′ N	32° 47′ N	19° 05′ N
Longitude	79° 27′ E	79° 41′ E	78° 58′ E	73° 40′ E
Mount	Equatorial	Equatorial	Alt-Az	Alt-Az
Altitude	1951m	2450m	4500m	1005m
Focal ratio	f/13	f/4	f/9	f/10
Primary mirror diameter	1.04m	1.30m	2.01m	2.00m
CCD				
Pixel count	2×2K (1×1K binned)	2×2K	2×4K (2×2K used)	2×2K
Pixel size	24.0μm	13.5μm	15.0μm	13.5μm
Plate scale	0.37″/pix	0.52″/pix	0.17″/pix	0.31″/pix
Read noise	5.3 e^-	7.0 e^-	4.8 e^-	4.0 e^-
Gain	10.0 e^-/ADU	2.0 e^-/ADU	1.22 e^-/ADU	1.5 e^-/ADU

All these telescopes are of Ritchey-Chrétien type.

and the collected photons are recorded digitally along with spatial information, i.e an 2-dimensional image.

CCD consists of a matrix of pixels, often in numbers of 1024×1024 (1×1k) or 2048×2048 (2×2k) pixels, arranged adjacent to one another almost leaving no space in between. CCDs are often explained by analogy of an array of buckets representing pixels which collects water droplets analogous to photos. These buckets are then systematically read out to get the intensity distribution over two dimension. CCD is a semiconductor device where each activated pixel act as a potential well, the photoelectrons generated from incident photons are trapped and accumulated within it for a given exposure time. Then each pixel is read out isolatedly, converting the accumulated electronic charge into a digital value. The conversion factor of the analog electronic charge to digital unit (ADU) is termed as CCD "gain" (e^-/ADU). This entire process of CCD read out introduces some electronic noise know as "read noise" and the time involved in the process in called "readout time". The gain, read noise and readout time are characteristic properties for a given CCD. The gain

which is set by a CCD manufacturer depends upon the dynamic range, full well capacity of the pixels and the digital storage system, i.e, 16 or 32 bit. Whereas the read noise and readout time are generally inverse-proportionally dependent on each other, thus a optimal choice is done for minimal readout time and noise. High grade modern astronomical CCDs are constructed such that these parameters are as low as possible. Another quality defining parameter for a CCD is "quantum efficiency" (QE), which indicate the effectiveness of a detector to measure incident photons. It is defined as the ratio of total incident photons to that converted to electrons, though photo-electric effect. An ideal CCD pixel would have 100% QE, when every single photon is detected and accounted for output. in practical scenario QE is dependent on wavelength of incident photons and the spectral range within which the detector is sensitive, termed as "Band pass". Thus, for observations in different wavebands specialized CCDs are essential to maximized sensitivity in that particular spectral range.

The large matrix of pixels are fabricated on silicon chip in form of a CCD. To reduce the thermal and electronic noise during CCD operation, entire chip is cooled to very low temperatures (~ -100 °C), using liquid nitrogen or by reverse peltier effect. The entire detector chip along with cooling unit and Analog-to-digital converter comprises the CCD system. A modern astronomical CCD have a good linear response over a wide dynamical rage ($\sim 10^5$) with a peak QE of more than $80 - 90\%$.

The parameters of the CCDs mounted at the optical telescopes which as been used in this thesis, are listed in Table. 2.1. The read noise, gain and pixel count configuration are listed for CCDs when they used in photometric mode. The listed pixel sizes represents the physical dimension of each pixel which translates into the given plate-scale for corresponding telescope configuration. The wavelength dependent QE curves for these telescopes are shows in Fig. 2.2. The sensitivity for CCDs mounted at DFOT and IGO peaks near visual wavelengths, while for ST and HCT sensitivity peaks near red wavelengths and bandpass for all of these CCDs extends well over the optical domain.

The digital data or the images obtained from astronomical CCDs are generally

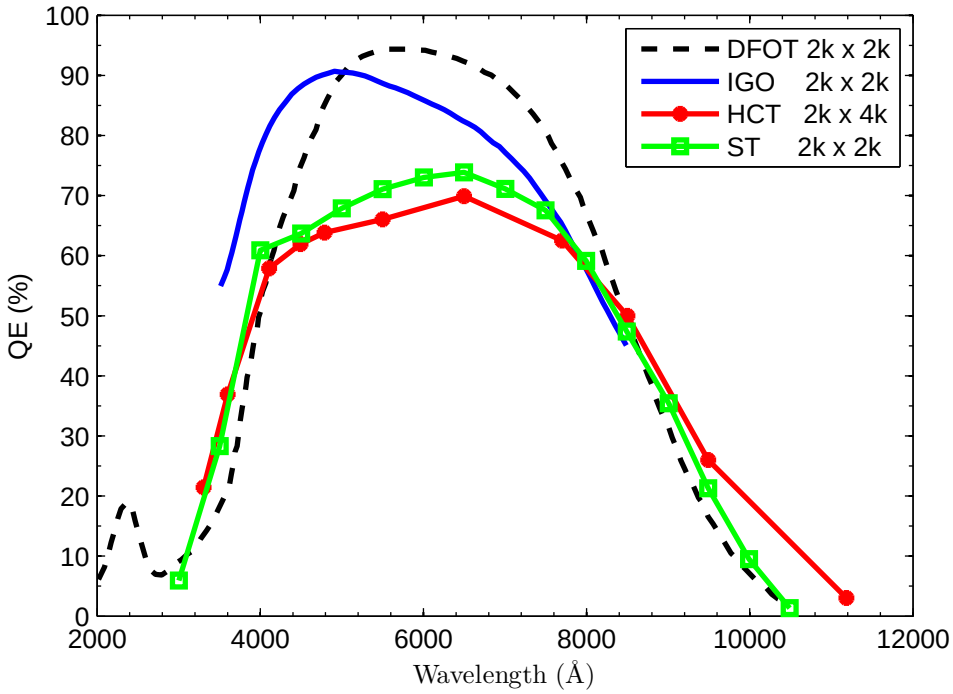

Figure 2.2: Quantum efficiency curves for different CCDs at $\sim -100°$C. The name of these CCDs are: DFOT - Andor 2K×2K; IGO - EEV 2K×2K; HCT - E2V 2K×4K and ST - Wright 2K×2K.

stored in a universally accepted format, namely the 'Flexible Image Transport System' (FITS). Along with the image data, FITS format also include a series of short ASCII information, which is collectively called header. FITS header include several vital telescope and CCD runtime information like exposure time, filter used, time of observation, etc., which are specific for that particular observation.

2.1.3 Optical broadband filters

In observational astronomy filters are used to restrict incident light only within a certain wavelength range. Multiple filters of different wavelengths are used simultaneously to measure corresponding flux and broadly determine the spectral energy distribution of the astronomical object. Each filter has a specific response function, allowing light to pass only within a certain wavelength window (pass-band) while having negligible or almost zero transmission at other wavelengths. The normalized

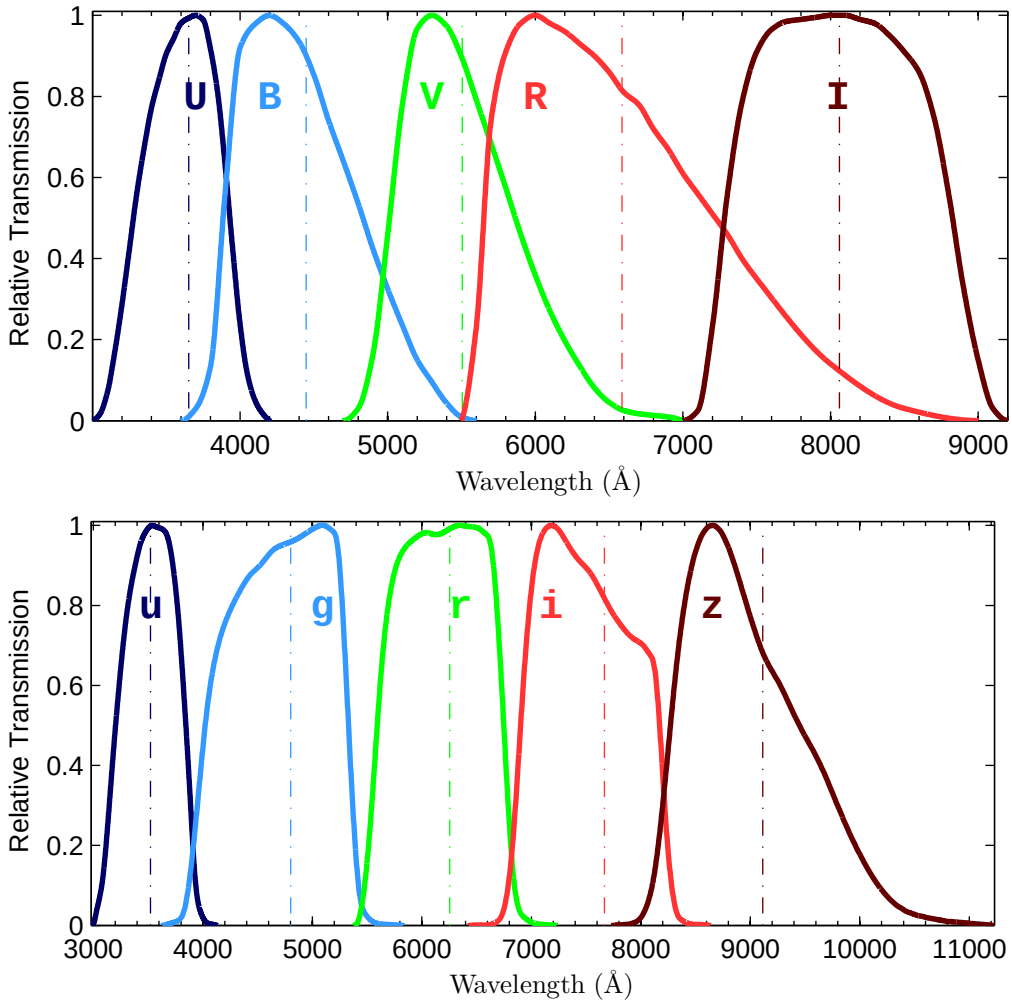

Figure 2.3: Filter response for Bessell *UBVRI* and SDSS *ugriz* are shown. The vertical dotted lines within each of the curves represents the effective wavelength for the corresponding filter.

response function of various optical filters are shown in Fig. 2.3. Therefor, simultaneous observations from these brad pass-band filters of various wavelengths can be described as spectroscopy of extreme low resolution.

The broadband filter sets mounted at telescopes used for observation in this thesis are: Jhonson *UBV* and Cousins *RI* at ST; Jhonson *UBV*, Cousins *RI* and SDSS *ugriz* at DFOT and Bessell *UBVRI* at HCT. Relevant filter parameters which are listed in Table. 2.2 are, (1) effective wavelength ($\lambda_{\rm eff}$) for the filter, which involves

Table 2.2: Parameters for optical filters

System	Filters	$\lambda_{\rm eff}$ (Å)	FWHM (Å)	F_0 (erg cm^{-2}s^{-1}Å^{-1})	Glass combination
Fukugita, Shimasaku, & Ichikawa (1995)					
Jhonson	U	3652	340	4.280×10^{-9}	UG 1(2) + CuSO4 (5)
	B	4448	781	6.190×10^{-9}	GG 385(2) + BG 18(1) + BG 12(1) + KG 3(2)
	V	5505	991	3.600×10^{-9}	GG 495(2) + BG 12(2) + KG 3(2)
Cousins	R	6888	1066	2.150×10^{-9}	OG 570(2) + KG 3(3)
	I	8060	2892	1.110×10^{-9}	RG 9(3) + WG 305(2)
Fukugita, Ichikawa, Gunn et al. (1996)					
SDSS	u	3522	634	9.111×10^{-9}	UG 11(1) + BG 38(1) + quartz (3)
	g	4803	1409	4.722×10^{-9}	GG 400(2) + BG 38(2)
	r	6254	1388	2.785×10^{-9}	OG 550(4) + BK 7(1)
	i	7668	1535	1.853×10^{-9}	RG 695(4) + BK 7(1)
	z	9117	1409	1.311×10^{-9}	RG 830(4) + BK 7(1)
Bessell, Castelli, & Plez (1998)					
Bessell	U	3660	650	4.175×10^{-9}	UG 1(1) + S8 612(2) + WG 295(2)
	B	4380	890	6.320×10^{-9}	BG 37(3) + BG 39(1) + GG 395(2)
	V	5450	840	3.631×10^{-9}	BG 40(3) + GG 495(2)
	R	6410	1580	2.177×10^{-9}	OG 570(3) + KG 3(2)
	I	7980	1540	1.126×10^{-9}	RG 9(2) + WG 305(3)

filter response curve $R(\lambda)$ and is defined as

$$\lambda_{\rm eff}^2 = \frac{\int \lambda R(\lambda) d\lambda}{\int \frac{R(\lambda)}{\lambda} d\lambda} \tag{2.1}$$

(2) the FWHM for filter response curves, (3) the zero-point flux (F_0) for the filter magnitude and (4) the glass combination used for manufacturing the filters.

2.1.4 Optical data analysis

In astronomy, photometry is the process of measuring photon, or more precisely, the flux of a target object. Computer aided analysis softwares are used with the digital images obtained from a CCD. Numerous specialized software are available which are often optimized for specific telescope data, while some are general purpose and more customizable for generic CCD images. `IRAF`, MIDAS and DAOPHOT are few of such software packages.

FITS is the universal standard format for CCD images, however, some CCDs produce generate images in non standard output format. For example, Wright 2K CCD mounted at ST produce a FTS file with minimal header information and image data, CCD specific software WR2FITS is used to convert the image to standard FITS file. Even though most CCD and telescope control systems saves directly in standard FITS format, several header information remains missing or sometimes saved in non standard FITS keyword or format. These header information are essential during data reduction and analysis. Some important keywords to describe the observation are exposure time (EXPOSURE/EXPTIME), object name (OBJECT), object's right ascension (RA), declination (DEC), observation data and time (DATE-OBS), filter used (FILTER), EPOCH, telescope name (TELESCOP), observatory name (OBSERVAT) and OBSERVER. In addition to these some other essential header information, which can be derived from existing keywords are sidereal time (ST), julian date (JD), modified julian date (MJD) and air mass (AIRMASS). Before we start processing the FITS images it is ensures that all these header information are present using FITSVERIFY or IMHEAD tasks, the missing keywords and associated information are then updated using HEDIT or ASTHEDIT tasks of `IRAF` package.

2.1.4.1 Pre-processing

Pre-processing involves the steps to clean images and correct for some of defects due to CCD and telescope system. Apart from the science-frame, which is taken to observe our object of interest for science purpose, number of other frames are also taken to clean or correct for defects. The entire pre-processing is done under `IRAF`

environment.

Bias correction

In CCD electronics, some residual electrons always remains in each pixel, even when unexposed to light. The positive offset in mean zero level also serves the purpose to avoid negative values while being readout and converted to digital image. This saves one extra bit by storing as unsigned binary integer, which can now be used to store larger values thereby increasing the dynamic range. Any frame acquired from CCD will contain this default offset values in each of the pixel. Thus, calibration measurement for bias level is required to correct the science frame. Bias or zero frames are zero exposure time frames taken in dark to record the offset value for each pixel. In order to do bias correction all CCD framed are subtracted by the bias frame to obtain counts due to incident photons only. Bias correction also takes care of any hot (defective) pixel column or rows in CCD. It is also to be noted that some readout and thermal noise are also introduced during the process of acquiring bias frames. Unlike bias, these noise are random in nature and may introduce over or under correction in counts while subtracting bias. To remove the noise part, generally at least three bias frames are acquired, which are then median combined to obtain 'Master bias' using ZEROCOMBINE task. Master bias now only have the fixed bias pattern of the CCD, with minimal or no random noise component. Master flat is subtracted form all images using CCDPROC task, before any observed frame is used for further processing.

Flat fielding

Under practical scenario sensitivity of each and every CCD pixes are not perfectly identical, there is slight variation of QE among the pixels in a single CCD. As a consequence of this, different pixel produce different number of photoelectrons even if they are exposed to same number of photons of same energies. In order to flatten the non uniformity of pixel sensitivity, flat fielding is done. Flat fielding calibration involves exposure of CCD to an almost uniform source of light, so that each pixel receive same amount of radiation, and then dividing the science frames by flat

frame (all bias subtracted) to flatten pixel sensitivities. It is ensured while taking flat frames, that the exposure time is sufficiently enough so that the counts remain well within the linearity range of the CCD. Flat fielding also takes care of the other artifact and defects which arises from dust or minor stray particles residing on filter or CCD glass plate, which very weakly obscure the incident light. This also corrects for minor imperfections in CCD and telescope optics which are tampering uniformity in obtained image. To increase statistical significance by reducing the noise, at least three flat frames are observed to median combine (after bias subtraction) them into 'master flat' using FLATCOMBINE task. Since, QE of a CCD pixels is a function of incident photons wavelength, entire flat fielding process is repeated for all the filters in use. Using CCDPROC task, science frames are divided by master flats of corresponding filters to obtain flat fielded images.

Due to practical limitations it is very difficult to construct a perfectly uniform light source for flat fielding. Generally, twilight sky is assumed to be a near perfect uniform light source. Twilight time is chosen so that, sky intensity is low enough to not to saturate CCD fames in small exposures, but high enough for stars not to appear in flat frames. Sky flats are taken sufficiently above the horizon so gradient in sky light would be negligible. While taking multiple flat frames in each filter for median combine, telescope is slightly moved to point to different sky position during each frame, to ensure that any non uniformity undetectable in naked eye in the sky is removed after median combine.

Cosmic ray removal

So far we have cleaned images for CCD and telescope system defects. We are yet to deal with another image artifact whose origin is extraterrestrial – the cosmic rays. Cosmic rays are energetic charged particles which randomly hits a CCD pixels by depositing a significant amounting of energy resulting to large pixel count in the image. With long exposure time more number of cosmic ray hits start to accumulate over the CCD. Cosmic rays are random and more likely to hits a single CCD pixel during the entire duration of exposure. Thus the intensity profile of a cosmic ray would be a dirac delta, i.e., high value at a particular pixel while low in adjacent pixels.

Cosmic rays can be easily distinguished from characteristic stellar intensity profile, which is more like a circular gaussian profile extended over more number of pixels. This distinguishing profile characteristics is used by subroutines like COSMICRAYS or more efficient L.A Cosmic, a laplacian kernel detection algorithm (van Dokkum, 2001), to detect and remove comic rays from CCD images. FINDTHRESH task is used to measure the background noise fluctuation of a image, which is used by above algorithms to set threshold value for efficient detection of cosmic rays above noise level.

2.1.4.2 Processing

Preprocessing now being done, images are free from instrumental artifacts and defects. We are now ready to work on our scientific objective. Our fundamental objective of optical photometry is to identify object in an image and measure its flux, which is then converted to standard magnitude system. Image processing is done primarily using the standalone version of DAOPHOTII (Stetson, 1987) software package. `IRAF` also include a package of similar algorithm and functionality called DIGIPHOT. Basic steps involved in processing are identical in both the package. Every pixel of the image has ADU values or counts, which is directly proportional to the physical flux value. The proportionality factor depends on numerous parameters which include telescope and CCD parameters, overall transmission of the telescope optics and atmospheric extinction. The proportionality factor will be only determined at calibration phase. Thus, till then all the flux and magnitudes computed will be instrumental values, which can be converted to physical values with simple zero point offsets.

For faint objects multiple frames are observed at same epoch in each filter which are then co-aligned and added to increase signal to noise ratio. `IRAF` tasks like IMALIGN or GEOMAP and GEOTRAN are first used to align frames then images are combined using the task IMCOMBINE. Then the processing steps are followed as usual expect where DAOPHOTII asks for summed or averaging information.

Finding objects

The FIND subroutine of DAOPHOTII identify star like object in image and estimate its centroid coordinates. A typical FWHM is supplied to the program to find and fit gaussian function on the stellar intensity profile of similar FWHM and compute its approximate centroid. A threshold value in units of sigma of sky fluctuation is given, such that the program will only identify those stars whose peak value is more than the threshold value above mean sky level. The given FWHM and threshold values are used to avoid false detection possibly arising from any cosmic ray of non uniformity in image. During this stage a number of additional constraints are placed to reject objects having unusual roundness or sharpness. The software is also set to rejects stars having bad pixel values or stars whose counts lie outside the linearity range of CCD, this also rejects saturated stellar images. The output file generated from the subroutine contains a catalog of all identified stars pixel coordinates along with relevant information indicating magnitude, roundness and sharpness.

Photometry

After identifying the stars using the FIND subroutine, photometry is performed on the stars to extract stellar flux and converting it to magnitude. Despite of stars being a point source in all practical limits, due to diffraction limitation of telescope and atmospheric turbulence, point source of light is always spread over certain viewing angle. As a result stellar images exhibit Gaussian like intensity profile. Thus it becomes necessary for a crowded field, where Gaussian tails may be significantly overlapping across one another, to have a different treatment while extracting flux. Primarily there are two types of widely used photometry methods, which mainly differers in flux extraction technique, namely 'Aperture photometry' or 'PSF / Profile fitting photometry'. For bright and isolated stars 'Aperture photometry' is preferred, whereas for stars in crowded field 'PSF photometry' is appropriate.

a. Aperture photometry

As the name suggest, aperture photometry is the method of flux extraction by placing a fixed aperture on a star. Count or ADU values are integrated within a circular aperture centered at the coordinate identified by FIND task. This integrated counts

contain both stellar and sky counts. To estimate background sky values, an annulus of few pixel thickness and radius considerably larger than the aperture radius is selected, and then median sky value is calculated within the annulus. This sky value is scaled to the aperture area and subtracted from the integrated aperture counts to obtain the star counts only, and which is then converted to magnitude scale. The sky subtracted aperture counts I can be expressed as, $I = \Sigma I_{i,j} - (\text{Sky} \times \text{Aperture Area})$, where $\Sigma I_{i,j}$ is the integrated counts within the aperture. The obvious shortcoming of aperture photometry is the direct extraction of flux within circular aperture which may be easily contaminated by flux from adjacent stars in crowded field.

Aperture photometry is performed using the PHOT subroutine which takes the coordinate list generated by FIND and compute the stellar instrumental magnitudes and associated errors of all stars and outputting them along with corresponding coordinates. PHOT subroutine has provision for defining multiple aperture radii, for each of them it will compute magnitudes for all the stars.

b. PSF photometry

PSF (point spread function) or profile fitting photometry is more suitable for crowded fields, where flux is extracted by fitting a PSF profile and integrating it. The non-trivial part is to determine an appropriate PSF model. The simplest PSF would be Gaussian function, however for a realistic PSF obtained from a telescope Gaussian is not the best model to use. Apart from two dimensional Gaussian function DOPHOTII provide option for Lorentz, Moffat and penny function.

The PSF we chose is the Penny function, which is best match to observed PSF obtained from a telescope. Penny function is sum of Gaussian and Lorentz function having five free parameters, which include FWHMs in two axis, amplitude scaling of Gaussian function and tilt components of Gaussian and Lorentz function. Among these parameters, some are generic for entire frame, whereas rest are specific for individual star to model. Ideally PSF model for all stars would be identical except for the intensity scaling which varies according to brightness. Before implementing the PSF model over all stars in the image, some of the model parameters including the spatial dependence are determined by fitting over few selected stars. This selection

is done using the PICK subroutine which select few tens of good isolated stars within a optimal range of their instrumental magnitudes obtained from aperture photometry. The PSF subroutine then fits the selected point-spread function and determine model parameters. After the PSF model is built, ALLSTAR routine implements the model to all the stars (on which aperture photometry was previously done) and extract the counts by integrating the fitted model. This method is arguable good in neglecting contamination from adjacent stars which have overlapping PSF tail or fall partially within one another's fitting radius. The model is fitted up to a radius of few FWHMs (1-3 times), while modal sky value is estimated from user selected sky annulus around the star and subtracted from image counts.

The generated output contains instrumental magnitudes and associated errors along with image coordinates, background modal sky value, number of iterations to converge the model, chi square value and sharpness.

All the DAOPHOTII subroutines, viz., FIND, PHOT, PSF, ALLSTAR have equivalent counterparts in `IRAF` which produce similar results, with an exception of count to instrumental magnitude conversion system. PHOT and ALLSTAR routines of DAOPHOTII converts ADU counts (I) straight away to instrumental magnitude ($m_{\rm inst}$) without any exposure time (t) correction, which can be expressed as $m_{\rm inst} = zpt - 2.5Log_{10}(I)$. Where zpt is the zero-point magnitude corresponding to 1 ADU, which has been defined as 25 mag in DAOPHOTII. In `IRAF`, magnitude is converted from counts per seconds [$m_{\rm inst} = zpt - 2.5Log_{10}(I) + 2.5Log_{10}(t)$] with a default zero-point of 25 mag.

2.1.4.3 Differential light curve

As long as we are interested in relative flux, instrumental magnitudes are good enough to study time evolution of SN light curves. At any point of time zeropoint offset can be applied to the instrumental light curve to obtain standardized light curve. To obtain instrumental light curve from the photometry performed on individual frames is a nontrivial task. Even if we observe a non-variable source at different times, we will get arbitrarily varying instrumental magnitude. This vari-

ability is not intrinsic to the object itself, rather it is due to varying extinction, airmass and overall instrumental throughput. Situation is even further complicated when light curve is to be extracted from images obtained from various telescopes. The easiest workaround of this issue if to perform differential photometry, in which we utilize the fact that all the objects in a given frame suffers same variation in magnitude (same ratio of flux variation), i.e, difference in magnitude between any pair of non-variable star would remain same in all the frames. Thus, if instrumental magnitudes of all non variable stars in all subsequent frames are linearly shifted to the magnitudes of any reference frame, then only the intrinsic variation would remain for a variable source.

Before we perform differential photometry, it is essential to cross-identify stars across all the frames. In order to cross-identify stars across multiple frames taken over different times spanning several days to years we use the DAOMATCH routine. The program solves for the transformation relation for all frames with respect to a singe reference frame, such that star of any given coordinate in a frame can be mapped to the reference frame. DAOMATCH use matching triangle method to solve for transformation relation having six free parameters, whose matrix representation is as follows:

$$\begin{pmatrix} x_0 \\ y_0 \end{pmatrix} = \begin{pmatrix} A_n \\ B_n \end{pmatrix} + \begin{pmatrix} C_n & D_n \\ E_n & F_n \end{pmatrix} \cdot \begin{pmatrix} x_n \\ y_n \end{pmatrix} \tag{2.2}$$

(x_n, y_n) is coordinate in a given frame and (x_0, y_0) is mapped coordinate in reference frame. A_n, B_n are translation components and C_n, D_n, E_n, F_n include the rotational and two dimensional scaling components. DAOMATCH generates a output file having transformation coefficients for all the frames with respect to reference frame.

Following this, DAOMASTER routine is executed which further refines the transformation coefficients and cross-identify all the stars to perform differential photometry in a method as described above. DAOMASTER generate differential light-curve for all the stars identified in the field. The non-variable stars will have almost constant (within errors) instrumental light curve whereas variable source like supernova will show its intrinsic variability.

2.1.4.4 Photometric calibration

Since now we are ready with instrumental light curves, only part left is to apply transformation of instrumental magnitudes to standard magnitude system. For the purpose of calibration, several standard stars are observed (Landolt, 2009) with varying air mass and hour angle (HA) ranging at lest from 0 to 4 Hrs (either east or west), or even better -4Hrs (E) to $+4$Hrs (W). Some additional standard are also observed close to 0Hr HA along with our target field. Object is also observed couple of times during the same night of calibration when it's HA is within -1 to $+1$ Hr, to have minimum airmass contribution. Good photometric night is chosen for calibration observation when sky extinction is negligibly varying throughout the night and atmospheric turbulence is low so that seeing is minimum.

Time and aperture correction

As the magnitudes from DAOPHOTII routines does not include time correction, the instrumental magnitudes in all frames need to be converted for unit second (in flux level) before proceeding to calibration. For which a factor of $2.5Log_{10}(t)$ is needed to be added to the instrumental magnitude, where t is the total exposure time.

Aperture and PSF photometry is done on all standard and object frames. On performing aperture photometry on series of increasing apertures we obtain the growth curve, where magnitude value will be decreasing up to a certain aperture radius as more and more flux from PSF tail is included in the integration of counts. In order to extract the full light from a star, aperture correction is applied on PSF magnitudes. Aperture correction is computed from few (n) bright and isolated stars, where full light is extracted from aperture growth curve ($m_{\rm gro}$) and correction factor is calculated from corresponding PSF magnitudes ($m_{\rm psf}$). The aperture correction factor ($\bar{\Delta}_{\rm cor}$) is computes as,

$$\bar{\Delta}_{\rm cor} = \frac{\sum_{1}^{n}(m_{\rm psf} - m_{\rm gro})}{n} \tag{2.3}$$

DAOGROW routine computes the corrected aperture magnitudes from growth curve

and the aperture correction is applied using COLLECT routine of DAOPHOTII.

Therefore, the corrected instrumental magnitude after applying both the corrections, is m = Aperture or PSF magnitude $- \bar{\Delta}_{\rm cor} + 2.5Log_{10}(t)$, which should be used for determining transformation coefficients for calibration.

Transformation to standard magnitude system

The transformation equations relating the instrumental to standard magnitudes for a given set of filters (say $UBVRI$) are as follows:

$$\begin{aligned} u &= U + zp_{\rm u} + c_{\rm u} \cdot (U - B) + k_{\rm u} \cdot X \\ b &= B + zp_{\rm b} + c_{\rm b} \cdot (B - V) + k_{\rm b} \cdot X \\ v &= V + zp_{\rm v} + c_{\rm v} \cdot (B - V) + k_{\rm v} \cdot X \\ r &= R + zp_{\rm r} + c_{\rm r} \cdot (V - R) + k_{\rm r} \cdot X \\ i &= I + zp_{\rm i} + c_{\rm i} \cdot (V - I) + k_{\rm i} \cdot X \end{aligned} \tag{2.4}$$

where *u, b, v, r, i* and *U, B, V, R, I* are set of instrumental and standard magnitudes in $UBVRI$ filters and X is the airmass. $zp_{\rm u..i}$ are zeropoint coefficients, $c_{\rm u..i}$ are color coefficients and $k_{\rm u..i}$ are atmospheric extinction coefficients for corresponding filters.

The overall throughput of the system is taken care by the zeropoint terms and the color coefficients are to correct for the broad bandpass of the filters, higher order terms of color coefficients are neglected as they tend to be very small. The extinction coefficient takes care of the extinction suffered by light as it propagates through earth atmosphere. Atmospheric extinction is highly varying parameter which changes from night to night and may even vary over few hours if night is not of photometric quality. Amount of extinction is proportional to the path traversed by light though earth atmosphere and thus dependent on zenith angle (Z) of the object, where minimum extinction suffered will be at zenith ($Z = 0$). The total path traversed by light through atmosphere is represented by airmass (X), where one unit represents entire vertical column of atmosphere and it first order approximation is $X = sec\, Z$, in plane parallel atmosphere model. In more realistic atmosphere model,

X is approximated with higher order terms as (Hardie & Ballard, 1962),

$$X = \sec Z - 0.0018167\,(\sec Z - 1) - 0.002875\,(\sec Z - 1)^2 - 0.0008083\,(\sec Z - 1)^3 \tag{2.5}$$

The transformation equations are fitted on instrumental vs. standard magnitude values of Landolt (2009) standard stars to obtain the calibration coefficients. The CCDSTD routine perform this task and compute the coefficient vales with associated errors. Then the CCDAVE and FINAL routines apply the transformation equations on unknown object frame to calibrate all stars in the given field. Now we select few isolated and non variable stars in the newly calibrated field of the object, which we call secondary standards. These secondary standards are such chosen that their brightness is closely comparable to SN. Since now we have secondary standards in the SN field itself, automatically these standards will be observed in each frame of SN observation, which we can use to calibrate SN magnitude at any point of time. All we need to do is to compute color and zeropoint coefficient for a given frame at any epoch using these secondary standards and apply those on the SN or entire instrumental light curve to obtain calibrated light curve.

As a crosscheck to the integrity of the calibration, the obtained transformation relation is applied to all standard stars to re-calibrate and compare with the values given in Landolt (2009) catalog. The Fig. 2.4 shows the scatter plot for the difference in standards and re-calibrated magnitude vs. standard magnitude in each filter. The standard deviation and mean of the scatter are checked to be in error limits. If any particular star is found to be significantly off from zero, then they are exclude from calculation and transformation coefficients are recomputed to further refine the calibration.

2.1.5 Template for background subtraction

Supernova are often found to be embedded within the host galaxy, where background flux is significantly contaminating the extracted SN flux. PSF photometry and the local sky subtraction using annulus removes significant fraction of background flux. However, this is not sufficient enough if background has varying intensity gradient

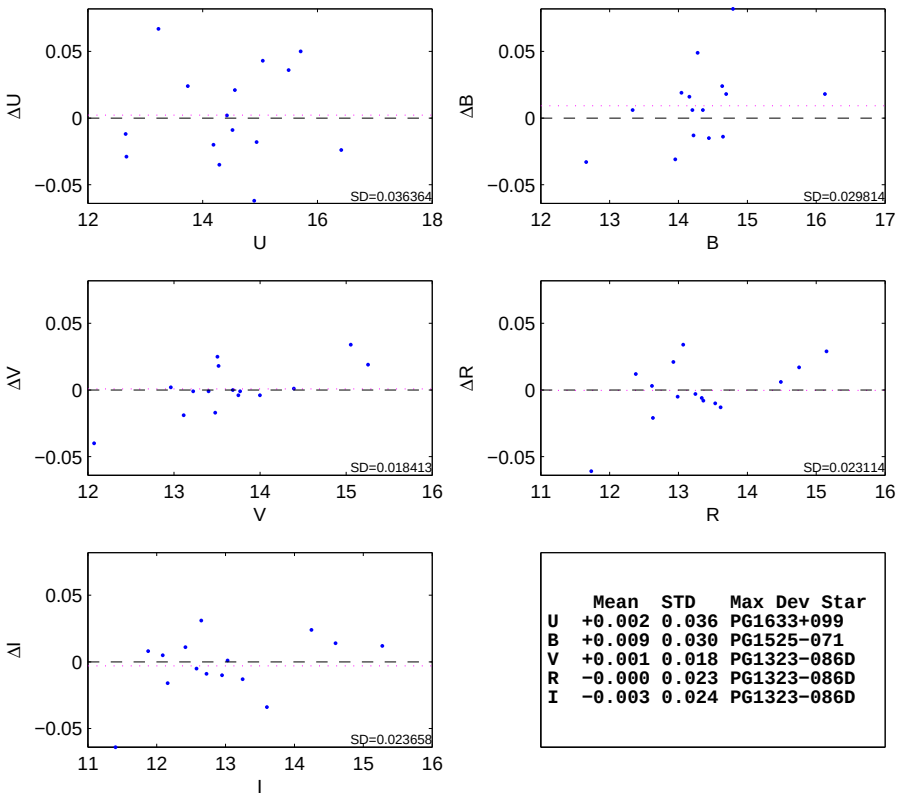

Figure 2.4: Plot of difference in standard and recalibrated magnitudes vs. standard magnitude in each of UBVRI filters. The mean and standard deviation of the scatter is tabulated in the bottom right inset. Star with most deviant value is also identified and listed.

or if the SN is residing in unresolvable close proximity to nucleus or star forming knots of the host. As the supernova becomes fainter the fractional contribution of background flux increases and it may even dominate at late phases of light curve.

One of the most efficient and widely adopted technique is template image subtraction. Template image of the host galaxy alone is taken either from available archival pre-supernova images or from observation long after the supernova has fainted. The template image should be as best in quality as possibly, i.e, low sky brightness and maximum sharpness of image PSF. In order to do template subtraction, template and SN frames are co-aligned, template image PSF is degraded to match SN frame, corresponding sky levels are subtracted from images, image intensities are scaled to same level and then template image is subtracted arithmetically. This entire pro-

cess can be achieved by series of `IRAF` tasks – GEOMAP and GEOTRAN to align images; IMARITH for all subtraction and scalings; GAUSS for PSF matching. The subtracted resulting image should be free form all foreground stars and host galaxy brightness, only flux enhancement from SN will be visible. Subtraction process is repeated for all SN frames and for all filter sets using corresponding template images. Dedicated packages like ISIS (Alard, 2000; Alard & Lupton, 1998) and HOTPANTS (Becker, 2015) also have similar algorithm but with more robust PSF matching and subtraction methods.

However one of the frequently faced problem with images from ground based telescopes are image defects like coma or off-axis (not along x or y axis only) trailing. These defects may also vary from frame to frame. PSF matching is the most crucial component of image subtraction technique, which will mostly fail with these image defects. As a result, improper PSF matched and subtracted image would introduce huge uncertainties rather than correcting the extracted flux. One better alternative in such a scenario is to do flux subtraction after extracting flux with a fixed radius aperture. Fixed aperture is used for flux extraction in template and SN image, centered at exactly same coordinate (WCS / sky coordinate). Local sky is also subtracted from apertures in each image. Same amount of flux from host will be there in both image apertures and SN flux enhancement will be only in SN frame aperture. Despite of image defects total flux will be retained within the aperture, as a result there will be less uncertainty introduced as compared to image subtraction. This method also works well even with non uniform sky background, which may happen due to moon light. The template aperture flux is then subtracted from SN aperture flux to obtain the final photometric magnitude.

2.2 Ultraviolet photometry

Ultraviolet (UV) observations used in the thesis are from 'Ultraviolet Optical telescope' (UVOT), on-board *Swift* satellite (Gehrels et al., 2004). *Swift* is uniquely designed for fast response to transients like GRB and SN, where preplanned regular observations are immediately superseded by high priority transients as soon as

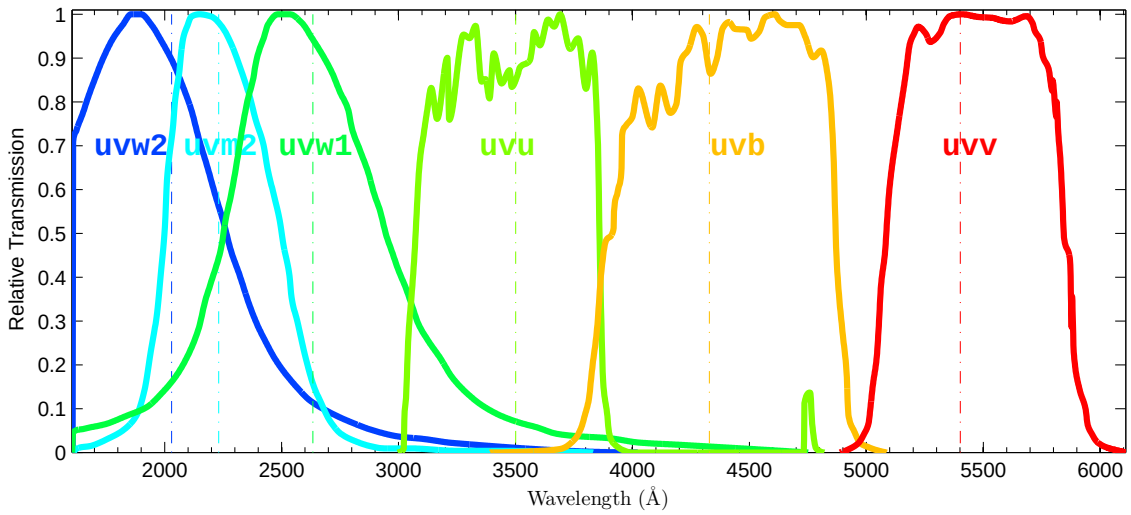

Figure 2.5: Filter response for UVOT ultraviolet optical filters are shown. The vertical dotted lines within each of the curves represents the effective wavelength for the corresponding filter.

target coordinate is uploaded from ground control. This makes it possible to begin observation within hours of discovery of SNe. UVOT (Roming et al., 2000, 2004) is a 30-cm Modified Ritchey-Chrétien telescope with a f/12.7 f-number forming a diffraction limited PSF of 0.9″ (at 3500Å). A 2K CCD is mounted on the telescope having a $17' \times 17'$ field of view with a plate scale of 0.5″/pix. UVOT sensitivity extends from 1700 to 6500 Å and is capable of simultaneous photometric and low resolution spectroscopic observations.

Seven photometric filters are mounted on UVOT (Poole et al., 2008), among which three are UV bands, three optical/near optical bands and one white band filter. UV band filters are *uvw2, uvm2* and *uvw1*. Optical/near optical band filters are *u, b* and *v* whose effective wavelengths closely resemble Jhonson *UBV* bands. To avoid confusion with SDSS filter, hereafter I would denote these filters as *uvu*, *uvb* and *uvv*. The white band filter is of 2600Å FWHM and its response curve extends between near-UV to near-IR wavelengths. White (clear) band filter are not used for SN observations as it is unsuitable due to broad bandpass. The normalized response curves for six UV and optical filters are shown in Fig. 2.5.

Observed data are regularly downloaded from spacecraft and made publicly avail-

able within few hours at *Swift* archive website[1], after initial processing of raw data. The downloaded data contains masked bad pixels and FITS images are transformed to World Coordinate System (WCS). Standard routines of `HEASOFT` package are used for performing photometry on UVOT data and the procedure followed is same as outline in Brown et al. (2009).

The UVOTSOURCE routine of `HEASOFT` is used to perform photometry along with the UVOTMAGHIST routine to generate output of the extracted and calculated magnitude. Generally an aperture size of 5″ is used for the source and 15″ for the sky background. Sky background is chosen at location free from contaminating sources but similar to SN background. Extracted counts rates are corrected for coincidence-loss which is computed independently for both sky and source. The counts are corrected for loss of sensitivity over time and zero points from updated calibration database (CALDB), as given in Breeveld et al. (2011), are used to convert counts to UVOT magnitudes. To remove contamination from host galaxy, template images are either taken from pre supernova archival images of the host galaxy (if available) or observed long after the SN has completely fainted. Photometry is performed in same procedure as it was done for SN, for same location and aperture on the host galaxy image. This template flux is then subtracted from SN flux measurements.

2.3 Optical spectroscopy

Spectroscopic observations and its reduction techniques are discussed in this section.

2.3.1 Telescope and spectrograph

IGO and HCT are the two Indian telescopes which are operated in spectroscopic mode, and low resolution slit spectra obtained from these telescopes have been extensively used in this thesis. The telescope and CCD parameters are already listed in Table. 2.1 and their pictures are in Fig. 2.1. In slit spectroscopy, light from a source is made to pass through a slit and then dispersive element called grism.

[1]http://swift.gsfc.nasa.gov/cgi-bin/sdc/ql?

The light is then dispersed according to grism properties, which is then recorded by CCD.

IGO is operated by IUCAA and the spectrograph instrument – IUCAA Faint Object Spectrograph Camera (IFOSC) is mounted at the Cassegrain focus. Instrument design is based on the working FOSC model which was developed at at the Copenhagen University Observatory for the ESO and Nordic Telescopes. The instrument is equipped with a 2K EEV CCD and is capable of simultaneous spectroscopy and imaging without changing instrument at the prime port. In imaging mode, the instrument has $0.31''$/pix plate scale given a $10.5'$ field of view. Under spectroscopic configuration, a range of grisms are available in IFOSC with resolution varying from 190 to 3700 covering a wavelength range of 3300 – 10300 Å. Provision for slit-less or long-slit with custom slit-width is also available along with number of pre-set slit-widths. Helium-Neon lamps are inbuilt to take 'Arc' spectra for wavelength calibration and halogen lamp for flat fielding. In this thesis, depending upon science requirement of wavelength range, resolution and SNR, primarily three grisims have been used – *IFORS5* ($\lambda \sim$ 3300-6300Å), *IFOSC7* ($\lambda \sim$ 3800-6840Å) and *IFOSC8* ($\lambda \sim$ 5800-8300Å). For all the grisims, long slit mode is used with $1.5''$ slit-width configuration.

HCT is another Indian telescope operated by IIA, whose data has been used for both spectroscopy as well as photometry. Hanle Faint Object Spectrograph Camera (HFOSC) is mounted at the Cassegrain focus of the telescope and was built in collaboration with Copenhagen University Observatory. HFOSC has both simultaneous spectroscopic and imaging capability with the 2K × 4K E2V CCD covering a $10'$ field-of-view. Although in photometry generally 2K × 2K pixels used, but in spectroscopic mode thin and longer strip (e.g, 250 × 3500 pix) is used to record the dispersed light. HFOSC has several interface units though which light is made to pass, Filter and Spectral Lamp Unit (FASU) house narrow band filters and calibration lamps, aperture wheel holds various mounted slits, and at the last, filter and grism wheels, which has position to hold eight filters and eight grisms. HFOSC under spectroscopic mode is capable to attain a resolution of 150 to 4500 Å using set of 11 grisms. For our observations, we used *Gr 7* ($\lambda \sim$ 3800–8000Å)

and *Gr 8* ($\lambda \sim$ 5800–9200Å) with long slit of width 1.92″. Iron-Argon (Fe-Ar) and Iron-Neon (Fe-Ne) Arc lamp spectra are also observed for wavelength calibration of *Gr 7* and *Gr 8* grisms respectively.

2.3.2 Spectroscopic data reduction

In the spectrograph the object star is positioned at a narrow long slit and light is made to pass through a grism to disperse the light which is then recorded on a strip of CCD pixels. The dispersion axis in general is along y in HFOSC and along x in IFOSC. The output FITS image does include standard header information, which are checked and necessary but missing keywords like RA, DEC, OBSERVAT, OBJECT, JD, ST etc. are updated as required. Reduction procedure for long slit spectra are described in this section. Entire reduction is done under IRAF environment.

2.3.2.1 Preprocessing

Similar to photometry, spectroscopic observations also include bias, flats and additionally *Arc* spectrum for wavelength calibration.

Bias and Overscan correction

As already discussed in §2.1.4.1, the purpose bias correction here also remains the same. Several bias frames are taken over the night and they are combined to form *Master bias* using ZEROCOMBINE task, which are then subtracted from all other frames. For IFOSC data, additionally *overscan* correction is also necessary as the mean bias level significantly varies over the night and two halves of the CCD have different amplifier electronics. Each CCD image contain a additional strip of few pixels width on two edges ($\sim$ 10 pixels) which represents the mean bias level for that halve of the CCD. All the bias processing is done using CCDPROC tasks.

Flat fielding

Here also the purpose of flat fielding remains the same, i.e, to flatten the CCD response. Although in principle flat fielding can be avoided in spectroscopy, as that

may be taken care while doing flux calibration. However that would require the dispersion line of Arc, object and standard to lie along the same pixel positions, thus it is always preferred to observe flats. Flats are taken with halogen lamps inbuilt in the spectrograph as they roughly produce continuum emission in their spectrum. Master flat is produced by median combining number of observed flats using FLATCOMBINE task, which is then normalized and used for flat fielding all sky as well as arc frames. To produce normalized flat, first a smoothed flat is produced by box averaging few tens of columns along the dispersion axis, then the master flat is divided by this smoothed flat to produce the normalized flat. `IRAF` tasks BOXCAR and IMARITH is used for producing normalized flat and finally CCDPROC is used for flat fielding.

Cosmic ray correction

The source of cosmic ray hits and its distinguishing characteristics is same as discussed in §2.1.4.1. However, some special care is taken while removing cosmic rays from spectral images. The spectroscopic version of L. A. Cosmic (van Dokkum, 2001) is used for cosmic ray removal, which offers the provision to fit and subtract sky lines and object spectrum before convolving with Laplacian kernel.

2.3.2.2 Aperture extraction

So far we are dealing with two dimensional images which contain the spectral information in form of dispersed light of the source along one direction only. To begin with extraction of one dimensional spectrum, first the exact spatial center of the stellar profile is located at a some point (preferably middle) along the dispersion axis. This cross-section of the dispersion line is a gaussian like profile and so the peak and base to base width of the aperture is easily selected. A small portion of background region is selected on both side of the profile, but outside the profile range, and low order (~ 2) *chebyshev* function is used to estimate the background profile which is subtracted from the aperture along that column. The dispersion line is not exactly straight running through the dispersion axis, some geometric distortion of the dispersion line will be there due to telescope optics and CCD alignment. The peak

of the aperture is now traced throughout the dispersion line by fitting a low order (4-8) *chebyshev* or *cubic spline* function on the peak values. Manual verification is done to check for the fit of the trace and outliers are omitted which are generally present towards the end of the spectrum, where grism transmission is low. The APALL task is used to performs the entire extraction process on all of the standard and object frames to produce one dimensional spectrum, which has only intensity vs pixel values. The extracted aperture contain four bands of spectra, which are 1 – optimally extracted object spectrum, 2 – unweighted spectrum, 3 – sky spectrum and 4 – error spectrum. The Arc spectra, which is to be used as comparison for wavelength calibration, does require a special attention while extracting aperture. Extraction of Arc spectrum is done with identical centering and trace as used for object spectrum, this is also achieved by APALL task by putting the object spectrum as the reference. To perform any spectral analysis one need to have wavelength information corresponding to intensity values, for which wavelength calibration is required.

2.3.2.3 Wavelength calibration

Wavelength calibration is done to map each pixel of the extracted 1D spectrum to wavelength values. The Arc lamp spectra which are obtained during observations, has several characteristic line emission whose laboratory wavelengths are know with high accuracy, and these lines serves as standards for wavelength calibration. He-Ne Arc spectra are used as standard for IFORS5, IFOSC7 and IFOSC8 grisms. Likewise, Fe-Ar and Fe-Ne Arc spectra are used to calibrate HFOSC *Gr 7* and *Gr 8* grisms respectively. The narrow and strong emission lines of the Arc spectra are identified manually using IDENTIFY task, which is then further compared and refined with standard *atlas* (or line list) for corresponding *Arc* spectrum. The *Arc atlas* is either available inbuilt or provided externally to the IDNTIFY task. The dispersion solution, i.e, pixel-to-wavelength solution, is computed by fitting a *chebyshev* or *cubic spline* to this line identification data. Manual refinement is done by omitting the outliers in the fitting and the order of fit function is also varied accordingly to obtain minimum residual. Identify task is allowed to re-identify lines

based on the provided atlas and iteratively the refinement is done. After obtaining satisfactory dispersion solution, DISPCOR task is executed to apply the solution on the object and standard spectra in all containing bands. The output spectrum now contain intensity vs. wavelength information for all the associated bands in the aperture.

The wavelength calibrated spectra are crosschecked for the easy identifiable λ 5577 O I sky line and any difference found is corrected by applying a offset using SPECSHIFT task.

2.3.2.4 Flux calibration

Now the spectrum is calibrated in wavelength scale, but with an instrumental intensity scale. In order to convert into absolute flux scale, flux calibration is done using a standard spectrophotometric star observed along with target object. Spectrophotometric fluxes of these standard stars are usually available within `IRAF` or obtained from Hamuy et al. (1994, 1992); Hayes & Philip (1985); Oke (1990). The observed spectrum of the standard star is integrated over a bandpass appropriate for standard data, divided by exposure time and corrected for atmospheric extinction. Wavelength dependent atmospheric extinction coefficients for the observatory site is also required for this purpose. Sensitivity profile (as a function of wavelength) is calculated as a ratio of standard flux and corrected instrumental intensity or counts. The obtained profile is then fitted interactively using high order polynomial to compute the sensitivity function for observed spectra. Computation of sensitivity function is done using the STANDARD and SENSEFUNC tasks. The determined sensitivity function is applied to the object spectra, after correcting for atmospheric extinction and time, to obtain flux calibrated spectrum.

The calibrated spectra are crosschecked against broadband photometric fluxes (if available at similar epochs) for any significant deviations. For the comparison, the observed spectrum is convolved with broadband filter responses which are then compared with observed broadband fluxes. To tie the spectra, a wavelength dependent low order polynomial is multiplied with spectrum and its convolved fluxes are minimized against the observed broadband fluxes (interpolated at the same epoch

of spectrum), keeping polynomial coefficients as fitting parameters. Thus the shape and scaling are both corrected for the spectrum. This task is executed with a self written program.

To increase signal to noise ratio of spectrum for faint objects, often multiple spectra are obtained in same grism configuration. After processing all the spectra, they are median combined using the SCOMBINE task. Doppler correction for the SN host galaxy is applied on the spectrum using DOPCOR task, to bring the observed spectrum to rest frame of the host galaxy. Spectra from different grism are also merged together by averaging overlapping wavelength regions after rejecting the low transmission portions from each spectrum.

2.4 Broadband polarimetry

Broadband polarimetric observations and its reduction are discussed here.

2.4.1 Telescope and polarimeter

ARIES IMaging POLarimeter (AIMPOL) has been used for polarimetric observation, which is mounted at Cassegrain focus of 1.0m ST telescope at ARIES. The telescope has been already described and relevant parameters were presented in Table 2.1. The instrument is paired with a 1K CCD imager having readnoise of 7 e^- and gain 11.98 e^-/ADU. Effective unvigenetted FOV of image is $\sim 8'$ with a platescale of $1.5''$/pix.

Optical layout of AIMPOL: The design of the polarimeter is illustrated in Fig. 2.6. The f/13 beam arriving from telescope secondary mirror is made incident on the field lens (50mm, f/6). The beam then passes through the most vital optical components of the system, which consists of a rotatable half-wave plate (HWP) followed by a Wollaston Prism. Fast axis of both HWP and Wollaston prism are aligned normally to the optical axis of the system. The beam finally passes through broadband filter assembly and a camera lens (85mm, f/1.8) to form the image at the CCD plane.

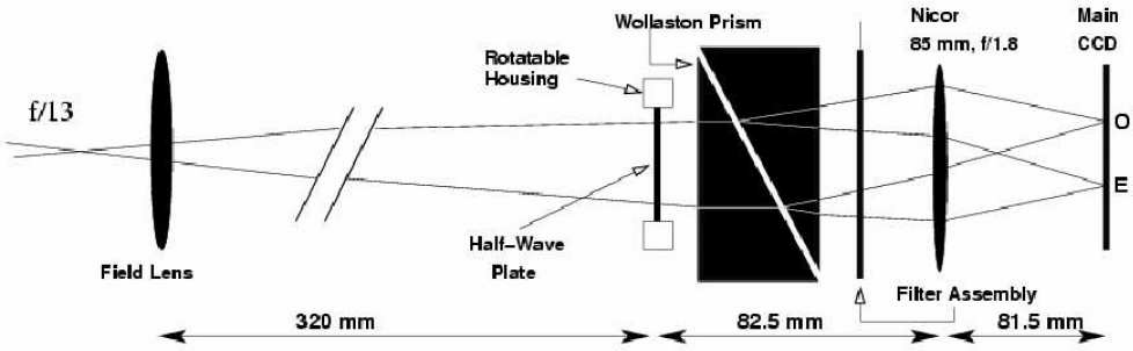

Figure 2.6: Optical layout of AIMPOL. *Image credit:Rautela et al. (2004)*

More detailed description of the instrument can be found in Rautela et al. (2004).

2.4.2 Working principle of the polarimeter

The principle idea behind this schematic is to use the Wollaston prism as the analyzer to split the incoming linearly polarized light into relative intensity of two orthogonally polarized beams, namely ordinary (o) and extra-ordinary (e), which being incident on CCD forms a pair of image separated by $\sim$ 28 pixels along the north-south axis on the sky plane (considering instrument is aligned). This is sufficient to obtain one of the Stokes parameter Q or U. In order to obtain the other stokes parameter the role of half-wave plate (HWP) comes into play. The HWP mounted on a rotatable housing before the Wollaston prism acts a modulator to rotate the plane of polarization of the incoming light. Thus, the second stokes parameter can be determined by rotating the HWP relative to analyzer, by a known angle α, thereby rotating the plane of polarization by 2α, and measuring the orthogonally polarized beams o and e at this new position. Therefore, for such an arrangement the intensities of ordinary and extraordinary beams (I_o and I_e) at a given position α is,

$$\begin{aligned} I_e(\alpha) &= \frac{I_{\rm up}}{2} + I_{\rm p}\cos^2(\theta - 2\alpha) \\ I_o(\alpha) &= \frac{I_{\rm up}}{2} + I_{\rm p}\sin^2(\theta - 2\alpha) \end{aligned} \tag{2.6}$$

where $I_{\rm up}$ and $I_{\rm p}$ are unpolarized and polarized intensities and θ is the position angle of the polarization vector. Since the conventional reference position for θ is celestial north and increasing towards east, the fast axis of the Wollaston prism is also aligned along the north-south celestial axis.

A ratio $R(\alpha)$ is defined as,

$$R(\alpha) = \frac{I_e(\alpha)/I_o(\alpha) - 1}{I_e(\alpha)/I_o(\alpha) + 1} = P\cos(2\theta - 4\alpha), \tag{2.7}$$

where $P = \frac{I_{\rm p}}{I_{\rm p}+I_{\rm up}}$ is the fraction of linearly polarized light or simply the degree of polarization. The ratio $R(\alpha)$ is effectively the reduced stokes parameters $q = \frac{Q}{I}$ and $u = \frac{U}{I}$ for $\alpha = 0^\circ$ and $\alpha = 22.5^\circ$. In practice, measurements are done in four positions for $\alpha = 0^\circ,\ 22.5^\circ,\ 45^\circ$ and 67.5° to get two sets of stokes parameters q_1 (Q/I), u_1 (U/I), q_2 $(-Q/I)$ and u_2 $(-U/I)$ respectively. Although, in principle a single set of stokes parameters is sufficient to determine polarization parameters p and θ, this double set of measurements have additional advantages: (i) this acts as an redundancy check and (ii) to normalize responsivity in o and e intensity measurements, which is further discussed in §2.4.4.

2.4.3 Observation and image processing

2.4.3.1 Observation

The target object is observed in all four positions of HWP for a given broadband filter, and multiple set of frames are taken to increase SNR by combining afterwards. Raw data is stored in PMI format which is converted to standard FITS files using CCD specific software. Similar to photometry *Bias* frames are also taken during observations, however *Flat* frames are not essential as non uniform pixel responsivity get automatically corrected during data analysis, which we shall discuss in the next section. For the purpose of calibration, polarized as well as unpolarized standard stars are also observed during each night of observation, whose accurate standard broadband polarization (degree of polarization as well as angle) values are listed in Schmidt et al. (1992b).

2.4.3.2 Processing

Data processing follows the same procedure as outlined for photometry. Images are first processed to subtract bias and remove cosmic rays. To increase SNR, multiple frames taken under same filter and position are combined together after carefully aligning at sub-pixel accuracy. In polarimetry obtaining very good SNR is essential even for photometrically bright objects. This is because, rather than direct flux, we are dealing with relative fluxes of ordinary and extraordinary images for a object exhibiting very low degree of polarization ($< 2\%$), for which flux ratios will also be a small quantity and may be immersed into noise if SNR is not good enough. Standard procedure of aperture photometry is followed using DAOPHOT routines, to extract magnitudes of o and e image for each of the target object(s) as well as standard stars. The extracted instrumental magnitudes are converted to counts (I_e and I_o) which are then used to compute $R(\alpha)$ values.

2.4.4 Data analysis

In Equation 2.7 we have seen that two unknowns, P and θ can be determined using a single set of q and u. However, in a practical scenario there are two issues which need to be addressed before implementing the relation – (i) the responsivity of the underlying pixels of ordinary and extraordinary images are not truly identical and (ii) the responsivity of the optics and entire system may bot be uniform to orthogonal polarized rays. Thus the measured orthogonal intensities (I_o, I_e) differs from true intensities (I'_o, I'_e) by some factors (F_o, F_e) as,

$$\begin{aligned} I_o(\alpha) &= I'_o(\alpha)F_o \\ I_e(\alpha) &= I'_e(\alpha)F_e \end{aligned} \tag{2.8}$$

This ratio of factors can be obtained by using the fact that by rotating HWP by 45° simply led to the interchange of o and e images, and which is calculated as

(Ramaprakash et al., 1998),

$$\frac{F_o}{F_e} = \left[\frac{I_o(0°)}{I_e(45°)} \times \frac{I_o(45°)}{I_e(0°)} \times \frac{I_o(22.5°)}{I_e(67.5°)} \times \frac{I_o(67.5°)}{I_e(22.5°)}\right]^{0.25}, \tag{2.9}$$

Which on multiplying with the ratio of measured orthogonal intensities, we can recover the true ratio,

$$\frac{I'_e(\alpha)}{I'_o(\alpha)} = \frac{I_e(\alpha)}{I_o(\alpha)} \times \frac{F_o}{F_e}. \tag{2.10}$$

Now this corrected ratio of orthogonal intensities are to be substituted in Eq. 2.7 to compute $R(\alpha)$ values for all four HWP positions $\alpha = 0°$, $22.5°$, $45°$ and $67.5°$, which corresponds to normalized stokes parameters ($q_1,\ u_1,\ q_2,\ u_2$).

The associated errors (σ_{q1}, σ_{u1}, σ_{q2} and σ_{u2}) in computed stokes parameters are governed by photon statistics and is primarily dominated by photon noise coupled with electronic noise, which can be estimated as (Ramaprakash et al., 1998),

$$\sigma_{R(\alpha)} = (\sqrt{N_e + N_o + N_{be} + N_{bo}})/(N_e + N_o), \tag{2.11}$$

where N_e and N_o are extracted counts in ordinary and extraordinary images, while N_{be} and N_{bo} are subtracted background sky counts in ordinary and extraordinary images.

The computed normalized stokes parameter along with associated errors are then fitted with the function $R(\alpha) = P\cos(2\theta - 4\alpha)$, to get the polarization parameters P and θ with corresponding fitting errors σ_P and σ_θ. As a crosscheck we also compute two sets of polarization parameters from two sets of q and u.

For q_1 and u_1 polarization parameters are,

$$\begin{aligned} p_1 &= \sqrt{q_1^2 + u_1^2} \\ \theta_1 &= \frac{1}{2}\tan^{-1}\left(\frac{u_1}{q_1}\right), \end{aligned} \tag{2.12}$$

Table 2.3: Correction in polarization angle for AIMPOL

q_1	u_1	q_2	u_2	Corrected angle θ' (°)
−	−	+	+	$\lvert\theta\rvert$
−	+	+	−	$90 - \lvert\theta\rvert$
+	+	−	−	$90 + \lvert\theta\rvert$
+	−	−	+	$180 - \lvert\theta\rvert$

and associated errors are,

$$\sigma_{p1} = \frac{1}{p_1}\sqrt{q_1^2\sigma_{q_1}^2 + u_1^2\sigma_{u_1}^2}$$
$$\sigma_{\theta 1} = \frac{1}{2p_1^2}\sqrt{u_1^2\sigma_{q_1}^2 + q_1^2\sigma_{u_1}^2}\ , \tag{2.13}$$

same follows for q_2 and u_2 to calculate $p_2 \pm \sigma_{p2}$ and $\theta_2 \pm \sigma_{\theta 2}$. Then final mean values are,

$$P = (p_1 + p_2)/2 \qquad \sigma_P = \frac{1}{2}\sqrt{\sigma_{p1}^2 + \sigma_{p2}^2} \tag{2.14}$$

$$\theta = (\theta_1 + \theta_2)/2 \qquad \sigma_\theta = \frac{1}{2}\sqrt{\sigma_{\theta 1}^2 + \sigma_{\theta 2}^2} \tag{2.15}$$

The $P,\ \theta$ values obtained mathematically and fitting should be fairly consistent for good observations.

To find for the quadrant for the angle (basically 2θ) obtained from inverse trigonometric functions or by fitting, specifically for AIMPOL, one need to apply the corrections to θ following the $q,\ u$ pattern as described in Table 2.3.

Calibration

The major calibration process involved in polarimetric observations is to find the zero-point polarization angle (ZPA) with reference to true celestial north. Ideally the fast axis of the Wollaston prism, and so the entire instrumental setup should be perfectly co-aligned with celestial north-south axis, then only the correct polarization angle can be measured. However, in practical scenario due to imperfection in manual alignment some offset, albeit very small, remains in ZPA. The observed polarized

standards (Schmidt et al., 1992b) with accurately know polarization angles are used to calculate this ZPA, which is nothing but the difference in standard and observed polarization angle. After finding the ZPA, a linear offset is applied in observed polarization angles for target objects to get correct values and this is repeated for each night of observations.

The optics of the instrument also introduce very small degree of polarization to the light traversing through it. This can be estimated by observing unpolarized standard stars, which in fact are also polarized but at a very low percentage. The observed polarization of these stars give us an estimate of the instrumental polarization contributed to it. We find the instrumental polarization for AIMPOL is typically less than 0.1%, with variations from $\sim$ 0.05 to 0.11%. The electric vector of instrumental polarization is not confined to any particular plane, and so it will not have any preferred polarization angle. Thus, considering these reasons and also because the value itself is very small, we do not apply any correction due to instrumental polarization in our measurements.

Chapter 3

Distance determination to eight galaxies using expanding photosphere method

3.1 Introduction

A majority of core-collapse events showing hydrogen lines in their optical spectra are classified as type II SNe (Filippenko, 1997), and their progenitors are thought to have retained enough hydrogen until the time of explosion. About ninety percent of all type II events are sub-classified as IIP (Arcavi et al., 2010; Smartt et al., 2009; Smith et al., 2011). The V-band light curve of IIP SNe are described by a fast rise (up to 10-15 days post explosion); a long plateau phase for about hundred days which is sustained by cooling down of shock-heated expanding ejecta by hydrogen recombination and then an exponential decline powered by radioactive decay of newly formed ^{56}Co (Bose et al., 2013). Study of pre-supernova stars from the archival pre-explosion images proves beyond doubt that the progenitors of IIP SNe are red supergiant stars (Poznanski, 2013; Smartt et al., 2009).

Observations of type IIP SNe have been used to determine distances to their host galaxies using expanding photosphere method (EPM), which is a variant of Baade-Wesselink method, developed and implemented first by Kirshner & Kwan (1974) for

two SNe. The EPM provides an estimate of cosmological distances, independent of extragalactic distance ladder, and offers alternative to verify results obtained using other tools e.g. SN Ia. Schmidt et al. (1992a, 1994) applied EPM to several IIP SNe out to 180 Mpc to constrain value of Hubble constant (H_0). Eastman et al. (1996) quantified the dilution factors of supernova atmospheres relative to black-body function and gave a firm theoretical foundation to EPM. However, there have been discrepancies in the distances derived using EPM, e.g. a value in the range 7 to 8 Mpc is obtained for SN 1999em (Elmhamdi et al., 2003b; Hamuy et al., 2001; Leonard et al., 2002c), while a value of 11.7 ± 1.0 Mpc is derived using Cepheids (Leonard et al., 2003). Subsequently, spectral-fitting expanding atmosphere method (SEAM) employing the full `NLTE` supernova model atmosphere codes have been used to derive distances to SN 1999em (Baron et al., 2004; Dessart & Hillier, 2006) and the estimated value was found to be in fair agreement with the Cepheid distance. However, the SEAM is computationally intensive and it can only be applied to events having high signal-to-noise spectra at early phases. The EPM need to be explored further.

Jones et al. (2009) derived EPM distances to 12 IIP SNe using two sets of SN atmospheres, three filter subsets, the photospheric velocity estimated from Doppler-shifts of spectral lines and they found variation in EPM distances up to 50% depending on the models and subsets used. Recently, Vinkó et al. (2012) applied EPM to SNe 2005cs and 2011dh, both in M51 and both having densely sampled light-curves and spectra and they derived distance in good agreement with that in NED database. Takáts & Vinkó (2012) applied EPM to 5 IIP SNe and found that photospheric velocity estimated using SYNOW models of spectral lines are preferred.

Due to their high intrinsic luminosity, type IIP SNe have been detected out to z=0.6 and are expected to be more abundant at higher redshifts (Hopkins & Beacom, 2006). After finding a correlation between plateau luminosity and the photospheric velocity, Hamuy & Pinto (2002) first established IIP SNe as standardizable candles. This standard candle method (SCM) is consistent with red supergiants as their progenitors. Using model light curves of IIP SNe, Kasen & Woosley (2009) gave a firm theoretical basis to the tight relationship between luminosity and expansion velocity,

though they found a sensitivity to progenitor metallicity and mass. Olivares et al. (2010) applied SCM to 37 nearby (z $<$ 0.06) SNe with relative distance precision of 12-14%, though they found systematic differences between distances derived using EPM and SCM.

The observed mid-plateau properties of type II-P SNe form a sequence from subluminous $M_V \sim -15$ mag, low-velocity $v \sim 2000$ km s^{-1} to bright ~ -18 mag, high-velocity ~ 8000 km s^{-1} events (Hamuy, 2003). Recently, a spectroscopically subluminous IIP showing light curve properties similar to a normal luminosity event have also been observed, e.g. SN 2008in (Roy et al., 2011) and SN 2009js (Gandhi et al., 2013). Several bright events showing signs of circumstellar interaction have been observed, e.g. SNe 2007od (Inserra et al., 2011) and 2009bw (Inserra et al., 2012b). The main factors governing the observed properties are nature and environments of progenitors. In view of diversity in the properties of IIP SNe, as well as the availability of good quality data for several events in the literature, more and newer events need to be tested for its applicability as reliable distance indicators. In this work, we extend the EPM analysis to eight type IIP SNe having sufficient early time photometric and spectroscopic data to test the full applicability of EPM and know the limitations and strength of the method.

The chapter is organized as follows. The basic ingredients of the EPM are briefly described in §3.2. The sample and data are given in §3.3. The EPM analysis, sources of errors and results are presented and discussed in §3.4, followed by discussions on individual events and summary in §3.5.

3.2 Method

The expanding photosphere method (EPM) is fundamentally a geometrical technique (Kirshner & Kwan, 1974; Schmidt et al., 1992a), in which we compare the linear radii determined from the velocity of supernova expansion with that of angular radii estimated by fitting blackbody to the observed supernova fluxes at different epochs. For extragalactic supernovae, it is not possible to measure radii directly as they are seen as point sources, however, we may relate linear radius R and angular

radius θ as $\theta = R/D$, where D is distance to the supernova. Furthermore, assuming a spherically symmetric expansion of the photosphere moving with velocity $v_{\rm ph}$ at time t and neglecting other deceleration factor such as gravity and interstellar medium, we may write the above geometric relation as

$$t = D\left(\frac{\theta}{v_{\rm ph}}\right) + t_0 \tag{3.1}$$

where t_0 is the time of explosion. We use this linear equation to determine D and t_0. Given t_0, we can estimate D for each value of $\theta/v_{\rm ph}$ and alternatively, the relation can also be solved to estimate unique values of D and t_0. We note that for many supernovae, the later is not known with sufficient precision and the method can also be used to get an independent estimate of t_0 as well as to test the consistency of the fitted parameters.

Thus, to derive distance by EPM, all we need are values of $v_{\rm ph}$ and θ at different t. The former is derived from low-resolution optical spectroscopic data while the later is estimated from broad-band photometric data.

3.2.1 Determination of $v_{\rm ph}$

The determination of expansion velocity of supernova at the photosphere $v_{\rm ph}$ at time t is a non-trivial issue and several approaches have been evolved in the literature, see Takáts & Vinkó (2012) for a summary on merits and demerits of various approaches. The photosphere represents the optically thick and ionized part of the ejecta which emits most of the continuum radiation as a diluted blackbody and it is understood to be located in a thin spherical shell where electron-scattering optical depth of photons is 2/3 (Dessart & Hillier, 2005a). In type IIP SNe, no single measurable spectral feature is directly connected with the true velocity of photosphere, however, during the plateau-phase, it is best represented by blue-shifted absorption components of P-Cygni profiles of Fe II at 4924Å, 5018Å and 5169Å. In early-phase ($t \leq$ 10-15 d) of SNe, the Fe II lines are either weak or absent and in such cases, the He I 5876Å line can be used to estimate photospheric velocity with an accuracy of 2–4% (e.g. Takáts & Vinkó, 2006; Vinkó & Takáts, 2007), however at later phases ($t >$ 20 d),

He I lines disappear and Na I D lines start to dominate in same spectral region. We can estimate velocities either by measuring Doppler-shift of the absorption minima using SPLOT task of `IRAF` (denoted as $v_{\rm pha}$) or by modelling the observed spectra with SYNOW ($v_{\rm phs}$). We use both the methods in this work.

SYNOW (Branch et al., 2002; Fisher et al., 1999, 1997) is a highly parameterized spectrum synthesis code with number of simplified assumptions: homologous expansion, spherical symmetry, line formation is purely due to resonant scattering in which the radiative transfer equations are solved by Sobolev approximation and the most important assumption is `LTE` atmosphere with a sharp photosphere radiating like a blackbody. However, despite such simplified assumptions, the basic physics of expanding photosphere is preserved which gives rise to P-Cygni profiles for each spectral line. As a result, the underlying continuum of the synthetic spectra shall not match with observed ones because of the obvious fact that the physics of the continuum is significantly different and definitely not `LTE` but, the P-Cygni profiles shall be well reproduced in synthetic spectra which is directly related to the velocity of line formation layers. The SYNOW also has the potential to reproduce line blending features in synthetic spectra, as in case of Fe II line, these are moderately contaminated by other ions, among which most prominent ones are Ba II, Sc II and Ti II. Takáts & Vinkó (2012) have compared the velocities determined from SYNOW and CMFGEN as the later model solves the `NLTE` radiation-transfer equations for expanding photosphere, and it has been shown that the velocities from each of these model are very much consistent with each other.

3.2.2 Determination of θ

In order to determine θ at time t, we assume that the supernova is radiating isotropically as a blackbody and hence accounting for the conservation of radiative energy we may write,

$$f_{\lambda}^{obs} = \theta^2 \pi B_{\lambda}(T_c) 10^{-0.4 A_{\lambda}} \tag{3.2}$$

where $B_{\lambda}(T_c)$ is Planckian blackbody function at color temperature T_c, A_{λ} is the interstellar extinction and f_{λ}^{obs} is the observed flux.

Table 3.1: Basic properties for supernovae and their host galaxies.

ID (SN) (1)	Host galaxy (2)	$v_{\rm rec}$ ($\rm km\,s^{-1}$) (3)	$t_{\rm ref}$ (JD) (4)	$E(B-V)_{\rm tot}$ (mag) (5)	$M_{\rm V}$ (mag) (6)	References (7)
SN 1999gi	NGC 3184	552	1518.2±3.1	0.21±0.09	-16.3	Leonard et al. (2002b)
SN 2004et	NGC 6946	45	3270.5±0.9	0.41	-17.1	Sahu et al. (2006); Takáts & Vinkó (2012)
SN 2005cs	NGC 5194	463	3549.0±1.0	0.05±0.02	-15.1	Baron et al. (2007); Pastorello et al. (2006, 2009)
SN 2006bp	NGC 3953	987	3834.5±2.0	0.40	-17.1	Immler et al. (2007); Quimby et al. (2007) Dessart et al. (2008)
SN 2008in	NGC 4303	1567	4825.6±2.0	0.10±0.10	-15.7	Roy et al. (2011)
SN 2009bw	UGC 2890	1155	4916.5±3.0	0.31±0.03	-16.8	Inserra et al. (2012b)
SN 2009md	NGC 3389	1308	5162.0±8.0	0.10±0.05	-14.9	Fraser et al. (2011)
SN 2012aw	NGC 3351	778	6002.6±0.8	0.07±0.01	-16.7	Bose et al. (2013)

Notes : The columns are (1) identification of SN; (2) identification of supernova host-galaxy; (3) recession velocity of the galaxy used for doppler correction; (4) the reference epoch in JD since 2450000.0, these are adopted explosion epoch from corresponding literature; (5) the total reddening $E(B-V)_{\rm tot}$ towards the line-of-sight of SN; (6) appromximate absolute visual magnitude at ∼50 day; (7) references for t_{ref}, $E(B-V)_{\rm tot}$, $M_{\rm V}$, and the photometric and spectroscopic data.

In practice, the value of f_λ^{obs} from expanding photosphere of a supernova has significant departure from a true blackbody emission, for the thermalization layer from which the thermal photons are generated is significantly deeper than photospheric layer defining the last scattering ($\tau = 2/3$) surface. As a result, while comparing blackbody flux with that of f_λ^{obs}, the value of θ corresponds to the thermalization layer, whereas the value of $v_{\rm ph}$ to the photospheric layer and hence to take care of this discrepancy, the "dilution factor" ξ is introduced (Wagoner, 1981) as

$$\xi = \frac{R_{therm}}{R_{ph}} \tag{3.3}$$

and rewrite the equation 3.2 as,

$$f_\lambda^{obs} = \xi_\lambda^2 \theta^2 \pi B_\lambda(T_c) 10^{-0.4 A_\lambda} \tag{3.4}$$

Here, ξ is termed as distance correction factor as the distance derived without ac-

counting flux dilution will be overestimated by a factor of $1/\xi$. In principle, ξ depends on many physical properties including chemical composition and density profile of the ejecta. However, Eastman et al. (1996) have shown that ξ behaves more or less as one-dimensional function of T_c only. The computation of ξ requires realistic SN atmosphere models and to be compared with blackbody model, this requires high computing power and detailed physics of SN atmosphere, which is beyond the scope of this work. However, with the advent of faster and powerful computing, it is possible to execute such model codes. Till date, two prescription for dilution factor is available, given independently by Eastman et al. (1996) and by Dessart & Hillier (2005a), hereafter D05. An improved estimate of $\xi(T_c)$ based on the models of Eastman et al. (1996) was provided by Hamuy et al. (2001), hereafter H01. In this work we use prescriptions of both H01 and D05.

In principle, the value of f_λ^{obs} should be obtained from accurate spectrophotometry. However, due to easy availability, it is derived from the photometric data taken using broad-band filters. Consequently, the broadband filter response is inherently embedded within the quoted magnitudes. In order to remove the effect of filter response in observed flux f_λ^{obs} when compared with blackbody model $\pi B(\lambda', T_c)$ flux, we convolve the response function for each pass-band filter with the blackbody model to obtain the synthetic model flux. If $\Re_\lambda(\lambda')$ be the normalized response function of a particular filter whose effective wavelength is λ, then the convolved synthetic flux b_λ is,

$$b_\lambda(T_c) = \int_0^\infty \Re_\lambda(\lambda')\pi B(\lambda', T_c)d\lambda' \tag{3.5}$$

Hence the blackbody flux is replaced with convolved blackbody flux b_λ for each filter and equation 3.2 is rewritten as,

$$f_\lambda^{\rm obs} = \xi_\lambda^2\theta^2 b_\lambda(T_c)10^{-0.4A_\lambda} \tag{3.6}$$

In this work we adopted the response function $\Re_\lambda$ for each of $UBVRI$ filters from Bessell (1990).

In principle we should be able to use all filter passbands (UBVRI for optical) combination to apply EPM. However, in practice all passbands are not suitable

for such study; fast decaying magnitude in U-band, makes the SN too faint for good observations, so, U band is generally opted out from EPM; R-band is also unsuitable for EPM due to contamination from strong $H\alpha$ emission in type II SNe. Hence only, three filter combinations are used for EPM study viz., {BV}, {BVI} and {VI} in combination to two set of dilution factors obtained from H01 and D05.

In reference to the preceding discussions, we are required to solve for θ and T_c. Hence we construct X using equation 3.6 and recast in terms of broadband photometric fluxes,

$$X = \sum_{j=BVI} [f_j^{obs} - \xi_j^2 \theta^2 b_j(T_c) 10^{-0.4A_j}]^2 \tag{3.7}$$

On minimizing we obtain the quantities '$\theta\xi$' and 'T_c' simultaneously, it is also to be noted that $\xi(T_c)$ is itself the function of T_c. So we separate out θ by using the known ξ prescription for the particular filter combination used.

3.3 Data

The sample of type IIP SNe consists of two subluminous SNe 2005cs and 2009md; two normal-luminosity SNe 1999gi and 2012aw; three bright SNe 2004et, 2006bp and 2009bw and a intermediate luminosity SN 2008in having peculiar characteristics. The basic properties of SNe and their host galaxies are given in Table 3.1. The time of explosion $t_{\rm ref}$ is determined from observational non-detection in optical bands and it is constrained with an accuracy of a day for SNe 2005cs, 2004et and 2012aw, while for the remaining SNe, it is usually constrained by matching the spectra with known template of IIP SNe and the accuracy lies between 2 to 8 days. The total interstellar reddening $E(B-V)_{\rm tot}$ given in Table 3.1 includes combined reddening due to the Milky way and the host galaxy. For most of these SNe, the value of reddening is constrained quite accurately. Moreover, in this work, values of extinction in different filters (required as input in Eq. 7 and derived using adopted reddening) is estimated assuming the line-of-sight ratio of total-to-selective extinction Rv = 3.1, though a different reddening law towards the sightline of highly embedded SNe cannot

Table 3.2: Photospheric velocities ($v_{\rm ph}$) of supernovae at different phases.

SN 1999gi			SN 2004et			SN 2005cs		
Phase	$v_{\rm phs}$	$v_{\rm pha}$	Phase	$v_{\rm phs}$	$v_{\rm pha}$	Phase	$v_{\rm phs}$	$v_{\rm pha}$
4.7*	13.20 ± 0.30	12.79	11.1*	8.90 ± 0.40	8.59	3.4*	6.30 ± 0.30	6.48
6.8*	10.30 ± 0.40	11.09	12.3*	9.10 ± 0.40	9.54	4.4*	6.10 ± 0.20	6.04
7.8*	10.00 ± 0.40	11.07	13.0*	9.40 ± 0.40	8.79	5.4*	5.70 ± 0.25	5.59
30.7	4.85 ± 0.07	5.18	14.4*	8.40 ± 0.40	9.04	8.4*	5.30 ± 0.30	5.16
35.7	4.20 ± 0.10	4.67	15.0*	8.80 ± 0.20	8.31	8.8	5.30 ± 0.30	4.71
38.7	4.05 ± 0.10	4.47	16.0*	8.00 ± 0.30	7.79	14.4	4.00 ± 0.30	3.76
89.6	1.60 ± 0.20	2.78	24.6	7.30 ± 0.40	6.41	14.4	4.10 ± 0.20	3.83
			30.6	6.20 ± 0.20	5.69	17.4	3.60 ± 0.20	3.31
			35.5	5.30 ± 0.30	4.98	18.4	3.60 ± 0.20	3.52
			38.6	5.10 ± 0.15	4.98	22.5	3.20 ± 0.50	2.89
			40.7	4.90 ± 0.25	4.86	34.4	2.40 ± 0.10	2.26
			50.5	4.20 ± 0.25	4.28	36.4	2.25 ± 0.05	1.80
			55.6	4.00 ± 0.25	3.85	44.4	1.95 ± 0.10	1.43
			63.5	3.80 ± 0.10	3.66	61.4	1.40 ± 0.07	1.02
						62.4	1.35 ± 0.13	0.98
SN 2006bp			SN 2008in			SN 2009bw		
Phase	$v_{\rm phs}$	$v_{\rm pha}$	Phase	$v_{\rm phs}$	$v_{\rm pha}$	Phase	$v_{\rm phs}$	$v_{\rm pha}$
3.35 *	13.70 ± 0.30	12.99	7*	6.10 ± 0.10	5.72	4.0*	8.90 ± 0.35	8.90
6.30 *	12.10 ± 0.20	11.33	14	4.54 ± 0.15	4.36	17.8	6.70 ± 0.40	6.84
8.10 *	11.50 ± 0.15	11.21	54	2.80 ± 0.07	2.66	19.8	6.15 ± 0.30	5.66
10.10*	10.55 ± 0.20	10.41	60	2.66 ± 0.06	2.66	33.8	4.85 ± 0.20	4.68
12.13	9.20 ± 0.40	10.01				37.0	4.25 ± 0.25	4.37
16.10	9.00 ± 0.50	8.98				38.0	4.25 ± 0.15	4.56
21.28	8.10 ± 0.10	7.69				39.0	4.20 ± 0.10	4.25
25.26	6.75 ± 0.30	6.33				52.0	3.50 ± 0.20	3.60
33.22	6.05 ± 0.20	5.63				64.0	3.15 ± 0.10	3.16
42.22	5.05 ± 0.10	4.79				67.0	3.05 ± 0.10	3.08
57.20	4.23 ± 0.05	4.78						
SN 2009md			SN 2012aw					
Phase	$v_{\rm phs}$	$v_{\rm pha}$	Phase	$v_{\rm phs}$	$v_{\rm pha}$			
12	5.50 ± 0.40	6.22	7*	11.20 ± 0.30	10.31			
15	5.30 ± 0.35	4.76	8*	10.70 ± 0.30	9.55			
27	3.05 ± 0.10	2.92	12*	9.00 ± 0.35	8.39			
48	2.05 ± 0.07	2.22	15*	8.65 ± 0.30	8.14			
100	0.85 ± 0.10	1.43	16	8.60 ± 0.25	8.29			
			20	7.70 ± 0.20	7.46			
			26	6.55 ± 0.20	6.25			
			31	5.60 ± 0.10	5.51			
			45	4.50 ± 0.06	4.47			
			55	4.15 ± 0.08	4.02			
			61	3.50 ± 0.05	3.68			
			66	3.50 ± 0.10	3.61			

Notes : Velocity derived using SYNOW is denotated as $v_{\rm phs}$ whereas that by locating the absorption trough as $v_{\rm pha}$. The phases are expressed in days with reference to the $t_{\rm ref}$ adopted in Table 1, while velocities are given in units of $10^3\,{\rm km\,s^{-1}}$. Velocities at phases marked with astrisks are estimated using He I lines.

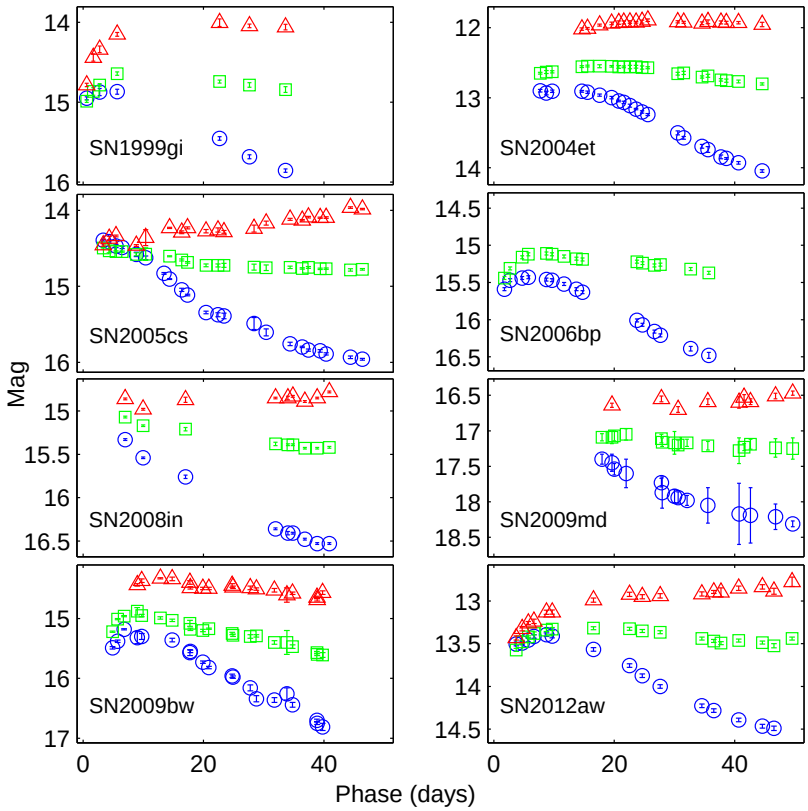

Figure 3.1: The BVI light curves of sample SNe. The colors blue, green and red indicate B, V and I bands respectively. The phases are in reference to the corresponding time of explosion $t_{\rm ref}$ adopted in table 3.1.

be ruled out. We study the implication of variation in reddening on the distance determinations in §3.4.

The criterion for selecting the present sample has been the availability of photometric and spectroscopic data on at least three phases by 50 days after explosion We restricted the use of data for EPM analysis up to the phase 50d, as the value of ξ depends on the color temperature and it varies sharply below 5 kK, i.e. about 50d post explosion for IIP SNe. The BVI photometric data are collected from the literature and Fig. 3.1 shows the photometric data used in this chapter. Barring SN 2009md, we have a dense coverage of early-time (< 50 day) data for all the events. A typical photometric accuracy for events brighter than 15 mag is 0.02 mag while for fainter events it is poorer.

Table 3.3: EPM derived results for the events.

		D05				H01			
		BV	BVI	VI	Mean	BV	BVI	VI	Mean
SN 1999gi	D	11.92±1.08	11.34±0.34	11.60±0.86	11.62±0.29	8.64±0.80	8.71±0.31	9.27±0.73	8.87±0.34
	t_0	1.71±0.99	2.22±0.47	1.37±0.83	1.76±0.43	2.87±0.69	2.78±0.45	1.58±0.89	2.41±0.72
SN 2004et	D	5.28±0.23	4.48±0.13	6.47±0.26	5.41±1.00	3.56±0.17	3.29±0.10	5.22±0.22	4.02±1.04
	t_0	0.28±0.86	4.64±0.53	0.95±0.94	1.96±2.35	2.39±0.75	5.88±0.56	1.72±0.93	3.33±2.23
SN 2005cs	D	7.62±0.26	7.70±0.25	8.61±0.33	7.97±0.55	5.86±0.24	5.98±0.20	6.76±0.27	6.20±0.49
	t_0	-0.49±0.68	-0.35±0.54	-1.77±0.73	-0.87±0.78	0.14±0.73	0.18±0.51	-1.24±0.73	-0.31±0.81
SN 2006bp	D	18.82±1.04	—	—	18.82±1.04	12.47±0.57	—	—	12.47±0.57
	t_0	-3.23±0.77	—	—	-3.23±0.77	-0.95±0.50	—	—	-0.95±0.50
SN 2008in	D	13.11±0.68	14.56±0.76	15.86±0.83	14.51±1.38	12.71±0.84	11.62±0.64	12.58±0.64	12.31±0.59
	t_0	-5.56±1.34	-6.51±1.13	-2.84±1.11	-4.97±1.91	-11.45±2.04	-7.01±1.19	-2.14±0.96	-6.87±4.66
SN 2009bw	D	15.70±1.67	16.15±1.07	22.26±1.57*	15.93±0.32	12.53±1.39	12.68±0.98	17.11±1.36*	12.61±0.11
	t_0	-0.49±4.90	-2.27±1.87	-12.28±5.69*	-1.38±1.26	-2.55±8.10	-2.46±2.12	-10.35±4.25*	-2.51±0.06
SN 2009md	D	21.06±4.21	24.09±3.79	24.72±3.62	23.29±1.96	18.74±3.44	20.29±3.24	19.29±2.43	19.44±0.78
	t_0	6.29±0.46	2.42±4.78	3.73±4.00	4.15±1.97	2.23±0.46	0.16±5.18	4.55±3.16	2.31±2.19
SN 2012aw	D	11.06±0.44	10.51±0.21	12.24±0.49	11.27±0.88	8.22±0.35	8.06±0.16	9.72±0.43	8.67±0.92
	t_0	-2.55±0.71	-1.53±0.32	-2.99±0.71	-2.36±0.75	-1.74±0.61	-0.86±0.35	-2.44±0.82	-1.68±0.79
EPM with fixed explosion epoch									
SN 2004et	D	5.36±0.13	5.50±0.05	6.73±0.10	5.86±0.76	4.07±0.09	4.32±0.04	5.60±0.07	4.66±0.82
SN 2005cs	D	7.34±0.19	7.52±0.18	7.62±0.19	7.49±0.14	5.93±0.16	6.05±0.13	6.19±0.15	6.06±0.13
SN 2012aw	D	9.46±0.27	9.74±0.12	10.27±0.27	9.83±0.41	7.30±0.20	7.70±0.09	8.41±0.22	7.80±0.56

Notes: D denotes the distance in Mpc. t_0 denotes the time of explosion in days, derived in this study and measured with reference to the adopted time of explosion ($t_{\rm ref}$) in Table 3.1. Negative values of t_0 indicate dates prior to the adopted value. The values marked with asterisks are considered deviant and these are not considered in computing the mean value.

3. DISTANCE DETERMINATION TO EIGHT GALAXIES USING EXPANDING PHOTOSPHERE METHOD

We obtained the wavelength- and flux-calibrated spectra either from SUSPECT[1] database or from corresponding authors of papers (see Table 3.1). A typical spectral resolution in the visible range of spectra lies between 5 to 10Å ($\sim$ 300 to 600 km s^{-1}at 5500 Å). For SN 2004et, we have also included 6 epoch spectra between +11d to +16d from Takáts & Vinkó (2012). The spectra were corrected for respective recession velocity of their host galaxy before estimating the photospheric velocity. Table 3.2 provides value of photospheric velocities derived using both the methods described in §3.2.1, i.e. $v_{\rm pha}$ and $v_{\rm phs}$. A detailed description of the SYNOW modelling of spectra and determination of $v_{\rm phs}$ and its error followed in this work is given elsewhere (Bose et al., 2013). We briefly describe the method below. As we are only interested in obtaining photospheric velocity we fit the observed and synthetic spectra locally around Fe II lines (4923.93, 5018.44 and 5169.03 Å) within 4700 - 5300Å, and in early phases where Fe II lines are not available we fit around He I 5876Å line within 5500-6200 Å only; since employing the whole wavelength range may introduce over or under-estimation of photospheric velocities as different lines form at different layers. After attaining optimal fit of observed spectra locally, we only vary model parameter $v_{\rm ph}$ to get eye estimate of maximum possible deviation from optimal value and this is attributed as the uncertainty in $v_{\rm ph}$ for that spectrum. We note that as P-Cygni profiles are quite sensitive to $v_{\rm ph}$ and hence the best fits are easily attainable through eye inspection. The typical uncertainty in velocities estimated by deviation seen visually from best-fit absorption troughs varies between 50 to 500 km s^{-1}with a typical value of $\sim$ 150 km s^{-1}. This is consistent with the values obtained using automated computational techniques viz. χ^2-minimization and cross-correlation methods employing entire spectra (Takáts & Vinkó, 2012). A comparison of $v_{\rm pha}$ and $v_{\rm phs}$ is also made and deviations as large as 1000 km s^{-1} is seen in early spectra for a a few SNe, while random deviations are apparent at later epochs to the level of quoted uncertainty. We study implication of using these velocities on the distance determinations in §3.4.

[1]http://suspect.nhn.ou.edu/~suspect/

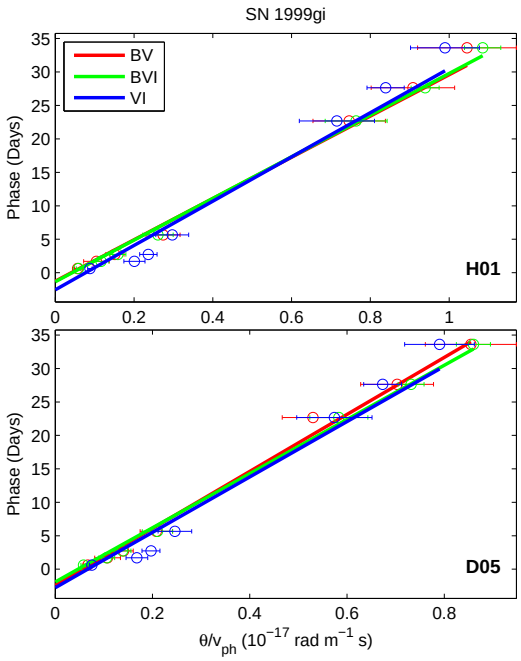

Figure 3.2: EPM fitting for SN 1999gi using two sets of dilution factors H01 (top) and D05 (bottom) in combination to three filter subsets BV, BVI and VI. The phases are in reference to the corresponding $t_{\rm ref}$ adopted in table 3.1.

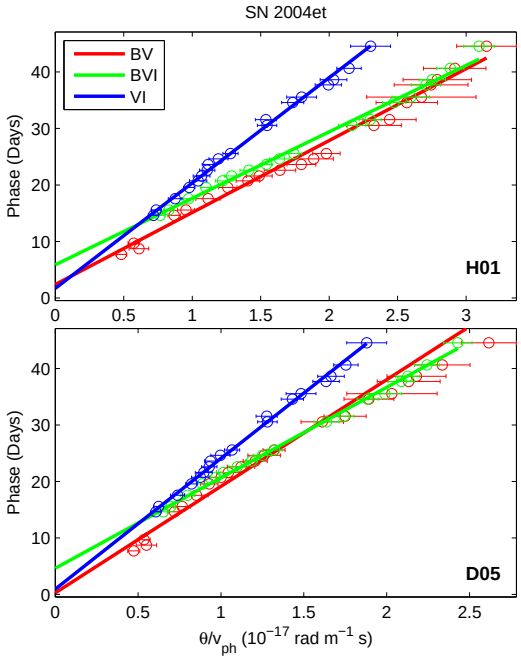

Figure 3.3: Same as Fig. 3.2, but for SN 2004et.

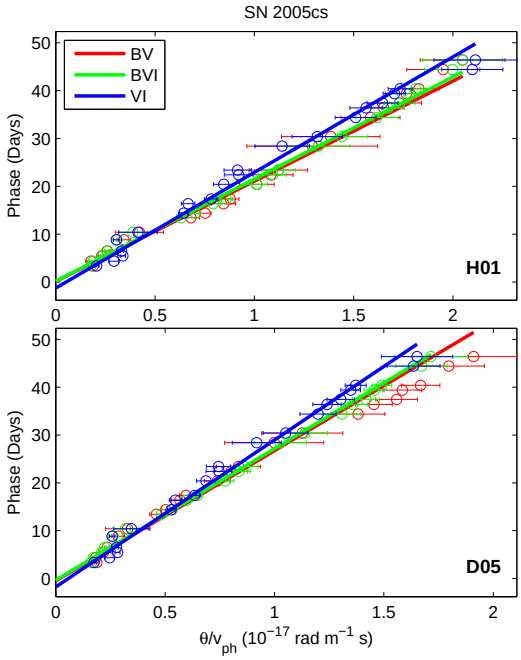

Figure 3.4: Same as Fig. 3.2, but for SN 2005cs.

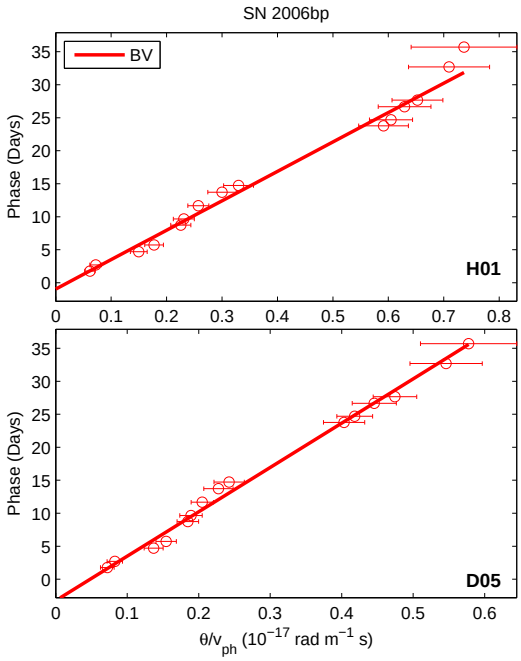

Figure 3.5: Same as Fig. 3.2, but for SN 2006bp using only BV filter subset.

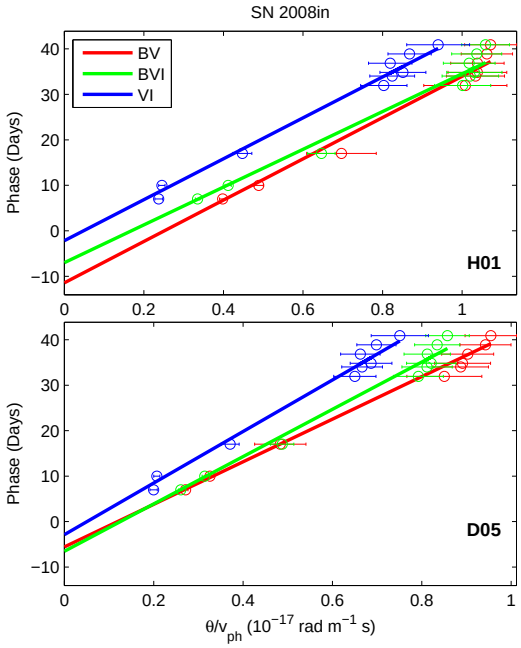

Figure 3.6: Same as Fig. 3.2, but for SN 2008in.

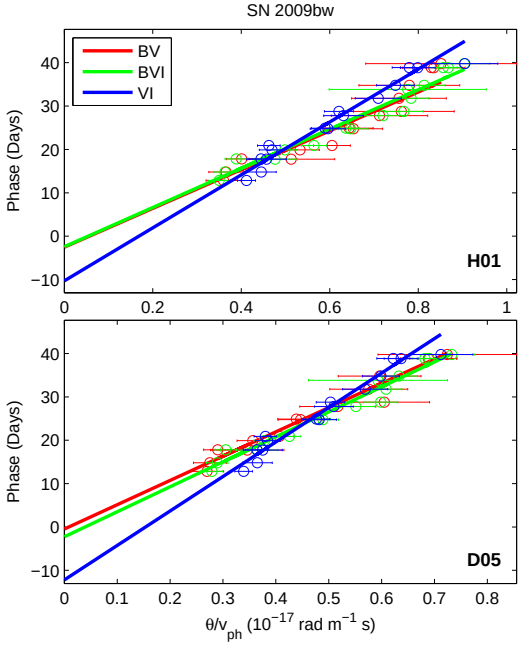

Figure 3.7: Same as Fig. 3.2, but for SN 2009bw.

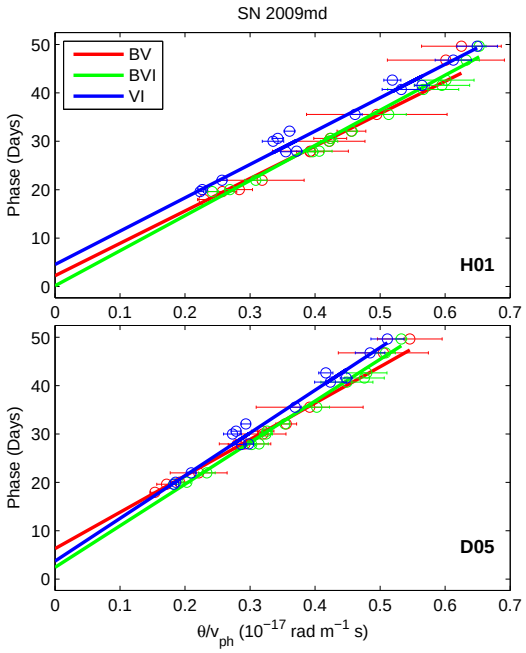

Figure 3.8: Same as Fig. 3.2, but for SN 2009md. Error bars are reduced by factor of five.

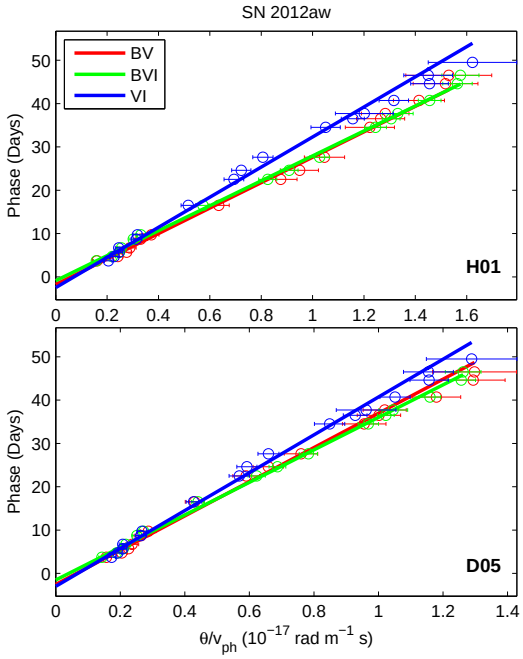

Figure 3.9: Same as Fig. 3.2, but for SN 2012aw.

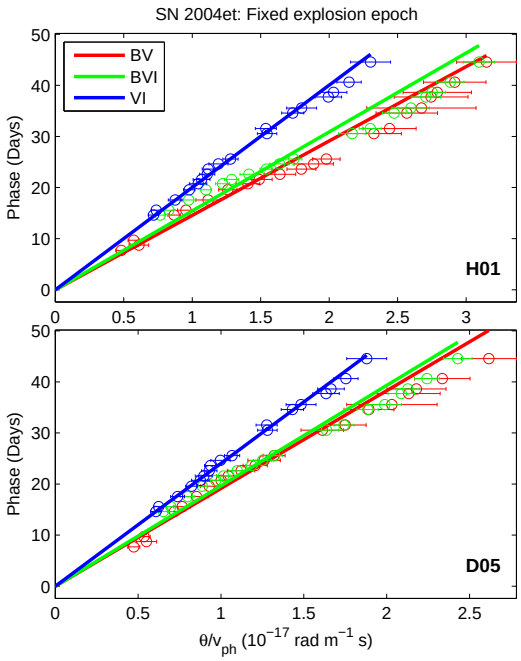

Figure 3.10: Same as Fig. 3.2, but for SN 2004et with fixed explosion epoch at JD 2453270.5.

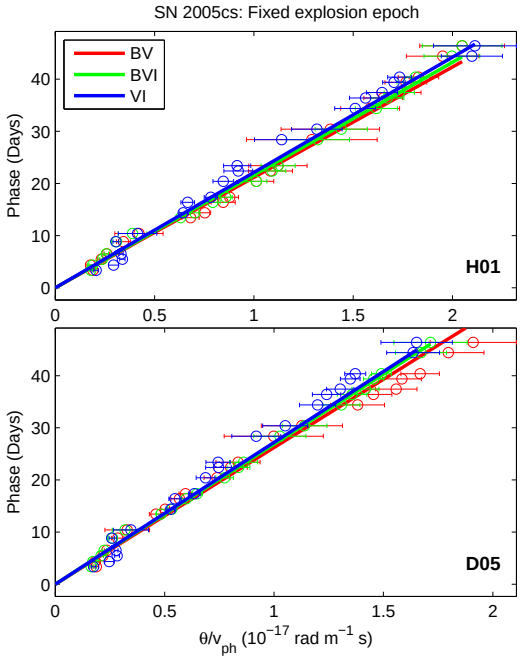

Figure 3.11: Same as Fig. 3.2, but for SN 2005cs with fixed explosion epoch at JD 2453549.0.

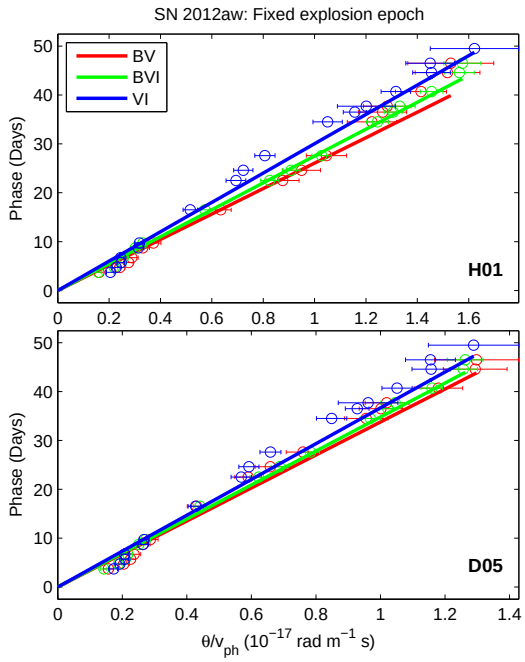

Figure 3.12: Same as Fig. 3.2, but for SN 2012aw with fixed explosion epoch at JD 2456002.6.

3.4 EPM analysis

At each t for which photometric data is available, we derive the value of θ for three sets of filter combinations and for two sets of ξ prescriptions. Wherever spectroscopic data do not coincide with the epoch of photometric data point, the value of $v_{\rm ph}$ at t is derived by polynomial interpolation of third or fourth order. It is noted here that in comparison to photometry, spectroscopy of SNe is more demanding in terms of telescope time and as a result, many of our sample have large spectroscopic data gap. In this work, we have therefore, opted to use the interpolated spectroscopic data for the corresponding epoch of photometric data presented in Fig. 3.1. We performed χ^2-minimization for $\theta/v_{\rm ph}$ versus time to derive D and t_0 (see Eq 3.1). Here, we use SYNOW-derived value of $v_{\rm ph}$ (i.e. $v_{\rm phs}$, see Table 3.2). Fig. 3.2 to 3.9 show plots for SNe 1999gi, 2004et, 2005cs, 2006bp, 2008in, 2009bw, 2009md, and 2012aw respectively whereas Fig. 3.10 to 3.12 show plots to estimate D with fixed t_0 ($= t_{\rm ref}$, see Table 3.1) for SNe 2004et, 2005cs and 2012aw.

The results are listed in Table 3.3. The errors quoted for distance and explosion epoch are mainly contributed by errors in θ and $v_{\rm ph}$; we discuss errors briefly. Error in quantities $\theta\xi$ and T (see Eq. 3.7) for a fixed value of $E(B-V)$ are estimated using Monte Carlo technique in which a sample of one thousand data points are drawn from normal distribution of uncertainty in the observed photometric fluxes. Considering that ξ is one dimensional function of temperature only, the error in ξ is numerically estimated using error in T. So, the error in θ is computed by combining errors of ξ and $\theta\xi$ in quadrature. We note that, intrinsically, the factor ξ is a major source of systematic error and it may lead to over or under estimation of EPM-derived distance.

The source of error in v_{ph} is random in nature and the relative error in it varies between 2 to 5% whereas in θ it varies between 5 to 10%. While interpolating velocities at desired photometric epochs, the errors are estimated by Monte Carlo method with a sample size of 1000. For the final EPM fit, the error in θ/v_{ph} is propagated from θ and v_{ph} and the weighted least-squared fitting is performed to estimate distance and explosion epoch. The error in finally derived distance for each filter subset is estimated by Monte Carlo technique with a sample size of 1000.

It can be seen from Table 3.3 that for each prescription, we derive three sets of D and t_0 corresponding to each of the three filter sets. Barring SN 2009bw, the values of D and t_0 for each of the filter sets are consistent within uncertainties. We, therefore, combine individual distances and explosion epochs derived for each filter set, to compute mean values of D and t_0 for D05 and H01 ξ prescriptions. The quoted uncertainty in the mean values is the standard deviation of the values obtained for the three filter sets and it can be seen that statistical errors in mean value are consistent with the errors derived in individual filter-sets, barring the case of SN 2009bw which has deviant values for VI set. It can be noted that the relative precision with which EPM distances are derived for either of the atmosphere models (D05 or H01) lies between 2 to 13% having a median value of 6%.

Another source of error in D and t_0 is the value of $E(B-V)$. Though, we have taken its value from literature, and adopted value derived using most reliable method, but its precise determination is extremely difficult and it can introduce

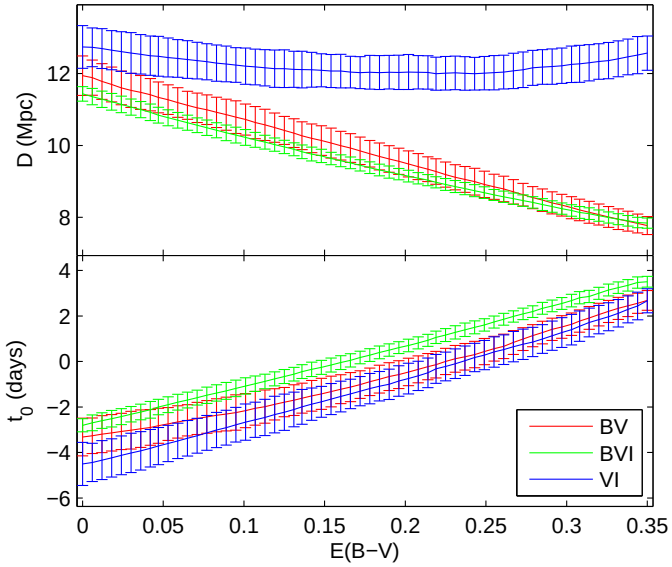

Figure 3.13: Variation of EPM distances and explosion epoch for each filter sub-set {BV}, {BVI} and {VI} with the variation of E(B-V) for the SN 2012aw using D05 prescription.

systematic error in determination of EPM distance. We have studied the effect of $E(B-V)$ for SN 2012aw by varying its value for each filter subset. Figure 3.13 shows the variation of EPM distance and explosion epoch with $E(B-V)$. The variation of distance differs significantly among each filter subset, however the overall variation in distance is not very significant. In order to further study the effect of $E(B-V)$ variation on EPM results for each SNe, we derive mean distances and explosion epochs with the upper and lower limit of $E(B-V)$ and tabulate them in Table 3.4. We took this approach to estimate deviations of EPM results from corresponding $E(B-V)$ errors because of it's systematic dependence on analysis and we found that it would have been inappropriate to propagate $E(B-V)$ errors all throughout the analysis. It is noted here that EPM results have non-linearly dependence on $E(B-V)$ and thus the resulting tabulated errors are asymmetric. The relative variation in D is found to lie between 0 to 9% with median value of 5%.

Table 3.5 compares mean value of distances to host galaxies which are taken from NED and are derived using redshift independent methods, such as Cepheids, Tully-

Table 3.4: Dependence of EPM derived parameters on the errors of $E(B-V)$.

SN event	$E(B-V)$ (mag)	D (Mpc)	t_0 (day)
SN 1999gi	0.21 ± 0.09	$11.62^{-0.78\pm0.50}_{+0.93\pm0.51}$	$1.76^{+0.95\pm0.49}_{-0.87\pm0.46}$
SN 2004et	0.41 ± 0.04	$5.86^{+0.09\pm0.96}_{-0.05\pm0.58}$	–
SN 2005cs	0.05 ± 0.02	$7.97^{-0.20\pm0.62}_{+0.11\pm0.56}$	$-0.87^{+0.37\pm0.84}_{-0.22\pm0.93}$
SN 2006bp	0.40 ± 0.04	$18.82^{-1.10\pm1.12}_{+0.99\pm1.04}$	$-3.23^{+0.94\pm0.89}_{-0.72\pm0.77}$
SN 2008in	0.10 ± 0.10	$14.51^{-1.13\pm1.93}_{+1.34\pm1.81}$	$-4.97^{+1.68\pm2.18}_{-1.50\pm1.41}$
SN 2009bw	0.31 ± 0.03	$15.93^{-0.62\pm0.09}_{+0.79\pm0.50}$	$-1.38^{+0.69\pm0.57}_{-0.92\pm1.71}$
SN 2009md	0.10 ± 0.05	$23.29^{-0.92\pm1.88}_{+1.10\pm2.04}$	$4.15^{+0.56\pm1.58}_{-0.62\pm2.27}$
SN 2012aw	0.07 ± 0.01	$9.83^{-0.02\pm0.43}_{+0.00\pm0.30}$	–

The superscript and subscript values in t_0 and D signify the values derived using upper and lower value of $E(B-V)$ respectively. Further uncertainties quoted in these values are the standard deviation of values obtained from three band sets for each limit of $E(B-V)$.
The references for the values and corresponding errors of $E(B-V)$ are given in Table 3.1. The errors for SN 2004et and SN 2006bp were unavailable in literature, thus for sake of reasonable approximation, we have attributed 10% error in $E(B-V)$ for these SNe.

Fisher, Standard Candle Method, Surface Brightness Fluctuation. with that derived using EPM . The comparison clearly illustrates that the distance derived using D05 prescription is in better agreement with the NED ones, whereas the ones using H01 prescription are systematically lower in each of the cases. Similar systematic differences in the two atmosphere models (D05,H01) have also been reported in the EPM implementation to 12 type IIP SNe by Jones et al. (2009).

For D05 models, a comparison of distances derived using $v_{\rm phs}$ and $v_{\rm pha}$, see Table 3.6, indicate that barring a few cases, there is notable difference in both of the value of distances. For SN 2005cs and 2009md the difference is as high as 18 and 15% respectively, for SN 1999gi, 2004et and 2009bw the values differ by 6 - 9%. However, for SN 2006bp, 2008in and 2012aw the difference is quite negligible and lies in 0 - 3% which is within the internal precision of both values.

EPM analysis of the individual cases are discussed in §3.5.

Table 3.5: Comparison of EPM distances to host galaxies with that derived using other methods.

Host Galaxy	Supernova Event	$D_{\rm EPM}$ (Mpc)	$D_{\rm NED}$ (Mpc)
NGC 3184	SN 1999gi	11.62±0.29	11.95±2.71
NGC 6946	SN 2004et	5.86±0.76	5.96±1.97
NGC 5194	SN 2005cs	7.97±0.55	7.91±0.87
NGC 3953	SN 2006bp	18.82±1.04	18.45±1.60
NGC 4303	SN 2008in	14.51±1.38	16.46±10.8
UGC 2890	SN 2009bw	15.93±0.32	—
NGC 3389	SN 2009md	23.29±1.96	21.29±2.21
NGC 3351	SN 2012aw	9.83±0.41	10.11±0.98

Notes: $D_{\rm NED}$ denote distances to host galaxies as collected from NED (http://ned.ipac.caltech.edu) and derived using redshift-independent methods (see §3.4). $D_{\rm EPM}$, taken from Table 3.3, denote EPM distances derived using D05 atmosphere model and SYNOW derived velocities $v_{\rm phs}$. For SNe 2004et and 2012aw, the distance are with fixed t_0.

3.5 Discussions

In the following, we shall discuss results for each of the event and also any anomaly if found in the result.

SN 1999gi : The photometric and spectroscopic data are taken from Leonard et al. (2002b) and the epm-fitting is shown in Fig. 3.2. For H01 ξ prescription, we derived a distance of 8.87 ± 0.34 Mpc whereas, Leonard et al. (2002b) and Jones et al. (2009) derived a value of 11.1 ± 2.0 Mpc and 11.7 ± 0.8 Mpc respectively. We attribute a lower value of distance in our case to the method adopted in this work i.e. velocity estimates using SYNOW which is significantly different in some epochs and the filter-response deconvolution in SED fitting; and also to less number of data points available for SN 1999gi. Removing first photometric point, our EPM implementation yields a value of ~ 10 Mpc.

For D05 prescription, we derived a value of 11.62 ± 0.29 Mpc while Jones et al. (2009) derived a value of 17.4 ± 2.3 Mpc. It is noted that later has excluded the first spectroscopic data point and have used the spectroscopic epochs for EPM fitting, in contrast to photometric epochs used in the present work, see §3.4. Our estimate for

Table 3.6: Comparison of EPM distances derived using SYNOW modeled velocities and from velocities determined by locating the absorption trough.

SN event	$D_{\rm phs}$ (Mpc)	$D_{\rm pha}$ (Mpc)
SN 1999gi	11.62±0.29	12.72±0.47
SN 2004et	5.41±1.00	4.96±0.88
SN 2005cs	7.97±0.55	6.56±0.42
SN 2006bp	18.82±1.04	18.13±1.18
SN 2008in	14.51±1.38	14.52±1.39
SN 2009bw	15.93±0.32	16.92±0.62
SN 2009md	23.29±1.96	26.84±3.78
SN 2012aw	11.27±0.88	11.27±0.92

$D_{\rm phs}$ denote EPM distances derived using SYNOW model velocities, i.e. $v_{\rm phs}$, whereas, $D_{\rm pha}$ denote the ones derived by locating the absporption minima of Fe II lines, i.e. $v_{\rm pha}$. For consistency, the D05 presciption and unconstrained explosion epoch have been used for all the cases.

D05 is in good agreement with the other redshift independent estimate, see Tab 3.5.

SN 2004et : We used 21 epochs of photometric data taken from Sahu et al. (2006) and Takáts & Vinkó (2012) to derive EPM distance. For this event the time of explosion is determined observationally with an accuracy of a day, and hence, EPM fitting is attempted and shown with t_0 as free and fixed parameters respectively in Fig. 3.3 and Fig. 3.10. For D05 prescription, we derive a EPM distance of 5.41±1.00 Mpc and 5.86 ± 0.76 Mpc respectively; which are consistent with each other as well as with the host galaxy distances derived using other methods. For the former t_0 is estimated as 1.96 ± 2.35 days; which is also consistent with the time of explosion adopted from literature ($t_{\rm ref}$). Takáts & Vinkó (2012) derived an EPM distance of 4.8 ± 0.6 using D05 prescriptions and SYNOW velocities.

However, it is noted that the VI fit is quite inconsistent in comparison to the BV and BVI sets. In order to understand this discrepancy, we looked into the possibility of lower value of $E(B-V)$. Sahu et al. (2006) stated that they found equivalent width of 1.7Å for Na ID from low resolution spectra which corresponds to total $E(B-V)$= 0.43 mag, employing empirical relation of Barbon et al. (1990).

On adopting a similar empirical relation by Turatto et al. (2003) which we find more convincing, we arrive at a much lower value of $E(B-V)$ which is 0.26 mag. Being backed by this possibility of lower $E(B-V)$, we re-derive EPM distances considering only the Galactic reddening value of 0.29 mag (Schlafly & Finkbeiner, 2011) and arrive to EPM distances 5.59, 5.65 and 6.14 Mpc for BV, BVI and VI band sets respectively which are fairly consistent with each other. Despite of favorable results with lower $E(B-V)$ we can not rule out the higher value of $E(B-V)$= 0.40 mag which was derived by Zwitter et al. (2004) using high resolution spectra.

SN 2005cs: We have used 14 epochs spectroscopic and 22 epoch of photometric data from Pastorello et al. (2006, 2009). This is another event for which explosion epoch is constrained observationally within a day hence we have done the fitting by keeping t_0 as free (Fig. 3.4) as well as fixed (Fig. 3.11). We obtain a distance of 7.97 ± 0.55 Mpc and 7.49 ± 0.14 Mpc respectively. In case of free t_0, we arrived at an explosion epoch of -0.87 days which is well within uncertainty and consistent with that known observationally. Hence, in this case it is absolutely unnecessary to fix the explosion epoch.

EPM has been applied to this SN (Takáts & Vinkó, 2006) and a distance of 7.1 ± 1.2 Mpc has been determined. However for this a $E(B-V)$=0.11 has been used, the value of reddening was updated to 0.05 by Pastorello et al. (2009) which we adopt in our work, this accounts for the higher value of D estimated in this work. Vinkó et al. (2012) has presented an improved distance estimate of 8.4 ± 0.7 Mpc for the host galaxy M51 by applying EPM on both 2005cs and 2011dh. Another EPM estimate for the SN has been presented by Dessart et al. (2008) in which they derived distance of 8.9 ± 0.5 Mpc. Both of these EPM estimates are in good agreement with our results.

SN 2006bp: Photometric data presented by Quimby et al. (2007) is available for $UBVri$ filter, but due to lack of ξ prescriptions for SDSS filter, viz., {BVi} or {Vi}, ri data may not be directly used. We have therefore, carried out EPM analysis using {BV} subset only and the results are shown in Fig. 3.5. For D05 ξ prescription, we derived a distance of 18.82 ± 1.04 Mpc. Dessart et al. (2008) has also applied EPM

on the SN in which they estimated the distance using re-computed set of dilution factors and obtained a distance 17.5 ± 0.8 Mpc which is consistent with our estimate within the limit of errors.

SN 2008in: We used photometric data at 21 epochs from Roy et al. (2011) to estimate EPM distance. The spectroscopic coverage of the event is not very good specially within +50 day and hence we had to largely rely upon interpolation (see Table 3.2). It is noteworthy to mention that we found the velocity of profile of the event is quite less varying and overall velocities are much less as compared to other normal type events. This is also supported by the fact that it is classified as spectroscopically sub-luminous (Roy et al., 2011). The EPM fitting is shown in Fig. 3.6 and we derive a distance of 14.51 ± 1.38 Mpc and $t_0 = -4.97 \pm 1.91$ days for D05 prescription. Utrobin & Chugai (2013) has estimated the explosion epoch for this event using hydrodynamical modelling and estimated an explosion epoch nearly 4 days prior to our adopted reference epoch, thus this shows a very good agreement with EPM estimated t_0.

SN 2009bw: Fig. 3.7 shows the EPM fitting for this event. It is noted that even though we were having photometric data starting from +5 day (see Fig. 3.1), but due to single spectra at +4d and unavailability of any other spectra before +18d, we could only include data points within +10 to +50 days for the EPM fit. This was necessary to do as in early phase the velocity profile is quite steeper as compared to later phases and thus in such phases velocity interpolation might go wrong due to less number of spectroscopic data.

Using both dilution factor prescription, we find that the distances derived using band sets {BV} and {BVI} are very much consistent with each other, whereas the distance derived using {VI} subset is significantly higher and the explosion epoch is also very much off (see Table 3.3). Thus making the EPM fit of {VI} quite inconsistent with the rest of two band-sets and also the explosion epoch is not consistent with SN age estimated from spectra and light-curve evolution. This particular inconsistency can be justified by the fact that {VI} band-set are at the cooler ends of SED as compared to {BV} and {BVI} band-sets. As in early phase SED is hotter and estimation of SED parameters viz., θ and temperature, using {VI}

band-set will be more prone to errors if the photometric magnitude uncertainty is significant as we have in literature data of SN 2009bw.

Using D05 prescription, we derive a distance of 15.93 ± 0.32 Mpc. Tully et al. (2009) derive a distance of 11.1 Mpc to the host galaxy using Tully-Fisher method. No other redshift-independent distance estimate is available for this galaxy. We, however, note that Inserra et al. (2012b) adopted a distance of 20.2 Mpc based on the redshift of the galaxy.

SN 2009md: Figure 3.8 shows the EPM fit for this event. Extremely large errors in θ/v_{ph} quantity can be noted and it is attributed entirely due to large photometric errors, as errors in photometric magnitudes have amplified exponentially in fluxes and propagated all throughout to θ/v_{ph} quantities. Using D05 prescription we obtained a distance of 23.29 ± 1.96 Mpc and the time of explosion of 4.15 ± 1.97 days. Fraser et al. (2011) has applied SCM to this event and derived a distance of 18.9 Mpc using optical data and of 21.2 Mpc using near infrared data. For this case, the EPM result is consistent with that derived using SCM.

SN 2012aw: This is a well studied nearby event. The explosion epoch is known fairly accurate with an error of ± 0.79 days, see Bose et al. (2013) and references therein. Figure 3.12 and Fig. 3.9 show the EPM fit respectively with fixed and free t_0. For D05 prescription, we derive a distance of 9.83 ± 0.41 Mpc and 11.27 ± 0.88 Mpc with explosion $t_0 = -2.36 \pm 0.75$. No previous EPM study exist for the galaxy NGC 3351, but recent Cepheids (Freedman et al., 2001) and Tully-Fisher (Russell, 2002) distance estimates are in good agreement with our result.

3.6 Summary

In this study we present EPM distances for eight host galaxies derived using photometric and spectroscopic data of IIP SNe The SNe have mid-plateau absolute V-magnitudes in the range -17 to -15. Detailed EPM analysis is done for five of the events, viz., SN 2004et, 2008in, 2009bw, 2009md and 2012aw for the first time. We use two dilution factor models, three filter sub-sets, and two methods for photospheric velocity determination. The value of reddening are known quite accurately

and for few of the events the explosion epochs are constrained observationally with an accuracy of a day. We find that EPM-derived distances using above two models differs by 30-50%. The EPM distances derived using Hamuy's model (Hamuy et al., 2001) are found to be systematically lower than that of Dessart ones (Dessart & Hillier, 2005a). For all the events in our sample, the distances using Dessart model is found to be consistent with that derived using other redshift independent methods, i.e. Tully Fisher, Standard Candle Method, Cepheid, Surface brightness fluctuation. We also note that EPM method is applicable only to the early (< 50 d) photometric data of supernovae.

We have also studied the effect of two methods of velocity estimation on the derived distance. It is found that the SYNOW model velocities are significantly different than that estimated by locating absorption trough of P-Cygni. The distances derived from two different velocity determination methods have notable differences as high as 15-18%, however we did not find any systematic trend of this difference. This suggests the difference is the direct effect of the measurement error of absorption minima method when the photospheric lines are blended or weak relative to continuum.

Chapter 4

Supernova SN 2012aw - a high-energy clone of archetypal type IIP SN 1999em

4.1 Introduction

The observed properties of IIP SNe differ greatly (Hamuy, 2003; Smartt et al., 2009), for example, the mid-plateau bolometric luminosity vary by an order of magnitude from $\sim 10^{42.5}\,\mathrm{erg\,s^{-1}}$ for archetypal IIP SN 2004et to $\sim 10^{41.5}\,\mathrm{erg\,s^{-1}}$ for under luminous SN 2005cs. The class of subluminous events (Pastorello et al., 2004, 2009) are also accompanied by lower ejecta velocity during plateau ($\sim 1000\ \mathrm{km\,s^{-1}}$) and lower luminosity in the light curve tail owing to small yield of ^{56}Ni ($\sim 2-5\times 10^{-3}\ \mathrm{M_\odot}$), in comparison to the normal luminosity IIP SNe 1999em, 2004et with velocities ($\sim 5000\ \mathrm{km\,s^{-1}}$) and the mass of ^{56}Ni ($\sim$0.1 $\mathrm{M_\odot}$). The subluminous IIP events are associated with O-Ne-Mg core originating from lower-mass progenitors (8-10 $\mathrm{M_\odot}$), while the normal ones originate from iron-core collapse of massive ($>$ 10$\mathrm{M_\odot}$) progenitors (Fraser et al., 2011; Janka, 2012). However, there are cases, i.e. SN 2008in (Roy et al., 2011) and SN 2009js (Gandhi et al., 2013), where a spectroscopically subluminous IIP event show light curve properties similar to a normal luminosity event.

4. SUPERNOVA SN 2012AW - A HIGH-ENERGY CLONE OF ARCHETYPAL TYPE IIP SN 1999EM

The stellar evolution models suggest that type IIP SNe originate from red supergiants having initial masses between 9-25$M_\odot$ having an upper mass cut of 32$M_\odot$ for solar metallicity stars (Heger et al., 2003), however, the observational constraints are ambiguous and the mass of progenitors recovered from the analysis of pre-explosion archival HST images for 20 IIP SNe lie in the range 9-17 $M_\odot$ (Smartt et al., 2009) while the hydrodynamical modelling of light curves for a handful of well studied IIP SNe indicate that they primarily originate from 15-25 $M_\odot$ progenitors (Bersten et al., 2011; Utrobin & Chugai, 2009). Some of the problems in inferring physical properties are the lack of good quality data for nearby SNe.

SN 2012aw was discovered on March 16.9, 2012 by Fagotti et al. (2012) in the nearby galaxy M95 ($\sim$ 10 Mpc) at R-band magnitude of 15. The first non-detection is reported on March 15.27 (Poznanski et al., 2012a) to a 3σ limit of $R \sim 20.7$. Thus, we adopt March 16.1, 2012 (JD=2456002.6 $\pm$ 0.8 days) as the time of explosion (0 d) through out the chapter. The spectra obtained at 2d by Munari et al. (2012) showed a featureless blue continuum while the subsequent spectra at later phases by Itoh et al. (2012); Siviero et al. (2012) identifies the event as young type IIP. The ultraviolet follow-up observations with UVOT/Swift is done by Bayless et al. (2013) and similar to the optical, they report emergence of plateau in the UV light curve after 27d. The analysis of pre-explosion archival HST images of M95 in the vicinity of SN 2012aw, by two independent group of researchers indicate that the progenitor was a red superergiant with masses in the range 14-26$M_\odot$ (Fraser et al., 2012) and 15-20$M_\odot$ (Van Dyk et al., 2012) respectively. However, by accounting for appropriate extinction laws to the circumstellar and interstellar dust, Kochanek et al. (2012) determine that the luminosity of the progenitor star lie between 4.8 to 5.0 dex in solar units and the mass was less than 15$M_\odot$. SN 2012aw was also detected in X-rays observations with swift/XRT by Immler & Brown (2012) and in radio observations by Stockdale et al. (2012); Yadav et al. (2012) indicating interaction of ejecta with the circumstellar material. The early time (17d) optical spectropolarimetric observations with 8-m ESO VLT by Leonard et al. (2012) finds continuum polarization at the level of 0.3% implying substantial asymmetries in the outer ejecta of SN 2012aw.

In this work, we present results from optical photometric ($UBVRI$ and/or $griz$) photometric follow-up observations at 45 phases during 4d to 269d and low-resolution optical spectroscopic observations at 14 phases during 7d to 270d of SN 2012aw. The chapter is organized as follows. In §4.2.1 and §4.2.2, we present the photometric and spectroscopic observations respectively and a brief description of light curves and spectra. Determination of reddening and extinction is given in §4.3. In §4.4, we analyze light and color curves, derive bolometric light-curves and estimate mass of nickel. In §4.5, we study spectra, evolution of spectral features, SYNOW modelling and derive velocity of hydrogen envelope and the photosphere. The characteristics of explosion is described in §4.6 and conclusions are presented in §4.7.

We adopt the distance to the host galaxy M95 as 9.9 ± 0.1 Mpc which is a weighted mean of three most reliable redshift-independent distance measurements in the literature, i.e. 10 ± 0.40 Mpc by Freedman et al. (2001) using cepheids; 9.86 ± 0.14 Mpc by Russell (2002) using Tully-Fisher method and 9.83 ± 0.13 Mpc by Bose & Kumar (2014b) using SN Expanding photosphere method. SN 2012aw occurred in the outskirts of the host galaxy at a deprojected distance of 6.8 kpc and the oxygen abundance (12+log[O/H]) of the galactic ISM at the position of SN is estimated as 8.8 ± 0.1 from the radial metallicity gradient relation in M95 given by Pilyugin et al. (2006) and this value is close to the solar abundance for oxygen of 8.65 (Asplund et al., 2009). Some basic properties of the host galaxy and SN 2012aw is listed in Table 4.1.

4.2 Observation and data reduction

4.2.1 Photometry

The broadband photometric data in $UBVRI$ Johnson-Cousins and $griz$ SDSS systems are collected using the 104-cm Sampurnanand Telescope (ST) at Manora Peak, Nainital and the 130-cm Devasthal Fast Optical Telescope (DFOT) at Devasthal, Nainital. Both the telescopes are operated by the Aryabhatta Research Institute of Observational sciences, India (Sagar et al., 2013). The 104-cm ST is equipped

Table 4.1: Properties of the host galaxy NGC 3351 and SN 2012aw.

Parameters	Value	Ref.[a]
NGC 3351:		
Type	Sb	1
RA (J2000)	$\alpha = 10^{\rm h}43^{\rm m}57\overset{\rm s}{.}67$	1
DEC (J2000)	$\delta = 11°42'13\overset{''}{.}0$	1
Abs. Magnitude	$M_B = -20.36$ mag	1
Distance	$D = 9.9 \pm 0.1$ Mpc	§4.1
Scale	$1'' \sim 48$ pc, $1' \sim 2.9$ kpc	
Distance modulus	$\mu = 29.97 \pm 0.03$	
Apparent radius	$r_{25} = 3\overset{'}{.}6$ (~ 10.5 kpc)	1
Inclination angle	$\Theta_{\rm inc} = 54.6°$	1
Position angle	$\Theta_{\rm maj} = 9.9°$	1
Heliocentric Velocity	$cz_{\rm helio} = 778 \pm 2\,{\rm km\,s^{-1}}$	1
SN 2012aw:		
RA (J2000)	$\alpha = 10^{\rm h}43^{\rm m}53\overset{\rm s}{.}73$	2
DEC (J2000)	$\delta = 11°40'17\overset{''}{.}9$	
Galactocentric Location	58″ W, 115″ S	
Deprojected radius	$r_{\rm SN} = 139\overset{''}{.}1$ (~ 6.75 kpc)	
Time of explosion	t_0 =16.1 March 2012 (UT) (JD 2456002.59)	§4.1
Reddening	$E(B-V)$ =0.074 ± 0.008	§4.3

[a] (1) HyperLEDA - http://leda.univ-lyon1.fr; (2) Van Dyk et al. (2012)

with a 2k×2k liquid-nitrogen cooled CCD camera having square pixels of 24 μm; and with a plate scale of $0\overset{''}{.}37$ per pixel, the CCD covers a square field-of-view of about $13'$ on a side in the sky. While operating at 27 kHz, the gain and readout noise of the CCD are $10e^-$ per analog-to-digital unit and $5.3e^-$ respectively. The 130-cm DFOT is equipped with a 2k×2k Peltier-cooled CCD camera having a pixel size of 13.5 μm; and with a plate scale of $0\overset{''}{.}54$ per pixel, the CCD covers a square field-of-view of $18'$ on a side. The CCD was operated at 31 kHz speed with readout

noise of 2.5e$^-$ – a detailed technical description and performance of this camera can be found elsewhere (Sagar et al., 2012). A binning of 2×2 is used in CCDs wherever required to improve the signal-to-noise ratio. At 104-cm ST, we had $UBVRI$ while at 130-cm, we had BVR as well as $griz$ filters. A typical exposure time of 300s were given for U and B filters while 80-200s were given for remaining filters. For V-band, the full width at half maximum (FWHM) of the stellar point spread function (PSF) varied between 2.″1 to 3.″5, with a median value of 2.″6. In addition to the target exposures, several bias and twilight flat frames are also obtained for calibration purpose.

The bias subtraction, flat fielding, cosmic ray removal, alignment and determination of mean FWHM and ellipticity for each object frames are done using the standard tasks available in the data reduction softwares IRAF[1] and DAOPHOT[2]. Whenever multiple frames are available, the photometry is performed on co-added frames. As the location of SN is fairly isolated from the galaxy center and it lies on a smooth and faint galaxy background (see Fig. 4.1), we chose to perform aperture photometry; and an aperture radius equal to the mean FWHM of a given frame and a 10 pixel wide sky annulus at 6 FWHM radius were chosen. This whole scheme of aperture photometry is achieved using standalone version of DAOPHOT subroutines. The differential instrumental magnitude for each filter was generated using DAOMASTER task.

In order to calibrate instrumental magnitude of SN 2012aw , the Landolt (2009) standard fields PG 1323, PG 1525 and PG 1633 were observed on 22nd March 2012 in $UBVRI$ filters with the 104-cm ST under photometric night conditions viz. transparent sky, FWHM seeing in $V \sim 2''$. The observations of standard fields were taken at five locations covering airmass from 1.06 to 2.36. The SN field is also observed on the same night. The data reduction of SN and Landolt fields are done using profile fitting technique and the instrumental magnitudes were converted into standard system following least-square linear regression procedures outlined in Stetson (1992),

[1] IRAF stands for Image Reduction and Analysis Facility distributed by the National Optical Astronomy Observatories which is operated by the Association of Universities for research in Astronomy, Inc. under co-operative agreement with the National Science Foundation.

[2] DAOPHOT stands for Dominion Astrophysical Observatory Photometry (Stetson, 1987)

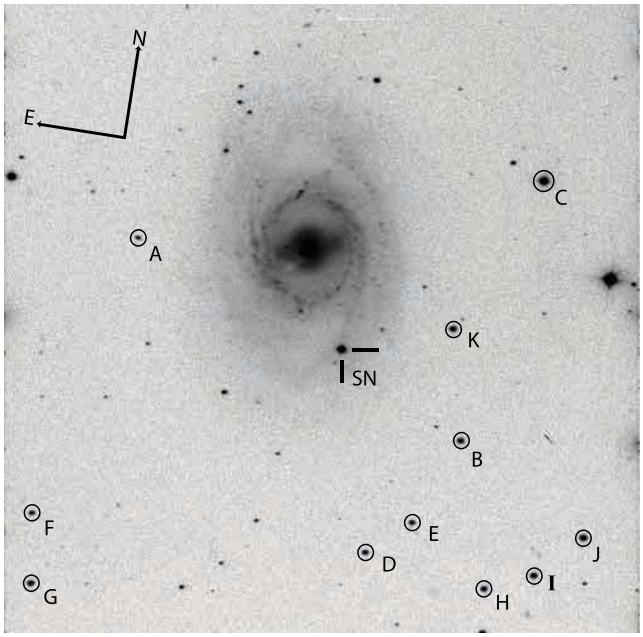

Figure 4.1: SN 2012aw in NGC 3551. The V-band image taken from 104-cm ST covering an area of about $13' \times 13'$ is shown. The location of SN and local standard stars are marked.

in which zero-points, color coefficients and the atmospheric extinction coefficients are fitted simultaneously for 17 stars having V magnitude from 12.0 to 16.4 and $B-V$ from -0.22 to 1.14 mag. The root-mean-squared (RMS) scatter between the transformed and the standard magnitudes of Landolt stars is found to be ~ 0.04 mag in U, 0.02 mag in B and 0.01 mag in VRI. The transformation coefficients were used to generate local standard stars in the field of SN 2012aw observed on the same night and a set of 11 stars with V range from 12 to 17 mag and $B-V$ range of 0.36 to 1.06 mag were selected. These stars are identified in Fig. 4.1 and are listed in Table 4.2. The quoted errors include both photometric and calibration errors propagated in quadrature. The frame-to-frame photometric variability of these stars during 4d to 269d were found to lie within quoted uncertainties. Four of these stars are in common with the study of Henden et al. (2012) who provided calibrated $BVRI$ magnitudes of 14 stars in $20' \times 20'$ field of SN 2012aw. A comparison with their photometry gives a mean and RMS scatter of -0.04 ± 0.04, -0.01 ± 0.03, 0.02 ± 0.04 and 0.00 ± 0.03 mag respectively for B, V, R and I; indicating that the

Table 4.2: Identification number (ID), coordinates (α, δ) and calibrated magnitudes of stable secondary standard stars in the field of SN 2012aw. The field of SN 2012aw was calibrated using Landolt standards observed on the night of 22nd March 2012. The quoted errors in magnitude include both photometric and calibration errors and it denote 1σ uncertainty.

Star ID	α_{J2000} (h m s)	δ_{J2000} ($^\circ\,'\,''$)	U (mag)	B (mag)	V (mag)	R (mag)	I (mag)
A	10:44:11.82	+11:41:54.5	18.168 ± 0.078	17.650 ± 0.045	16.775 ± 0.057	16.316 ± 0.024	15.841 ± 0.017
B	10:43:42.70	+11:38:51.1	15.801 ± 0.024	15.611 ± 0.008	14.897 ± 0.011	14.493 ± 0.013	14.049 ± 0.016
C	10:43:39.17	+11:44:21.3	13.774 ± 0.014	12.882 ± 0.007	11.878 ± 0.026	11.358 ± 0.035	10.866 ± 0.035
D	10:43:49.09	+11:36:17.4	16.277 ± 0.024	16.179 ± 0.012	15.522 ± 0.017	15.139 ± 0.021	14.748 ± 0.019
E	10:43:45.65	+11:37:02.8	16.804 ± 0.037	16.453 ± 0.012	15.668 ± 0.013	15.243 ± 0.016	14.817 ± 0.022
F	10:44:17.02	+11:36:02.1	16.540 ± 0.026	16.760 ± 0.012	16.399 ± 0.014	16.123 ± 0.026	15.795 ± 0.016
G	10:44:16.18	+11:34:37.0	16.277 ± 0.031	15.687 ± 0.015	14.851 ± 0.014	14.397 ± 0.019	13.966 ± 0.018
H	10:43:38.86	+11:35:56.5	16.160 ± 0.023	15.919 ± 0.012	15.207 ± 0.016	14.818 ± 0.020	14.453 ± 0.023
I	10:43:34.96	+11:36:22.2	15.746 ± 0.022	15.494 ± 0.009	14.787 ± 0.012	14.406 ± 0.025	13.966 ± 0.016
J	10:43:31.33	+11:37:17.7	15.954 ± 0.018	14.955 ± 0.006	13.896 ± 0.013	13.300 ± 0.025	12.712 ± 0.016
K	10:43:44.75	+11:41:04.4	15.190 ± 0.020	15.328 ± 0.009	14.944 ± 0.009	14.727 ± 0.012	14.467 ± 0.014

Table 4.3: Photometric evolution of SN 2012aw. Errors denote 1σ uncertainty.

UT Date (yy/mm/dd)	JD 2456000+	Phase[a] (day)	U (mag)	B (mag)	V (mag)	R (mag)	I (mag)	Tel[b]	Seeing[c] ($''$)
2012-03-19.82	006.32	4	12.671 ± 0.042	13.504 ± 0.021	13.574 ± 0.017	13.463 ± 0.018	13.433 ± 0.025	ST	2.6
2012-03-20.80	007.30	5	12.582 ± 0.042	13.492 ± 0.021	13.478 ± 0.017	13.372 ± 0.018	13.325 ± 0.025	ST	2.3
2012-03-21.81	008.31	6	12.517 ± 0.042	13.457 ± 0.021	13.420 ± 0.012	13.300 ± 0.018	13.258 ± 0.018	ST	2.0
2012-03-22.76	009.26	7	12.599 ± 0.042	13.415 ± 0.021	13.380 ± 0.017	13.262 ± 0.018	13.239 ± 0.025	ST	2.0
2012-03-24.84	011.34	9	12.652 ± 0.042	13.394 ± 0.021	13.340 ± 0.017	13.175 ± 0.018	13.132 ± 0.025	ST	1.9
2012-03-25.78	012.28	10	12.676 ± 0.043	13.411 ± 0.021	13.328 ± 0.017	13.192 ± 0.014	13.130 ± 0.025	ST	2.3
2012-04-01.63	019.13	17	13.010 ± 0.042	13.567 ± 0.021	13.318 ± 0.017	13.089 ± 0.018	12.990 ± 0.025	ST	2.2
2012-04-07.63	025.13	23	13.627 ± 0.043	13.756 ± 0.021	13.325 ± 0.017	13.073 ± 0.018	12.923 ± 0.025	ST	2.2
2012-04-09.74	027.24	25	13.909 ± 0.042	13.875 ± 0.021	13.351 ± 0.017	13.086 ± 0.018	12.950 ± 0.025	ST	2.3
2012-04-12.71	030.21	28	14.199 ± 0.042	14.000 ± 0.021	13.366 ± 0.017	13.111 ± 0.018	12.940 ± 0.025	ST	2.4
2012-04-19.65	037.15	35	14.788 ± 0.043	14.228 ± 0.021	13.439 ± 0.017	13.140 ± 0.018	12.918 ± 0.025	ST	2.5
2012-04-21.61	039.11	37	14.905 ± 0.043	14.284 ± 0.021	13.468 ± 0.017	13.151 ± 0.018	12.895 ± 0.018	ST	2.9
2012-04-22.82	040.32	38	—	—	13.493 ± 0.017	13.135 ± 0.018	12.899 ± 0.052	ST	2.7
2012-04-25.75	043.25	41	15.189 ± 0.044	14.392 ± 0.021	13.463 ± 0.017	13.124 ± 0.018	12.851 ± 0.025	ST	2.1
2012-04-29.70	047.20	45	15.377 ± 0.050	14.466 ± 0.021	13.487 ± 0.017	13.126 ± 0.018	12.836 ± 0.025	ST	2.8
2012-05-01.61	049.11	47	15.455 ± 0.057	14.491 ± 0.025	13.725 ± 0.024	13.115 ± 0.023	12.887 ± 0.035	ST	2.9
2012-05-04.63	052.13	50	15.552 ± 0.089	—	13.439 ± 0.018	13.115 ± 0.018	12.776 ± 0.055	ST	2.1
2012-05-06.62	054.12	52	15.725 ± 0.041	14.574 ± 0.021	13.471 ± 0.017	13.116 ± 0.018	12.790 ± 0.052	ST	2.4
2012-05-08.61	056.11	54	—	—	13.526 ± 0.018	13.113 ± 0.019	12.812 ± 0.026	ST	2.7
2012-05-09.61	057.11	55	15.802 ± 0.067	14.688 ± 0.024	13.494 ± 0.017	13.088 ± 0.018	12.775 ± 0.025	ST	2.9
2012-05-11.65	059.15	57	—	14.518 ± 0.022	13.534 ± 0.017	13.085 ± 0.018	—	DFOT	3.1
2012-05-13.68	061.18	59	16.049 ± 0.059	14.697 ± 0.021	13.539 ± 0.017	13.097 ± 0.018	12.804 ± 0.025	ST	2.6
2012-05-14.69	062.19	60	16.133 ± 0.068	14.711 ± 0.022	13.566 ± 0.017	13.139 ± 0.018	12.797 ± 0.025	ST	2.6
2012-05-17.64	065.14	63	16.239 ± 0.049	14.771 ± 0.021	13.556 ± 0.017	13.102 ± 0.018	12.774 ± 0.025	ST	2.8
2012-05-24.63	072.13	70	16.424 ± 0.089	14.817 ± 0.021	13.571 ± 0.017	13.106 ± 0.018	12.787 ± 0.025	ST	3.1
2012-05-27.66	075.16	73	16.577 ± 0.144	14.882 ± 0.022	13.596 ± 0.018	13.118 ± 0.018	12.778 ± 0.025	ST	2.9
2012-05-27.65	075.15	73	—	14.611 ± 0.023	13.596 ± 0.012	13.110 ± 0.018	—	DFOT	2.8
2012-05-28.63	076.13	74	—	14.609 ± 0.025	13.637 ± 0.018	13.115 ± 0.018	—	DFOT	3.1
2012-05-30.65	078.15	76	—	14.872 ± 0.031	13.627 ± 0.018	13.126 ± 0.018	12.786 ± 0.025	ST	3.8
2012-06-06.64	085.14	83	16.840 ± 0.061	14.990 ± 0.021	13.687 ± 0.017	13.127 ± 0.018	12.804 ± 0.018	ST	3.4
2012-06-09.62	088.12	86	17.010 ± 0.062	15.042 ± 0.022	13.664 ± 0.017	13.174 ± 0.018	12.828 ± 0.025	ST	2.5
2012-06-11.63	090.13	88	16.886 ± 0.052	15.057 ± 0.021	13.670 ± 0.017	13.159 ± 0.018	12.815 ± 0.025	ST	2.8
2012-06-16.66	095.16	93	—	14.694 ± 0.029	13.727 ± 0.018	13.206 ± 0.013	—	DFOT	3.3
2012-06-25.65	104.15	102	—	15.231 ± 0.029	13.873 ± 0.022	13.361 ± 0.023	12.995 ± 0.031	ST	3.7

Table 4.3 - continued.

UT Date (yy/mm/dd)	JD 2456000+	Phase[a] (day)	U (mag)	B (mag)	V (mag)	R (mag)	I (mag)	Tel[b]	Seeing[c] ($''$)
2012-06-27.63	106.13	104	16.979 ± 0.219	15.158 ± 0.018	13.824 ± 0.017	13.296 ± 0.018	12.947 ± 0.025	ST	3.7
2012-10-16.96	217.46	215	—	17.526 ± 0.083	16.577 ± 0.025	15.794 ± 0.020	—	DFOT	3.5
2012-10-17.96	218.46	216	—	17.657 ± 0.053	16.617 ± 0.024	15.823 ± 0.014	—	DFOT	3.5
2012-10-23.98	224.48	222	—	18.069 ± 0.361	16.918 ± 0.366	—	15.413 ± 0.059	ST	3.4
2012-10-24.97	225.47	223	—	18.033 ± 0.026	16.711 ± 0.019	15.832 ± 0.019	15.368 ± 0.026	ST	2.2
2012-10-26.97	227.47	225	—	18.106 ± 0.023	16.730 ± 0.019	15.860 ± 0.019	15.389 ± 0.026	ST	2.7
2012-10-29.99	230.49	228	—	—	16.667 ± 0.015	—	—	ST	1.7
2012-10-30.98	231.48	229	19.551 ± 0.361	18.088 ± 0.038	16.765 ± 0.020	15.899 ± 0.014	15.447 ± 0.025	ST	1.8
2012-11-02.97	234.47	232	—	18.163 ± 0.030	16.803 ± 0.020	15.949 ± 0.011	15.454 ± 0.026	ST	2.0
2012-11-04.96	236.46	234	—	18.126 ± 0.030	16.841 ± 0.016	15.975 ± 0.020	15.456 ± 0.026	ST	2.0
2012-11-07.97	239.47	237	—	18.278 ± 0.078	16.721 ± 0.046	15.955 ± 0.031	15.454 ± 0.040	ST	2.2
2012-11-10.95	242.45	240	—	17.850 ± 0.051	16.911 ± 0.022	15.992 ± 0.019	—	DFOT	2.9
2012-11-11.94	243.44	241	—	17.875 ± 0.051	16.963 ± 0.021	15.996 ± 0.019	—	DFOT	3.0
2012-11-16.98	248.48	246	20.291 ± 0.239	18.264 ± 0.019	16.908 ± 0.014	16.039 ± 0.019	15.586 ± 0.019	ST	2.0
2012-11-18.98	250.48	248	19.934 ± 0.153	18.289 ± 0.020	16.927 ± 0.018	16.054 ± 0.019	15.610 ± 0.026	ST	1.7
2012-11-25.95	257.45	255	19.821 ± 0.111	18.323 ± 0.018	17.011 ± 0.014	16.132 ± 0.019	15.709 ± 0.026	ST	1.9
2012-12-04.90	266.40	264	—	18.325 ± 0.060	17.051 ± 0.040	16.012 ± 0.036	15.726 ± 0.050	ST	2.0
2012-12-04.86	266.36	264	—	—	17.130 ± 0.071	—	—	DFOT	3.0
2012-12-09.02	270.52	268	—	18.415 ± 0.070	17.109 ± 0.022	16.225 ± 0.020	15.811 ± 0.026	ST	2.6
2012-12-09.98	271.48	269	20.166 ± 0.165	18.429 ± 0.022	17.113 ± 0.019	16.242 ± 0.019	15.837 ± 0.026	ST	2.2
			g (mag)	r (mag)	i (mag)	z (mag)			
2012-05-11.66	059.16	57	13.922 ± 0.031	13.242 ± 0.028	13.187 ± 0.021	13.185 ± 0.070		DFOT	3.1
2012-05-27.68	075.18	73	14.038 ± 0.031	13.259 ± 0.028	13.199 ± 0.021	13.164 ± 0.049		DFOT	2.8
2012-05-28.65	076.15	74	14.052 ± 0.031	13.269 ± 0.028	13.192 ± 0.021	13.172 ± 0.070		DFOT	3.1
2012-06-16.67	095.17	93	14.173 ± 0.031	13.326 ± 0.028	13.259 ± 0.021	13.192 ± 0.070		DFOT	3.3
2012-10-16.97	217.47	215	17.150 ± 0.033	15.948 ± 0.028	15.907 ± 0.022	15.376 ± 0.071		DFOT	3.5
2012-10-17.98	218.48	216	17.161 ± 0.033	15.971 ± 0.028	15.914 ± 0.022	15.399 ± 0.071		DFOT	3.5
2012-11-10.93	242.43	240	17.339 ± 0.033	16.171 ± 0.028	16.158 ± 0.022	15.570 ± 0.071		DFOT	2.9
2012-11-11.93	243.43	241	17.353 ± 0.033	16.173 ± 0.028	16.167 ± 0.022	—		DFOT	3.0
2012-12-04.95	266.45	264	—	—	—	—		DFOT	3.0

[a] with reference to the explosion epoch JD 2456002.59

[b] ST : 104-cm Sampurnanand Telescope, ARIES, India; DFOT : 130-cm Devasthal fast optical telescope, ARIES, India

[c] FWHM of the median stellar PSF at V band frame.

two photometric measurements are consistent within uncertainties. The magnitude of local standards in *griz* were taken from Lupton et al. 2005. The final photometry of SN 2012aw is given in Table 4.3.

4.2.2 Spectroscopy

During 7d to 270d, long-slit low-resolution spectra in the optical range were collected at 14 epochs; nine from 2m IUCAA Girawali Observatory (IGO) telescope and five from 2m Himalayan Chandra Telescope (HCT). Journal of spectroscopic observations are given in Table 4.4. Observations at 2m IGO have been carried out using IUCAA Faint Object Spectrograph and Camera (IFOSC) mounted at the cassegrain focus of f/10 reflector (Chakraborty et al., 2005; Gupta et al., 2002). Grisms 5 ($\lambda \sim$ 0.33-0.63 μm; $\Delta\lambda \sim$8.8 Å) and pair of grism 7 & 8 ($\lambda \sim$ 0.38-0.83μm; $\Delta\lambda \sim$4 Å) along with a slit width of 1$''$.5 are used to record spectra on 2048 $\times$ 2048 E2V CCD with 13.5 μm pixel size; having a gain of 1.5 e^- per analog-to-digital unit (ADU) and readout noise of 4 e^-. Calibration frames (bias, flat, HeNe arc) and spectrophotometric flux standard stars (Feige34, Hr4468 and Hz44) were observed on each night. Observations from 2m HCT have been carried out in similar fashion with HFOSC using pair of grisms 7&8 ($\lambda \sim$ 0.38-0.84μm; $\Delta\lambda \sim$4 Å) and a slit width of 1$''$.92. For flux calibration, stars Feige66, Feige110 and Grw70d5824 are observed and FeAr and FeNe arcs are observed for wavelength calibrations.

Spectroscopic data reduction was done under `IRAF` environment. Bias and flat fielding were performed on each frames. Cosmic ray rejection on each frame were done using Laplacian kernel detection algorithm for spectra, L.A.Cosmic (van Dokkum, 2001). One-dimensional spectra were extracted using *apall* task which is based on optimal extraction algorithm by Horne (1986). Wavelength calibration were performed using *identify* task and about 15-18 emission lines of HeNe (for IGO) or FeNe and FeAr (for HCT) were used to find dispersion solution. The position of OI emission skyline at 5577Å was used to check the wavelength calibration and deviations were found to lie between 0.3 to 5.5Å and this was corrected by applying a linear shift in wavelength. The instrumental FWHM resolution of 2m IGO spectra as measured from O I 5577Å emission skyline was found to lie between ∼6 to 12Å

($\sim$ 317 - 671 km s^{-1}) and that of 2m HCT was found to lie between $\sim$8 to 10Å .

The flux calibration of wavelength-calibrated spectra was done using *standard, sensfunc* and *calibrate* tasks. We used spectrophotometric standard fluxes from Hamuy et al. (1994); Oke (1990) and the spectral extinction coefficients from Chakraborty et al. (2005); Stalin et al. (2008) for the respective sites. All the spectra were tied to an absolute flux scale using zeropoints determined from $UBVRI$ magnitudes. To tie the spectra with photometry, individual spectrum is multiplied by wavelength dependent polynomial function and it's $BVRI$ filter-response convolved fluxes are compared with photometric fluxes at corresponding epoch. The multiplied polynomial is tuned to minimize the flux difference and obtain the tied spectrum. The one-dimensional spectra are corrected for heliocentric velocity of the host galaxy (778 km s^{-1};§4.1) using *dopcor* tasks.

4.3 Extinction

In order to derive intrinsic properties of explosion, the reddening due to interstellar matter in both the Milky Way and the host galaxy, towards the sight-line of SN 2012aw should be known accurately. Using all-sky dust-extinction map of Schlegel et al. (1998), we derived the value of Galactic reddening as $E(B-V)_{\rm MW} = 0.0278 \pm$ 0.0002 mag. The reddening due to host galaxy $E(B-V)_{\rm host}$ was estimated using two methods viz. the blackbody approximations to the 4d fluxes and the narrow blended Na I doublet absorption lines in the spectra.

The observed spectral energy distribution (SED) of a few days old SNe can be approximated as a blackbody and hence, we generated observed spectral fluxes between 0.26 μm to 0.81 μm using photometric data at 4d in $uvw1$ band (λ_c = 2600 Å) of *Swift* Ultra-violet Optical Telescope (UVOT) taken from Bayless et al. (2013) and in $UBVI$ bands from the present study. The 4d data for UVOT filters $uvw2$ (λ_c = 1928 Å) and $uvm2$ (λ_c = 2246 Å) are not used because of higher errors and also we did not rely on R flux because of the high contamination due to Hα emission. In Fig. 4.2, we have plotted the dereddened observed fluxes for varying $E(B-V)$ and here, the dereddening is done using reddening law of Cardelli et al. (1989) for

Table 4.4: Journal of optical spectroscopic observations of SN 2012aw. The spectral observations are made at 14 phases between 7d to 270d.

UT Date (yy/mm/dd.dd)	JD 2456000+	Phase[a] (days)	Range[b] μm	Telescope[c]	Grating (gr mm^{-1})	Slit width ($''$)	Dispersion (Å pix^{-1})	Exposure (s)	S/N[d] (pix^{-1})
2012-03-22.752	9.25	7	0.38−0.68	HCT	600	1.92	1.43	900	85
			0.58−0.84	HCT	600	1.92	1.26	900	66
2012-03-23.768	10.26	8	0.33−0.63	IGO	300	1.50	2.75	900	147
2012-03-27.615	14.12	12	0.38−0.68	HCT	600	1.92	1.49	1200	123
			0.58−0.84	HCT	600	1.92	1.26	900	75
2012-03-30.659	17.16	15	0.38−0.68	HCT	600	1.92	1.49	900	91
			0.58−0.84	HCT	600	1.92	1.26	900	68
2012-03-31.809	18.30	16	0.38−0.68	HCT	600	1.92	1.49	900	48
			0.58−0.84	HCT	600	1.92	1.26	900	35
2012-04-04.714	22.21	20	0.38−0.68	HCT	600	1.92	1.61	1200	127
			0.58−0.84	HCT	600	1.92	1.25	1200	86
2012-04-10.715	28.21	26	0.38−0.68	IGO	600	1.50	1.39	2700	112
			0.58−0.83	IGO	600	1.50	1.16	1200,2104	71
2012-04-15.802	33.30	31	0.33−0.63	IGO	300	1.50	2.89	1800x2	171
2012-04-29.685	47.18	45	0.33−0.63	IGO	300	1.50	2.89	1200x2	114
2012-05-09.713	57.22	55	0.38−0.68	HCT	600	1.92	1.61	1200	139
			0.58−0.84	HCT	600	1.92	1.25	1200	104
2012-05-15.680	63.19	61	0.38−0.68	IGO	600	1.50	1.38	1800	103
			0.58−0.83	IGO	600	1.50	1.16	1800	85
2012-05-20.730	68.23	66	0.38−0.68	HCT	600	1.92	1.61	900	95
			0.58−0.84	HCT	600	1.92	1.25	900	64
2012-06-27.629	106.13	104	0.38−0.68	HCT	600	1.92	1.61	1200	56
			0.58−0.84	HCT	600	1.92	1.25	1200	38
2012-12-10.846	272.37	270	0.38−0.68	HCT	600	1.92	1.43	2400	26
			0.58−0.84	HCT	600	1.92	1.26	2400	20

[a] With reference to the burst time JD 2456002.59
[b] For transmission ≥50%
[c] HCT : HFOSC on 2 m Himalyan Chandra Telescope, Hanle; IGO : IFOSC on 2 m IUCAA Girawali Observatory, India.
[d] At 0.6 μm

a total-to-selective extinction ratio (R_V) of 3.1. We also show the corresponding blackbody model fluxes with best-fit temperatures; and corresponding to $E(B-V)$ of 0.028 mag, we derive a temperature of 14.2 kK. For $E(B-V) = 0.25$ mag, we obtain an unphysical high temperature of 32 kK. The theoretical modelling of Bersten et al. (2011); Dessart & Hillier (2006) indicate that a value of temperature above 20kK is not expected for 4d old type IIP SNe and hence we derive an upper limit for total $E(B-V)$ of 0.15 mag.

The equivalent width (EW) of Na I D absorption feature is found to be correlated with the reddening $E(B-V)$ estimated from the tail of SN Ia color curves (Barbon et al., 1990; Turatto et al., 2003), though it may be a bad proxy in certain cases, e.g. see Poznanski et al. (2011). In the low-resolution spectra presented in this work, it is not possible to resolve the individual component of Na I doublet (D_1 5889.95Å and D_2 5895.92Å) and hence we can expect to see the blended feature at the gf-weighted rest wavelength of 5893Å. At all the 14 phases of spectra, a weak impression of Na I D due to the host is seen overlaid on the broad P Cygni profile due to SN (see Fig. 4.3), whereas, the feature due to Milky Way is comparatively weak and it is visible only for spectra with high SNR. In Table 4.5, we list the EW of Na I D due to host galaxy only and no attempt is made to estimate EW due to Milky Way. Due to poor SNR (< 50; Table 4.4), the 16d, 104d and 270d spectra were not included in the EW determination. The error in EW is calculated using the relation given by Vollmann & Eversberg (2006) for weak-line limit. The weighted mean of EW derived from 11 individual measurements is 0.394 ± 0.067Å. Employing empirical relation from Poznanski et al. (2012b), i.e. $\log_{10}E(B-V)_{\rm host} = 1.17 \times {\rm EW} - 1.85 \pm 0.08$ (where EW in Å), a value of 0.041 ± 0.011 mag is obtained for reddening due to host galaxy and the error quoted here includes both that in EW and that in the empirical relation. This value is consistent with the $E(B-V)_{\rm host} = 0.055 \pm 0.014$ mag which is derived by Van Dyk et al. (2012) using high-resolution Echelle spectra of SN 2012aw obtained from 10-m Keck telescope at 25d. We derive a weighted mean of the two above measurements, i.e. 0.046 ± 0.008 mag for the host galaxy and by adding the Galactic reddening, a total $E(B-V)_{\rm tot} = 0.074 \pm 0.008$ mag is derived for SN 2012aw and is adopted throughout this chapter. This corresponds to a visual

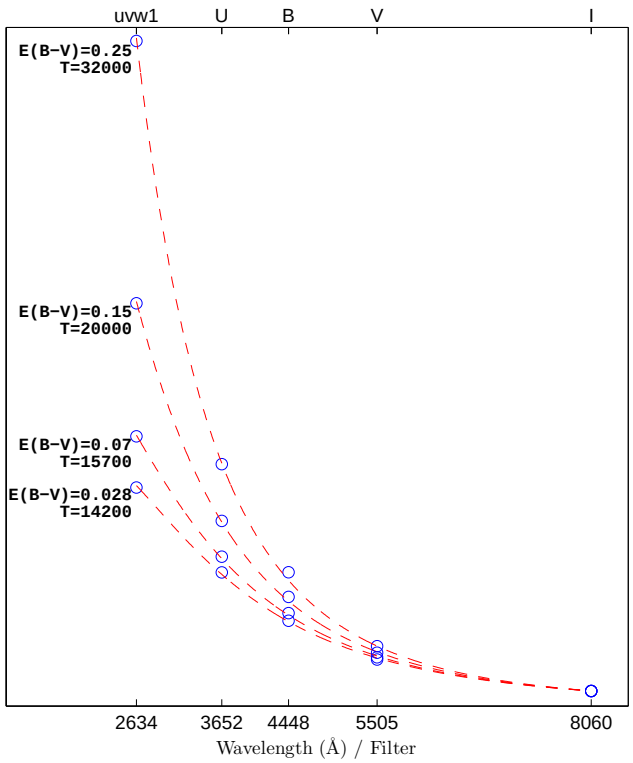

Figure 4.2: The spectral energy distribution of SN 2012aw at 4d is compared with blackbody function. The open circles denote observed fluxes in $uvw1$, U, B, V and I bands corrected for respective reddening values while the dotted line is the best-fit models for different temperature. The fluxes are normalized relative to I-band flux.

extinction $A_V = 0.23 \pm 0.03$ mag, assuming line-of-sight ratio of total-to-selective extinction $R_V = 3.1$.

4.4 Optical light-curve

4.4.1 Apparent magnitude light-curves

The optical light-curve of SN 2012aw in $UBVRI$ filters is shown in Fig. 4.4. The photometric measurements are made at 54 phases during 4d to 269d. The SDSS $griz$ magnitudes are converted to $BVRI$ using empirical relations given by Jordi et al. (2006) and are over-plotted. For comparison the light-curves of archetypal type IIP SN 1999em (Leonard et al., 2002c) is also shown. The early light-curve

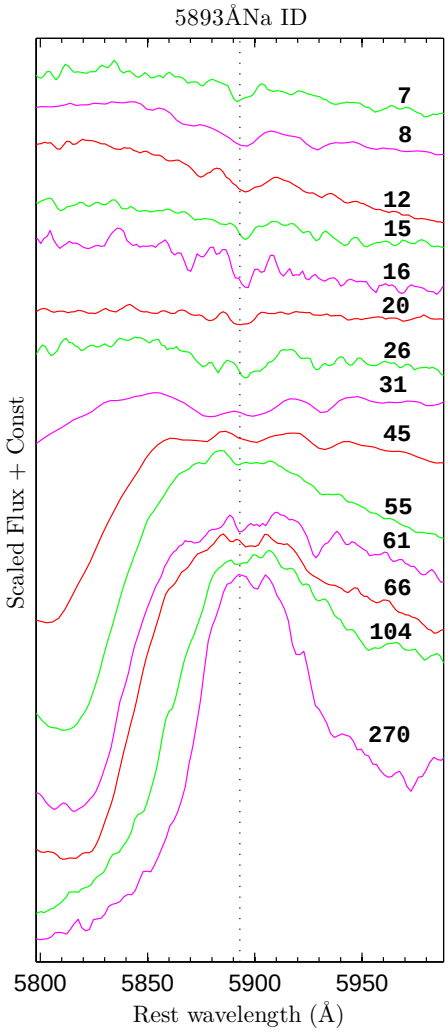

Figure 4.3: The Na I D blended feature due to host galaxy at around 5893Å is shown by dotted line.

shows sharp initial rise of brightness in all the optical bands and then declining slowly into plateau-phase followed by a sharp fall at around 110d to the nebular-phase. On the contrary, the observations in UVOT bands do not show any initial rise in the light-curve observed since as early as 3d (Bayless et al., 2013). The peak in early-time light-curve occurs at about 8d, 11d, 15d, 22d, 24d respectively for $UBVRI$ bands, followed by a continuous decline in UB and a short decline then a continuous rise in VRI peaking at 52d, 56d and 71d respectively (see inset in

Table 4.5: Equivalent widths of Na I D absorption feature due to host galaxy.

UT Date (yyyy-mm-dd)	Phase[a] (day)	EW Å
2012-03-22	7	0.415±0.204
2012-03-23	8	0.410±0.185
2012-03-27	12	0.400±0.233
2012-03-30	15	0.374±0.361
2012-04-04	20	0.399±0.172
2012-04-10	26	0.370±0.226
2012-04-15	31	0.364±0.189
2012-04-29	45	0.413±0.276
2012-05-09	55	0.363±0.237
2012-05-15	61	0.419±0.233
2012-05-20	66	0.400±0.272
Weighted mean		0.394±0.067

[a] With reference to the time of explosion JD 24546002.59

Fig. 4.4). The early-time light-curve of SN 2012aw is almost similar to other nearby ($\leq$ 11 Mpc), well-studied normal type IIP SNe, e.g in SN 1999em - UBV peaked at 6d, 8d and 10d (Leonard et al., 2002c); in SN 2004et, $UBVRI$ peaked at 9d, 10d, 16d, 21d and 25d (Sahu et al., 2006); in SN 1999gi, BV peaked at 8d and 12d (Leonard et al., 2002b). Appearance of initial peaks in $UBVRI$ seems to be a generic feature of early-time light-curves of IIP SNe and in absence of early-time data, it can provide a good handle on estimating the time of explosion with accuracy of a few days, e.g. at V-band, the initial peak occurs at 13 ± 3 d for well studied IIP SNe. Unlike other SNe, the densely-sampled light-curve of SN 2012aw offers the opportunity to see, for the first time, the minima near 42d in V, 39d in R, 31d in I band and then a slow rise to a plateau at about 51d, 59d and 73d respectively. The change in flux from initial early-time rise to the minima is about 16% ($\sim$0.18 mag) in V, 6% ($\sim$0.07 mag) in R, 2% ($\sim$0.02 mag) in I. We note that these values are larger than the typical photometric errors at these epochs. This observed minima around which the SN cools down to hydrogen recombination temperature $\sim$ 6000 K, most likely marks the tail-end of the flux from the adiabatic cooling phase of the shock-breakout and the dominance of the flux from the hydrogen recombination

phase in the supernova envelope (Cowen et al., 2010; Kasen & Woosley, 2009; Roy et al., 2011). However, a dense coverage of this early time data for more number of events would be required to confirm the nature and exact cause of this re-brightening in the light-curves.

As the SN goes behind the sun, we have a data gap between 105d to 214d, however, a prolonged plateau phase of about 100d is apparently seen. The decline rates up to 104d after maxima in UBV is 5.60, 1.74, 0.55 mag/100d respectively, which is similar to the values observed for SN 1999em (see Fig. 4.4) and to SN199gi (Leonard et al., 2002b). The rate of decline for SN 2004et is a bit higher, e.g. at B-band it is 2.2 mag/100d. During plateau-phase, R-band light-curve shows almost no change in brightness, whereas the I-band shows slow increase in brightness until mid-plateau of $\sim$ 60 days, then it remains almost constant until the end of plateau. The decline rate (mag/100d) in light-curve of the nebular phase between 215d to 269d is estimated as 1.24, 0.88, 0.88, 0.81, and 0.95 respectively for $UBVRI$.

4.4.2 Absolute magnitude and color evolution

After correcting for distance and extinction (§4.3; Table 4.1), the absolute magnitude V-band light-curve is shown in Fig. 4.5 and it is compared with other well-studied SNe of normal type IIP 1999em, 2004et, 1999gi, 2004dj; subluminous type IIP 2005cs and peculiar type II 1987A. The V-band light-curves of SNe from literature are also corrected for distance and extinction and the time of explosion for all (except SN 2004dj) of them is known with an accuracy of a day. The comparison shows striking similarity with SN 1999em in both shape and flux. If we ignore the effect of distance, then the duration of plateau, the nebular phase luminosity and the overall shape of light-curve are similar for SNe 1999em, 1999gi, and 2012aw; in contrast to that seen for SNe 2005cs and 2004et. For SN 2012aw the plateau-to-nebular phase transition occurs at $\sim$ 117d and the mid-plateau M_V^p is -16.66 mag and hence it belongs to a normal type IIP events (Patat et al., 1994), in contrast to the subluminous IIP like 2005cs with $M_V^p \sim -15$ mag (Pastorello et al., 2009). The peak absolute magnitude of SN 2012aw is equal to that of SN 1999em, about 0.31 mag brighter than SN 1999gi and about 0.49 mag fainter than SN 2004et. The light-curve evolution in the

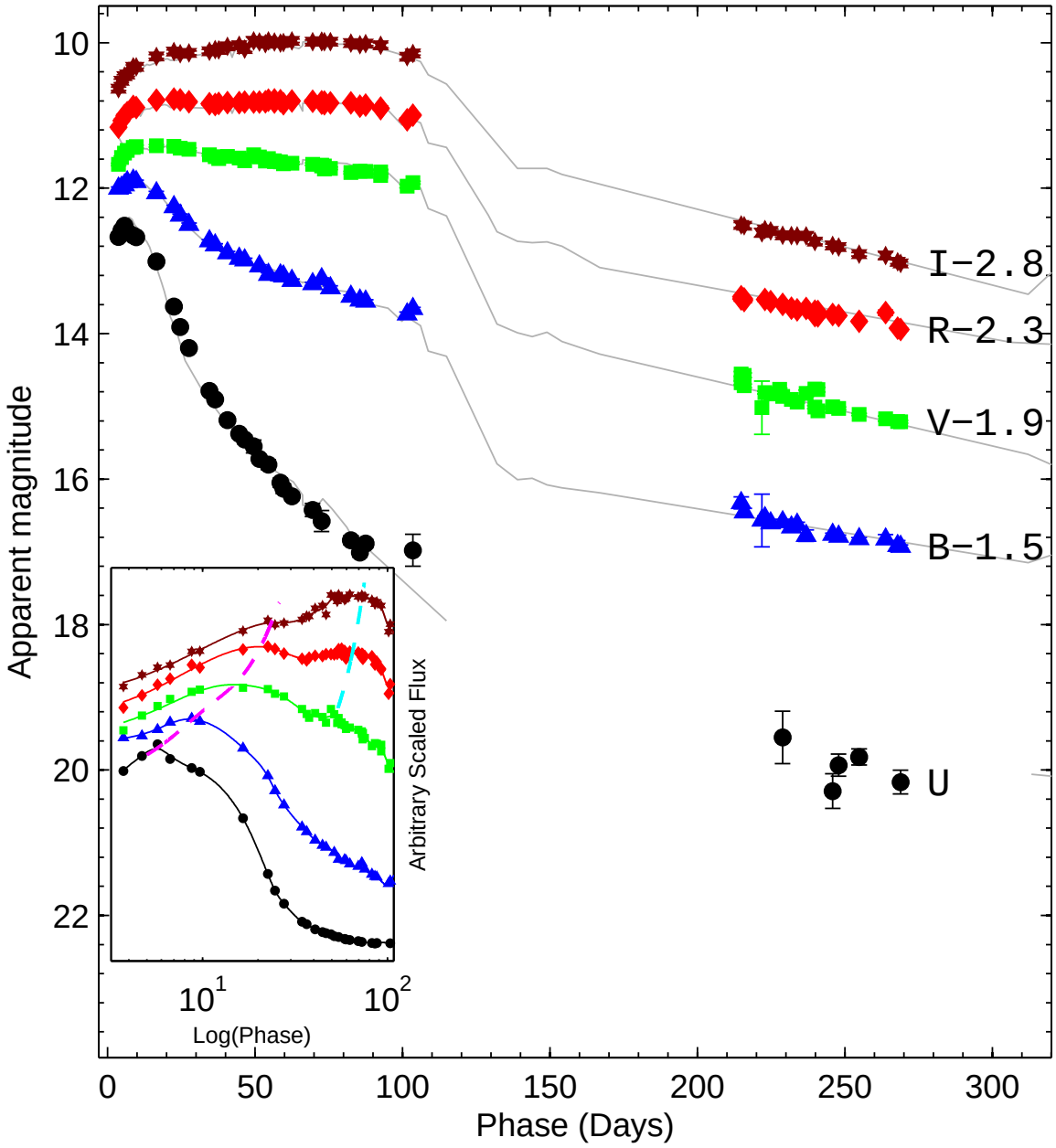

Figure 4.4: The photometric light-curve in Johnson-Cousins $UBVRI$ system. The light-curves are shifted for clarity, while for SN 1999em (gray solid lines), it is scaled in magnitude to match with SN 2012aw. The evolution of early-time time light-curve is shown in inset, wherein, the primary peaks in U, B, V, R, and I at 6d, 9d, 14d, 20d and 23d respectively; and the secondary peak in V, R and I at 52d, 56d, and 71d respectively are clearly visible. Primary and secondary peaks of the light-curve are connected by pair of dashed lines (magenta and cyan respectively).

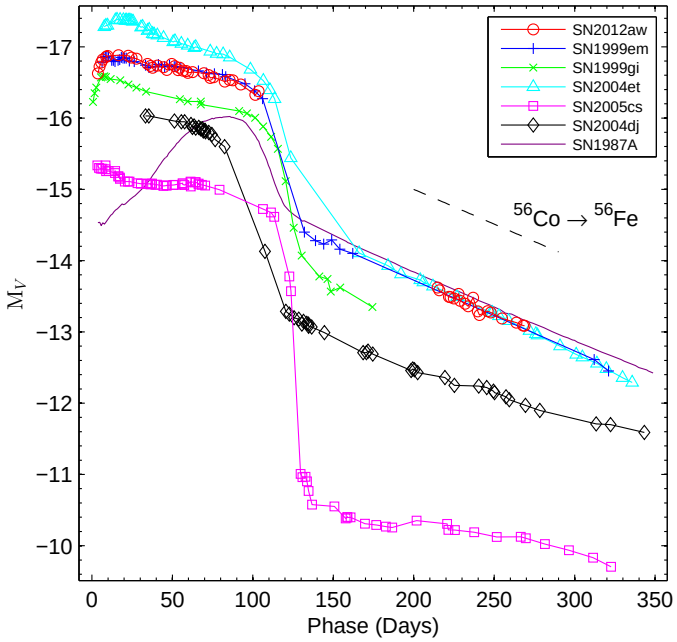

Figure 4.5: Comparison of M_V light curve of SN 2012aw with other type IIP SNe. The exponential decline of the radioactive decay law is shown with dashed lines. The time of explosion in JD-2400000, distance in Mpc, reddening $E(B-V)$ in mag and the reference for apparent V-band magnitude, respectively, are : SN 1999em – 51475.6, 11.7, 0.10; Elmhamdi et al. (2003b); Leonard et al. (2002c); SN 2004et – 53270.5, 5.4, 0.41; Sahu et al. (2006); SN 2005cs – 53549.0, 7.8, 0.11; Pastorello et al. (2009); SN 2004dj – 53187.0, 3.5, 0.07; Tsvetkov et al. (2008); SN 1987A – 46849.8, 0.05, 0.16; Hamuy & Suntzeff (1990); SN 1999gi – 51522.3, 13.0, 0.21; Leonard et al. (2002b).

nebular phase follows the decay rate 0.92 mag/100d. The photometric evolution of type IIP SNe in nebular phase is powered by the radioactive decay of ^{56}Co into ^{56}Fe and the expected decay rate is 0.98 mag $(100\mathrm{d})^{-1}$. The values for SN 2012aw is consistent with this.

The evolution of broad-band colors provides important clues for the expansion and cooling behavior of the supernova envelope. In Fig. 4.6, the evolution of intrinsic colors $U-B$, $B-V$, $V-R$ and $V-I$ are shown. The $U-B$ color evolves very rapidly in early phases up to $\sim$ 50d, primarily due to high temperature and rapid cooling; and it becomes redder from -0.94 to 1.11 mag; though it evolves slowly thereafter and reaches 1.96 mag by 90d. By 260d, it becomes blue again by 0.6 mag

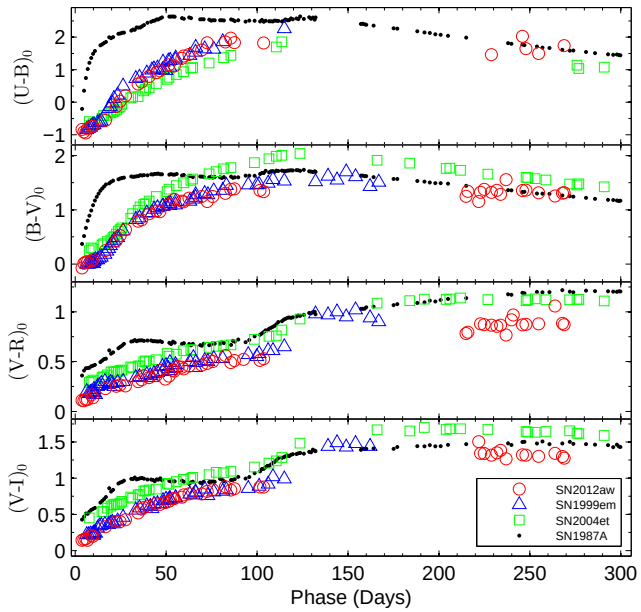

Figure 4.6: The evolution of intrinsic colors of SN 2012aw is compared with other well-studied normal type IIP SNe 1999em, 1999gi and 2004et. The reference for the data is same as in Fig. 4.5.

in about 150d. The $B-V$ also evolves similar to $U-B$, and in nebular phases both colors follow the evolution completely similar to SN 1987A. The evolution in all the colors shows striking resemblance to that of SN 1999em. The $V-I$, $V-R$ and $B-V$ colors of SN 2012aw are significantly ($\sim$ 0.2-0.8 mag) bluer than that of SN 2004et at all phases, while the $U-B$ color is observed to be redder.

In order to have an idea on the temporal evolution of temperature, we fitted blackbody on the observed fluxes in $uvw1$ band (data taken from Bayless et al., 2013) and in $UBVRI$ bands covering the wavelength region 0.26-0.81 μm. The $uvm2$ and $uvw2$ bands are not used as these have large uncertainties in magnitudes and also they result in unrealistic blackbody fits at early phases. The fluxes were corrected for interstellar extinction and we also applied dilution factors as per the prescription by Dessart & Hillier (2006). The fitted values of temperature and the radius are plotted in Fig. 4.7. The blackbody temperature ($T_{\rm bb}$) thus derived can be approximated as a photospheric temperature. During the phases 4-10d, the ejecta temperature drops from 16 kK to 11 kK and by 20d it drops down to about 6500

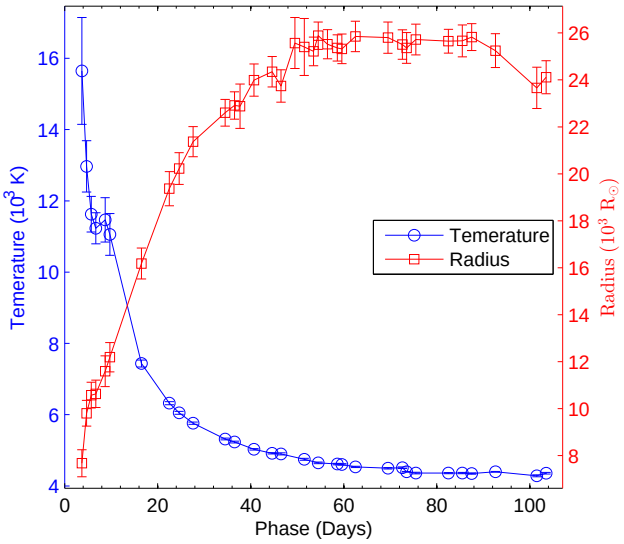

Figure 4.7: The temperature and radius of SN 2012aw as derived from blackbody fits to the observed fluxes in the ultraviolet-optical range 0.17-0.88 μm.

K, with a very slow decline thereafter to 4300 K by 104d. This indicates that the plateau seen in the absolute magnitude light-curve between $\sim$ 20d to 104d is mainly sustained by the recombination of hydrogen. The sharp change in slope of $T_{\rm bb}$ around 20-30d is consistent with the similar trend seen in the color-curve evolution of $U-B$ and $B-V$.

4.4.3 Bolometric light-curve

The bolometric light-curves provide constraint on the amount of radioactive ^{56}Ni synthesized during explosion as well as on the energy of supernova explosion. At early phases ($\leq$ 30d), when supernova ejecta is hotter, the major contribution ($\sim$ 80%) to the bolometric light comes from the ultraviolet and UB bands, while at later phases the flux contribution from RI and near-infrared band dominates (Misra et al., 2007). Here, we determine pseudo-bolometric light-curve by integrating a spline fitted on the $UBVRI$ fluxes derived at their respective effective wavelengths using zero-points from Fukugita et al. (1995). Fluxes are integrated over wavelength range from 3335 Å to 8750 Å; the lower and upper bounds are extended to the HWHM

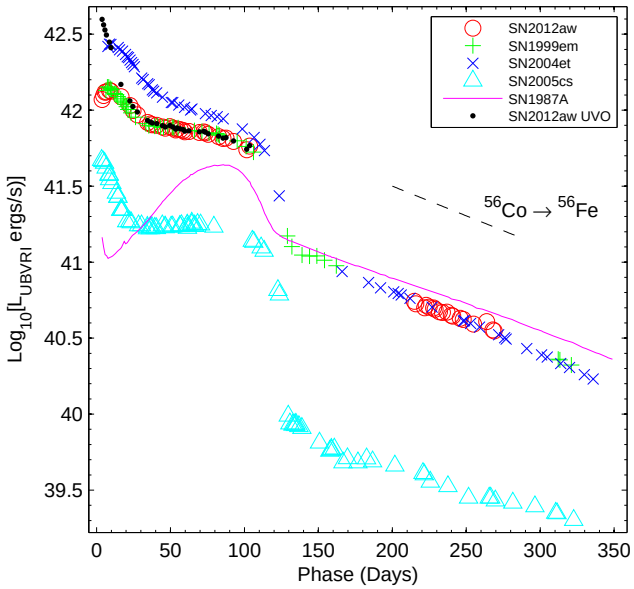

Figure 4.8: The $UBVRI$ bolometric light-curve of SN 2012aw is compared with other well studied supernovae. The adopted distances, reddening and time of explosion are same as in Fig. 4.5. The exponential decline of the radioactive decay law is shown with dashed lines.

(half width half maximum) of U and I bands. Wherever, the observations in a bandpass were missing, the magnitudes were obtained by interpolating the light-curves using low-order cubic-spline. In order to remove the effect of overlapping wavelengths in the $UBVRI$ passbands on the determination of SED from observed fluxes, we equated the known splines convolved with the filter response with that of the observed fluxes. As a guess, we provide initial SED as the spline fitted on observed fluxes and iteratively we construct the true spline SED (whose filter-convolved fluxes matches with observed fluxes). In Fig. 4.8, we plot the bolometric light-curve of SN 2012aw and in the same figure we also show the bolometric light derived using UVOT fluxes in $ubw2$ and $uvw1$ bands taken from Bayless et al. (2013). The $uvm2$ flux is not used due to less number of measurements and large uncertainties in magnitudes. To ensure proper comparison, we have applied same scheme to compute bolometric light-curve in $UBVRI$ bands for other well-studied type II SNe 1987A (Hamuy & Suntzeff, 1990), 1999em (Leonard et al., 2002c), 2004et (Sahu et al., 2006) and 2005cs (Pastorello et al., 2009). Similar to color-curve, the

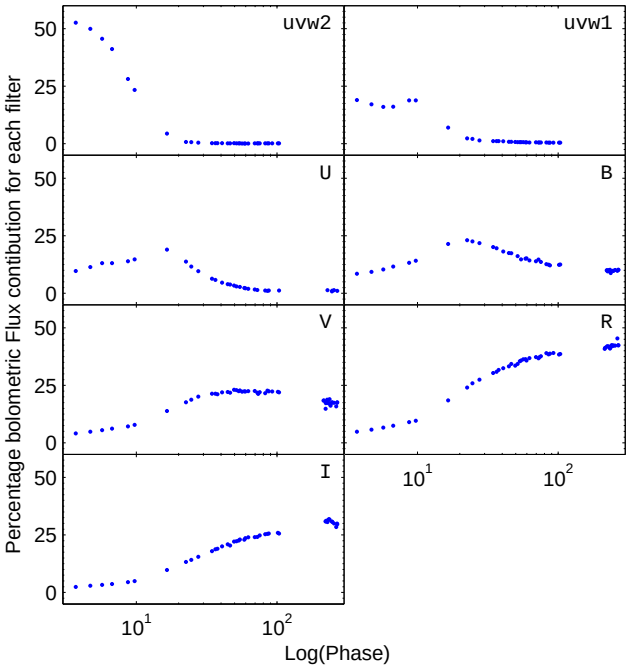

Figure 4.9: The percentage flux contribution in different passbands in the UVOT $uvw2$, $uvw1$ and optical $UBVRI$. Fluxes are corrected for extinction.

evolution of bolometric luminosity is also similar to SN 1999em. The bolometric luminosity declines rapidly by 0.5 dex in first 30d of evolution, and then it slowly declines by 0.2 dex by 104d.

In Fig. 4.9, we plot the percentage flux contribution in reference to the total bolometric light in the ultraviolet-optical region (0.17 to 0.88 μm) from the different passbands. The contribution due to UVOT bands and the optical UB, show a sudden change at around 20d. In uvw2, the contribution falls from approximately 50% to 0%; in uvw1, it drops to 0% from a level of 25%; while in U and B, it rises from 10% at 4d to 22% at about 20d and falls slowly thereafter to a few percent level in plateau and nebular phases. In V, R and I bands, the trend in flux contribution behaves in a similar fashion and it slowly rises from a few % at 7d to above 25% in the plateau phases and beyond. The bolometric luminosity at 25d and beyond is mainly contributed by the VRI bands.

4.4.4 Mass of nickel

In type IIP SNe, the radioactive ^{56}Ni is synthesized by explosive burning of Si and O during shock breakout phase of the explosion (Arnett, 1980) and hence the nebular phase light-curve is mainly powered by radioactive decay of ^{56}Ni to ^{56}Co with half-life time of 6.1d and ^{56}Co to ^{56}Fe with e-folding time of 111.26d emitting energetic γ-rays and positrons. The nebular phase luminosity is assumed to be directly proportional to mass of ^{56}Ni. For a nearby type II-pec SN 1987A, the mass of ^{56}Ni ($M_{\rm Ni}$) has been determined fairly accurate to be 0.075 ± 0.005 M$_\odot$ (Arnett, 1996), and hence by assuming similar γ-ray energy deposition and by comparing the bolometric luminosity of SN 1987A at comparable epochs, we can estimate $M_{\rm Ni}$ of SN 2012aw . We note that for comparison, we use $UBVRI$ bolometric luminosity of 1987A computed in this work (§4.4.3) instead of already available accurately calculated UV-optical-IR luminosity. For SN 2012aw, the $UBVRI$ bolometric luminosity at 240d is estimated using a linear fit over 18 epochs between 210d to 270d, which is $4.53 \pm 0.11 \times 10^{40}$ erg s^{-1}. Similarly for 1987A, it is estimated to be $5.82 \pm 0.06 \times 10^{40}$ erg s^{-1}. The ratio of SN 2012aw to 1987A is found to be 0.778 ± 0.021 and hence we calculate the value of $M_{\rm Ni}$ for SN 2012aw to be 0.058 ± 0.002 M$_\odot$[1]

The value of $M_{\rm Ni}$ can be independently estimated using the tail luminosity ($L_{\rm t}$) as described by Hamuy (2003), assuming the γ-rays emitted during radioactive decay of ^{56}Co makes the ejecta thermalized viz.

$$M_{\rm Ni} = 7.866 \times 10^{-44} \times L_t \exp\left[\frac{(t_t - t_0)/(1+z) - 6.1}{111.26}\right] {\rm M}_\odot$$

where t_0 is the explosion time, 6.1d is the half-life of ^{56}Ni and 111.26d is the e-folding time of the ^{56}Co decay emitting energy in the form of γ-rays. We compute L_t at 11 epochs between 215 to 265 days using the observed V magnitude, a bolometric correction of 0.26 ± 0.06 mag during nebular phase (Hamuy, 2003), and the adopted reddening and distance (see Table 4.1). The weighted mean of $L_{\rm t}$ is $8.97 \pm 0.19 \times 10^{40}$ erg s^{-1}corresponding to mean phase of 240.35d, and this results in a value of

[1] Using the same method and adopting the distance and extinction as given in Fig. 4.5, we estimate $M_{\rm Ni}$ for comparison SNe 2005cs, 1999em and 2004et as 0.004 ± 0.001 M$_\odot$, 0.053 ± 0.001 M$_\odot$, and 0.058 ± 0.001 M$_\odot$ respectively.

$M_{\rm Ni} = 0.057 \pm 0.012 {\rm M}_{\odot}$. Taking weighted average of the values derived above using two photometric methods, we adopt value of $M_{\rm Ni}$ as $0.058 \pm 0.002 {\rm M}_{\odot}$ for SN 2012aw.

We note that the value of $M_{\rm Ni}$ estimated for type IIP SNe using bolometric luminosity of nebular phase depends considerably on the adopted distance and extinction. For example, the value of $M_{\rm Ni}$ reported in the literature (Takáts & Vinkó, 2012, see their Table 1, hereafter TV12) for SNe 2005cs, 1999em and 2004et varies from 0.003 to $0.008 {\rm M}_{\odot}$, from 0.022 to $0.036 {\rm M}_{\odot}$, and from 0.056 to $0.068 {\rm M}_{\odot}$ respectively. However, in view of the empirical correlation found between mass of ^{56}Ni and mid-plateau photospheric velocity by Hamuy (2003) using a large sample of type IIP SNe, the observed object-to-object variation in mass of ^{56}Ni for the above three cases appears to be realistic as the mid-plateau (∼50d post explosion) photospheric velocity of SNe 2005cs, 1999em and 2004et estimated using SYNOW modelling of spectra is found to be 1200 km s^{-1}, 3400 km s^{-1} and 3750 km s^{-1} respectively (TV12). Considering the uncertainty in the adopted distance and extinction for SN 2012aw we anticipate that it produced the amount of ^{56}Ni equal to or a bit less than that for SN 2004et and this is further corroborated by the fact that the mid-plateau photospheric velocity of SN 2012aw is found to be higher than that of SN 1999em but similar to SN 2004et at comparable epochs (§4.5.4).

4.5 Optical spectra

4.5.1 Key spectral features

The spectroscopic evolution of SN 2012aw is presented in Fig. 4.10, in which a preliminary identifications of spectral features is done as per the previously published lines for type IIP events by Leonard et al. (2002c) and the absorption component of some prominent lines are marked. All the spectra are corrected for recession velocity of the host galaxy (§4.2.2). The early phase (7d and 8d) spectra can be distinguished with featureless blue continuum having broad P-Cygni profiles of hydrogen H I (Hα 6562.85Å, Hβ 4861.36Å, Hγ 4340.49Å, Hδ 4101.77Å) and helium He I 5876Å. The He I line disappears by ∼ 16d as the continuum becomes redder with time corresponding to a sudden drop in $T_{\rm bb}$ by a factor of two to 7 kK since early phase. The

appearance of He I line since early phases and its disappearance exactly at $\sim$ 16d is also seen in SN 1999em (Leonard et al., 2002c). The Balmer lines of H I are seen at all the phases until 270d. The FWHM of the emission component of Hα decreases from $\sim$ 17000 km s^{-1} at 7d to about 2500 km s^{-1} at 270d, indicating a decrease in temperature and opacity of the H I line-emitting regions.

In addition to the regular features of H I and He I, the early (7d and 8d) spectra have a couple of peculiar absorption features. Two weak absorption features are present at $\sim$ 4300Å and $\sim$ 4850Å while two relatively strong absorption features are seen near $\sim$ 5500Å (marked with A) and near 4500Å (marked with B). Similar features have also been identified in the early spectrum of type IIP SNe 1999em (Leonard et al., 2002c), 1999gi (Leonard et al., 2002b), and 2007od (Inserra et al., 2011). The origin of these features is not completely understood and in most of the cases they are explained as high-velocity component of H I and He I lines, however, the presence of N II lines 4623Å 5029Å and 5679Å have also been explored and these lines cannot be completely ruled out (Baron et al., 2000; Inserra et al., 2012a).

In SN 2012aw, the feature A at 7d is at $\sim$ 17665 km s^{-1} with reference to He I rest wavelength, thus making it $\sim$ 7198 km s^{-1} higher over the existing He I absorption feature velocity. This component decreases to $\sim$ 16643 km s^{-1} at 8d making an offset by $\sim$ 6586 km s^{-1} higher than existing He I feature. Another absorption feature B is also located at a velocity position of $\sim$ 21785 km s^{-1} on 7d in reference to rest Hβ making it higher by $\sim$ 11293 km s^{-1} over the existing Hβ absorption trough. This feature decreases to $\sim$ 21477 km s^{-1} on 8d. Both of these features tend to decrease in velocity with time, however, none of these features could be detected on 12d and after. The HV absorption features are not seen in Hα. In Fig. 4.11, we compare the early-phase spectra with other SNe and it can be seen that such HV features indicating existence of very high-velocity line-forming material have also been observed for SN 1999gi (Leonard et al., 2002b) and SN 1999em (Baron et al., 2000; Leonard et al., 2002c). In the day 1 spectra of SN 1999gi, the HV component was more dominant and it appeared at $-$30000 km s^{-1} with no trace of normal absorption components. Inserra et al. (2012a) detect HV absorption to Hβ and Hγ lines only in a bright (Mv = -18) type IIP SN 2007od, and a detailed spectral

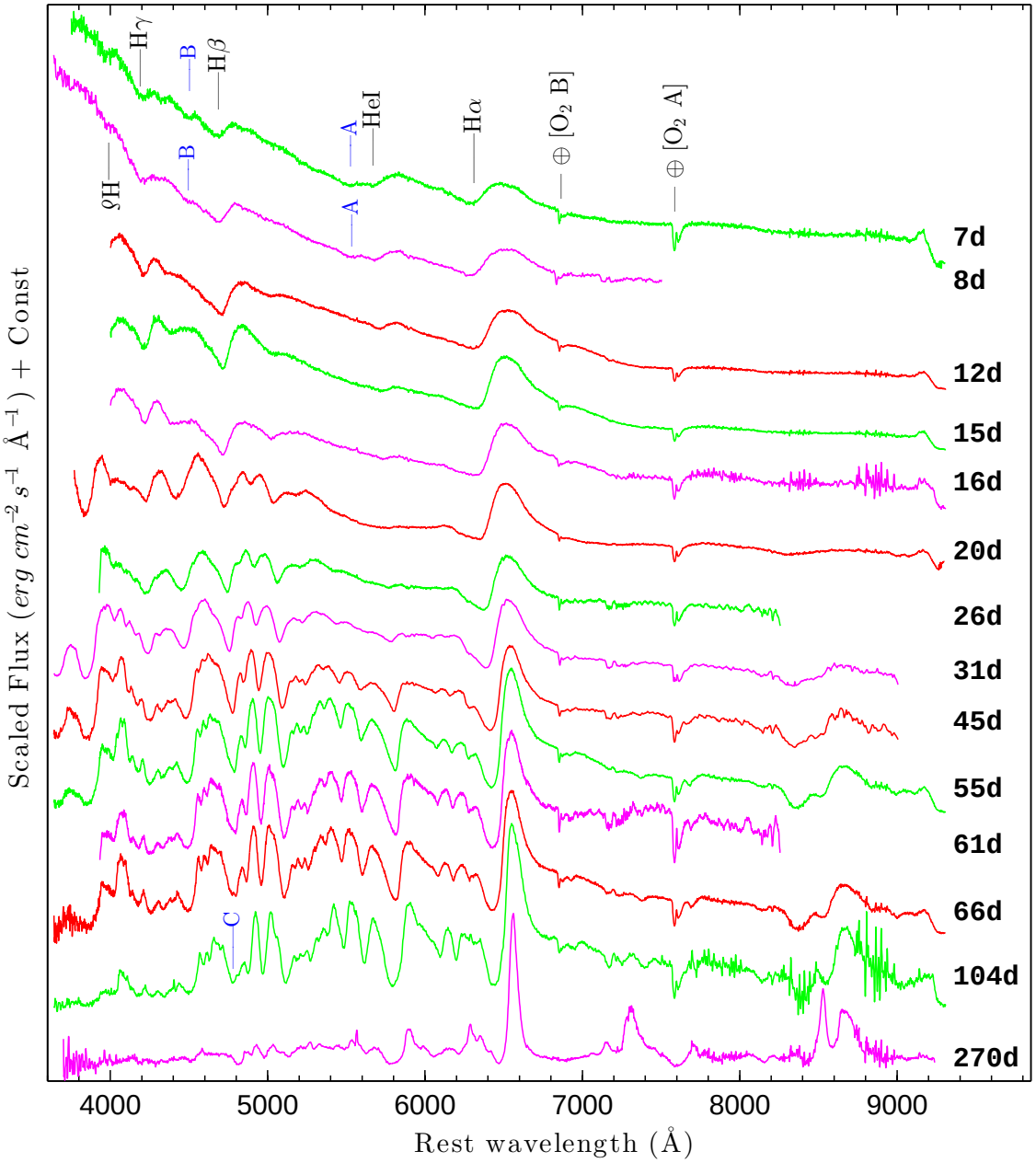

Figure 4.10: The Doppler corrected spectra of SN 2012aw are shown for 14 phases during 7d to 270d. The prominent P-Cygni profiles of hydrogen (Hα, Hβ, Hγ, Hδ) and helium (He I 5876Å) lines are marked. The peculiar absorption features marked with A, B and C are discussed in text. The telluric absorption features are marked with $\oplus$ symbol. The portions of spectrum at extreme blue and red end have poor signal-to-noise ratio.

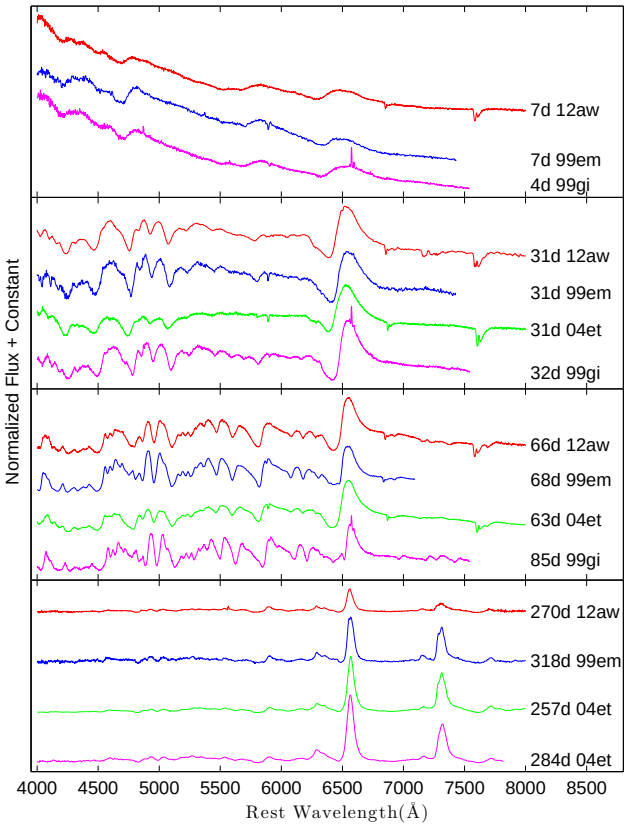

Figure 4.11: Comparison of early (7d), plateau (31d, 66d) and nebular (270d) phase spectra of SN 2012aw with other well-studied type IIP SNe 1999em (Leonard et al., 2002c), 1999gi (Leonard et al., 2002b), 2004et (Maguire et al., 2010; Sahu et al., 2006). Observed fluxes of all the SNe are corrected for extinction and redshift (adopted values same as in Fig. 4.5).

analysis using PHOENIX favored presence of HV feature. It appears that such high-velocity features in Hβ and He I are ubiquitous in normal luminosity type IIP SNe at early phases ($\leq$ 8d) though its origin (i.e. whether it is caused by abundance and/or density enhancements in the layers of ejecta above photosphere) and exact geometry remains open questions to be addressed using detailed modelling. We attempt to identify these peculiar absorption features using SYNOW modelling in §4.5.2.

The spectra at 12d, 15d and 16d represent transition from a hotter (∼16kK) early phase to a cooler (∼6kK) plateau phase when photosphere begin to penetrate Fe-rich ejecta. These spectra mark the emergence of permitted lines of singly ionized

atoms of calcium, iron, scandium, barium, titanium and of neutral sodium atoms. The strong lines of Ba II 4554Å blend and Fe II 5169Å begin to appear at 12d, and the weaker lines of Fe II at 4929Å and 5018Å are clearly seen at 20d. The spectra at 8 epochs from 20d to 104d represent plateau-phase corresponding to further slow cooling of the supernova envelope and appearance of more number of metallic lines. The lines of Na I D 5893Å and Ca II IR Triplet 8498, 8542, 8662Å emerge at 20d and they are clearly visible by 31d. The blend of Ca II H 3934Å & K 3968Å appear at the gf-weighted rest wavelength 3945Å and it is very strong at 20d; seen until 104d. A definite identifications of Ca II is seen in early spectrum of IIP SNe as well, e.g. at 12d in SN 1999em (Baron et al., 2000). The Fe II 5535Å blend, Sc II 5665Å multiplet, Ba II 6142Å, and Sc II 6246Å, are clearly seen at 45d. The above features are present in the spectra until 104d and their comparison with other SNe (Fig. 4.11) indicate that the plateau phase spectral features are similar to normal type IIP events.

The only late time spectrum at 270d shows emission lines with no absorption components, which is a typical characteristic feature of nebular phase spectra of IIP SNe. A comparison of 270d spectrum are made with other SNe in Fig. 4.11 and a preliminary identification of nebular lines are shown in Fig. 4.12. The forbidden emission lines of [O I] 6300, 6364Å, [Ca II] 7291, 7324Å and [Fe II] 7155, 7172 Å; permitted emission lines of H I, Na I 5893Å doublet and Ca II 8600Å triplet become the dominant spectral features.

The presence and evolution of spectral features of SN 2012aw during early, plateau and nebular phases show striking similarity with other well-studied normal type IIP SNe 1999em (Leonard et al., 2002c), 1999gi (Leonard et al., 2002b), and 2004et (Sahu et al., 2006). However, in order to identify and interpret weak spectral features; to estimate the velocities of photospheric/ejecta layers and to understand how the layers of line-forming regions evolve with time and vary among object-to-object, we perform SYNOW modelling of the spectra in the next section.

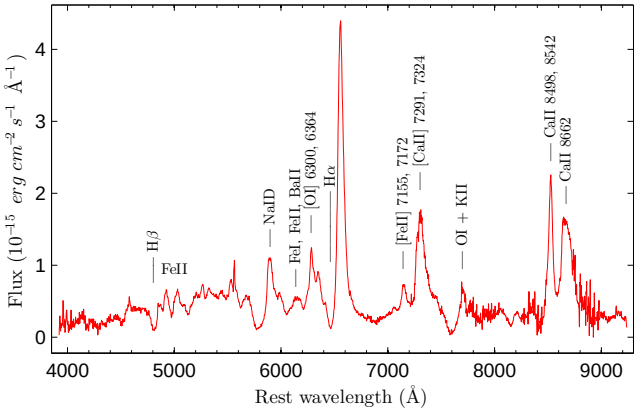

Figure 4.12: The nebular phase spectrum of SN 2012aw at 270d.

4.5.2 synow modelling of spectra

We modeled the spectra of SN 2012aw with parameterized supernova spectrum synthesis code `synow 2.3`[1] (Branch et al., 2002; Fisher et al., 1999, 1997). In contrary to the full non-local thermodynamic equilibrium (`NLTE`) model codes CMFGEN (Dessart & Hillier, 2005c) and PHOENIX (Baron et al., 2004), SYNOW assumes - simple `LTE` model atmospheres having a sharp photosphere emitting a blackbody continuum; a spherically symmetric supernova expanding homologously; the line formation is due to pure resonant scattering and radiative transfer is computed by employing Sobolev approximation. We tried three different options for optical depth profiles (viz., Gaussian, exponential and powerlaw), no significant differences were noticed, however while matching absorption minimum the exponential profile, $\tau \propto exp(-v/v_e)$, were v_e, a profile fitting parameter, e-folding velocity, was found to be most suitable and is adopted here. One important aspect of SYNOW model is detachment of an ion (line-forming layer) from photosphere which is achieved by setting the minimum velocity of the ion greater than photospheric velocity resulting into flat-topped emission and blue-shifted absorption counterpart. Strong Hα P-Cygni can be partially fitted in absorption minima with detached H I only, while the strong emission part remain unfitted with flat-topped crest.

The observed spectra are Doppler-corrected and dereddened, before visually fit-

[1]http://www.nhn.ou.edu/∼parrent/synow.html

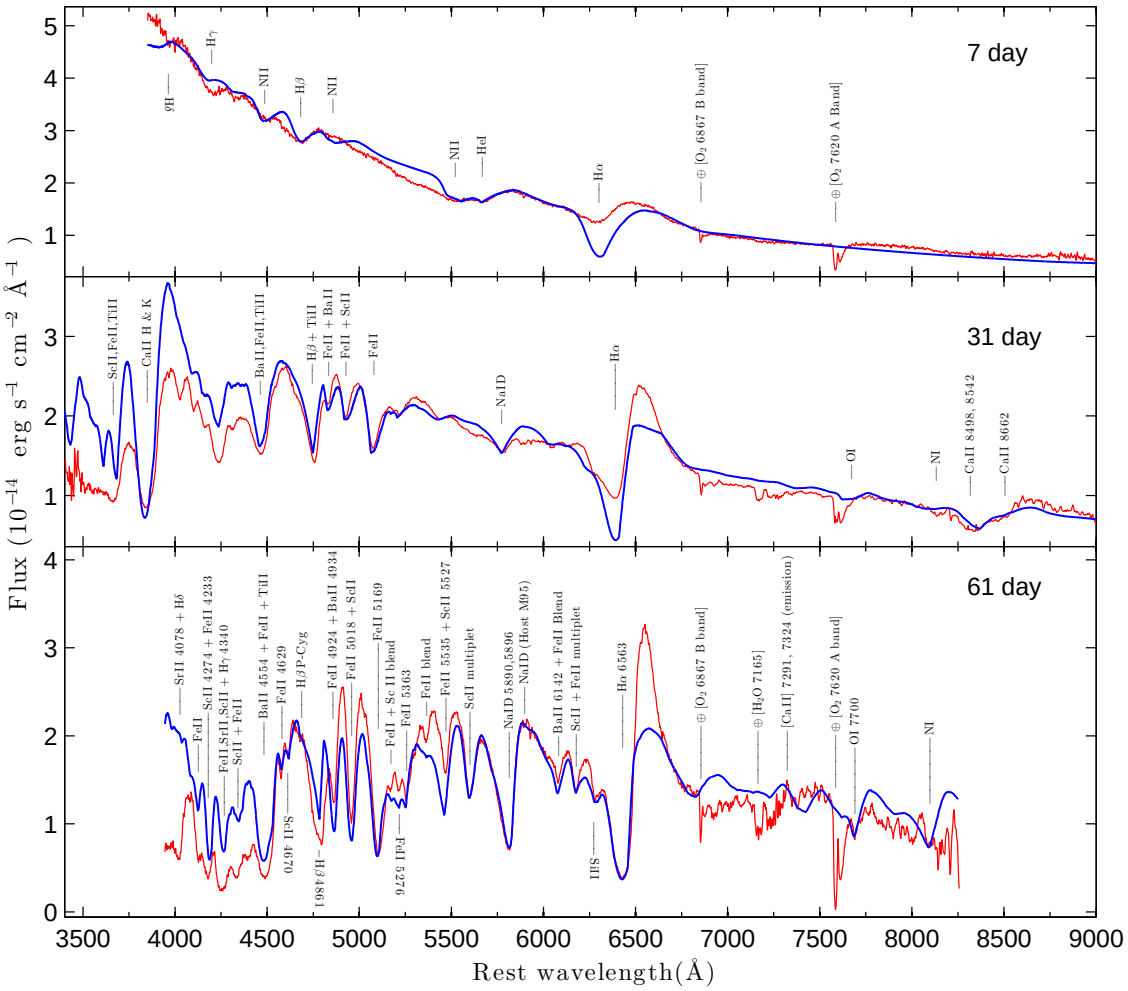

Figure 4.13: SYNOW modelling of 7d, 31d and 61d spectra of SN 2012aw. Model spectra are shown with thick solid line (blue), while the observed ones are in thin solid line (red). Observed fluxes are corrected for extinction.

ting the model SYNOW spectra with the observed ones. We have modeled the spectra for all the 14 phases and the best-fit values of T_{bb} to match the continuum are given in Table 4.6. These SYNOW-derived temperatures are consistent with the ones derived photometrically (§4.4.2). In the early-phase spectra continuum is fitted properly as it agrees well with the SYNOW's approximation of LTE atmosphere, whereas at later phases, the continuum is quite deviant, though we are able to match the spectral lines. In Fig. 4.13, we show the modeled spectra at 7d, 31d and 61d including the common set of contributing species (H I, He I etc) and additional set of species N II;

Table 4.6: The best-fit blackbody continuum temperature (T_{bb}) and the line velocities of Hα, Hβ, Fe II (4924Å, 5018Å, 5169Å) and He I 5876Å as estimated from the SYNOW modeling of the observed spectra of SN 2012aw. Velocities derived using lines of Fe II or He I are taken to represent the velocity of photosphere ($v_{\rm phm}$).

UT Date (yyyy-mm-dd)	Phase[a] (day)	T_{bb}^{b} (kK)	v(He I) 10^3 km s^{-1}	v(Fe II) 10^3 km s^{-1}	v(H$_\alpha$) 10^3 km s^{-1}	v(H$_\beta$) 10^3 km s^{-1}
2012-03-22	7	16.5	11.2	-	12.8	11.2
2012-03-23	8	15.5	10.7	-	12.8	11.0
2012-03-27	12	14.0	9.0	-	11.7	9.7
2012-03-30	15	13.5	8.65	-	10.6	9.3
2012-03-31	16	12.5	8.5	8.6	10.4	9.2
2012-04-04	20	10.5	-	7.7	10.0	8.6
2012-04-10	26	7.5	-	6.55	8.8	7.3
2012-04-15	31	7.5	-	5.6	7.9	6.6
2012-04-29	45	5.5	-	4.5	6.4	5.2
2012-05-09	55	5.2	-	4.15	5.5	4.8
2012-05-15	61	5.2	-	3.5	5.0	4.2
2012-05-09	66	5.2	-	3.5	5.0	4.2
2012-06-27	104	4.9	-	2.9	3.8	3.0
2012-12-10	270	3.9	-	1.6	3.4	1.6

[a] With reference to the time of explosion JD 24546002.59
[b] Best-fit blackbody termperature of photsphere to match the continuum in observed spectrum.

Fe II; Ti II; Sc II; Ca II; Ba II; Na I; Si II; O I and N I respectively. It can be seen that model spectra is able to match and reproduce most of the features present in the observed spectra. The optimization of v_{ph} is done to match the absorption minima of Fe II multiplet (4924, 5018, 5169Å) during plateau phase and of He I 5876Å line during early phase spectra.

The 7d spectrum shows well-matched continuum with P-Cygni profiles of Hα, Hβ, Hγ, Hδ and He I. The suspected absorption due to high-velocity component of Hβ and He I are explored further by introducing nitrogen, and the SYNOW modelling appears to be consistent with the absorption dips near 4512Å, 4834Å, 5528Å which correspond to N II lines of rest-wavelength 4623Å, 5029Å and 5679Å respectively. The N II lines of 4623 and 5679Å are also seen in 8d spectrum (Fig. 4.11) and they

disappear thereafter. Using full-NLTE modelling with PHOENIX of 7d spectrum of SN 1999em, Barbon et al. (1990) have reproduced absorption features using N II lines indicating presence of enhanced nitrogen and helium. We conclude that early-time spectral features of SN 2012aw were very much similar to normal IIP SNe 1999em as well as 1999gi. We however, note that in 5d spectrum of bright type IIP SN 2007od, the presence of absorption dips near 4500Å & 4800Å and absence of dip near 5500Å favored presence of HV components (Inserra et al., 2012a). The He I feature in SN 2012aw disappears at ∼16d and a prominent Na I D feature begin to emerge from 26d at similar location. In plateau-phase spectra, we have also incorporated ions Fe II, Sc II, Si II, Ca II and heavy ions Ti II, Ba II of which most are present as blended or weaker features in the spectra.

The lines of Si II at 6347Å and 6371Å appearing as a blend at 6355Å can be seen in the bluer wing of broad P-Cygni Hα absorption, which starts to appear at about 26d when T_{bb} drops down to about 7500 K and it can been seen until 104d (Fig. 4.10, 4.13,& 4.14). This feature is also seen in the spectra of SN 1999em at similar phases, though it has been identified as a high-velocity component of Hα (Leonard et al., 2002c). In SN 2012aw this feature is fitted well with Si II 6355Å blend in 31d and 61d spectra for the photospheric velocity at respective phases and hence we rule out the possibility of this being a high-velocity component. We note that the Si II feature is also identified in the hotter early time ($<$ 10d) spectra of SN 1999em, which we do not see in SN 2012aw.

The feature marked with C in Fig. 4.10 is analyzed further using SYNOW modelling. We find that it is most probably a high velocity component of Hβ blended with Ba II and Ti II lines. A careful inspection of model fits in Fig. 4.14, it can be seen that this feature actually starts to appear much earlier than 104d. At 55d, a very faint impression of this feature appears which does not fit with the SYNOW model feature of Hβ and continues to become increasingly stronger until our last plateau spectra at 104d. At 104d (modeled with Hβ regular and high velocity component blend) this feature became strong enough to suppress the existing regular Hβ feature and appear as a entire separate absorption component. By SYNOW modelling the 104d spectra, none of the independent atomic species and single Hβ component

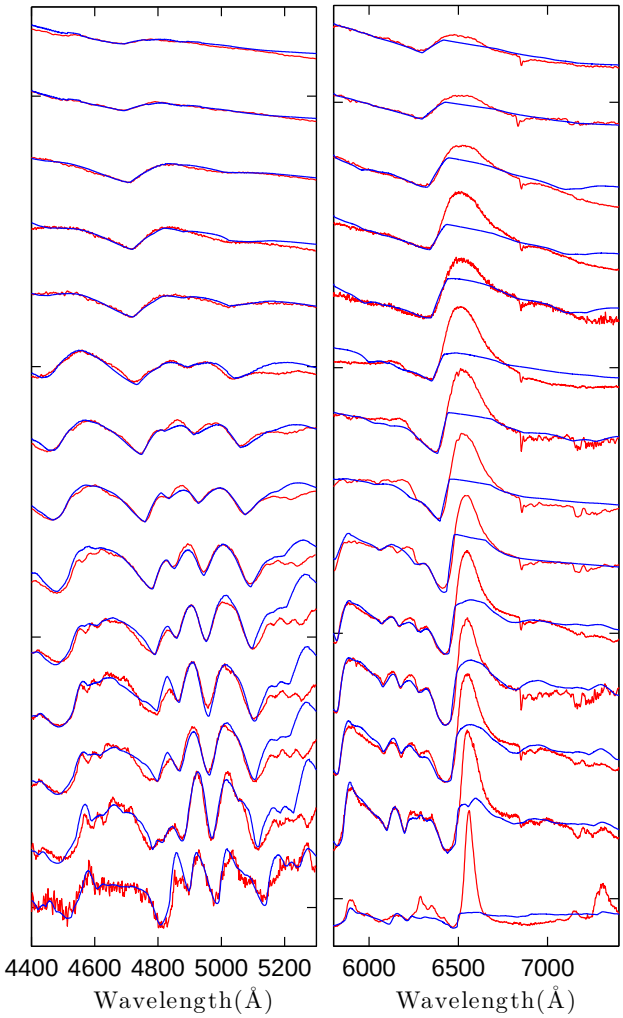

Figure 4.14: SYNOW modelling (blue) for Fe II multiplet (left) and Hα (right) profiles over the observed spectra (red) are shown. The spectral evolution is shown top to bottom at 14 phases from 7d to 270d. Detached H is used to fit the absorption dip. In addition to Fe II and H I; other ions (Sc II, Ba II, Si II and Na I, Ti II are also incorporated in model to fit some weaker features, specially at later phases. The phases of plotted spectra are 7d, 8d, 12d, 15d, 16d, 20d, 26d, 31d, 45d, 55d, 61d, 66d, 104d and 270d (top to bottom).

could be accounted for this feature. Only a high velocity Hβ component of $\sim$ 5200 km s^{-1} along with blend of Ba II and Ti II lines could match the feature, whereas the regular Hβ component remains in line with the existing velocity trend at a velocity of $\sim$ 3000 km s^{-1} only. Similar problem was also encountered with 104d Hα feature

which is not much apparent by eye inspection, but single Hα component in model spectra was unable to fit the broadened Hα absorption dip in the observed spectra. Although no separate absorption dip was seen here, but the absorption feature of Hα is somewhat broadened which only a blend of high velocity component along with regular Hα can fit. This high velocity component is found to be at ~ 5800 km s^{-1} whereas the regular Hα component is at ~ 3800 km s^{-1} which falls in line with the existing Hα velocity evolution. It is also to be noted that velocity difference of high velocity component with the regular component is ~ 2000 km s^{-1} for both Hα and Hβ, which might indicate that the origin of both high velocity component is from a single H-layer whose velocity is ~ 2000 km s^{-1} higher than the actual layer responsible for photospheric velocity. A careful examination of Hβ profiles in Fig. 4.11 at phase 60d indicate that the feature similar to C is absent in the spectra of SNe 1999em and 1999gi, however, this feature is present in spectrum of SN 2004et. The presence of HV components of Hα and Hβ have been observed through out photospheric phase until 105d in a bright ($M_V = -17.67$) type IIP SN 2009bw (Inserra et al., 2012b) suggestive of interaction between the SN ejecta and the pre-existent circumstellar material (CSM). We, therefore, suggest that the broadening of Hβ and possibly Hα during 55d to 104d indicate ejecta-CSM interaction in SN 2012aw.

The presence of absorption feature due to O I line at 7774Å is clearly reproduced by SYNOW in the 61d spectrum. The O I line begin to appear at 31d and it is clearly seen until 104d. The N I 8130Å line is marginally detected as its identification is affected by the poor SNR. The absorption feature seen ∼9000Å in 55d and 66d spectra (see Fig. 4.10) are most likely due to C I 9061Å. The appearance of absorption features in the plateau-phase spectra due to O I and occasionally also due to C I and N I have also been observed in normal type IIP SN 1999em (Leonard et al., 2002c), bright IIP SN 2009bw (Inserra et al., 2012b), subluminous IIP SNe 2009md (Fraser et al., 2011), 2005cs (Pastorello et al., 2009) and 2008in (Roy et al., 2011). Several weak absorption features viz. Fe II 4629Å, Sc II 4670Å, Fe II 5276Å and Fe II 5318Å are identified.

4.5.3 Evolution of spectral lines

The evolution of spectral features provide important clues about the interaction of expanding ejecta with the circumstellar material, formation of dust in the ejecta and geometrical distribution of ejecta. To illustrate the evolution of individual lines, a portion of spectrum is plotted in Fig. 4.15 from 7d to 207d in velocity domain corresponding to rest wavelengths of Hβ 4861Å, Na I D 5893Å, Ba II 6142Å and Hα 6563Å. Broad Hα P-Cygni (FWHM $\sim$ 17000 km s^{-1}) is prominent from as early as first epoch 7d spectra and is present all throughout which evolves into narrow feature (FWHM $\sim$ 2500 km s^{-1}at 270d) with time. Apart from blue-shifted absorption trough of the P-Cygni, which is the indicator of expansion velocity, the emission peak is also blue shifted by 4500 km s^{-1} at 7d (2700 km s^{-1}at 15d, 2100 km s^{-1} at 31d), it almost disappears by 66d (600 km s^{-1}) and settles to rest in late plateau spectrum of 104d (300 km s^{-1}). The blue shift of emission peak in early time (plateau) spectra is also seen in Hβ and such features are similar with that observed in other type II SNe namely SNe 1999em (Elmhamdi et al., 2003b), 2004et (Sahu et al., 2006) and 1987A (Hanuschik & Dachs, 1987) and it has been theoretically explained as being due to scattering of the photons from the receding part of the ejecta (Chugai, 1988; Jeffery & Branch, 1990).

A comparison of nebular phase 270d Hα line profile with other SNe (Figs. 4.11, 4.16) indicate that the Hα line flux was lower than that of SNe 1999em and much lower than 2004et. Whereas the FHWM of Hα appears to or similar (i.e. $\sim$2600 km s^{-1}) for these three SNe, suggesting that the expansion velocity of line-emitting region have been quite similar. Moreover, Hα appears to be quite symmetric around zero velocity indicating a spherically symmetric distribution of hydrogen envelope. This is in contrary to that observed for SN 2006bp, whose profile is highly asymmetric suggesting that explosion have been quite asymmetric or the dust is forming. The blue shift in Hα emission peak can also result from preferential attenuation of red wings due to formation of dust in the ejecta. The indication of dust formation is seen in SN 1999em after 500d (Elmhamdi et al., 2003b) and in SN 2004et after 320d (Maguire et al., 2010; Sahu et al., 2006). The presence of blueshift ($\sim$ 1500 km s^{-1}) in Hα emission peak have been seen from 226d to 452d spectra of IIP SN

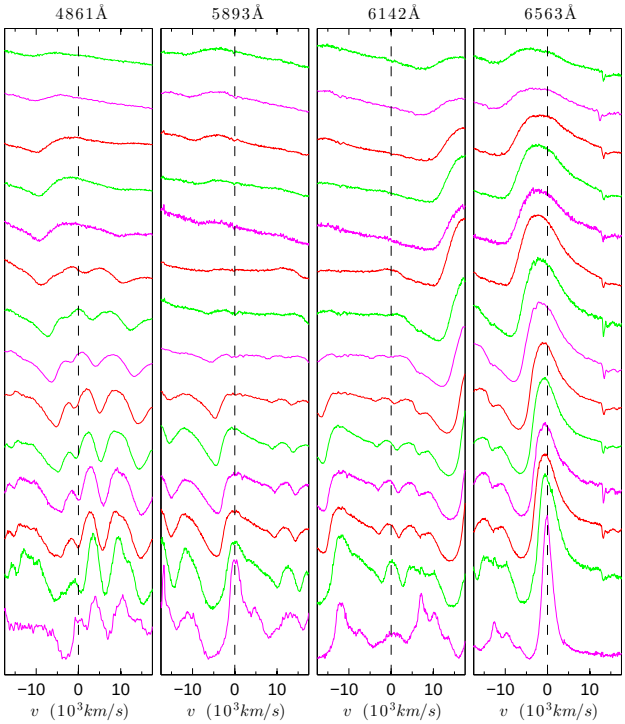

Figure 4.15: Evolution of line profiles for Hβ, Na I D, Ba II and Hα are plotted at 14 phases from 7d to 270d top to bottom. The zero-velocity line is plotted with dotted line and the corresponding rest wavelength is written on top. The phases of plotted spectra are 7d, 8d, 12d, 15d, 16d, 20d, 26d, 31d, 45d, 55d, 61d, 66d, 104d and 270d (top to bottom).

2007od (Inserra et al., 2012b) and this has been explained by presence of dust in the ejecta. We note that observational signatures related to early dust formation and the ejecta-CSM interaction for SN 2012aw are unlike that of bright ($M_V \sim -18$ mag) IIP SNe 2007od, 2009bw and 2006bp.

The He I 5876Å is prominent from early 7d spectra which disappear rapidly and can be traced only upto 16d. Several metal features start to appear from 26d. The Si II 6355Å feature is found to appear on the blue wing of Hα at $\sim -12000\,\mathrm{km\,s^{-1}}$ and evolved monotonically until last plateau phase spectra at 104d. The Na I D doublet 5890, 5896Å feature start to appear at position very close to earlier He I feature, and it persists upto nebular phase at 270d. The location of Na I D emission peak at zero velocity indicates an almost spherical distribution of the Na in the

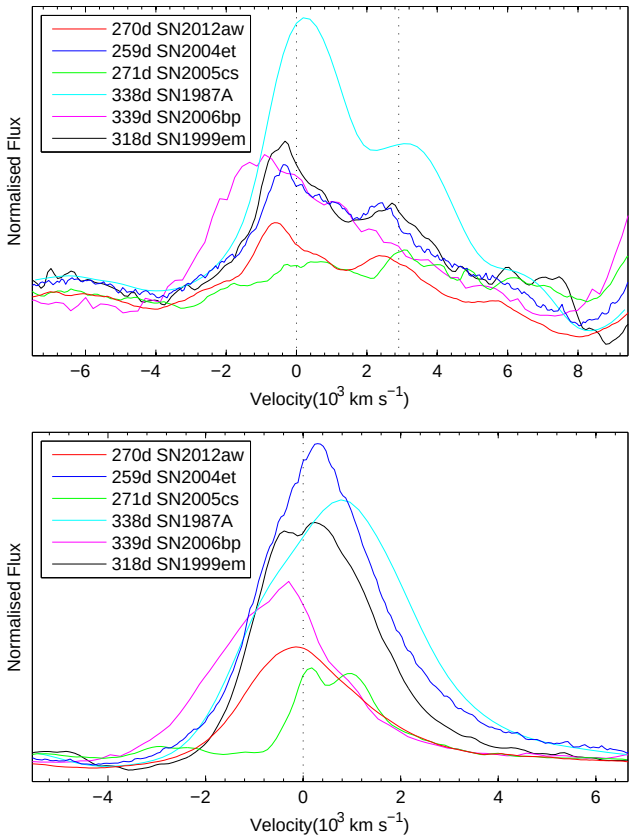

Figure 4.16: The velocity profiles of O I doublet (left) and Hα are compared with other SNe from literature. The spectra have been corrected for recession velocities of respective host galaxies. The sources for the spectra are : SN 1987A (Pun et al., 1995), SN 1999em (Leonard et al., 2002c), SN 2004et (Sahu et al., 2006), SN 2005cs (Pastorello et al., 2009), SN 2006bp(Quimby et al., 2007).

ejecta material. The absorption dips due to s-process elements Ba II 6142Å and Sc II 6248Å start to appear and strengthens until the last plateau spectra 104d. The O I lines start to appear at 104d and it is seen clearly in 270d spectrum. Similar to Hα line, the O I line flux is too smaller than that of SNe 1999em and 2004et, though the terminal velocity is of similar order (see Fig. 4.16).

4.5.4 Ejecta velocity

The expansion velocity of photosphere ($v_{\rm ph}$) coupled with the mass of ejected matter ($M_{\rm ej}$) provides strong constraints on the kinetic energy ($E_{\rm kin}$) of explosion. The photosphere represents the optically thick and mostly ionized part of the ejecta which emits most of the continuum radiation as a "diluted blackbody". This photosphere is located in a thin spherical shell where electron-scattering optical depth of photons is $\sim {}^{2}/_{3}$ (Dessart & Hillier, 2005b). In type IIP SNe, no single measurable spectral feature is directly connected with the true velocity of photosphere, however, during the plateau-phase, it is best represented by blue-shifted absorption components of P-Cygni profiles of Fe II at 4924Å, 5018Å and 5169Å, while in early-phase lines of He I 5876Å or Hβ act as a good proxy (see TV12 for a detailed review on estimating photospheric velocities of type IIP SNe). We can estimate velocities either by measuring Doppler-shift of the absorption minima using SPLOT task of `IRAF` or by modelling the observed spectra with SYNOW. The later gives better estimate of $v_{\rm ph}$ as it can take care and reproduce line blending, however, for the sake of comparing velocities of SN 2012aw with other SNe in literature, we use both the methods in this work and the corresponding velocities are denoted as $v_{\rm pha}$ and $v_{\rm phm}$ respectively. Apart from Fe II lines, the expansion velocities of line-forming layers for Hα, Hβ, He I, and Sc II are also estimated.

Using SYNOW we obtain the best fit locally, for employing the whole wavelength range may lead to over- or under-estimate of velocities due to formation of lines at different layers. Fig. 4.14 shows best fitted profiles over $\sim$ 1000Å wide wavelength regions around Hα and Fe II along with Hβ features. It can be seen that the best-fit model spectra are able to reproduce the absorption components of Hβ , Fe II 4924Å, Fe II 5018Å, and Fe II 5169Å simultaneously. At early phases from 7d to 16d, the best-fit model velocity for He I 5876Å line is also estimated. The model-derived velocities are listed in Table 4.6 and the value of $v_{\rm phm}$ represent He I line until 15d and Fe II lines at phases thereafter. The typical uncertainty in velocities estimated by deviation seen visually from best-fit absorption troughs by varying $v_{\rm phm}$ is $\sim$ 150 km s^{-1}. This is consistent with the values obtained using automated computational techniques viz. χ^2-minimization and cross-correlation methods (TV12).

The expansion line velocities of Hα, Hβ, He I, Fe II (4924Å, 5018Å and 5169Å) components, Sc II 6246Å and Sc II 4670Å blend has also been determined using IRAF by fitting the absorption trough with a Gaussian function and these are shown in Fig. 4.17. It can be seen that H I (Hα, Hβ) lines formed at larger radii (i.e. higher optical depths) than He I, while the Fe II lines are formed at lower radii. The Sc II lines are formed at even lower optical depths and the velocities derived using Sc II 4670 and 6247Å at phases 26d onwards are systematically lower by ∼1000 km s^{-1} from that of Fe II lines or of $v_{\rm phm}$. During 16d to 104d, it can be seen that velocities derived using individual lines of Fe II are same within errors and these values are further in agreement with that determined using SYNOW (i.e. simultaneous fits to Fe II lines). At early phases (< 15d), the SYNOW-determined values from He I are found to be consistently higher by ∼ 1000 km s^{-1} from that determined using absorption minima, however, at phases 7d and 8d these values are consistent with that obtained from Hβ absorption minima. The Hα velocity is higher than $v_{\rm phm}$ by ∼ 2000 km s^{-1}at early phases and by ∼ 1000 km s^{-1}at later phases. As noted by TV12, we confirm that the line velocities of Hβ are in agreement with that of $v_{\rm phm}$ above 10000 km s^{-1} , while below this it is consistently higher than that determined using Fe II lines. The value of $v_{\rm phm}$ falls from 2900 km s^{-1} at 104d to 1600 km s^{-1} at 270d.

Fig. 4.18 shows the comparison of photospheric velocity of SN 2012aw with other well-studied SNe 1999em, 1999gi, 2004et, 1987A and 2005cs. For this comparison purpose the absorption trough velocities (average of Fe II lines at late phases and He I at early phases) have been used as the SYNOW-derived velocities are not available for all the SNe considered for comparison[1]. The velocity evolution of SN 2012aw is similar to the normal type IIP SNe 2004et, 1999em and 1999gi; thought it is strikingly different than that of subluminous SN 2005cs and the type II-peculiar SN 1987A. The velocities of SN 2005cs are extremely less than SN 2012aw at all phases by ∼ 3000 km s^{-1}, whereas the profile of SN 1987A shows sharp decline in early phases (<15 days) and comparatively slower decline in later phases. The entire photospheric velocity profile of SN 2012aw is identical to 2004et at all phases

[1]Barring SN 1999em, taken from Leonard et al. (2002c), the velocities for all other comparison SNe are determined in this work using spectra available at SUSPECT http://suspect.nhn.ou.edu .

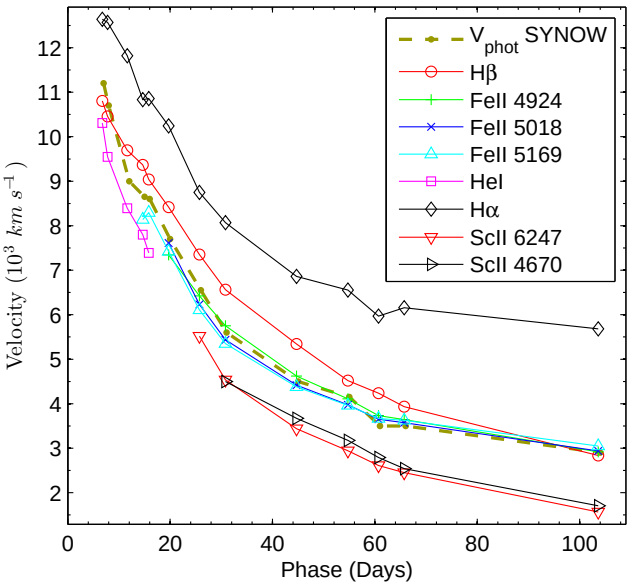

Figure 4.17: Line velocity evolution of Hα, Hβ, He I, Sc II and Fe II. The velocities are estimated using Doppler-shift of the absorption minima. The expansion velocity of photosphere ($v_{\rm phm}$) estimated from SYNOW fits of He I line until 15d and simultaneous fits for Fe II lines at later phases (see Table 4.6) are overplotted for comparison.

whereas it is consistently higher than that of SNe 1999em and 1999gi by $\sim$ 600 km s^{-1} at all phases. We note that while comparing Sc II 6247Å absorption velocities of SNe 2004et and 1999em, no difference is seen in velocity evolution (Maguire et al., 2010), however, velocities obtained using SYNOW model fits to the Fe II lines result in systematical higher velocities for SN 2004et (TV12). Similarly a comparison of expansion velocities of Hα and Hβ with other SNe indicate that these too are systematically higher than that observed for SNe 1999em and 1999gi; and are comparable with that observed for SN 2004et. For example, at phases 11d, 30d, and 50d respectively, the velocities of Hβ are 11000, 7400, and 5800 km s^{-1} for SN 2004et (TV12); 10000, 6600, and 5000 km s^{-1} for SN 2012aw (Table 4.6); 8400, 5200 and 3500 km s^{-1} for SN 1999em (TV12).

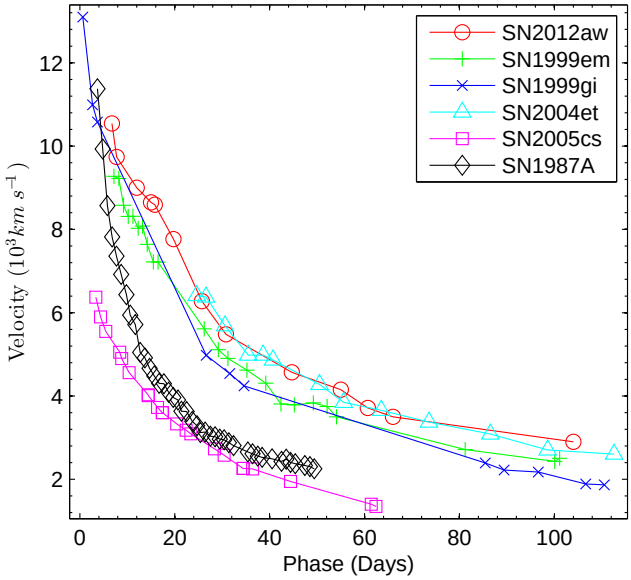

Figure 4.18: The evolution of photospheric velocity ($v_{\rm ph}$) of SN 2012aw is compared with other well-studied supernovae. The ($v_{\rm ph}$) plotted here are the absorption trough velocities (average of Fe II lines at late phases and He I at early phases.

4.6 Characteristics of explosion

4.6.1 Explosion energy

The radiation-hydrodynamics simulations provided by Dessart et al. (2010) for core-collapse SNe generated artificially by driving a piston at the base of the envelope of a rotating and non-rotating red-supergiant progenitor stars, suggest that the $v_{\rm ph}$ at 15d after shock breakout is a good and simple indicator of the explosion energy (E_0), no matter what the initial mass is. For non-rotating solar metallicity models with progenitor masses 11-30M$_\odot$, a simulated plot of $v_{\rm ph,15d}$ and the velocity at the outer edge of the oxygen-rich shell $v_{\rm ej,O}$ (see Fig.4 in their paper) for different energy of explosion ranging from 0.1 to 3 foe (1 foe =10^{51} erg), indicate that the for SN 2012aw corresponding to the value of $v_{\rm ph,15d} = 8650$ km s^{-1}(see Table 4.6), the value of E_0 lies in the range 1-2 foe. The value of $v_{\rm ph,15d}$ for SN 1999em is 7650 km s^{-1} whereas for SN 2004et it is 8800 km s^{-1} (TV12) and hence assuming similar nature of progenitor star, the strength of explosion for SN 2012aw should have been similar

to SN 2004et but higher than that of SN 1999em. We note that a detailed radiation-hydrodynamic simulations of bolometric light-curves obtain value of E_0 of 1.3 ± 0.3 foe for SN 1999em (Utrobin, 2007) and of 2.3 ± 0.3 foe for SN 2004et (Utrobin & Chugai, 2009).

Furthermore, the simulated models by Dessart et al. (2010) when combined with the width of observed nebular-phase O I 6300-6364Å line, can also be used to place an upper limit of the progenitor main-sequence mass. In nebular-phase spectra, an assessment of $v_{\rm ej,O}$ can be made by measuring half-width half-maxima (HWHM) of O I feature and for SN 2012aw it is found to be $\sim$ 1340 $\rm km\,s^{-1}$ at 270d and for comparison SNe 2004et, 1999em, 1987A, it is $\sim$1300 $\rm km\,s^{-1}$ $\sim$1200 $\rm km\,s^{-1}$ and $\sim$1400 $\rm km\,s^{-1}$ respectively (see Fig. 4.16). Hence the simulations for non-rotating models suggests an upper mass of $15 M_{\odot}$ for the progenitor star of SN 2012aw. Rotating models suggest lower-mass star. This upper mass limit for SN 2012aw is consistent with that determined by Kochanek et al. (2012) using data on pre-supernova stars and the stellar evolutionary models. We however note that the simulations of Dessart et al. (2010) assume no mixing of ejecta whereas the study of velocity distribution in line profile shapes of nebular lines by Maguire et al. (2012) indicate that mixing in ejecta is likely to have occurred in type IIP SNe. Consequently the width of [O I] lines may not represent true velocity of the oxygen-rich zones and hence the simulations-derived progenitor mass may be regarded as first hand estimates.

4.6.2 Mass of progenitor star

The mass of progenitor star can be estimated using nebular-phase emission line of O I 6300, 6364Å doublet as a detailed nucleosynthesis yields of stellar evolution/explosion models indicate that the core mass of metals in the inner ejecta is found to scale with the zero-age main-sequence mass of the progenitor (Woosley & Weaver, 1995). Additionally, we also consider that in type II SNe, the nucleosynthesis yield is largely unaffected by late-time evolution of supernova ejecta. The mass of oxygen in type II SNe can be estimated by analysis of emission from the nebular phase [O I] doublet which is mainly powered by γ-ray depositions and more than

half of the [O I] doublet luminosity during nebular phase is contributed by newly synthesized oxygen in the ejecta (Jerkstrand et al., 2012). Also, considering the fact that the SNe 2004et and 1987A have similar ejecta velocities and ^{56}Ni masses; and the mass of oxygen for SNe 2004et and 1987A is modeled quite accurately and is available for comparison. We however note that the comparison with SN 2004et is more relevant as it is spectroscopically and photometrically similar to SN 2012aw. Following Elmhamdi et al. (2003b), the luminosity of [O I] doublet can be written as:

$$L_{6300} = \eta \frac{M_{\rm O}}{M_{\rm ex}} L(^{56}{\rm Co})$$

where $M_{\rm O}$ is the mass of oxygen, $M_{\rm ex}$ is the 'excited' oxygen mass in which bulk of decay energy is deposited, η is the efficiency of transformation of decay energy deposited into [O I] doublet radiation and $L(^{56}{\rm Co})$ is the luminosity of ^{56}Co which is directly proportional to the mass of ejected ^{56}Ni.

The O I luminosity of $\sim 1.36 \times 10^{39}$ erg s^{-1} is obtained for SN 2012aw by integrating the flux within local minima (6214 – 6471Å) and subtracting the local continuum in that region. Similarly a value of $\sim 1.64 \times 10^{39}$ erg s^{-1} is estimated for SNe 2004et at 270d by interpolating the value using 259d and 301d spectra taken from Sahu et al. (2006). Assuming that in both SNe 2004et and 2012aw, η and $M_{\rm ex}$ are similar and given 0.83 times lower luminosity of [O I] doublet in SN 2012aw at 270d and equal ^{56}Ni mass (§4.4.4), we derive a rough estimate of oxygen in SN 2012aw to be a factor 0.83 lower than in SN 2004et. Considering the oxygen mass of SN 2004et as 0.8 M$_\odot$, estimated using spectral modelling of nebular phase (140d to 700d) spectra from ultraviolet to mid-infrared (Jerkstrand et al., 2012), the mass for SN 2012aw translates to be 0.66 M$_\odot$ and using nucleosynthesis yield computations in massive stars (11-40 M$_\odot$) by Woosley & Weaver (1995) corresponds to the main-sequence solar metallicity stellar mass of 14-15 M$_\odot$.

The comparison with O I luminosity of SN 1987A (a value of $\sim 2.1 \times 10^{39}$ erg s^{-1} is estimated by interpolating values obtained at 197d and 338d using spectrum taken from Pun et al. (1995)) with SN 2012aw indicate that mass of oxygen in SN 2012aw to be a factor 0.84 lower than in SN 2004et. Considering the oxygen mass

Table 4.7: Explosion parameters of well-studied type IIP SNe. The references for the adopted time of explosion (t_0), distance (D) and reddening $E(B-V)$ are given in Fig. 4.5. See §4.6.3 for further details.

Name	t_0 (2450000+)	$\Delta t_{\rm p}$ (day)	$t_{\rm p}$ (day)	$M_V^{\rm p}$ (mag)	$v_{\rm p}$ ($\rm km\,s^{-1}$)	E_0 ($\times 10^{50}$ erg)	$M_{\rm ej}$ ($\rm M_\odot$)	R_0 ($\rm R_\odot$)
SN 1999em	1475.6	92 ± 8	55 ± 4	-16.69 ± 0.01	3512 ± 122	7 ± 2	11 ± 3	399 ± 54
SN 1999gi	1522.3	97 ± 8	58 ± 4	-16.26 ± 0.02	2746 ± 217	4 ± 1	10 ± 3	421 ± 99
SN 2004et	3270.5	87 ± 8	63 ± 4	-17.01 ± 0.03	3630 ± 142	6 ± 2	9 ± 2	591 ± 90
SN 2012aw	6002.6	96 ± 11	57 ± 6	-16.67 ± 0.03	3631 ± 200	9 ± 3	14 ± 5	337 ± 67

determinations of SN 1987A in range 1.2-1.5 $\rm M_\odot$ (Chugai, 1994; Kozma & Fransson, 1998; Li & McCray, 1992), the mass range for SN 2012aw translates to be 1.0-1.26 $\rm M_\odot$ and using nucleosynthesis computations this corresponds to the main-sequence solar metallicity stellar mass of 17-19 $\rm M_\odot$ (Woosley & Weaver, 1995).

The minimum mass of oxygen can also be obtained independently using the equation (Uomoto, 1986):

$$M_{\rm O\,I} = 10^8 F_{\rm O\,I} D^2 e^{2.28/T_4}$$

where $\rm F_{O\,I}$ is the O I doublet flux in units of $\rm erg\,s^{-1}$, D is the distance to the SN in units of Mpc and $\rm T_4$ is the temperature in units of 10^4 K. From Liu & Dalgarno (1995), the O temperature of SN 1987A at 300 days was $\sim$ 4200 K. Assuming a similar O temperature for SN 2012aw at a comparable epoch, the oxygen mass for SN 2012aw was calculated for temperatures in the range 3500–4500 K as 0.18 – 0.77 $\rm M_\odot$ with the corresponding minimum main-sequence masses in the range 11-16$\rm M_\odot$.

4.6.3 Explosion parameters

Accurate estimates of explosion parameters of type IIP SNe require detailed hydrodynamical modelling of their bolometric light-curve (e.g. Bersten et al., 2011, references therein) which is beyond the scope of this work, however the analytical relations connecting the observed parameters (viz. the duration of plateau $\Delta t_{\rm p}$, the mid-plateau absolute magnitude $M_V^{\rm p}$ magnitude and mid-plateau photospheric velocity v_p) with physical parameters of the explosion (viz. the energy of the explosion E_0, the radius of progenitor star R_0 and the mass of the ejected matter $M_{\rm ej}$)

do exist (Arnett, 1980). Litvinova & Nadezhin (1983, 1985, LN85) made numerical calibration of these relations for a wide range of observables using a grid of hydrodynamical models for different values of E_0, R_0 and $M_{\rm ej}$. The applicability of such a relation have been questioned as the ejected masses derived using LN85 relations for large set of IIP SNe (14-56 $M_\odot$by Hamuy, 2003); (10-30 $M_\odot$ by Nadyozhin, 2003); are consistently higher than that obtained using direct pre-SN imaging (6-15 $M_\odot$by Smartt et al., 2009). Some of the problems lie in the lack of good quality data, simplified physical assumptions and non-inclusion of nickel heating effects (e.g. see Bersten et al., 2011), however, these relations are still useful in comparing the relative explosion properties of IIP SNe.

For the sake of estimating observed parameters for SN 2012aw and comparing with other SNe, having similar light-curve/spectra behavior, in a consistent manner, we consider nearby normal type IIP SNe 1999em, 1999gi and 2004et for which the distances, reddening and time of explosions are known quite accurately and all of these have good photometric and spectroscopic observations during plateau phase. The value of $\Delta t_{\rm p}$ to be determined using M_V light-curve (see Fig. 4.5) in a manner described by Nadyozhin (2003) is non trivial, however, a plateau duration of $\sim$ 100 days is clearly apparent for all the four SNe. As noted in §4.4.1, the V-band light-curve of sample SNe peaks between 10-16d post explosion and show a slow linear decline until $\sim$ 110d, we have therefore fitted a straight line to the linear part of the plateau to estimate the phases at which the slope changes significantly by including two consecutive points at the ends. The value of $\Delta t_{\rm p}$ determined in this way and the phase $t_{\rm p}$ corresponding to mid-point are given in Table 4.7. Furthermore, at $t_{\rm p}$, we obtain both, the value of $M_V^{\rm p}$ by linear interpolation (data from Fig. 4.5) and the value of $v_{\rm p}$ by third order polynomial interpolation of $v_{\rm pha}$ values shown in Fig. 4.18, which were determined by absorption minima to Fe II lines. The explosion parameters determined in this way is listed in Table 4.7 and it can be seen that the properties of SN 2012aw is very much similar to SNe 1999gi, 1999em and 2004et.

The value of E_0 is close to the standard energy of SNe explosion ($\sim 10^{51}$ erg) and the pre-supernova radius is consistent with that of Galactic red supergiant stars measured observationally by Levesque et al. (2005). The value of $M_{\rm ej}$ lies in the

range 9-14 $M_{\odot}$ and accounting for a total of $2M_{\odot}$ including mass of neutron star (a possible endpoint of IIP SNe) and the mass loss during red supergiant phase, this corresponds to a main sequence mass of 11-16 $M_{\odot}$. It is noted that using Sc II 4670Å line for the photospheric velocities in our computation provides lower values of ejected masses. These values are consistent with the values determined using direct imaging of pre-supernova stars (Smartt et al., 2009). Furthermore, it is seen that all these SNe have similar properties in terms of explosion energy, ejected mass and the radius of pre-supernova star and considering uncertainty in estimating $\Delta t_{\rm p}$ and $v_{\rm p}$, it is difficult to find any trend in their relative explosion parameters, and we need a larger sample of nearby IIP SNe having good-quality data and a uniform approach to verify the applicability of analytical relations. For example, we note that using the LN85 relations, Maguire et al. (2010) derived the value of $M_{\rm ej}$ for SNe 1999em, 1999gi and 2004et in the range 14-21 $M_{\odot}$ and they employed plateau duration in the range 110-120 days and the photospheric velocity derived from Sc II 6246Å line.

4.7 Conclusions

We present new $UBVRI$ photometric and low resolution spectroscopic observations of a supernova event SN 2012aw which occurred in the outskirt of a nearby (9.9 ± 0.1 Mpc) galaxy M95. The time of explosion is constrained with an accuracy of a day and the position of SN in the galaxy is consistent with being located in a solar metallicity region. The photometric observations are presented at 45 phases during 4d to 269d while the low-resolution (6-12Å) spectroscopic observations are presented at 14 phases during 7d to 270d. Employing the high-resolution spectrum of Na I D region and the early time photometric spectral energy distribution, the value of $E(B-V)$ is constrained quite accurately to be 0.07 ± 0.01 mag.

The light-curve characteristics of apparent magnitudes, colors and the bolometric luminosity is found to have striking similarity with the archetypal IIP SNe 1999em, 1999gi and 2004et; all showing plateau duration of about 100 days. For all these SNe, the light-curve in V-band rises to a peak between 10-16d post explosion and

then follows slow decline during plateau-phase. However, for SN 2012aw our early time observations clearly detect minima in the light-curve of V, R and I bands near 32 days after explosion and this we suggest to be an observational evidence seen for the first time in any type IIP SNe, for the emergence of flux due to onset of recombination phase. The value of mid-plateau M_V is -16.67 ± 0.04 for SN 2012aw lies in between the bright IIP SNe (~ -18 mag; e.g 2007od, 2009bw) and the subluminous IIP SNe (~ -15 mag; e.g. 2005cs, 1997D). Employing nebular-phase bolometric luminosity, we estimate mass of ^{56}Ni to be 0.06 ± 0.01, similar to the SNe 1999em, 2004et and 1987A.

The presence and evolution of prominent optical spectral features show striking similarity with the IIP SNe 1999em, 1999gi and 2004et. We have identified and studied the evolution of spectral features using SYNOW modelling. Similar to SNe 1999em, and 1999gi, two peculiar high-velocity components associated with the regular Hβ and He I P-Cygni features are seen in the early (7 & 8d) spectra, indicating early interaction of ejecta with the circumstellar material. However, these absorption features are consistent with being reproduced by invoking N II lines in the SYNOW modelling. During 55-104d, the absorption profiles of Hβ and Hα is broadened and it only fit by invoking high-velocity components showing signs of ejecta interaction with CSM during late plateau phase. We note that interaction scenario is consistent with the detection of SN 2012aw in X-rays (0.1-10 keV) during 4-6d (Immler & Brown, 2012) and at 21 GHz radio observations during 8-14d (Stockdale et al., 2012; Yadav et al., 2012)

The velocity of Hα and [O I] doublet line-emitting regions in the nebular phase spectrum at 270d is found to be similar to that observed for SNe 1999em and 2004et; and the line profile shapes are consistent with being originated from spherically symmetric regions, showing no signs of dust formation.

The value and evolution of photospheric velocity as derived using Fe II lines is found to be similar to SN 2004et, but about $\sim$600 km s^{-1} higher than that of SNe 1999em and 1999gi at similar epochs. This trend was more apparent in the line velocities of Hα and Hβ. The comparison of photospheric velocity at 15d with that derived using radiation-hydrodynamics simulations of IIP SNe by Dessart et al.

(2010) indicate that the energy of explosion is about $1 - 2 \times 10^{51}$ erg and this coupled with the velocity of [O I] line suggests an upper mass limit of $15M_{\odot}$ for a non-rotating solar metallicity progenitor star. We further constrain, the progenitor mass by comparing [O I] emission luminosity with the SNe 2004et and 1987A and we find that the core of oxygen mass was smaller than that of SNe 2004et and 1987A; and assuming similar physical conditions, we derive mass of progenitor star about 14-15 $M_{\odot}$.

We have also estimated explosion parameters using analytical relations of LN85 for SNe 1999gi, 1999em, 2004et and 2012aw; all having good coverage of photometric and spectroscopic data during plateau phase, in a consistent manner. We find no trend in relative parameters but ensemble parameters are found to be consistent with that expected for a normal luminosity IIP SNe, i.e., the explosion energy is consistent with 1×10^{51} erg, the pre-supernova radius is similar to what is expected from a red-supergiant star and the mass of progenitor lies between 11-16$M_{\odot}$.

SN 2012aw along with type IIP SNe 1999gi, 1999em and 2004et forms a golden sample to test results from radiation hydrodynamical simulations.

Chapter 5

SN 2013ab : A normal type IIP supernova in NGC 5669

5.1 Introduction

The cosmological importance of type IIP SNe and the ambiguity in the present understanding of their evolution and physical mechanisms are key motivations to study individual events with a range of properties. One of the best observed recent type IIP event is SN 2013ab.

SN 2013ab was discovered on February 17.5 UTC, 2013 by Blanchard et al. (2013) in the galaxy NGC 5669 ($\sim$ 25 Mpc) (see Fig. 5.1) at $R \sim 17.6$ mag. The last non-detection was reported on February 15 (Zheng et al., 2013) to a limiting magnitude $R \sim 18.5$. We therefore adopt February 16.5, 2013 (JD=2456340.0 $\pm$ 1.0 days) as the time of explosion (0d phase) throughout the chapter. Some basic parameters of SN 2013ab and its host galaxy are listed in Table 5.1.

In this work, we present results from optical photometric (*UBVRI* and *gri*) follow-up observations of SN 2013ab at 136 phases (from 3 to 190d), *Swift* UVOT observations at 25 epochs (from 4 to 103d) and low-resolution optical spectroscopic observations at 25 phases (from 2 to 184d). The chapter is organized as follows. The §5.2 provides details of the photometric and spectroscopic observations. Determination of reddening and extinction is described in §5.3. In §5.4, we study the

Table 5.1: Properties of the SN 2013ab and its host galaxy NGC 5669.

Parameters	Value	Ref.[a]
NGC 5669:		
Type	Sb	2
RA (J2000)	$\alpha = 14^{\rm h}32^{\rm m}43\overset{\rm s}{.}8$	2
DEC (J2000)	$\delta = 09°53'28\overset{''}{.}8$	2
Abs. Magnitude	$M_B = -19.28$ mag	2
Distance	$D = 24.0 \pm 0.9$ Mpc	1
Distance modulus	$\mu = 31.90 \pm 0.08$ mag	
Heliocentric Velocity	$cz_{\rm helio} = 1374 \pm 2\,{\rm km\,s^{-1}}$	2
SN 2013ab:		
RA (J2000)	$\alpha = 14^{\rm h}32^{\rm m}44\overset{\rm s}{.}49$	3
DEC (J2000)	$\delta = 09°53'12\overset{''}{.}3$	
Galactocentric Location	$7''.5$ E, $18''.1$ S	
Time of explosion	$t_0 = 16.5$ February 2013 (UT)	1
	(JD 2456340.0 ± 1.0) day	
Total reddening	$E(B-V) = 0.044 \pm 0.066$ mag	1

(1) This work; (2) HyperLEDA - http://leda.univ-lyon1.fr (Makarov et al., 2014); (3) Zheng et al. (2013)

light and colour curves, derive bolometric light curves whose tail luminosities are used to estimate the ^{56}Ni mass. In §5.5, we study the spectral evolution, present SYNOW modelling and derive line velocities. Application of EPM and estimate of distance to SN is described in §5.6. Hydrodynamical modeling to estimate physical parameters is described in §5.7. A brief summary of the work is given in §5.8.

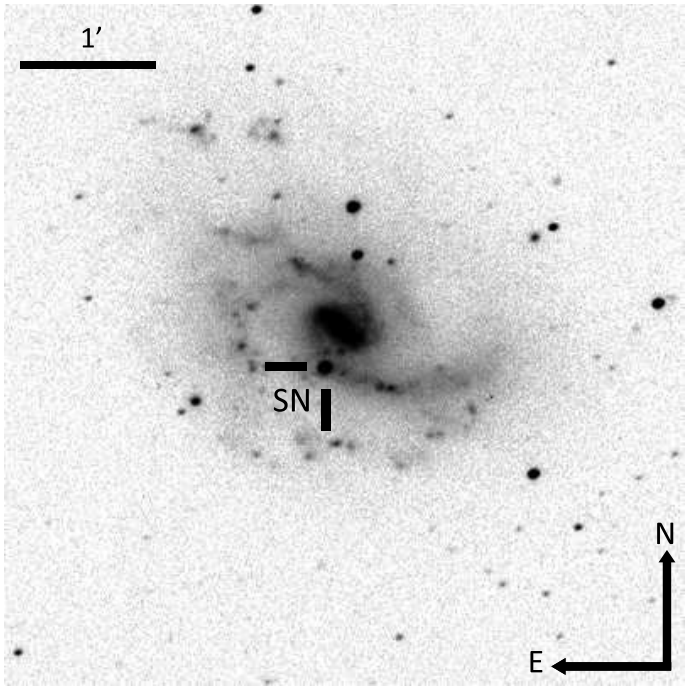

Figure 5.1: SN 2013ab in NGC 5669. The V-band image taken from 104-cm ST covering a subsection of about $5'.1 \times 5'.1$ is shown.

5.2 Observations

Broadband photometric data have been collected in Johnson BV and Sloan gri systems using the Las Cumbres Observatory Global Telescope (LCOGT) network, description of instrument and telescopes are presented in Brown et al. (2013). We have also used ARIES 104-cm Sampurnanand Telescope (ST) and the 130-cm Devasthal Fast Optical Telescope (DFOT) to acquire broadband data in Johnson-Cousin $UBVRI$ filters. The instrument details are presented in Bose et al. (2013) and Sagar et al. (2012). *Swift* UVOT has also observed SN 2013ab in ultra-violet (UV) and optical broadbands. A detailed description of data reduction and derivation of photometric magnitudes are given in Appendix 5.A.

Low resolution spectroscopic observations have been carried out at 25 phases from 2 to 184d after explosion: 12 epochs of data were collected using Floyds spectrograph on Faulkes Telescope North (FTN), 6 epochs on Faulkes Telescope South (FTS), 5 epochs using HFOSC on Himalayan Chandra Telescope (HCT) and 2

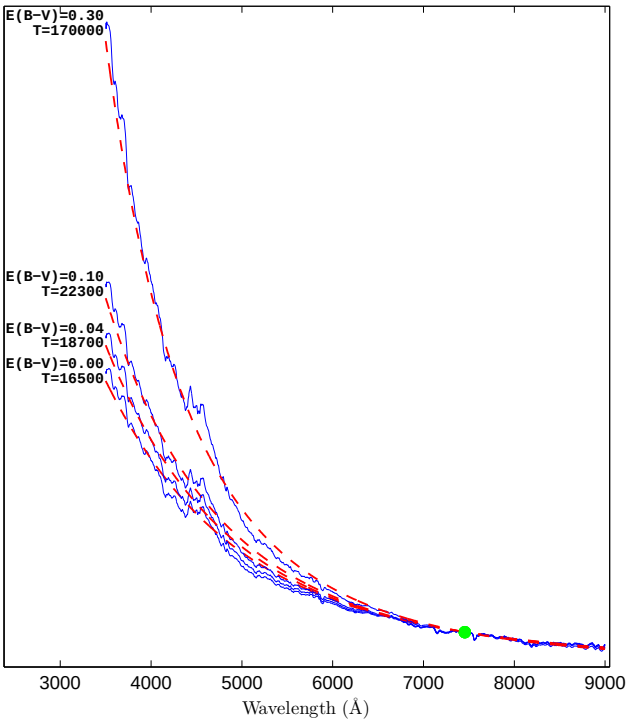

Figure 5.2: The spectral energy distribution of SN 2013ab at 2.2d is compared with a blackbody function (dotted line). The fluxes are normalized relative to an arbitrary line-free region in the spectra marked with a green filled circle. Temperature units are kelvin (K) and $E(B-V)$ in magnitude.

epochs using the B&C spectrograph mounted on Galileo Telescope in Asiago. The data reduction process is given in Appendix 5.B and the journal of spectroscopic observations in Table 5.B.1.

5.3 Extinction and Distance

In order to derive intrinsic properties of the explosion, the line-of-sight reddening of SN 2013ab due to interstellar dust in both the Milky Way and the host galaxy should be known accurately. Using all-sky dust-extinction map of Schlafly & Finkbeiner (2011)[1], we adopt the following value of Galactic reddening: $E(B-V)_{\rm MW} = 0.0234 \pm 0.0002$ mag.

[1]http://irsa.ipac.caltech.edu/applications/DUST/

One of the widely adopted techniques for reddening estimate is using the narrow Na I D interstellar absorption dips. The equivalent width (EW) of Na I D absorption feature is found to be correlated with the reddening $E(B-V)$ estimated from the tail of SN Ia colour curves (Barbon et al., 1990; Turatto et al., 2003). However in our low resolution set of spectra, we did not identify any Na I D absorption feature indicating that extinction due to the host galaxy is very low and of the order of Galactic reddening. To further constrain $E(B-V)$ due to the host galaxy, we implement "colour-method" (Olivares et al., 2010), which assumes that at the end of plateau phase the intrinsic $(V-I)$ colour is constant. Thus, it is possible to obtain the host colour excess from observed $(V-I)$ colour and relate it to the visual extinction. The relation found by Olivares et al. (2010) is :

$$A_V(V-I) = 2.518[(V-I)-0.656] \quad (5.1)$$

$$\sigma_{(A_V)} = 2.518\sqrt{\sigma^2_{(V-I)}+0.053^2+0.059^2} \quad (5.2)$$

Using the mean $(V-I)$ colour within 78-82 d (corresponds to the end of plateau phase), and correcting it for Galactic reddening, we obtain $A_{V_{host}} = 0.0624 \pm 0.2060$ mag which corresponds to $E(B-V)_{host} = 0.0201 \pm 0.0664$ mag assuming total-to-selective extinction $R_V = 3.1$. Hereafter, we adopt a total $E(B-V) = 0.044 \pm 0.066$ mag along the line of sight to SN 2013ab providing a total $A_V = 0.14 \pm 0.21$ mag.

To seek further justification of the derived $E(B-V)$ we look into the earliest spectra at 2.2 d. At early phases the spectral energy distribution (SED) can be well approximated as a blackbody. Hence we de-redden the spectra with different values of $E(B-V)$ and estimate corresponding blackbody temperatures (see Fig. 5.2). For $E(B-V) = 0.30$ mag we obtain an unphysically high temperature of 170 kK. The theoretical modelling of Bersten et al. (2011); Dessart & Hillier (2006) indicate that for a 2.2d old type IIP SN, the temperature must be around 25-30 kK. Our blackbody fit to the spectra with $E(B-V) = 0.10$ mag results in a temperature estimate of 22.3 kK. This is consistent with the values predicted by theoretical modeling. Also we estimate a temperature of 18.7 kK corresponding to our adopted $E(B-V) = 0.044$ mag. This analysis provides an approximate upper

limit of $E(B-V) = 0.10$ mag which is consistent with the adopted reddening value determined using colour-method.

A number of distance estimates to NGC 5669 using the Tully-Fisher method are available in the literature with a wide variation in values ranging from 18 to 32 Mpc. Hence to seek for a reliable estimate, we applied EPM to the SN and derived a distance of 24.26 ± 0.98 Mpc. The detailed EPM analysis will be discussed in §5.6. We adopt the distance to host galaxy to be 24.0 ± 0.9 Mpc which is the weighted mean of EPM and two other recent Tully-Fisher estimates from the literature, viz. Theureau et al. (2007) (25.23 ± 4.65 Mpc) and Tully et al. (2009) (19.67 ± 3.35 Mpc), assuming $H_0 = 73$ km s^{-1}Mpc^{-1}, $\Omega_m = 0.27$, $\Omega_\Lambda = 0.73$.

5.4 Optical light curve

5.4.1 Apparent magnitude light curves

Photometric measurements in Johnson-Cousins *UBVRI* and SDSS *gri* are available at 136 phases from 1 to 189d after the explosion, with a stringent non-detection at -1d. Additional 25 epoch observations are from *Swift* UVOT in all six UVOT filters. The resulting light curves are shown in Fig. 5.3 and data is tabulated in Table 5.A.1.

The early light curve initially shows a sharp rise in r band, which is also visible in all other optical bands as well, but only during first few phases. Then the light curve declines slowly until the end of plateau-phase. Since 95d, a steep decline to the radioactive nebular tail follows. After that, since $\sim$ 113d, the light curve settles on to this relatively slower declining phase. Observations in the UVOT bands do not show any initial rise in the light curve, although observations started with the same delay as the optical bands (+4d). The early peak is found to occur at 6.4, 7.2, 7.8, 8.3, 8.3, 7.8, 8.4 and 7.8d in *UBVRIgri* bands respectively, with uncertainties of about 1d. This is consistent with most fast-rising SNe (e.g SN 2005cs, Pastorello et al., 2009), and is significantly different from some SNe which exhibit a slow-rising early phase light curve (see e.g. the delayed V-band maximum attained at 16d in SN 2006bp (Quimby et al., 2007); 13d in SN 2009bw (Inserra et al., 2012b); and 15d

in SN 2012aw (Bose et al., 2013);).

The decline rates after the initial maximum to the plateau-end in *UBVRIgri* are 7.60, 2.72, 0.92, 0.59, 0.30, 1.68, 0.77, 0.51 mag 100 d^{-1} respectively. This is steeper than the values reported for SN 1999em (Leonard et al., 2002c), SN 1999gi (Leonard et al., 2002b) and SN 2012aw (Bose et al., 2013). For example in the *UBV*-bands, SN 2012aw experienced a decline rate of 5.60, 1.74, 0.55 mag 100 d^{-1}. However, the decline rate of SN 2013ab is similar to that of SN 2004et (2.2 mag 100 d^{-1} in *B* band; Sahu et al., 2006). During the nebular phase, the decline rate (mag 100 d^{-1}) of the light curves are estimated to be 0.36, 0.97, 0.76, 0.66 and 1.16 for *BVgri* respectively.

SN 2013ab is luminous in the UVOT *UV* bands at early phases, but it declines steeply at a rate of 0.169, 0.236 and 0.257 mag d^{-1} in *uvw1, uvw2 and uvm2* bands respectively. After 30d, the light curves settle on a slow-declining plateau until $\sim$ 103d corresponding also with the end of *Swift* UVOT observations. SN 2012aw is the only known SN which shows a UV plateau (Bayless et al., 2013) similar to that observed in SN 2013ab. Although, a UV plateau is expected, not many type II SNe have been observed so far at these wavelengths until relatively late phases. This is possibly because of their low apparent brightness due to large distance and extinction, making them unsuitable for UVOT detections. However, these limitations did not hinder SN 2013ab making this event as one of the best observed SNe IIP in the UV domain.

5.4.2 Absolute magnitude and colour evolution

The *V*-band absolute light curve of SN 2013ab is shown in Fig. 5.4, and is compared with those of other well-studied type IIP SNe. All data are corrected for their corresponding distances and extinction values. SN 2013ab is compared with the normal SNe 1999em, 1999gi, 2004dj, 2004et and 2012aw; the subluminous SN 2005cs and the photometrically peculiar SN 1987A. The comparison shows that the V-band mid-to-late plateau absolute magnitude of SN 2013ab is very similar to those of SNe 1999em and 2012aw. However the plateau light curve decay rate, especially during the early-plateau (from 10 to 50d) phase is significantly larger than those of SNe

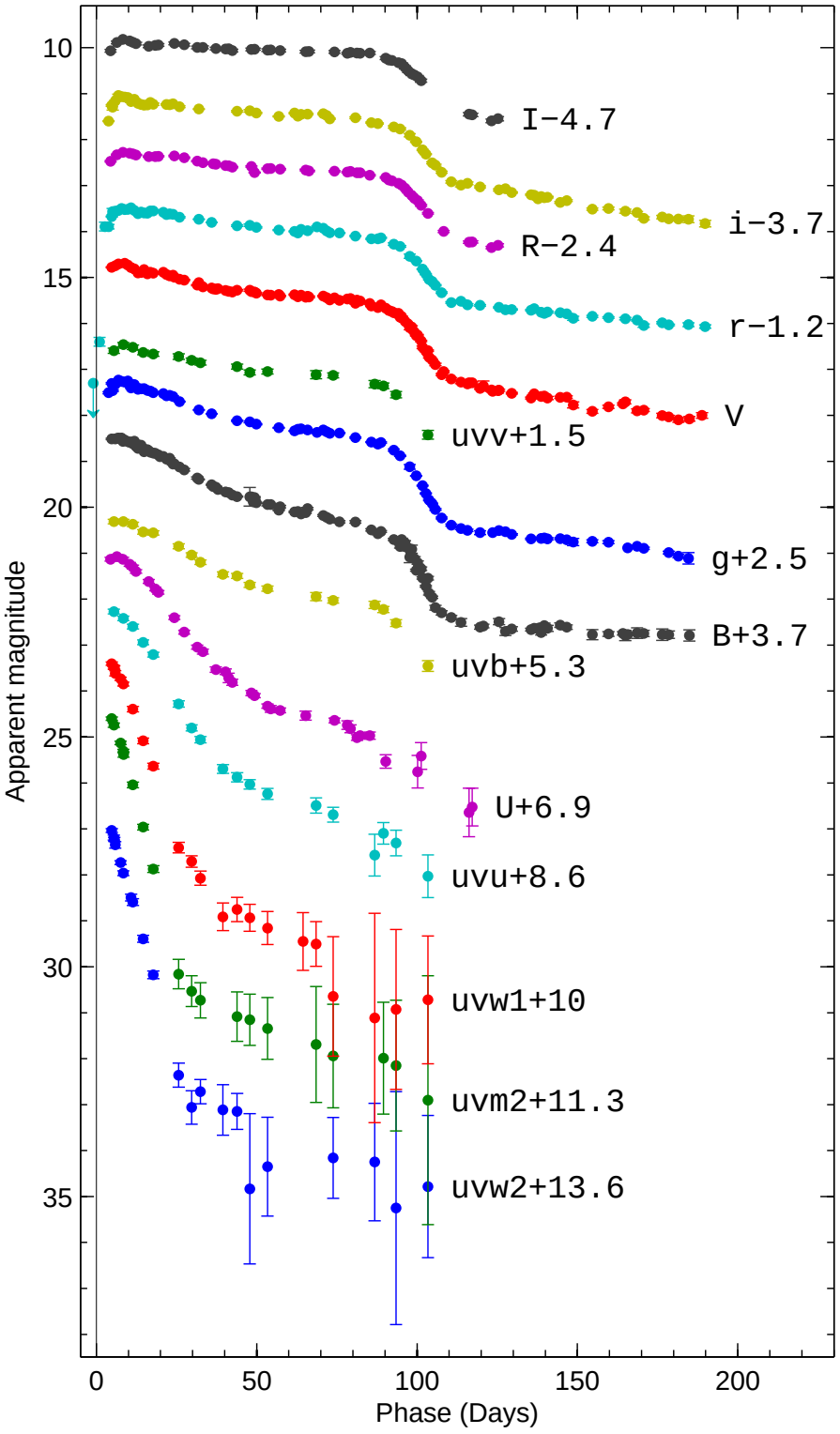

Figure 5.3: The photometric light curve of SN 2013ab in Johnson-Cousins *UBVRI*, SDSS *gri* and *Swift* UVOT bands. The light curves are shifted arbitrarily for clarity. The large errors in late UV data points are due to faint SN flux extracted after subtracting host background.

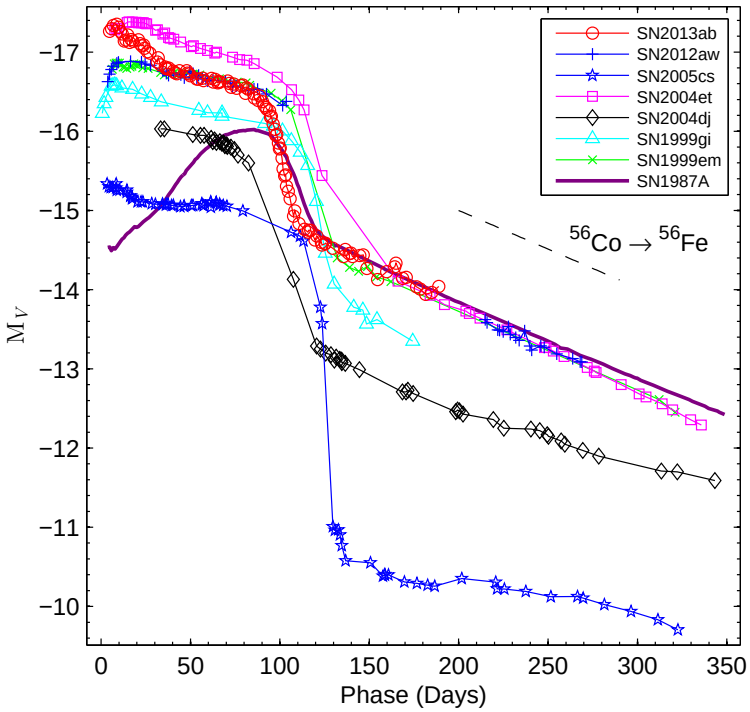

Figure 5.4: Comparison of the V-band absolute light curve of SN 2013ab with those of other type IIP SNe. The exponential decline of the radioactive decay law is indicated with a dashed line. The time of explosion in JD-2400000, distance in Mpc, reddening $E(B-V)$ in mag and the reference for apparent V-band magnitude, respectively, are : SN 1999em – 51475.6, 11.7, 0.10, Elmhamdi et al. (2003b); Leonard et al. (2002c); SN 2004et – 53270.5, 5.4, 0.41, Sahu et al. (2006); SN 2005cs – 53549.0, 7.8, 0.11, Pastorello et al. (2009); SN 2004dj – 53187.0, 3.5, 0.07, Tsvetkov et al. (2008); SN 1987A – 46849.8, 0.05, 0.16, Hamuy & Suntzeff (1990); SN 1999gi – 51522.3, 13.0, 0.21, Leonard et al. (2002b); SN 2012aw – 56002.6, 9.9, 0.07, Bose et al. (2013).

1999em and 2012aw (by 1.58 and 2.61 times respectively), although later on (during late-plateau phase) the slopes are somewhat similar. The decay rate of the early-plateau light curve is as high as 1.58 mag 100 d^{-1}, which is significantly higher than that of the late-plateau light curve (0.49 mag 100 d^{-1}). The nebular-phase light curve evolution follows a decay rate of 0.97 mag 100 d^{-1} which is similar to those of other SNe in our comparison sample. This is consistent with the expected decay rate of the ^{56}Co to ^{56}Fe (0.98 mag 100 d^{-1}). The mid-plateau absolute magnitude

is $M_V^p = -16.7$ mag, categorizing SN 2013ab as a normal type IIP event (Patat et al., 1994). This magnitude make SN 2013ab significantly brighter than sub-luminous class of events like SN 2005cs ($M_V^p \sim -15$ mag; Pastorello et al., 2009). Another noticeable difference with the compared SNe is the relatively shorter plateau duration, ∼78d in SN 2013ab, in contrast to ∼90d and 92d for SNe 1999em and 1999gi respectively. Anderson et al. (2014b) found an anti-correlation between the slope of early plateau and full-plateau duration for type II SNe, which is consistent with the faster decline but shorter plateau duration of SN 2013ab. However, it fits somewhat at the lower end of the scatter relation.

Swift UVOT absolute light curves (in *uvu, uvw1, uvm2* and *uvw2* bands) of SN 2013ab are shown in Fig. 5.5 and are compared with other well observed IIP SNe. Distance and extinction has been corrected for each of the events. For SN 2006at, extinction is not known, hence a minimal reddening has been adopted accounting only for Milky Way extinction. SN 2013ab is on the brighter end among the compared events. Most SNe were not detected in UV after about a month, this is primarily due to large distances and extinction values. Both of these factors being not a major issue in SN 2013ab, which has been in fact observed for more than 100d. SNe 2012aw and 2013by are comparable with SN 2013ab in terms of data coverage and clear detection of a plateau in the UV domain. The plateau is evident in all UV bands after 30d and follows a similar trend as that observed in SN 2012aw.

The broadband colour evolution provides important information about the temporal variation of the SN envelope properties. The expansion and cooling behavior of the envelope can be studied from the colour evolution at different phases. The intrinsic colour evolutions (*U-B*, *B-V*, *V-R* and *V-I*) are shown in Fig. 5.6. All colours show a rapid evolution towards redder colours until ∼ 50d, due to a rapid cooling of fast expanding ejecta. Thereafter, they evolve relatively slowly until the onset of the nebular-phase. The colour evolution is very similar in other archetypal SNe IIP such as SN 1999em and SN 2012aw. The $(B - V)$ colour shows a bluer trend after 120d, when the nebular-phase begins. In this phase, the ejecta become sufficiently optically thin to allow photons from radioactive decay of ^{56}Co to ^{56}Fe to escape.

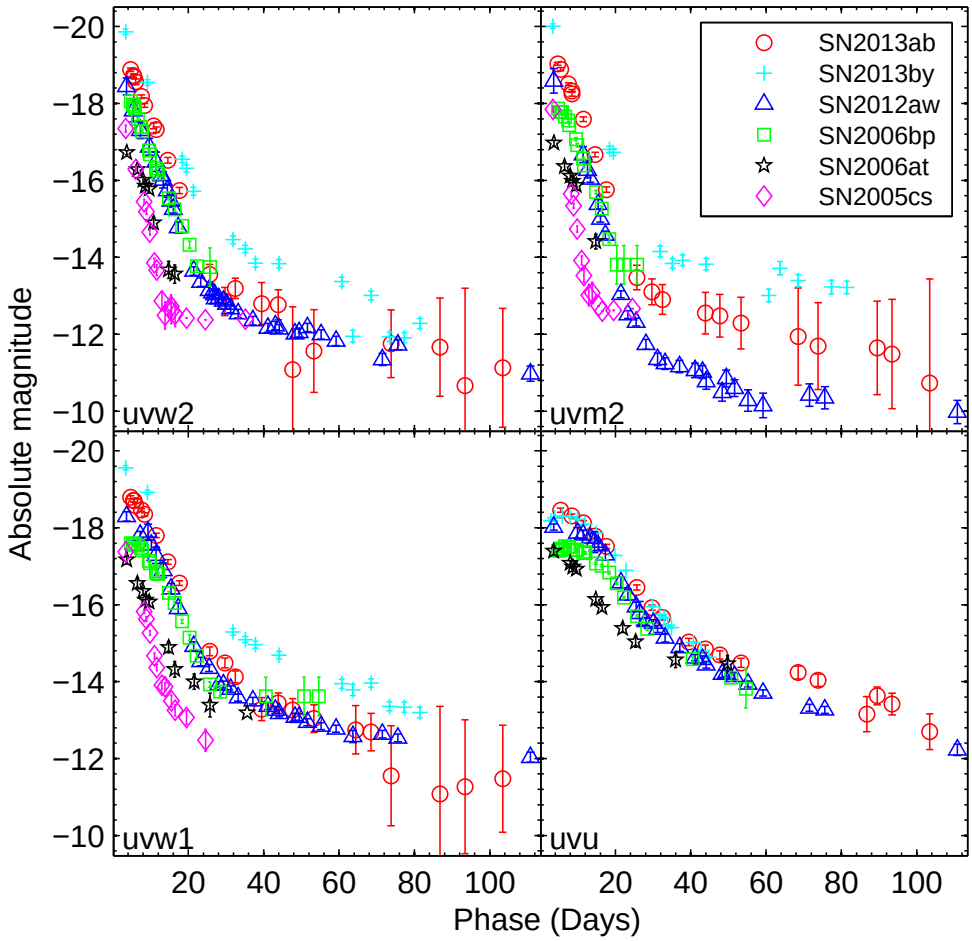

Figure 5.5: *Swift* UVOT UV absolute light curves of SN 2013ab, are compared with other well observed IIP SNe from UVOT. For the compared SNe, references for UVOT data, extinction and distance are: SN 2005cs – Brown et al. (2009); Pastorello et al. (2009), SN 2006at – Brown et al. (2009); Distance 65 Mpc; $E(B-V) = 0.031$ mag (only Galactic reddening Schlafly & Finkbeiner, 2011), SN 2006bp – Dessart et al. (2008), SN 2012aw – Bayless et al. (2013); Bose et al. (2013), SN 2013by – Valenti et al. (2015).

To have an idea of the temporal evolution of temperature and photospheric radius, we fit blackbody functions to the broadband optical fluxes (after correcting for total line-of-sight extinction). The blackbody radii are further corrected by dilution factors (using the prescription of Dessart & Hillier, 2005a) to estimate photospheric radii (where optical depth is $\tau = 2/3$) rather than thermalization

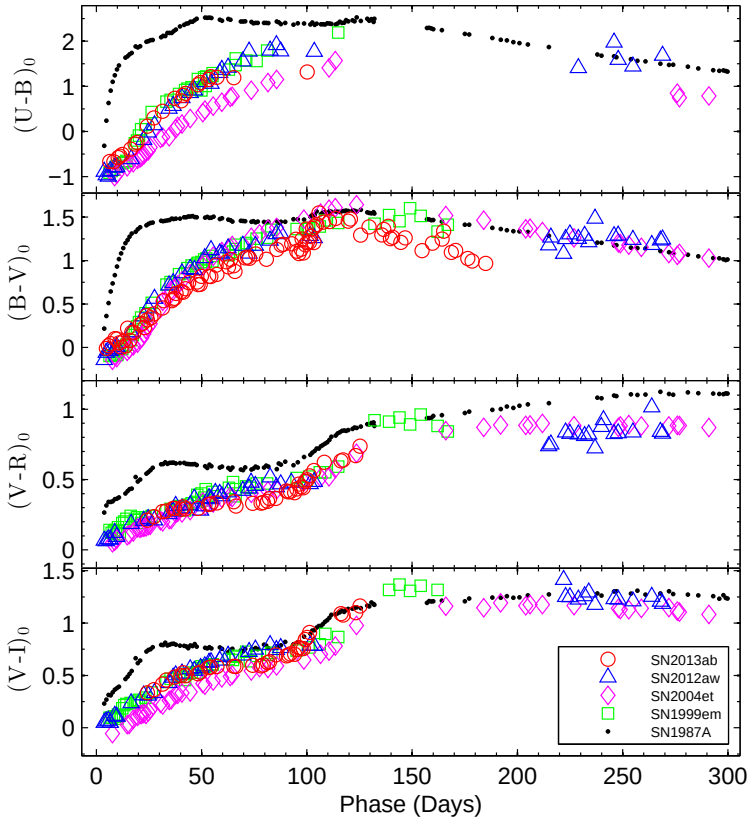

Figure 5.6: The evolution of intrinsic colours of SN 2013ab is compared with those of other well-studied type IIP SNe 1987A, 1999em, 2004et and 2012aw. Reference for data are the same as in Fig. 5.4.

radii. The plot with the photospheric temperature and radius evolutions is shown in Fig. 5.7. The temperature drops very rapidly from 5 to 25d due to adiabatic cooling of the rapidly expanding envelope. Thereafter, the decline flattens as the SN progressively enters the nebular phase. The photospheric radius increases rapidly as the SN expands and thereafter the radius remains almost constant until around 85d, which marks the end of plateau phase. This apparent contradiction to the expansion is due to the fact, that with the fall of temperature the ionized hydrogen starts to recombine by depleting the free electrons thereby optically thinning the outer ejecta. This results to a receding photospheric layer on top of the expanding envelope, ultimately leading to an unchanged photospheric radius. After 85d the radius falls off very rapidly with the end of the hydrogen recombination. During

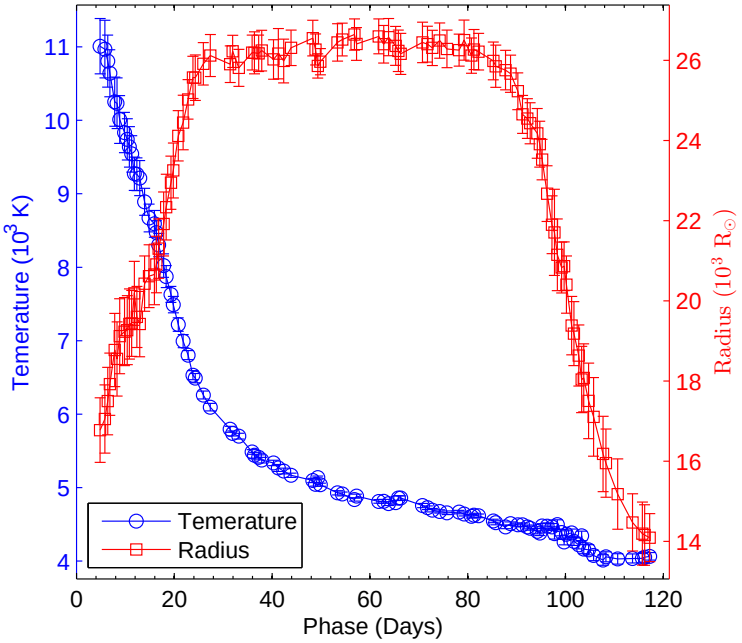

Figure 5.7: The evolutions of temperature and radius in SN 2013ab, as derived from blackbody fits to the observed fluxes in the optical range (0.36-0.81 μm).

this phase, the ejecta become cooler and almost optically thin leaving behind no free electrons. Moreover, the dilution factor corrections are no longer applicable as radiation does not have thermal origin.

5.4.3 Bolometric light curve

Pseudo-bolometric luminosities have been computed at all phases adopting the same method as described in Bose et al. (2013), i.e. by constructing a SED from the extinction corrected photometric fluxes which are semi-deconvolved from broadband filter responses. At early phases ($\leq$ 30d), when the SN is hot, the bolometric fluxes are dominated by the UV bands. At later phases ($\geq$ 100d) a major fraction of the bolometric contribution comes from infrared domain. The luminosity is computed within the optical domain (3335 – 8750Å), which includes *UBVRI* and *gri* contributions. We have also used UVOT data in the bolometric luminosity computation which covers the wavelength range from the *uvw2* to the *I* bands (1606 – 8750 Å).

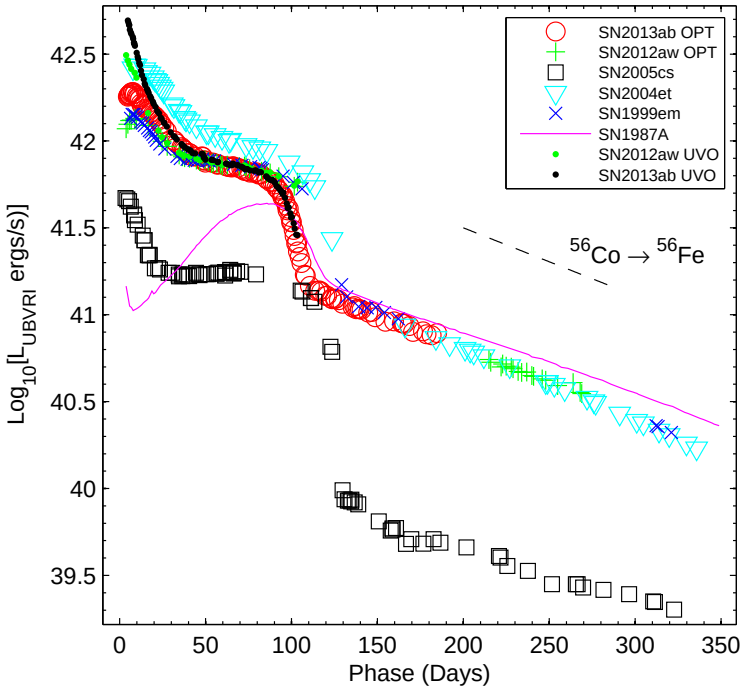

Figure 5.8: The *UBVRI* pseudo-bolometric light curve of SN 2013ab is compared with those of other well studied SNe. Light curves with added UVOT UV contributions are also shown for SN 2013ab and SN 2012aw (labeled as UVO). The adopted distances, reddening and time of explosion values are same as in Fig. 5.4. The exponential decline of the radioactive ^{56}Co decay law is shown with a dashed line.

The contribution from the UV fluxes yields a significantly higher value of the early luminosity.

In Fig. 5.8, we plot the optical pseudo-bolometric luminosities of SN 2013ab along with other well-studied objects, including SNe 1987A, 1999em, 2004et, 2005cs, 2012aw. To have homogeneity in the comparison of bolometric light curves, all luminosities have been computed using the same algorithm and wavelength range. We also include UV-Optical bolometric light curves of SNe 2013ab and 2012aw for comparison. The bolometric luminosity declines rapidly by 0.4 dex from 8 to 50d and then goes down further but slowly by 0.1 dex until 85d. It is evident from the comparison that the plateau bolometric luminosity of SN 2013ab is close to those of SNe 1999em and 2012aw but with a much steeper decline rate of the light curve

during the plateau. However, the decline rate and shape of light curve matches well with that of SN 2004et. The UV-optical bolometric light curve of SN 2013ab also shows a sharp decline by 0.8 dex during the first 50d, which is steeper than that observed for SN 2012aw. Thereafter, it declines relatively slowly and coincides with the optical light curve. The tail bolometric luminosity is similar to those of SNe 1999em, 2004et and 2012aw, and the slope of the tail is nearly identical to that expected for ^{56}Co to ^{56}Fe radioactive decay. Since this powers the tail luminosity, it is directly proportional to the amount of radioactive ^{56}Ni synthesized during the explosion.

5.4.4 Mass of nickel

The radioactive ^{56}Ni is produced in CCSNe by the explosive nucleosynthesis of Si to O (Arnett, 1980). Thus the nebular-phase light curve is mainly powered by the radioactive decay of ^{56}Ni to ^{56}Co and ^{56}Co to ^{56}Fe, with e-folding time of 8.8d and 111.26d respectively emitting γ-rays and positrons. Hence the tail luminosity will be proportional to the amount of synthesized radioactive ^{56}Ni. The mass of ^{56}Ni produced by SN 1987A has been determined with a fair degree of accuracy to be 0.075 ± 0.005 M$_\odot$ (Arnett, 1996). By comparing the bolometric luminosity of SN 2013ab with that of SN 1987A at similar phases, we can infer the amount of synthesized ^{56}Ni in SN 2013ab. Although UVOIR bolometric light curve is available for SN 1987A, we preferred to use our *UBVRI* pseudo-bolometric light curve computed using same algorithm that is used for SN 2013ab to have uniformity in the comparison. We estimated the *UBVRI* bolometric luminosity of SN 2013ab at 170d, by making a linear fit over 160 to 181d, to be $8.41 \pm 0.72 \times 10^{40}$ erg s^{-1}. Likewise, we estimated the luminosity of SN 1987A at similar phases to be $9.93 \pm 0.04 \times 10^{40}$ erg s^{-1}. The ratio of SN 2013ab to SN 1987A is found to be 0.847 ± 0.073, which gives a $M_{\rm Ni} = 0.064 \pm 0.006$ M$_\odot$for SN 2013ab.

Assuming the γ-photons emitted from the radioactive decay of ^{56}Co thermalize the ejecta, the ^{56}Ni mass can be independently estimated from the tail luminosity,

as described by Hamuy (2003).

$$M_{\rm Ni} = 7.866 \times 10^{-44} \times L_t \exp\left[\frac{(t_t - t_0)/(1+z) - 6.1}{111.26}\right] {\rm M}_\odot,$$

where t_0 is the explosion time, 6.1d is the half-life of ^{56}Ni and 111.26d is the e-folding time of the ^{56}Co decay. We compute the tail luminosity L_t at 8 epochs between 158 and 182d from the V-band data, corrected for distance, extinction and a bolometric correction factor of 0.26 ± 0.06 mag during nebular phase (Hamuy, 2003). The weighted mean value of $L_{\rm t}$ is $18.43 \pm 0.83 \times 10^{40}$ erg s^{-1}, corresponding to a mean phase of 172d. This tail luminosity corresponds to a value of $M_{\rm Ni} = 0.064 \pm 0.003$ M$_\odot$.

Elmhamdi et al. (2003a) has found a tight linear correlation between the $Log(M_{\rm Ni})$ and the plateau V-band absolute magnitude at $(t_i - 35)$ epoch, where t_i is inflection time. Which is defined as the moment when the slope of the light curve in the transition phase is maximum. For SN 2013ab light curve, we constrained $t_i = 102.99 \pm 0.02$ d. Following the above mentioned correlation we obtain $M_{\rm Ni} = 0.066 \pm 0.002$ M$_\odot$.

We adopt the mass of synthesized ^{56}Ni in SN 2013ab to be 0.064 ± 0.006 M$_\odot$, which is derived from the first method, and is found to be consistent with that obtained from the subsequent two methods described here. We anticipate that the estimated ^{56}Ni mass for SN 2013ab is almost equal to that obtained for SNe 2012aw, 2004et and 1999em. Whereas for sub-luminous SN 2005cs, ^{56}Ni mass is much less than SN 2013ab.

5.5 Optical spectra

5.5.1 Key spectral features

The spectroscopic evolution of SN 2013ab is presented in Fig. 5.9. Preliminary identification of spectral features has been done as in previous studies of IIP SNe (e.g. Bose et al., 2013; Leonard et al., 2002c). Early spectra, viz. 2.2d and 3.2d, shows featureless blue continuum with a broad and shallow P-Cygni dip detected near 4380 Å which is supposedly He II λ4686, which is blue shifted by about 19500 km s^{-1}.

Detection of such He II features has been reported in several early SN spectra (Fassia et al., 2001; Inserra et al., 2013; Pastorello et al., 2015; Quimby et al., 2007; Shivvers et al., 2014). The 8.2d spectrum also primarily shows blue continuum, although with developing Hβ, He I and Hα lines. The He I feature completely disappears after 18d and at similar position Na I D profile starts to emerge since the 43d spectrum.

The spectra from 12 to 18d mark the transition phase from a hot to cool SN envelope, when photosphere begins to penetrate the deeper Fe-rich ejecta. These spectra mark the emergence of other lines from heavier atomic species, such as calcium, iron, scandium, barium, titanium and neutral sodium. Among these lines, Fe II λ5169 appear during the early plateau phase (12d), whereas weaker lines start to emerge at the beginning of late plateau phase (18d). Na I D doublet $\lambda\lambda$ 5890, 5896 and Ca II triplets $\lambda\lambda$ 8498, 8542, 8662 are feebly traceable from 31d, and becomes prominent since the 43d spectrum. All weak and blended lines are seen to evolve and appear prominently by the end of plateau phase (82.1d). The following spectrum (88.3d) marks the onset of plateau to nebular transition. All subsequent spectra up to 118.1d are representative of the early nebular phase, when the outer ejecta has become optically thin. Fig. 5.10 compares SN 2013ab spectra with sample of archetypal IIP events at four different epochs, viz. early and hot plateau phase at 8d; cooler plateau phase at 31 and 74d; and nebular phase at 174d. SN 2013ab spectra show features identical to those of our comparison sample of normal events. The nebular spectrum at 183d is shown in Fig. 5.11 with preliminary identification of nebular lines typical of SNe IIP. This spectrum is mostly dominated by emission features of [O I] $\lambda\lambda$ 6300, 6364, [Ca II] $\lambda\lambda$ 7291, 7324, and [Fe II] $\lambda\lambda$ 7155, 7172. In addition, permitted emission lines of H I, Na I $\lambda\lambda$ 5890, 5896 doublet and the Ca II NIR triplet are still detected.

5.5.2 SYNOW modelling of spectra

Spectra of SN 2013ab have been modeled with `SYNOW 2.3`[1] (Branch et al., 2002; Fisher et al., 1999, 1997) for preliminary line identification and velocity estimates. SYNOW is a parametrized spectrum synthesis code which employs Sobolev approx-

[1] http://www.nhn.ou.edu/∼parrent/synow.html

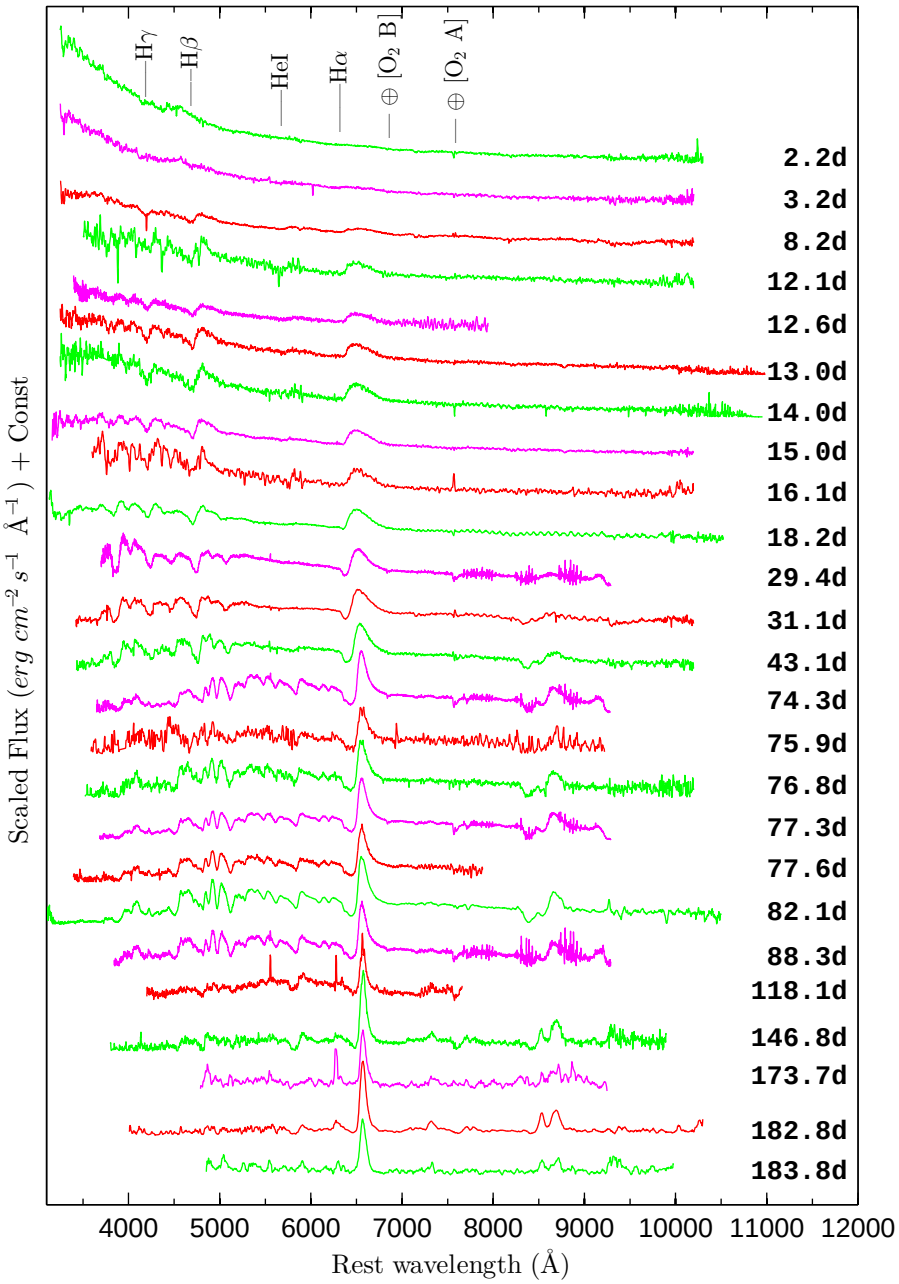

Figure 5.9: The Doppler-corrected spectra of SN 2013ab are shown at 14 phases from 7d to 270d. Prominent P-Cygni profiles of hydrogen (Hα, Hβ, Hγ) and helium (He I λ5876) lines are marked. The telluric absorption features are indicated with the $\oplus$ symbol. The portions of spectra at the extreme blue and red ends have poor signal-to-noise ratios.

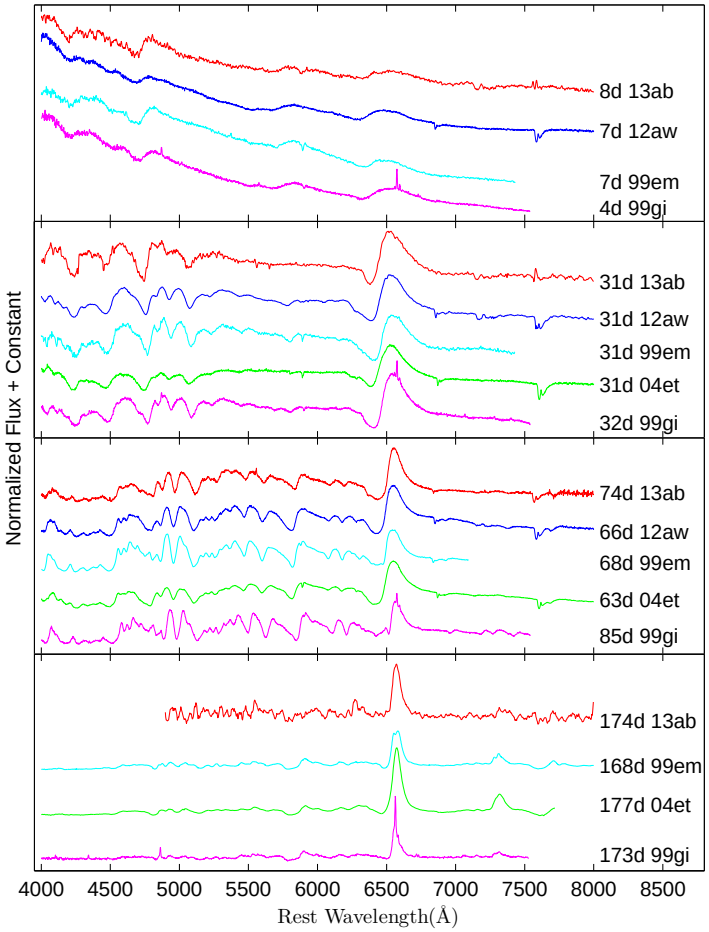

Figure 5.10: Comparison of early (8d), plateau (31d, 74d) and nebular (174d) phase spectra of SN 2013ab with those of other well-studied type IIP SNe 2012aw (Bose et al., 2013), 1999em (Leonard et al., 2002c), 1999gi (Leonard et al., 2002b), 2004et (Maguire et al., 2010; Sahu et al., 2006). Observed fluxes of all the SNe are corrected for extinction and redshift (adopted values same as in Fig. 5.4).

imation to simplify radiation transfer equations, assuming spherically symmetric supernova ejecta which expand homologously. Despite of the simplified LTE atmosphere assumption in SYNOW, it is capable to produce P-Cygni profiles like those produced in the expanding photosphere of a SN. SYNOW has been implemented on several recent SNe studies (e.g. Bose & Kumar, 2014a; Bose et al., 2013; Inserra et al., 2012a; Marion et al., 2014; Milisavljevic et al., 2013; Takáts et al., 2014) for line identification and estimation of line velocities. We tried three different options

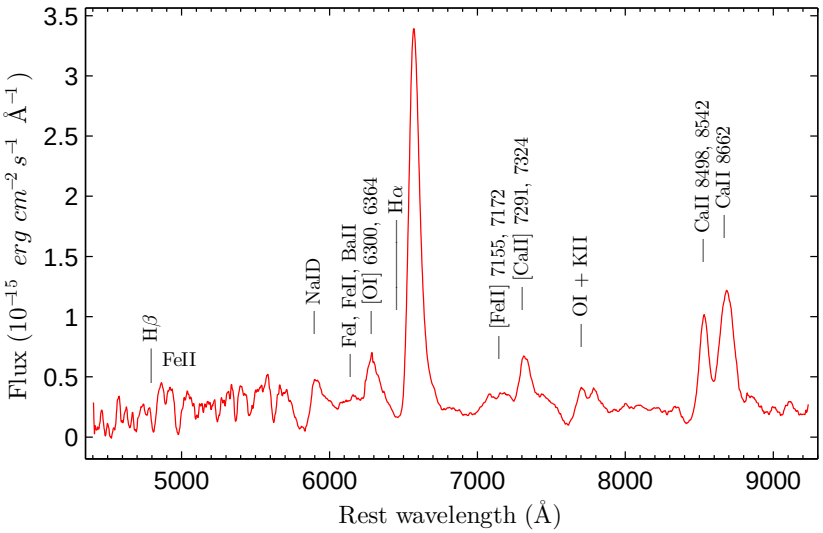

Figure 5.11: Line identification in the nebular phase spectrum of SN 2013ab (183d).

for optical depth profiles (viz. Gaussian, exponential and power law), no significant differences were noticed. However, while matching absorption minimum, the exponential profile, $\tau \propto exp(-v/v_e)$, where v_e, a profile fitting parameter, e-folding velocity, was found to be the most suitable and is adopted here for each individual atomic species. One important aspect of SYNOW modeling is the concept of detachment of an ion. When the minimum velocity of a line-forming layer is higher than that of the photospheric layer, the ion is said to be detached, which results into flat topped emission and blueshifted absorption counterpart of the line profile in synthetic spectra produced by SYNOW. This becomes important for H I lines as they are essentially formed at much higher velocities than photospheric velocities. Therefore, only the detached scenario for H I reliably fits the blue-shifted absorption trough in the observed spectra.

The observed spectra are dereddened and doppler-corrected before modelling with SYNOW. T_{bb} is supplied as a model input parameter which is actually the blackbody temperature to produce the underlying LTE continuum of synthetic spectra. For this reason, the observed spectral continuum is well matched at early phases, whereas at later phases this is a poor match with the model as SN emission significantly deviates from LTE assumption. Fig. 5.12 shows the observed spectrum at

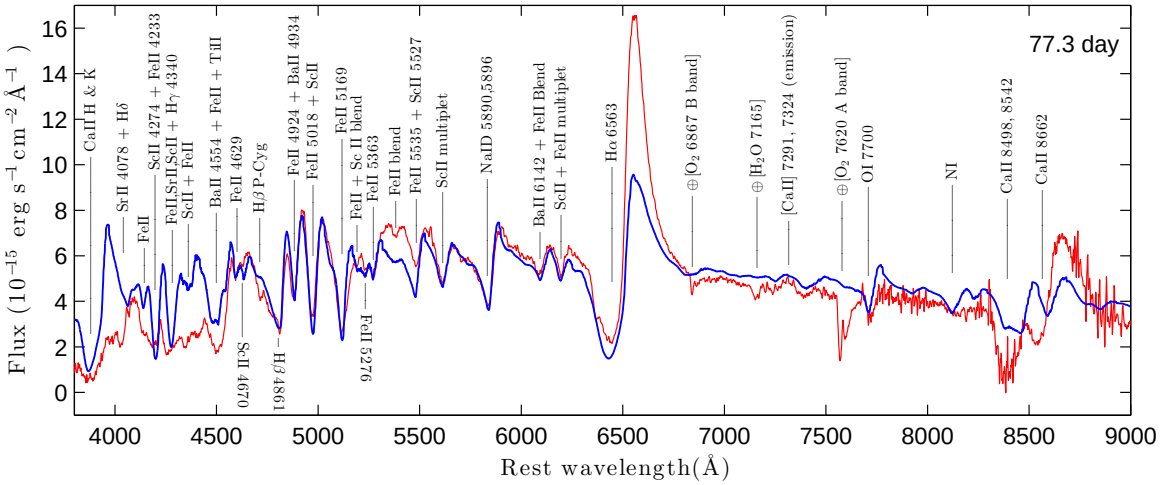

Figure 5.12: SYNOW modelling of the 77.3d spectrum of SN 2013ab. A SYNOW model spectrum is shown with thick solid line (blue), while the observed one is the thin solid line (red). Fluxes are corrected for interstellar extinction.

77.3d with our best-fit model. A set of atomic species (H I, He I; Fe II; Ti II; Sc II; Ca II; Ba II; Na I; Si II; O I; N I) has been incorporated to generate the synthetic spectrum. The model spectrum can very well reproduce most of the blended line profiles; v_{ph} is optimized to match the Fe II multiplet ($\lambda\lambda$ 4924, 5018, 5169), whilst the H I velocities are always dealt as a detached scenario.

Line velocities for Hβ, He I and Fe II are estimated from all spectra. The model fit is optimized for velocity locally around the respective lines of interest. Fitting is done locally to avoid any bias in velocity estimation, which may be imposed while accounting for entire spectrum due to other lines at different velocities. In Table 5.2, SYNOW estimated velocities for a few representative lines in the plotted spectral sequence are shown. Although Fe II line impression is detectable since 12d, we model those lines only from 29d onwards, as in earlier spectra Fe II triplet is either not full developed or only detectable Fe II λ5169 is too weak to model. SYNOW modelling is done until 77d, because after 78d spectra are limited because of low signal-to-noise ratio (SNR). In such low SNR spectra SYNOW may not provide any better estimation of line velocities than absorption-minima position measurements.

Table 5.2: The best-fit blackbody continuum temperature (T_{bb}) and line velocities of Hβ, Fe II ($\lambda\lambda$ 4924, 5018, 5169) and He I λ5876 as estimated from SYNOW modeling of the observed spectra of SN 2013ab. Velocities derived using lines of Fe II or He I are taken as representative of the velocity of photosphere ($v_{\rm ph}$).

UT Date (yyyy-mm-dd)	Phase[a] (day)	T_{bb}^{b} (kK)	v(He I) 10^3 km s^{-1}	v(Fe II) 10^3 km s^{-1}	v(H$_\beta$) 10^3 km s^{-1}
2013-02-24.71	8.21	11.8	10.2±0.3	-	10.4±0.6
2013-02-28.59	12.09	9.6	10.1±0.7	-	10.4±0.6
2013-03-01.08	12.58	1.1	9.4 ±0.4	-	10.3±0.3
2013-03-01.50	13.00	9.9	9.0 ±0.5	-	10.3±0.2
2013-03-02.51	14.01	1.0	8.7 ±0.9	-	10.2±0.5
2013-03-03.51	15.01	9.2	9.0 ±0.6	-	9.5±0.2
2013-03-04.59	16.09	8.4	8.2 ±0.8	-	9.3±0.8
2013-03-06.71	18.21	8.5	8.3 ±0.6	-	9.8±0.4
2013-03-17.93	29.43	6.8	-	6.1±0.3	7.0±0.3
2013-03-19.63	31.13	5.9	-	6.5±0.4	7.5±0.2
2013-03-31.58	43.08	5.6	-	4.9±0.4	6.0±0.3
2013-05-01.84	74.34	5.0	-	3.1±0.3	3.1±0.4
2013-05-03.35	75.85	5.2	-	-	-
2013-05-04.33	76.83	5.1	-	3.4±0.4	3.8±0.3
2013-05-04.85	77.35	5.2	-	2.9±0.3	3.0±0.3

[a] With reference to the time of explosion JD 2456340.0
[b] Best-fit blackbody temperature at the photosphere to match the continuum in the observed spectrum.

5.5.3 Evolution of spectral lines

The evolution of spectral features provides important clues about the interaction of expanding ejecta with the circumstellar material, formation of dust in the ejecta and geometrical distribution of the ejecta. To illustrate the evolution of individual lines, in Fig. 5.13 selected regions of spectra are plotted in the velocity domain corresponding to the rest wavelengths of Hβ, Na I D and Hα. There is no clear evidence of spectral lines in the early spectra (2.2 and 3.2d), except for a shallow and broad He II (λ4686) feature near 4380Å. The blue-shifted absorption troughs of the P-Cygni profiles give direct estimate of expansion velocity of the ejecta. The emission peaks are also seen to be blue-shifted. The amount of blue-shift decreases

with the decline of the expansion velocity and settles to the rest velocity while the SN enters the nebular phase. This is a generic feature seen in SN spectra, mostly at early phases; see, e.g., SNe 1987A (Hanuschik & Dachs, 1987), 1998A (Pastorello et al., 2005), 1999em (Elmhamdi et al., 2003b), 2004et (Sahu et al., 2006) and 2012aw (Bose et al., 2013). Blue-shifted emission peaks are explained by the diffused reflection of photons from expanding SN envelope (Chugai, 1988) which is in contrast to the pure-absorption model of expanding atmosphere ensuing unshifted emission peaks. However, recent study by Anderson et al. (2014a) suggests that these features are tied with the density structure of ejecta which in turn controls the amount of occultation of the receding part of ejecta, resulting in biasing of the emission peak. Such features are well reproduced by non-LTE models like CMFGEN (Dessart & Hillier, 2005c). The evolution of blue-shifted peaks are clearly seen in Hα, whilst other lines emission peaks are heavily contaminated by P-Cygni the absorptions from other adjacent lines. The emission peak blue-shift for Hα is found to be as high as $\sim -5000\,\mathrm{km\,s^{-1}}$at 8.2d and then progressively decreases (4400 $\mathrm{km\,s^{-1}}$ at 12d and 2300 $\mathrm{km\,s^{-1}}$at 29.4d) down to almost zero velocity at 88.3d, corresponding to the end of plateau phase.

Similar to Hα, Hβ are seen to evolve all throughout the spectral evolution (see Fig. 5.13). However, 18d onwards, the red side of Hβ emission profiles are found to be significantly dominated by emerging Fe II lines. All three Fe II lines ($\lambda\lambda$ 4924, 5018, 5169) are seen to have fully appeared in 31d spectrum, which continues to evolve till the last observation. Traces of He I line are seen in early spectra, which disappears after 18d. At similar position Na I D profile start to appear at 43d and it continues to evolve until last spectrum.

5.5.4 Ejecta velocity

The element distribution of the progenitor at the end of the sequence of nuclear burnings and before the SN explosion is stratified, with hydrogen being abundant in outermost layers and heavier elements (e.g. α-elements) towards the center and core being rich in iron. Thus it is expected that the expanding ejecta are constituted by layers of multiple elements and the so called "onion-like" structure. Therefore, dif-

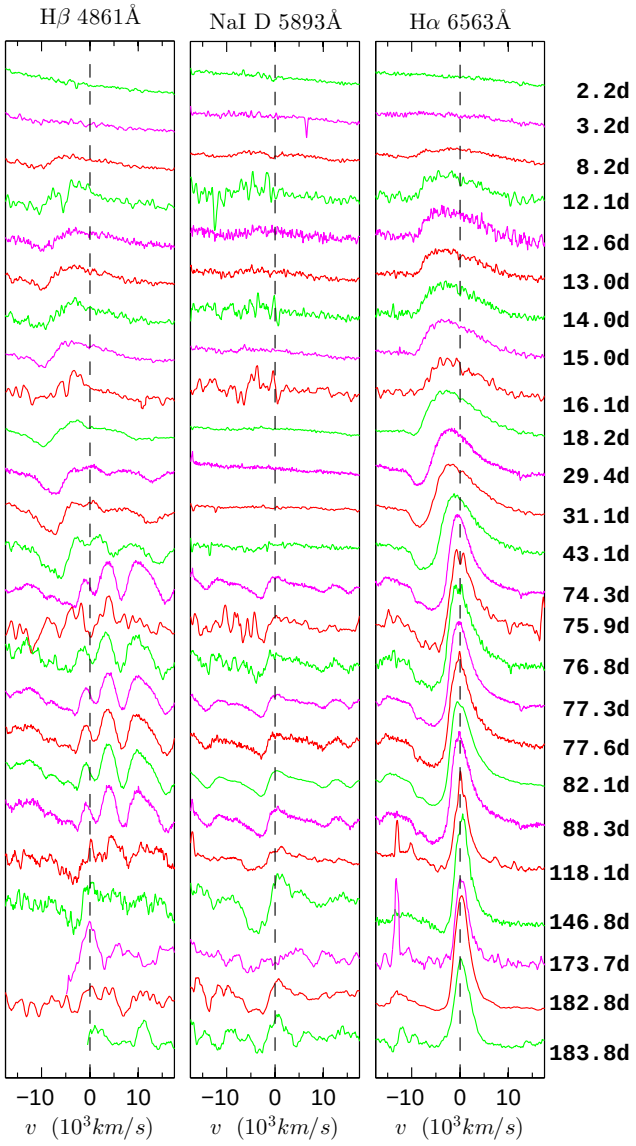

Figure 5.13: Evolution of the line profiles of Hβ, Na I D and Hα plotted at 25 epochs from 2d to 184d. The zero-velocity position is shown with a dotted line and the corresponding rest wavelength is indicated at the top.

ferent lines originate from different depths in the SN atmosphere. The photosphere is a region of special interest to study the kinematics and other related properties. The photosphere represents the layer of SN atmosphere where optical depth attains a value of $\sim {}^{2}/_{3}$ (Dessart & Hillier, 2005b). No single spectral line can represent the

true photospheric layer and its velocity. During the plateau phase, Fe II ($\lambda\lambda$ 4924, 5018 and 5169) or Sc II lines are thought to be the best estimators for the photospheric velocity ($v_{\rm ph}$), and at early phases when Fe II lines are not strongly detected, the best proxy for $v_{\rm ph}$ is He I or even Hβ (Takáts & Vinkó, 2012), at earlier phases.

Velocities can be estimated either by simply locating the blue-shifted absorption trough of the P-Cygni profiles or modeling the observed spectra where velocity is one of the input parameter. We have used both methods to estimate the velocities. SN spectral lines are often found to be blended with other lines in the neighborhood, as in case of Fe II multiplets, blended with Ti II and Ba II. This introduces some error, when lines velocities are estimated by locating the absorption minima, by simply fitting gaussian function on these blended profiles, which is further exacerbated in low-resolution and low-SNR spectra. SYNOW being capable to reproduce P-Cygni profile for multiple lines of different ions simultaneously, it can easily reproduce line blending as observed in SN spectra. Thus we get a better handle while fitting the entire blended profile with SYNOW and so the velocity estimates are better and less prone to errors. More detailed discussion on applicability and merits of SYNOW velocity estimates over absorption minima method can be found in Takáts & Vinkó (2012) and Bose & Kumar (2014a).

In order to estimate photospheric velocities from the model, SYNOW-generated synthetic spectra are locally fitted over Fe II lines in the observed spectra. This was done to avoid any over- or under- estimation of velocities as each line of any atomic species originating from different layers. The attributed uncertainties are visually estimated by noting the deviation of model absorption trough from observed one. The model velocities listed in Table 5.2 are estimated only until 77.3d, since thereafter the spectra are limited by SNR and hence there is no advantage in using SYNOW-estimated velocities over the absorption minima method. The Fe II velocities are estimated by assuming that the Fe II λ4924, Fe II λ5018, and Fe II λ5169 lines have velocities coincident with $v_{\rm ph}$, whereas the Balmer H I lines are treated as detached (with $v > v_{\rm ph}$) (Bose et al., 2013; Branch et al., 2002). He I line velocities have also been estimated as long as this ion can be traced in spectra (from 8.2 to 18.2 d).

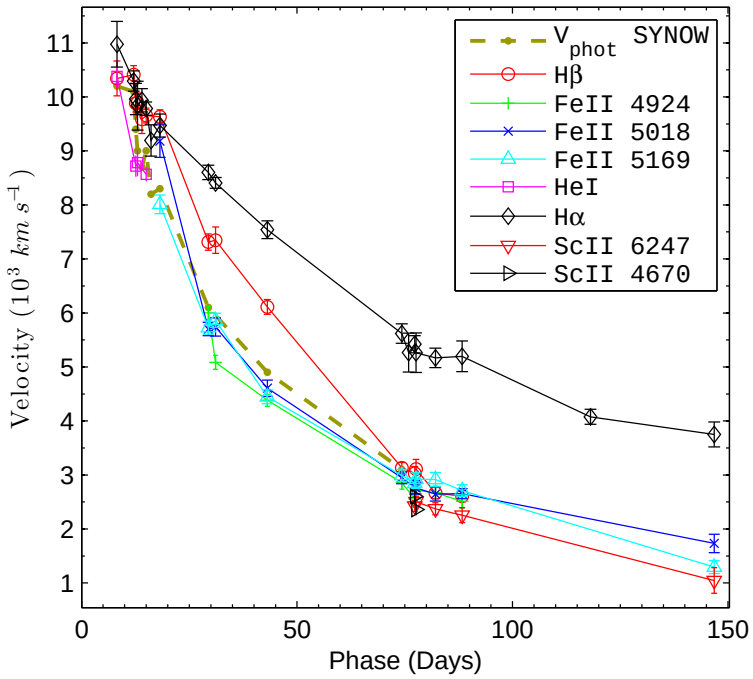

Figure 5.14: Evolution of the Hα, Hβ, He I, Sc II and Fe II line velocities. The velocities are estimated through the Doppler-shift of the absorption minima. The expansion velocities at the photosphere ($v_{\rm ph}$) estimated from SYNOW fits of He I line until 18d and simultaneous fits for Fe II lines at later phases (see Table 5.2) are shown as a comparison.

The expansion velocities of Hα, Hβ, He I, Fe II ($\lambda\lambda$ 4924, 5018 and 5169), Sc II λ6247 and Sc II λ4670 have also been determined using `IRAF` by fitting the absorption trough with a Gaussian profile. The results are plotted in Fig. 5.14. It can be seen that H I lines are formed at larger radii than He I whereas Fe II lines are formed at much smaller radii, having lower velocities. The Sc II lines are formed at a even smaller radius. Sc II lines are weak in strength and due to the limitation of our low SNR spectra, these lines are only detected during 77 to 147d.

Fig. 5.15 shows the comparison of photospheric velocity of SN 2013ab with those of other well-studied SNe 1987A, 1999em, 1999gi, 2004et, 2005cs and 2012aw. For the purpose of comparison, the absorption trough velocities have been used, taking the mean of Fe II lines (or He I lines at early phases where Fe II lines are not detected). The velocity profile of SN 2013ab is very similar to those of other normal SNe IIP.

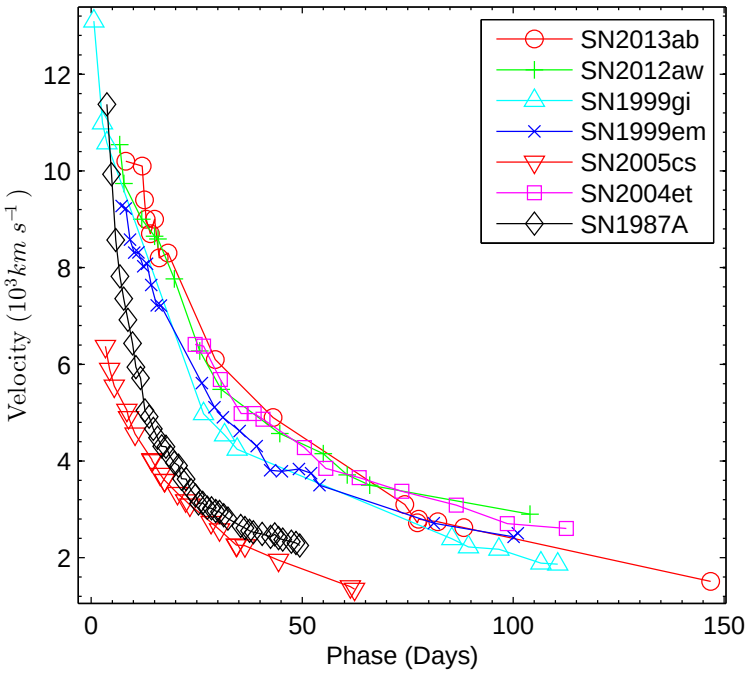

Figure 5.15: The evolution of photospheric velocity ($v_{\rm ph}$) of SN 2013ab is compared with those of other well-studied SNe. The $v_{\rm ph}$ plotted here are the absorption trough velocities (from He I lines at early phases, and Fe II at late phases.)

On the other hand, the velocities of SN 2005cs and SN 1987A are significantly smaller than those of normal events including SN 2013ab. The shape and values of the SN 2013ab velocity profile is strikingly similar to those of SNe 2004et and 2012aw, whereas the velocities are consistently higher than SNe 1999gi and 1999em by $\sim 800\,{\rm km\,s^{-1}}$.

5.6 Expanding Photosphere Method

Expanding photosphere method (EPM) is a geometrical technique (Eastman et al., 1996; Kirshner & Kwan, 1974) in which the angular radius is compared with physical radius of the SN photosphere to estimate its distance. Assuming homologous expansion of SN photosphere, the physical radius at any instant is approximated from expansion velocity(v_{ph}), and angular radius (θ) is estimated from blackbody fit

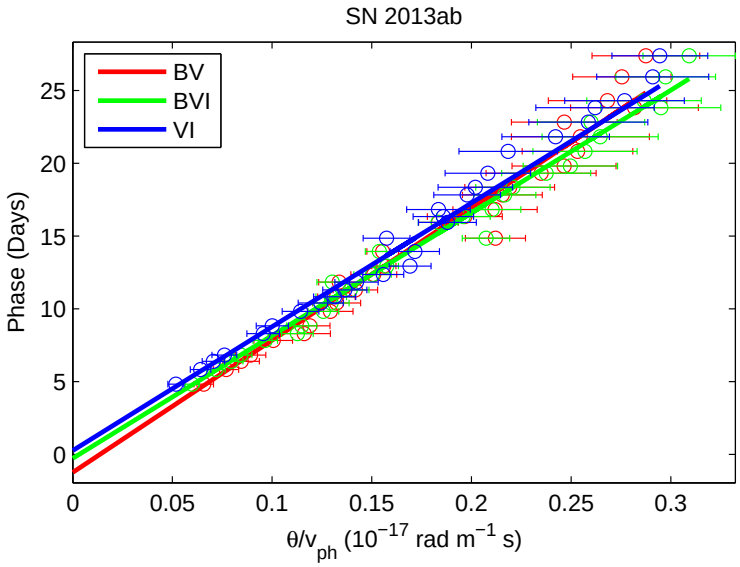

Figure 5.16: The EPM fit for SN 2013ab, using Dessart & Hillier (2005b) prescription for the dilution factor and using three filter sets.

corrected with the dilution factor (ξ) of Dessart & Hillier (2005b) for non-LTE SNe atmosphere. Distance (D) and explosion epoch (t_0) are related with the quantity θ/v_{ph} at any given time t as,

$$t = D\left(\frac{\theta}{v_{ph}}\right) + t_0 \tag{5.3}$$

Thus, the plot of t against θ/v_{ph}, yield distance as the slope and explosion epoch as the y-intercept.

EPM has been successfully applied to a considerably large sample of type IIP events by Jones et al. (2009) and Bose & Kumar (2014a). The merits and limitations of the method has also been tested for multiple aspects. Here, we followed the same approach as described in Bose & Kumar (2014a). It has also been shown that the two dilution factor prescriptions given by Hamuy et al. (2001) and Dessart & Hillier (2005a) have significant differences with the latter being more consistent with other redshift-independent distance estimates. In addition also the SYNOW-estimated velocities are better suited for such analysis. Taking into account all these factors, we have used the Dessart & Hillier (2005a) dilution factor prescription

and SYNOW estimated velocities for EPM analysis. We also restricted our data set up to 30d only. We derived an EPM distance of 24.26 ± 0.98 Mpc which is the mean value for BV, BVI and VI band-sets (Fig. 5.16). The corresponding derived explosion epoch from EPM is JD 2456339.59 ± 0.76 day, which is in good agreement with the uncertainty of adopted explosion epoch from observations (see §5.1). In principle we can constrain explosion epoch and keep distance as the only free parameter for the analysis. This yields a distance of 23.49 ± 0.77 Mpc. Since, the derived explosion epoch from unconstrained analysis is within the uncertainty of the observationally adopted explosion epoch, and the derived distances from constrained and unconstrained analysis are reasonably consistent within the limits of uncertainty, we prefer to adopt the EPM distance as derived from the unconstrained analysis. The EPM distance is found to be in good agreement with mean redshift independent distance estimates (24.9 ± 5.8 Mpc) listed in NED[1] database for the galaxy NGC 5669.

5.7 Characteristics of the explosion

5.7.1 Radius of progenitor

During the shock breakout CCSNe heats the envelope to extremely high temperatures and then it cools down as the envelope expands. This temperature evolution depends on several parameters, viz. progenitor radius, opacity, explosion energy and mass. A simplified analytic formulation relating all these parameters has been determined by Rabinak & Waxman (2011). For a progenitor with larger radius, the envelope remains at a higher temperature for a longer time as compared to a progenitor with smaller radius. The temperature evolution is weakly dependent on the progenitor mass and energy, whereas radius and opacity are the dominating parameters. We computed blackbody temperatures from photometric fluxes and spectra and constrained progenitor radius by fitting the relation on these values (Fig. 5.17). We restricted our fits only within one week of the explosion as the relation is valid

[1]NASA Extragalactic Database http://ned.ipac.caltech.edu/

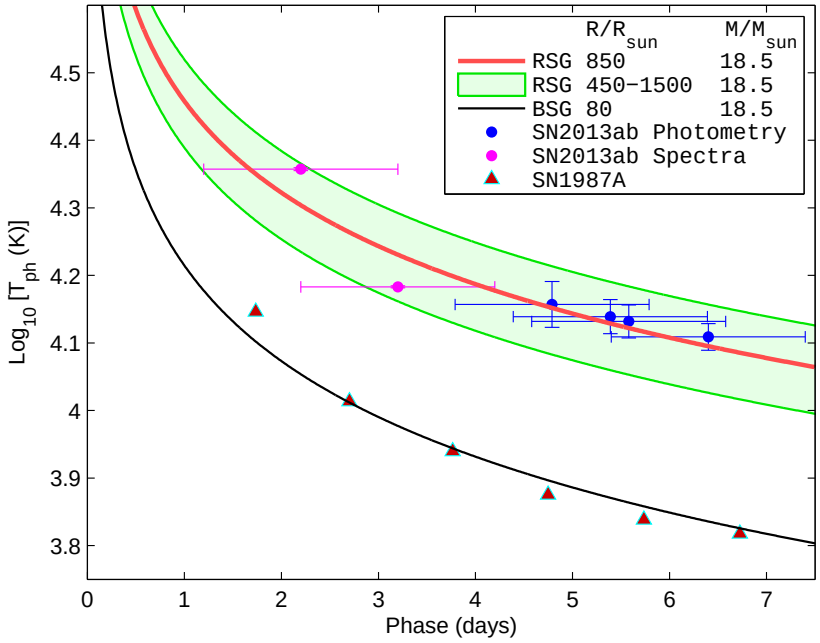

Figure 5.17: Constraining radius using Rabinak & Waxman (2011) prescription. The red solid line is the best fit for RGS of 850 $R_\odot$ for SN 2013ab temperatures and the black solid line is for BSG of 80 $R_\odot$ for SN 1987A temperatures (Menzies et al., 1987).

for the initial few days after the explosion. We adopted an optical opacity of 0.34 and a typical RSG density profile $f_p = 0.11$, however it is also noted that results are not very sensitive towards f_p. This analysis yields an initial radius of 750-950 $R_\odot$ for the progenitor of SN 2013ab, adopting minimal line-of-sight extinction (see §5.3). The radius estimate suggests that the progenitor is possibly a large RSG. With increased extinction value the estimated radius would increase even further.

5.7.2 Hydrodynamical modelling

With the same well-tested approach adopted for other observed SNe (e.g. SNe 2007od, 2009E, 2009N, 2012A, and 2012aw; see Dall'Ora et al., 2014; Inserra et al., 2011; Pastorello et al., 2012; Takáts et al., 2014; Tomasella et al., 2013), we constrain the main physical properties of SN 2013ab at the explosion (namely the ejected mass, the progenitor radius and the explosion energy) through the hydrodynamical

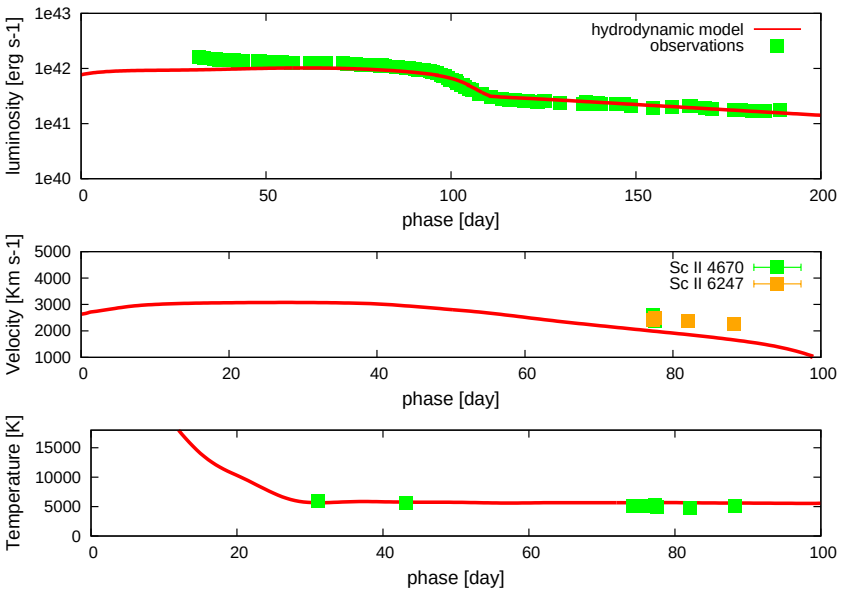

Figure 5.18: Comparison of the evolution of the main observables of SN 2013ab with the best-fit model computed using the general-relativistic, radiation-hydrodynamics code (total energy 0.35 foe, initial radius 4.2×10^{13} cm, envelope mass $7\,M_{\odot}$). Top, middle, and bottom panels show the bolometric light curve, the photospheric velocity, and the photospheric temperature as a function of time. To better estimate the photosphere velocity from observations, we use the minima of the profile of the Sc II lines which are considered good tracer of the photosphere velocity in Type II SNe. As for the photospheric temperature, we use the blackbody temperature derived from the blackbody fits to the spectral continuum.

modelling of the main observables (i.e. bolometric light curve, evolution of line velocities and continuum temperature at the photosphere).

According to this approach, a simultaneous χ^2 fit of the above mentioned observables against model calculations is performed. Two codes are employed for the computation of the models: 1) the first one is the semi-analytic code where the energy balance equation is solved for a homologously expanding envelope of constant density (for details see Zampieri et al., 2003); 2) the other one is the new general-relativistic, radiation-hydrodynamics Lagrangian code presented in Pumo et al. (2010) and Pumo & Zampieri (2011), which is able to simulate the evolution of the physical properties of the CC-SN ejecta and the behavior of the main observables from the breakout of the shock wave at the stellar surface up to the nebular

stage. The distinctive features of this new code are (cf. also Pumo & Zampieri, 2013): a) an accurate treatment of radiative transfer coupled to hydrodynamics, b) a fully implicit Lagrangian approach to solve the coupled non-linear finite difference system of general-relativistic, radiation-hydrodynamics equations, and c) a description of the evolution of ejected material which takes into account both the gravitational effects of the compact remnant and the heating effects linked to the decay of the radioactive isotopes synthesized during the SN explosion.

The semi-analytic code used to carry out a preparatory study aimed at constraining the parameter space describing the SN progenitor at the explosion. The results of such study are exploited to guide the more realistic, but time consuming model calculations performed with the general-relativistic, radiation-hydrodynamics code.

We note that modelling with both codes is appropriate, since the emission of SN 2013ab is dominated by the expanding ejecta. However, in performing the χ^2 fit, we do not include the observational data taken at early phases (first $\sim$ 20-30 days after explosion) because our model is not able to accurately reproduce the early evolution of the main observables, due to the approximate initial density profile used in the simulations which does not precisely reproduce the radial profile of the outermost high-velocity shell of the ejecta forming after the breakout of the shock wave at the stellar surface (cf. Pumo & Zampieri, 2011).

The explosion epoch (JD = 2456340.0) and distance modulus (μ = 31.90 mag) adopted in this chapter (see § 5.3) are used to fix the explosion epoch and to compute the bolometric luminosity of SN 2013ab, both necessary to perform the comparison with model calculations. Since we do not have infrared (IR) observations for SN 2013ab, we computed true bolometric luminosity by adding IR contribution, assuming SN 2013ab has similar optical to IR flux ratio as observed for SN 1999em. Adopting a ^{56}Ni mass of 0.06 $M_\odot$ (see § 5.4.4), the best fit procedure returns values of kinetic plus thermal energy of 0.35 foe, initial radius of 4.2×10^{13} cm ($\sim$ 600 $R_\odot$) and envelope mass of 7 $M_\odot$ (see Fig. 5.18), with an estimated uncertainty on the modelling parameters of about 15%. Adding the mass of the compact remnant ($\sim 1.5 - 2.0\, M_\odot$) to that of the ejected material, the mass of the progenitor of SN 2013ab at the explosion would be $\sim$ 9 $M_\odot$.

From the middle panel of Fig. 5.18 one can note a small (15-20%) discrepancy between the observed photospheric velocity and our best-fitting model. Such discrepancy may be linked to a systematic shift between the true photospheric velocity and the values estimated from the observed P-Cygni line profiles (Dessart & Hillier, 2005a), according to which the optical depth in the lines could be higher than that in the continuum, causing a shift of the line photosphere to a larger radius (see also Inserra et al., 2013). Nevertheless we notice that the discrepancy can be eliminated by adopting for the model higher values for the initial radius ($\sim 6 \times 10^{13}$ cm), the energy ($\sim$ 0.6 foe) and the envelope mass (up to 13 $M_{\odot}$). However in this case we get a worse fit to the observed light curve, with a longer (by about 30%) plateau.

The values reported above are consistent with a core collapse scenario from a typical red super-giant progenitor of relatively low mass. The radius estimate is also consistent within errors with that estimated from early photospheric temperatures described in §5.7.1.

5.8 Summary

In this chapter we present high-cadence broadband photometric and low resolution spectroscopic observations of SN 2013ab spanning a duration of about 6 months. In total, we collected 135 epoch of photometric and 25 epochs of spectroscopic observations. A brief summary of the results obtained in this work is given below.

1. The light curve and the bolometric luminosity comparisons with other SNe IIP suggest that SN 2013ab is a normal SN IIP, though with a relatively large plateau decline rate (0.92 mag 100 d^{-1} in the V band) and a shorter plateau duration ($\sim$ 78 d). The ^{56}Ni mass estimated by comparing the tail luminosity with that of SN 1987A yields a value of 0.064 $M_{\odot}$.

2. Spectroscopic comparisons show strong resemblance with canonical type IIP events. Earliest spectra show a featureless continuum. As the SN evolve, the spectra develop metal lines (calcium, iron, scandium, barium, titanium and neutral sodium). Nebular phase spectra show emission lines with little

or no P-Cygni signatures. Spectra until 77d with good signal-to-noise ratio are modeled using SYNOW to identify most of the prominent features and to estimate expansion velocities for the He I, Fe II and Hβ lines.

3. The EPM has been applied to SN 2013ab using the SYNOW-derived velocities and BVI photometric data. This provides an independent and reliable estimate of the distance of the galaxy NGC 5669 as 24.3 ± 1.0 Mpc.

4. We constrained the physical properties of SN 2013ab at the explosion by means of a hydrodynamical modelling of the main observables which uses the general-relativistic, radiation-hydrodynamics code described in Pumo & Zampieri (2011). The kinetic plus thermal energy is estimated to be ~ 0.35 foe, the progenitor mass is ~ 9 $M_\odot$ and the radius is about 600 $R_\odot$.

APPENDIX

5.A Photometry

Photometric images were bias subtracted and flat fielded, then cosmic ray removal were performed using standard tasks available in IRAF[1]. Due to the position of SN in its host galaxy, we performed PSF photometry on all frames using DAOPHOT [2] routines. The measured SN flux was significantly affected by the host galaxy flux, therefore an annulus has been chosen conservatively to estimate the host galaxy background.

To calibrate the instrumental light curves of SN 2013ab in *UBVRI*, obtained from ARIES telescopes, four Landolt (2009) standard fields PG 1323, PG 1633, SA 104 and SA 107 were observed on 8 March, 2014 with 104-cm ST under good photometric sky condition with low atmospheric extinction and a typical image FWHM $\sim$1″.9 in V band. Multiple standard fields at different airmasses were used to compute the zero points, colour coefficients as well as extinction for different filters. In total 27 standard stars were used for calibration having V magnitudes from 11.0 to 15.4. The root-mean-square scatter between standard and the re-calibrated magnitudes of these Landolt stars were found to be $\sim$ 0.4 mag in U, $\sim$ 0.2 mag in B, $\sim$ 0.1 mag in V,R and $\sim$ 0.3 mag in I band. We used the obtained coefficients to standardize 11 non-variable and isolated field stars in the SN frame, which are tabulated in Table. 5.A.1 . These secondary standards allows us to calibrate the SN light curve obtained using differential photometry. Similarly to standardize the data collected from LCOGT in *BVgri* bands, several secondary standard in the SN field are selected, few of which are also listed in Table. 5.A.1. Since, B and V bands are in common to ARIES and LOCGT data, to have an uniformity we preferred to used LCOGT secondary standards for all BV bands data. *Swift*/UVOT data were analyzed following the methods described by Poole et al. (2008) and Brown

[1] IRAF stands for Image Reduction and Analysis Facility distributed by the National Optical Astronomy Observatories which is operated by the Association of Universities for research in Astronomy, Inc. under co-operative agreement with the National Science Foundation.

[2] DAOPHOT stands for Dominion Astrophysical Observatory Photometry (Stetson, 1987).

Table 5.A.1: Coordinates (α, δ) and calibrated magnitudes of secondary standard stars in the field of SN 2013ab. The quoted errors in magnitude include both photometric and calibration errors and it denote 1σ uncertainty.

Secondary standards used to calibrate *URI* data.

α_{J2000} (h m s)	δ_{J2000} (° ′ ″)	U (mag)	R (mag)	I (mag)
14:32:38	+9:56:39	17.654 ± 0.085	15.452 ± 0.016	14.967 ± 0.014
14:32:36	+9:56:00	17.406 ± 0.028	16.134 ± 0.017	15.744 ± 0.016
14:32:33	+9:54:45	16.968 ± 0.022	15.851 ± 0.017	15.440 ± 0.016
14:32:38	+9:52:24	17.709 ± 0.034	16.034 ± 0.020	15.550 ± 0.021
14:32:28	+9:49:43	19.362 ± 0.204	15.628 ± 0.015	14.616 ± 0.015
14:32:45	+9:48:37	18.118 ± 0.062	16.549 ± 0.017	16.109 ± 0.020
14:33:02	+9:54:41	18.789 ± 0.097	15.133 ± 0.013	14.096 ± 0.015
14:33:07	+9:55:52	17.354 ± 0.023	16.085 ± 0.013	15.649 ± 0.013
14:33:02	+9:56:03	17.828 ± 0.031	16.422 ± 0.012	15.996 ± 0.014
14:33:01	+9:57:25	14.520 ± 0.011	13.770 ± 0.009	13.418 ± 0.013
14:32:46	+9:56:10	17.918 ± 0.071	16.882 ± 0.013	16.469 ± 0.015

Secondary standards used to calibrate *BVgri* data.

α_{J2000} (h m s)	δ_{J2000} (° ′ ″)	B (mag)	V (mag)	g (mag)	r (mag)	i (mag)
14:32:24	+9:52:12	18.947 ± 0.098	18.518 ± 0.032	18.749 ± 0.019	18.336 ± 0.022	18.241 ± 0.026
14:32:26	+9:50:09	16.924 ± 0.013	16.374 ± 0.011	16.648 ± 0.011	16.147 ± 0.010	16.009 ± 0.026
14:32:32	+9:47:16	17.557 ± 0.040	16.977 ± 0.025	17.321 ± 0.025	16.788 ± 0.016	16.629 ± 0.021
14:32:32	+9:57:48	17.994 ± 0.021	17.428 ± 0.016	17.733 ± 0.013	17.196 ± 0.012	17.055 ± 0.022
14:32:37	+9:58:48	18.937 ± 0.048	17.948 ± 0.023	18.461 ± 0.019	17.413 ± 0.013	16.961 ± 0.013
14:32:40	+9:45:54	14.499 ± 0.016	14.064 ± 0.010	14.286 ± 0.010	13.912 ± 0.010	13.814 ± 0.011
14:32:44	+9:54:24	16.593 ± 0.012	15.759 ± 0.010	16.166 ± 0.011	15.426 ± 0.016	15.203 ± 0.023
14:32:48	+9:46:33	19.776 ± 0.083	19.286 ± 0.056	19.547 ± 0.057	19.189 ± 0.042	19.132 ± 0.173
14:32:59	+9:45:23	17.241 ± 0.021	16.804 ± 0.013	17.022 ± 0.013	16.635 ± 0.012	16.497 ± 0.013
14:33:02	+9:54:41	17.423 ± 0.016	16.078 ± 0.011	16.746 ± 0.011	15.450 ± 0.011	14.661 ± 0.010
14:33:07	+9:55:52	17.096 ± 0.014	16.462 ± 0.012	16.746 ± 0.011	16.216 ± 0.011	16.033 ± 0.011
14:33:11	+9:59:27	17.485 ± 0.015	16.674 ± 0.012	17.092 ± 0.012	16.309 ± 0.011	16.042 ± 0.012
14:33:13	+9:49:03	16.591 ± 0.012	16.059 ± 0.011	16.329 ± 0.011	15.865 ± 0.011	15.725 ± 0.011
14:33:14	+9:52:02	18.502 ± 0.060	17.726 ± 0.028	18.161 ± 0.016	17.349 ± 0.012	17.049 ± 0.016
14:33:15	+9:51:37	15.060 ± 0.012	14.534 ± 0.010	14.776 ± 0.010	14.344 ± 0.010	14.230 ± 0.011
14:33:18	+9:47:11	17.575 ± 0.168	17.052 ± 0.062	17.586 ± 0.068	16.800 ± 0.013	16.531 ± 0.014

et al. (2009) but adopting the revised zeropoints and sensitivity from Breeveld et al. (2011). Template images in all UVOT bands are obtained on 13 March, 2015 (755d), which are used to estimate background fluxes, using same aperture as used for SN measurement. These fluxes are subtracted from SN to eliminate flux contamination due to host galaxy. The final photometry in the *UBVRI*, *gri* and UVOT bands is tabulated in Table 5.A.2.

5.A.1 Photometric data

Table 5.A.2: Photometric evolution of SN 2013ab. Errors denote 1σ uncertainty.

UT Date	JD	Phase[a]	U	B	V	R	I	g	r	i	Tel[b]
(yyyy/mm/dd)	2456000+	(day)	(mag)	(mag)	(mag)	(mag)	(mag)	(mag)	(mag)	(mag)	/Inst
2013-02-15.50	339.00	-1.00	—	—	—	—	—	—	>18.500	—	6
2013-02-17.50	341.00	1.00	—	—	—	—	—	—	17.600 ± 0.095	—	6
2013-02-19.20	342.70	2.70	—	—	—	—	—	—	15.093 ± 0.095	—	5
2013-02-20.29	343.79	3.79	—	—	—	—	—	15.007 ± 0.022	15.094 ± 0.047	15.297 ± 0.010	2,5
2013-02-20.93	344.43	4.43	14.231 ± 0.040	—	—	14.873 ± 0.015	14.767 ± 0.030	—	—	—	1
2013-02-21.34	344.84	4.84	—	14.812 ± 0.015	14.779 ± 0.012	—	—	14.805 ± 0.018	14.874 ± 0.011	14.956 ± 0.017	5
2013-02-21.57	345.07	5.07	—	—	—	—	—	14.964 ± 0.016	14.767 ± 0.068	14.994 ± 0.064	3
2013-02-22.34	345.84	5.84	—	14.813 ± 0.015	14.747 ± 0.018	—	—	14.825 ± 0.018	14.759 ± 0.017	14.855 ± 0.013	5
2013-02-22.90	346.40	6.40	14.173 ± 0.040	14.804 ± 0.025	—	14.730 ± 0.014	14.586 ± 0.029	—	—	—	1
2013-02-23.34	346.84	6.84	—	14.793 ± 0.013	14.705 ± 0.023	—	—	14.734 ± 0.028	14.744 ± 0.037	14.740 ± 0.030	5
2013-02-24.34	347.84	7.84	—	14.793 ± 0.014	—	—	—	14.761 ± 0.013	14.699 ± 0.010	14.763 ± 0.012	5
2013-02-24.80	348.30	8.30	14.231 ± 0.041	14.868 ± 0.025	—	14.677 ± 0.014	14.517 ± 0.030	—	—	—	1
2013-02-25.34	348.84	8.84	—	14.838 ± 0.015	14.691 ± 0.019	—	—	14.776 ± 0.013	14.721 ± 0.025	14.776 ± 0.016	5
2013-02-26.34	349.84	9.84	—	14.871 ± 0.011	14.729 ± 0.021	—	—	14.751 ± 0.020	14.717 ± 0.021	14.786 ± 0.009	5
2013-02-26.90	350.40	10.40	14.342 ± 0.041	14.885 ± 0.025	—	14.698 ± 0.014	14.552 ± 0.030	—	—	—	1
2013-02-27.34	350.84	10.84	—	14.880 ± 0.014	14.783 ± 0.011	—	—	14.903 ± 0.013	14.685 ± 0.022	14.871 ± 0.021	5
2013-02-27.80	351.30	11.30	14.402 ± 0.041	14.916 ± 0.025	—	14.712 ± 0.014	14.580 ± 0.029	—	—	—	1
2013-02-28.34	351.84	11.84	—	14.860 ± 0.015	14.814 ± 0.018	—	—	14.831 ± 0.016	14.741 ± 0.014	14.822 ± 0.015	5
2013-02-28.86	352.36	12.36	14.497 ± 0.040	14.974 ± 0.025	—	14.733 ± 0.014	14.612 ± 0.029	—	—	—	1
2013-03-01.44	352.94	12.94	—	15.018 ± 0.005	14.901 ± 0.006	—	—	14.935 ± 0.005	14.809 ± 0.005	14.911 ± 0.009	5
2013-03-02.44	353.94	13.94	—	14.950 ± 0.006	14.889 ± 0.010	—	—	14.925 ± 0.007	14.777 ± 0.009	14.934 ± 0.009	5
2013-03-03.39	354.89	14.89	—	15.092 ± 0.017	14.826 ± 0.018	—	—	14.917 ± 0.003	14.798 ± 0.006	14.951 ± 0.007	5
2013-03-04.44	355.94	15.94	—	15.046 ± 0.005	14.920 ± 0.005	—	—	14.957 ± 0.005	14.802 ± 0.005	14.945 ± 0.009	5
2013-03-04.84	356.34	16.34	14.715 ± 0.040	15.073 ± 0.025	—	14.770 ± 0.014	14.668 ± 0.029	—	—	—	1
2013-03-05.32	356.82	16.82	—	15.102 ± 0.023	14.885 ± 0.018	—	—	14.972 ± 0.015	14.753 ± 0.024	14.893 ± 0.027	5
2013-03-06.32	357.82	17.82	—	15.122 ± 0.012	14.905 ± 0.021	—	—	15.007 ± 0.019	14.750 ± 0.026	14.930 ± 0.023	5
2013-03-06.85	358.35	18.35	14.879 ± 0.040	15.124 ± 0.025	—	14.768 ± 0.014	14.652 ± 0.029	—	—	—	1
2013-03-07.82	359.32	19.32	14.951 ± 0.040	15.162 ± 0.025	—	14.762 ± 0.014	14.642 ± 0.029	—	—	—	1
2013-03-08.31	359.81	19.81	—	15.198 ± 0.017	—	—	—	—	—	—	5
2013-03-09.36	360.86	20.86	—	15.196 ± 0.016	14.886 ± 0.012	—	—	15.026 ± 0.009	14.783 ± 0.009	—	5
2013-03-10.35	361.85	21.85	—	15.254 ± 0.016	14.935 ± 0.026	—	—	15.075 ± 0.012	14.832 ± 0.013	14.934 ± 0.015	5
2013-03-11.33	362.83	22.83	—	15.236 ± 0.010	14.963 ± 0.014	—	—	15.067 ± 0.016	14.814 ± 0.019	14.939 ± 0.021	5
2013-03-12.37	363.87	23.87	—	15.363 ± 0.016	14.952 ± 0.019	—	—	15.091 ± 0.014	14.827 ± 0.004	14.923 ± 0.004	5
2013-03-12.80	364.30	24.30	15.503 ± 0.041	15.354 ± 0.025	14.994 ± 0.012	14.756 ± 0.014	14.605 ± 0.029	—	—	—	1

Table 5.A.2 - continued.

UT Date (yyyy/mm/dd)	JD 2456000+	Phase[a] (day)	U (mag)	B (mag)	V (mag)	R (mag)	I (mag)	g (mag)	r (mag)	i (mag)	Tel[b] /Inst
2013-03-14.44	365.94	25.94	—	15.422 ± 0.012	15.036 ± 0.013	—	—	15.202 ± 0.011	14.890 ± 0.015	14.985 ± 0.018	5
2013-03-15.88	367.38	27.38	15.819 ± 0.042	15.486 ± 0.025	15.056 ± 0.012	14.793 ± 0.014	14.636 ± 0.029	—	—	—	1
2013-03-19.94	371.44	31.44	16.145 ± 0.044	15.665 ± 0.025	15.166 ± 0.012	14.867 ± 0.014	14.693 ± 0.029	—	—	—	1
2013-03-20.44	371.94	31.94	—	15.695 ± 0.007	15.113 ± 0.005	—	—	15.383 ± 0.003	14.934 ± 0.004	15.035 ± 0.007	5
2013-03-21.71	373.21	33.21	16.243 ± 0.053	—	15.203 ± 0.013	14.900 ± 0.015	14.692 ± 0.031	—	—	—	1
2013-03-24.43	375.93	35.93	—	15.812 ± 0.010	15.230 ± 0.007	—	—	15.464 ± 0.005	15.003 ± 0.005	—	5
2013-03-24.90	376.40	36.40	—	15.848 ± 0.027	15.248 ± 0.013	14.927 ± 0.014	—	—	—	—	1
2013-03-25.75	377.25	37.25	16.633 ± 0.059	15.866 ± 0.027	15.257 ± 0.009	14.936 ± 0.015	14.718 ± 0.030	—	—	—	1
2013-03-26.38	377.88	37.88	—	15.911 ± 0.012	15.245 ± 0.012	—	—	—	—	—	5
2013-03-28.81	380.31	40.31	16.681 ± 0.062	15.968 ± 0.028	15.282 ± 0.013	14.966 ± 0.015	14.729 ± 0.030	—	—	—	1
2013-03-29.78	381.28	41.28	16.814 ± 0.104	15.982 ± 0.029	15.303 ± 0.013	14.971 ± 0.014	14.722 ± 0.030	—	—	—	1
2013-03-30.87	382.37	42.37	16.910 ± 0.066	16.035 ± 0.027	15.316 ± 0.013	14.997 ± 0.015	14.763 ± 0.029	—	—	—	1
2013-04-01.38	383.88	43.88	—	16.068 ± 0.013	15.278 ± 0.014	—	—	15.619 ± 0.014	15.073 ± 0.017	15.083 ± 0.018	5
2013-04-05.39	387.89	47.89	—	16.073 ± 0.204	15.277 ± 0.025	—	—	15.640 ± 0.020	15.064 ± 0.026	15.074 ± 0.028	5
2013-04-05.83	388.33	48.33	17.143 ± 0.055	16.074 ± 0.026	15.307 ± 0.012	14.986 ± 0.014	14.736 ± 0.029	—	—	—	1
2013-04-06.40	388.90	48.90	—	16.183 ± 0.030	—	—	—	—	—	—	5
2013-04-06.85	389.35	49.35	17.200 ± 0.042	16.087 ± 0.018	15.317 ± 0.008	15.117 ± 0.010	14.731 ± 0.021	—	—	—	1
2013-04-07.39	389.89	49.89	—	16.203 ± 0.010	15.340 ± 0.012	—	—	15.693 ± 0.013	15.110 ± 0.014	15.119 ± 0.012	5
2013-04-10.88	393.38	53.38	17.429 ± 0.047	16.243 ± 0.026	15.381 ± 0.012	15.032 ± 0.014	14.751 ± 0.029	—	—	—	1
2013-04-11.85	394.35	54.35	17.487 ± 0.073	16.243 ± 0.026	15.383 ± 0.012	15.030 ± 0.014	14.748 ± 0.029	—	—	—	1
2013-04-14.36	396.86	56.86	—	16.362 ± 0.011	15.372 ± 0.010	—	—	15.771 ± 0.008	15.167 ± 0.008	15.194 ± 0.009	5
2013-04-14.77	397.27	57.27	17.522 ± 0.052	16.288 ± 0.026	15.403 ± 0.012	15.042 ± 0.014	14.761 ± 0.029	—	—	—	1
2013-04-19.32	401.82	61.82	—	16.402 ± 0.014	15.373 ± 0.011	—	—	15.838 ± 0.007	15.197 ± 0.010	15.122 ± 0.013	5
2013-04-20.32	402.82	62.82	—	16.390 ± 0.012	15.420 ± 0.010	—	—	15.804 ± 0.006	15.229 ± 0.009	15.191 ± 0.012	5
2013-04-21.32	403.82	63.82	—	16.444 ± 0.018	15.387 ± 0.014	—	—	15.793 ± 0.013	15.153 ± 0.018	15.150 ± 0.016	5
2013-04-22.77	405.27	65.27	17.637 ± 0.098	16.415 ± 0.022	15.430 ± 0.009	15.061 ± 0.016	14.787 ± 0.030	—	—	—	1
2013-04-23.32	405.82	65.82	—	16.330 ± 0.026	15.411 ± 0.012	—	—	15.820 ± 0.014	15.182 ± 0.019	15.143 ± 0.017	5
2013-04-23.80	406.30	66.30	—	—	15.422 ± 0.017	15.084 ± 0.015	14.781 ± 0.030	—	—	—	1
2013-04-26.28	408.78	68.78	—	—	—	—	—	15.874 ± 0.018	15.099 ± 0.016	—	5
2013-04-28.28	410.78	70.78	—	16.480 ± 0.019	15.406 ± 0.014	—	—	15.818 ± 0.011	15.129 ± 0.016	15.137 ± 0.016	5
2013-04-29.28	411.78	71.78	—	16.520 ± 0.014	15.437 ± 0.011	—	—	15.858 ± 0.009	15.187 ± 0.008	15.175 ± 0.012	5
2013-04-30.28	412.78	72.78	—	16.557 ± 0.013	15.486 ± 0.012	—	—	15.889 ± 0.011	15.227 ± 0.010	15.246 ± 0.013	5
2013-05-01.77	414.27	74.27	17.740 ± 0.053	—	15.444 ± 0.013	15.086 ± 0.014	14.792 ± 0.030	—	—	—	1
2013-05-03.27	415.77	75.77	—	16.617 ± 0.025	15.498 ± 0.015	—	—	15.885 ± 0.011	15.231 ± 0.012	—	5
2013-05-05.75	418.25	78.25	17.841 ± 0.094	—	15.466 ± 0.012	15.107 ± 0.014	14.820 ± 0.021	—	—	—	1
2013-05-06.76	419.26	79.26	17.920 ± 0.086	—	15.457 ± 0.012	15.094 ± 0.014	14.802 ± 0.029	—	—	—	1
2013-05-08.27	420.77	80.77	—	16.620 ± 0.027	15.562 ± 0.019	—	—	15.985 ± 0.015	15.298 ± 0.013	15.224 ± 0.021	5
2013-05-08.79	421.29	81.29	18.113 ± 0.061	—	15.494 ± 0.012	15.123 ± 0.015	14.815 ± 0.030	—	—	—	1

Table 5.A.2 - continued.

UT Date (yyyy/mm/dd)	JD 2456000+	Phase[a] (day)	U (mag)	B (mag)	V (mag)	R (mag)	I (mag)	g (mag)	r (mag)	i (mag)	Tel[b] /Inst
2013-05-09.72	422.22	82.22	18.070 ± 0.057	—	15.510 ± 0.009	15.119 ± 0.015	14.823 ± 0.030	—	—	—	1
2013-05-12.74	425.24	85.24	18.069 ± 0.078	—	15.567 ± 0.013	15.174 ± 0.015	14.815 ± 0.032	—	—	—	1
2013-05-13.24	425.74	85.74	—	16.793 ± 0.023	15.621 ± 0.015	—	—	16.084 ± 0.010	15.360 ± 0.011	15.329 ± 0.014	5
2013-05-15.24	427.74	87.74	—	16.874 ± 0.021	15.653 ± 0.014	—	—	16.127 ± 0.010	15.360 ± 0.009	15.349 ± 0.013	5
2013-05-16.26	428.76	88.76	—	16.827 ± 0.021	15.597 ± 0.013	—	—	16.093 ± 0.015	15.337 ± 0.012	—	5
2013-05-17.74	430.24	90.24	18.634 ± 0.147	—	15.668 ± 0.013	15.223 ± 0.014	14.926 ± 0.030	—	—	—	1
2013-05-18.71	431.21	91.21	—	—	15.718 ± 0.010	15.279 ± 0.015	14.969 ± 0.031	—	—	—	1
2013-05-19.69	432.19	92.19	—	—	15.740 ± 0.015	15.298 ± 0.016	14.978 ± 0.031	—	—	—	1
2013-05-20.26	432.76	92.76	—	17.002 ± 0.021	15.764 ± 0.015	—	—	16.256 ± 0.021	15.474 ± 0.027	15.425 ± 0.025	5
2013-05-21.72	434.22	94.22	—	—	15.783 ± 0.015	15.350 ± 0.012	15.025 ± 0.034	—	—	—	1
2013-05-22.23	434.73	94.73	—	17.154 ± 0.034	15.864 ± 0.014	—	—	16.382 ± 0.013	15.523 ± 0.016	15.466 ± 0.020	5
2013-05-22.72	435.22	95.22	—	17.002 ± 0.030	15.850 ± 0.011	15.390 ± 0.012	15.048 ± 0.023	—	—	—	1
2013-05-23.73	436.23	96.23	—	17.075 ± 0.047	15.950 ± 0.022	15.456 ± 0.019	15.129 ± 0.034	—	—	—	1
2013-05-24.74	437.24	97.24	—	17.191 ± 0.062	16.017 ± 0.022	15.543 ± 0.020	15.204 ± 0.037	—	—	—	1
2013-05-25.23	437.73	97.73	—	17.383 ± 0.125	16.092 ± 0.044	—	—	16.621 ± 0.052	15.738 ± 0.047	15.605 ± 0.033	5
2013-05-25.83	438.33	98.33	—	17.213 ± 0.089	16.081 ± 0.032	15.613 ± 0.021	15.270 ± 0.036	—	—	—	1
2013-05-26.72	439.22	99.22	—	17.417 ± 0.040	16.191 ± 0.015	15.677 ± 0.017	15.293 ± 0.033	—	—	—	1
2013-05-27.23	439.73	99.73	—	17.671 ± 0.021	16.264 ± 0.011	—	—	16.816 ± 0.008	15.842 ± 0.010	15.749 ± 0.010	5
2013-05-27.70	440.20	100.20	18.856 ± 0.355	17.505 ± 0.037	16.254 ± 0.014	15.729 ± 0.017	15.335 ± 0.032	—	—	—	1
2013-05-28.76	441.26	101.26	18.513 ± 0.293	17.638 ± 0.038	16.382 ± 0.014	15.829 ± 0.019	15.417 ± 0.033	—	—	—	1
2013-05-29.23	441.73	101.73	—	17.841 ± 0.024	16.517 ± 0.029	—	—	17.030 ± 0.011	16.018 ± 0.008	15.922 ± 0.014	5
2013-05-30.23	442.73	102.73	—	18.019 ± 0.021	16.605 ± 0.014	—	—	17.199 ± 0.014	16.128 ± 0.011	16.017 ± 0.010	5
2013-05-30.80	443.30	103.30	—	17.844 ± 0.038	16.594 ± 0.015	16.004 ± 0.017	—	—	—	—	1
2013-05-31.24	443.74	103.74	—	18.170 ± 0.039	16.736 ± 0.020	—	—	17.345 ± 0.015	16.241 ± 0.013	—	5
2013-06-01.23	444.73	104.73	—	18.259 ± 0.025	16.800 ± 0.018	—	—	17.422 ± 0.012	16.289 ± 0.010	16.204 ± 0.020	5
2013-06-02.23	445.73	105.73	—	18.485 ± 0.051	16.894 ± 0.027	—	—	17.548 ± 0.018	16.370 ± 0.015	16.256 ± 0.023	5
2013-06-04.18	447.68	107.68	—	18.599 ± 0.046	17.113 ± 0.023	—	—	17.734 ± 0.021	16.529 ± 0.017	16.411 ± 0.022	5
2013-06-04.78	448.28	108.28	—	—	17.048 ± 0.020	16.399 ± 0.022	—	—	—	—	1
2013-06-07.18	450.68	110.68	—	18.700 ± 0.047	17.207 ± 0.029	—	—	17.888 ± 0.022	16.744 ± 0.018	16.619 ± 0.026	5
2013-06-10.22	453.72	113.72	—	18.806 ± 0.084	17.278 ± 0.031	—	—	17.962 ± 0.025	16.715 ± 0.026	16.691 ± 0.036	5
2013-06-12.22	455.72	115.72	—	—	17.316 ± 0.028	—	—	18.003 ± 0.024	16.794 ± 0.021	16.651 ± 0.030	5
2013-06-12.68	456.18	116.18	19.743 ± 0.527	—	17.291 ± 0.031	16.632 ± 0.025	16.146 ± 0.037	—	—	—	1
2013-06-13.72	457.22	117.22	19.625 ± 0.411	—	17.293 ± 0.023	16.627 ± 0.024	16.161 ± 0.036	—	—	—	1
2013-06-16.13	459.63	119.63	—	18.911 ± 0.044	17.414 ± 0.018	—	—	18.053 ± 0.042	16.806 ± 0.017	16.727 ± 0.024	5
2013-06-17.20	460.70	120.70	—	18.885 ± 0.038	17.362 ± 0.110	—	—	—	—	—	5
2013-06-19.72	463.22	123.22	—	—	17.446 ± 0.036	16.749 ± 0.026	16.292 ± 0.038	—	—	—	1
2013-06-20.10	463.60	123.60	—	—	17.478 ± 0.026	—	—	18.052 ± 0.020	—	—	5
2013-06-21.73	465.23	125.23	—	—	17.463 ± 0.053	16.700 ± 0.034	16.245 ± 0.045	—	—	—	1

Table 5.A.2 - continued.

UT Date (yyyy/mm/dd)	JD 2456000+	Phase[a] (day)	U (mag)	B (mag)	V (mag)	R (mag)	I (mag)	g (mag)	r (mag)	i (mag)	Tel[b] /Inst
2013-06-22.05	465.55	125.55	—	18.790 ± 0.065	17.454 ± 0.021	—	—	18.007 ± 0.021	16.851 ± 0.012	16.794 ± 0.022	5
2013-06-24.05	467.55	127.55	—	19.004 ± 0.086	—	—	—	18.032 ± 0.018	16.901 ± 0.013	16.770 ± 0.015	5
2013-06-26.05	469.55	129.55	—	18.950 ± 0.048	17.519 ± 0.018	—	—	18.091 ± 0.015	16.896 ± 0.011	16.851 ± 0.015	5
2013-07-02.06	475.56	135.56	—	18.963 ± 0.029	17.623 ± 0.018	—	—	18.190 ± 0.014	16.912 ± 0.012	16.898 ± 0.013	5
2013-07-03.06	476.56	136.56	—	18.936 ± 0.032	17.533 ± 0.021	—	—	—	16.880 ± 0.017	16.911 ± 0.024	5
2013-07-04.21	477.71	137.71	—	18.933	—	—	—	—	—	16.990 ± 0.022	5
2013-07-05.21	478.71	138.71	—	19.027 ± 0.052	17.588 ± 0.020	—	—	18.178 ± 0.024	16.956 ± 0.011	16.937 ± 0.014	5
2013-07-06.21	479.71	139.71	—	18.875 ± 0.052	17.579 ± 0.026	—	—	18.168 ± 0.020	16.983 ± 0.015	16.965 ± 0.021	5
2013-07-07.19	480.69	140.69	—	18.936 ± 0.068	17.624 ± 0.035	—	—	18.188 ± 0.022	16.952 ± 0.020	16.952 ± 0.017	5
2013-07-11.15	484.65	144.65	—	18.865 ± 0.050	17.611 ± 0.024	—	—	18.185 ± 0.019	16.968 ± 0.017	17.067 ± 0.020	5
2013-07-13.15	486.65	146.65	—	18.910 ± 0.050	17.604 ± 0.028	—	—	18.206 ± 0.016	16.993 ± 0.014	17.026 ± 0.019	5
2013-07-15.18	488.68	148.68	—	—	17.773 ± 0.066	—	—	18.258 ± 0.078	17.089 ± 0.045	—	5
2013-07-21.18	494.68	154.68	—	19.072 ± 0.111	17.914 ± 0.043	—	—	18.240 ± 0.034	17.047 ± 0.021	17.215 ± 0.024	5
2013-07-26.18	499.68	159.68	—	19.058 ± 0.053	17.814 ± 0.035	—	—	18.260 ± 0.032	17.073 ± 0.018	17.197 ± 0.029	5
2013-07-30.72	504.22	164.22	—	19.044 ± 0.038	17.753 ± 0.021	—	—	—	—	—	5
2013-07-31.43	504.93	164.93	—	19.090 ± 0.111	17.708 ± 0.044	—	—	—	17.096 ± 0.027	17.257 ± 0.046	3
2013-08-01.17	505.67	165.67	—	19.070 ± 0.150	—	—	—	18.384 ± 0.030	—	—	5
2013-08-04.12	508.62	168.62	—	19.039 ± 0.113	17.900 ± 0.044	—	—	18.350 ± 0.025	17.129 ± 0.017	17.285 ± 0.025	5
2013-08-06.18	510.68	170.68	—	19.047 ± 0.068	17.886 ± 0.031	—	—	18.392 ± 0.024	17.247 ± 0.037	17.413 ± 0.035	5
2013-08-11.97	516.47	176.47	—	19.073 ± 0.125	18.005 ± 0.049	—	—	—	17.186 ± 0.022	17.385 ± 0.036	5
2013-08-14.01	518.51	178.51	—	19.074 ± 0.080	18.035 ± 0.036	—	—	18.487 ± 0.028	17.231 ± 0.017	17.422 ± 0.035	5
2013-08-16.99	521.49	181.49	—	—	18.099 ± 0.051	—	—	18.563 ± 0.036	—	17.428 ± 0.035	5
2013-08-20.15	524.65	184.65	—	—	—	—	—	18.613 ± 0.125	17.227 ± 0.041	17.433 ± 0.072	5
2013-08-20.42	524.92	184.92	—	19.089 ± 0.122	18.078 ± 0.051	—	—	—	—	—	5
2013-08-24.38	528.88	188.88	—	—	18.002 ± 0.060	—	—	—	—	—	3
2013-08-25.36	529.86	189.86	—	—	—	—	—	—	17.267 ± 0.036	17.526 ± 0.071	3

Swift UVOT photometry

UT Date (yyyy/mm/dd)	JD 2456000+	Phase[a] (day)	$uvw1$ (mag)	$uvw2$ (mag)	$uvm2$ (mag)	uvu (mag)	uvb (mag)	uvv (mag)	Tel[b] /Inst
2013-02-21.18	344.68	4.68	13.404 ± 0.038	13.434 ± 0.042	13.301 ± 0.036	—	—	—	4
2013-02-21.94	345.44	5.44	13.486 ± 0.039	13.589 ± 0.052	13.442 ± 0.047	13.670 ± 0.052	15.010 ± 0.049	15.094 ± 0.056	4
2013-02-22.08	345.58	5.58	13.489 ± 0.037	13.629 ± 0.044	—	—	—	—	4
2013-02-22.51	346.01	6.01	13.616 ± 0.056	13.747 ± 0.071	—	—	—	—	4
2013-02-24.04	347.54	7.54	13.734 ± 0.035	14.133 ± 0.041	13.830 ± 0.035	—	—	—	4
2013-02-24.90	348.40	8.40	13.848 ± 0.043	14.363 ± 0.052	14.007 ± 0.037	13.819 ± 0.050	15.010 ± 0.046	14.962 ± 0.047	4

Table 5.A.2 - continued.

UT Date (yyyy/mm/dd)	JD 2456000+	Phase[a] (day)	$uvw1$ (mag)	$uvw2$ (mag)	$uvm2$ (mag)	uvu (mag)	uvb (mag)	uvv (mag)	Tel[b] /Inst
2013-02-24.98	348.48	8.48	—	—	14.083 ± 0.059	—	—	—	4
2013-02-27.30	350.80	10.80	—	14.895 ± 0.072	—	—	—	—	4
2013-02-27.98	351.48	11.48	14.395 ± 0.058	14.992 ± 0.072	14.742 ± 0.060	13.997 ± 0.051	15.072 ± 0.047	15.018 ± 0.049	4
2013-03-03.09	354.59	14.59	15.084 ± 0.060	15.792 ± 0.075	15.662 ± 0.063	14.340 ± 0.052	15.237 ± 0.047	15.132 ± 0.050	4
2013-03-06.13	357.63	17.63	15.635 ± 0.063	16.577 ± 0.082	16.574 ± 0.072	14.608 ± 0.052	15.258 ± 0.047	15.165 ± 0.049	4
2013-03-14.17	365.67	25.67	17.408 ± 0.116	18.759 ± 0.261	18.859 ± 0.320	15.680 ± 0.068	15.552 ± 0.054	15.220 ± 0.061	4
2013-03-18.21	369.71	29.71	17.710 ± 0.127	19.461 ± 0.364	19.231 ± 0.335	16.203 ± 0.066	15.739 ± 0.049	15.303 ± 0.051	4
2013-03-20.97	372.47	32.47	18.073 ± 0.153	19.120 ± 0.264	19.430 ± 0.385	16.458 ± 0.068	15.896 ± 0.049	15.354 ± 0.049	4
2013-03-27.97	379.47	39.47	18.913 ± 0.299	19.516 ± 0.549	—	17.096 ± 0.095	16.161 ± 0.054	—	4
2013-04-01.39	383.89	43.89	18.754 ± 0.266	19.548 ± 0.390	19.785 ± 0.538	17.276 ± 0.101	16.195 ± 0.053	15.439 ± 0.053	4
2013-04-05.20	387.70	47.70	18.935 ± 0.294	21.232 ± 1.634	19.854 ± 0.556	17.431 ± 0.105	16.391 ± 0.054	15.565 ± 0.053	4
2013-04-10.84	393.34	53.34	19.158 ± 0.359	20.750 ± 1.075	20.042 ± 0.671	17.637 ± 0.120	16.472 ± 0.055	15.548 ± 0.053	4
2013-04-21.92	404.42	64.42	19.450 ± 0.628	—	—	—	—	—	4
2013-04-26.01	408.51	68.51	19.505 ± 0.487	—	20.392 ± 1.262	17.890 ± 0.167	16.646 ± 0.087	15.615 ± 0.086	4
2013-05-01.32	413.82	73.82	20.646 ± 1.300	20.560 ± 0.882	20.642 ± 1.126	18.092 ± 0.160	16.728 ± 0.058	15.632 ± 0.054	4
2013-05-14.26	426.76	86.76	21.116 ± 2.278	20.650 ± 1.277	—	18.971 ± 0.456	16.825 ± 0.080	15.821 ± 0.080	4
2013-05-16.00	429.50	89.50	—	—	20.689 ± 1.217	18.496 ± 0.233	16.925 ± 0.066	15.858 ± 0.062	4
2013-05-20.95	433.45	93.45	20.929 ± 1.738	21.652 ± 2.536	20.850 ± 1.421	18.708 ± 0.279	17.223 ± 0.074	16.050 ± 0.067	4
2013-05-30.95	443.45	103.45	20.721 ± 1.389	21.184 ± 1.547	21.605 ± 2.708	19.429 ± 0.464	18.155 ± 0.115	16.923 ± 0.096	4

[a] with reference to the explosion epoch JD 2456340.0

[b] 1: 104-cm Sampurnanand Telescope (ST) and 130-cm Devasthal fast optical telescope (DFOT), ARIES, India; 2: Faulkes Telescope South; 3: Faulkes Telescope North; 4: Swift UVOT data; 5: 1-m class telescopes of Las Cumbres Observatory Global Telescope (LCOGT) network; 6: IAU circular report.

5.B Spectroscopy

Spectroscopic data were reduced in the `IRAF` environment. All frames are corrected by bias subtraction and flat fielding. Cosmic ray rejection on each frame was done using Laplacian kernel detection algorithm for spectra (L.A.Cosmic; van Dokkum, 2001). One-dimensional spectra were extracted using *apall* task which is based on optimal extraction algorithm by Horne (1986). Wavelength calibration was performed with the help of the *identify* task by using the arc spectra obtained for all telescopes during each night. The position of O I emission skyline at 5577Å was used to check the wavelength calibration and deviations were found to lie between 0.3 to 5.5Å, and this was corrected by applying a linear shift in wavelength.

The flux calibration of wavelength-calibrated spectra was done using *standard, sensfunc* and *calibrate* tasks. We used spectrophotometric standard fluxes from Hamuy et al. (1994); Oke (1990). All spectra were tied to an absolute flux scale using zeropoints determined from $UBVRI$ magnitudes. To tie the spectra with photometry, individual spectrum was multiplied by wavelength dependent polynomial function and its $BVRI$ filter-response convolved fluxes were compared with photometric fluxes at corresponding epoch. The multiplied polynomial was tuned to minimize the flux difference and obtain the tied spectrum. The one-dimensional spectra were corrected for heliocentric velocity of the host galaxy (1374 $\mathrm{km\,s^{-1}}$; see §5.1) using *dopcor* tasks.

Table 5.B.1: Journal of spectroscopic observations of SN 2013ab. The spectral observations are made at 25 phases from 2 to 184d.

UT Date (yyyy-mm-dd.dd)	JD 2456000+	Phase[a] (days)	Telescope[c]	Range[b] μm	Exposure (s)
2013-02-18.70	342.20	2.20	FTS	0.32-1.00	1500
2013-02-19.74	343.24	3.24	FTS	0.32-1.00	1500
2013-02-24.71	348.21	8.21	FTS	0.32-1.00	1500
2013-02-28.59	352.09	12.09	FTN	0.32-1.00	1800
2013-03-01.08	352.58	12.58	PEN	0.00-0.00	1800
2013-03-01.50	353.00	13.00	FTN	0.32-1.00	1800
2013-03-02.51	354.01	14.01	FTN	0.32-1.00	1800
2013-03-03.51	355.01	15.01	FTN	0.32-1.00	1800
2013-03-04.59	356.09	16.09	FTN	0.32-1.00	1800
2013-03-06.71	358.21	18.21	FTS	0.32-1.00	2000
2013-03-17.93	369.43	29.43	HCT	0.38-0.84	1800
2013-03-19.63	371.13	31.13	FTS	0.32-1.00	2000
2013-03-31.58	383.08	43.08	FTS	0.32-1.00	2400
2013-05-01.84	414.34	74.34	HCT	0.38-0.84	1200
2013-05-03.35	415.85	75.85	FTN	0.32-1.00	3600
2013-05-04.33	416.83	76.83	FTN	0.32-1.00	3600
2013-05-04.85	417.35	77.35	HCT	0.38-0.68	1800
2013-05-05.08	417.58	77.58	PEN	0.00-0.00	1200
2013-05-09.57	422.07	82.07	FTN	0.32-1.00	3600
2013-05-15.85	428.35	88.35	HCT	0.38-0.84	1200
2013-06-14.64	458.14	118.14	HCT	0.38-0.68	2400
2013-07-13.34	486.84	146.84	FTN	0.32-1.00	3600
2013-08-09.25	513.75	173.75	FTN	0.32-1.00	3600
2013-08-18.25	522.75	182.75	FTN	0.32-1.00	3600
2013-08-19.25	523.75	183.75	FTN	0.32-1.00	3600

[a] With reference to the explosion time JD 2456340.0

[b] For transmission $\geq$50%

[c] HCT : HFOSC on 2 m Himalyan Chandra Telescope, India; FTN : FLOYDS on 2 m Faulkes Telescope North, Hawaii; FTS: FLOYDS on 2 m Faulkes Telescope South, Australia; PEN: B&C spectrograph on 1.22 m Galileo Telescope, Italy.

Chapter 6

SN 2013ej - A type IIL supernova with weak signs of interaction

6.1 Introduction

The plateau slope of SN type II light curve primarily depends on the amount of hydrogen present in the ejecta. If hydrogen content is high, as in type IIP, the initial energy deposited from shock and decay of freshly produced ^{56}Ni shall be released slowly over a longer period of time. On the other hand if hydrogen content is relatively low, the light curve will decline fast but with higher peak luminosity. Thus if hydrogen content is low enough, one would expect a linear decline in the light curve classifying it as type IIL. By the historical classification, type IIL (Barbon et al., 1979) shows linear decline in light curve over 100 days until it reaches the radioactive tail phase. Arcavi et al. (2012) claimed to find type IIP and IIL as to distinct group of events which may further indicate their distinct class of progenitors. However, recent studies by Anderson et al. (2014b) and Sanders et al. (2015) on large sample of type II SNe do not favor any such bi-modality in the diversity, rather they found continuum in light curve slopes as well as in other physical parameters. The continuous distribution of plateau slopes in type II events is rather governed by variable amount of hydrogen mass left in the envelope at the time of explosion. Based on a sample of 11 type IIL events, Faran et al. (2014) proposed that any event having

decline of 0.5mag in V band light curve in first 50 days can be classified as type IIL. In light of these recent developments a large number of type IIP SNe classified earlier may now fall under IIL class. Thus many of the past studies collectively on samples of type IIP SNe, which we shall be referring in this work may include both IIP as well as IIL.

The geometry of the explosion and presence of pre-existent circumstellar medium (CSM), often associated with progenitor mass loss during late stellar evolutionary phase, can significantly alter the observables even though originating from similar progenitors. There are number of recent studies of II SNe, like 2007od (Inserra et al., 2011), 2009bw (Inserra et al., 2012b) and 2013by (Valenti et al., 2015) which show signature of such CSM interactions during various phases of evolution.

SN 2013ej is one of the youngest detected type II SN which was discovered soon after its explosion. The earliest detection was reported on July 24.125 UTC, 2013 by C. Feliciano in *Bright Supernovae*[1] and subsequent independent detection on July 24.83 UTC by Lee et al. (2013) at V-band magnitude of ∼14.0. The last non-detection was reported on July 23.54 UTC, 2013 by All Sky Automated Survey for Supernovae (Shappee et al., 2013) at a V-band detection limit of $>$ 16.7 mag. Therefore, we adopt an explosion epoch (0d) of July 23.8 UTC (JD = 2456497.3 ± 0.3), which is chosen in between the last non-detection and first detection of SN 2013ej. This being one of the nearest and brightest events, it provides us with an excellent opportunity to study the origin and evolution of type II SN. Some of the basic properties of SN 2013ej and its host galaxy are listed in Table 6.1.

Valenti et al. (2014) presented early observations of SN 2013ej and using temperature evolution for the first week, they estimated a progenitor radius of 400-600 $R_{\odot}$. Fraser et al. (2014) used high resolution archival images from *HST* to examine the location of SN 2013ej and identified the progenitor candidate to be a supergiant of mass $8 - 15.5 M_{\odot}$. Leonard et al. (2013) reported unusually high polarization using spectropolarimetric observation for the week old SN, as implying substantial asymmetry in the scattering atmosphere of ejecta. X-ray emission has also been

[1] http://www.rochesterastronomy.org/supernova.html

detected by *Swift* XRT (Margutti et al., 2013), which may indicate SN 2013ej has experienced CSM interaction.

In this work we present photometric and spectroscopic observation of SN 2013ej, and carry out qualitative as well as quantitative analysis of the various observables through modelling and comparison with other archetypal SNe. The chapter is organized as follows. In section 6.2 we describe photometric and spectroscopic observations and data reduction. The estimation of line of sight extinction is discussed in section 6.3. In section 6.4 we analyze the light curves, compare absolute magnitude light curves and color curves. We also derive bolometric luminosities and estimate nickel mass from the tail luminosity. Optical spectra are analyzed in section 6.5, where we model and discuss evolution of various spectral features and compare velocity profile with other type II SNe. In section 6.7, we model the bolometric light curve of SN 2013ej and estimate progenitor and explosion parameters. Finally in section 6.8, we summarize the results of this work.

6.2 Observation and data reduction

6.2.1 Photometry

Broadband photometric observations in *UBVRI* filters have been carried out from 2.0m IIA Himalayan Chandra Telescope (HCT) telescope at Hanle and ARIES 1.0m Sampurananand (ST) and 1.3m Devasthal Fast Optical (DFOT) telescopes at Nainital. Additionally SN 2013ej has been also observed with *Swift* Ultraviolet/optical (UVOT) telescope in all six bands.

Photometric data reductions follows the same procedure as described in Bose et al. (2013). Images are cleaned and processed using standard procedures of IRAF software. DAOPHOT routines have been used to perform PSF photometry and extracting differential light-curves. To standardize the SN field, three Landolt standard fields (PG 0231, PG 2231 and SA 92) were observed on October 27, 2013 with 1.0-m ST under good photometric night and seeing (typical FWHM $\sim 2''.1$ in V band) condition. For atmospheric extinction measurement, PG 2231 and PG 0231 were observed at different air masses. The SN field has been also observed in between

Table 6.1: Relevant parameters for the host galaxy NGC 0628 and SN 2013ej.

Parameters	Value	Ref.[a]
NGC 0628:		
Alternate name	M74	2
Type	Sc	2
RA (J2000)	$\alpha = 01^{\rm h}36^{\rm m}41\overset{\rm s}{.}77$	2
DEC (J2000)	$\delta = 15°46'59\overset{''}{.}8$	2
Abs. Magnitude	$M_B = -20.72$ mag	2
Distance	$D = 9.6 \pm 0.7$ Mpc	1
Distance modulus	$\mu = 29.90 \pm 0.16$ mag	
Heliocentric Velocity	$cz_{\rm helio} = 658 \pm 1\,{\rm km\,s^{-1}}$	2
SN 2013ej:		
RA (J2000)	$\alpha = 01^{\rm h}36^{\rm m}48\overset{\rm s}{.}16$	3
DEC (J2000)	$\delta = 15°45'31\overset{''}{.}3$	
Galactocentric Location	1′33″E, 2′15″S	
Date of explosion	t_0 =23.8 July 2013 (UT) (JD 2456497.3 ± 0.3)	1
Reddening	$E(B-V) = 0.060 \pm 0.001$ mag	1

(1) This work; (2) HyperLEDA - http://leda.univ-lyon1.fr; (3) Kim et al. (2013)

standard observations. The standardization coefficients derived are represented in the following transformation equations,

$$
\begin{aligned}
u &= U + (7.800 \pm 0.005) - (0.067 \pm 0.009) \cdot (U - B) \\
b &= B + (5.269 \pm 0.007) - (0.060 \pm 0.009) \cdot (B - V) \\
v &= V + (4.677 \pm 0.004) - (0.056 \pm 0.005) \cdot (B - V) \\
r &= R + (4.405 \pm 0.005) - (0.038 \pm 0.010) \cdot (V - R) \\
i &= I + (4.821 \pm 0.006) - (0.048 \pm 0.006) \cdot (V - I)
\end{aligned}
$$

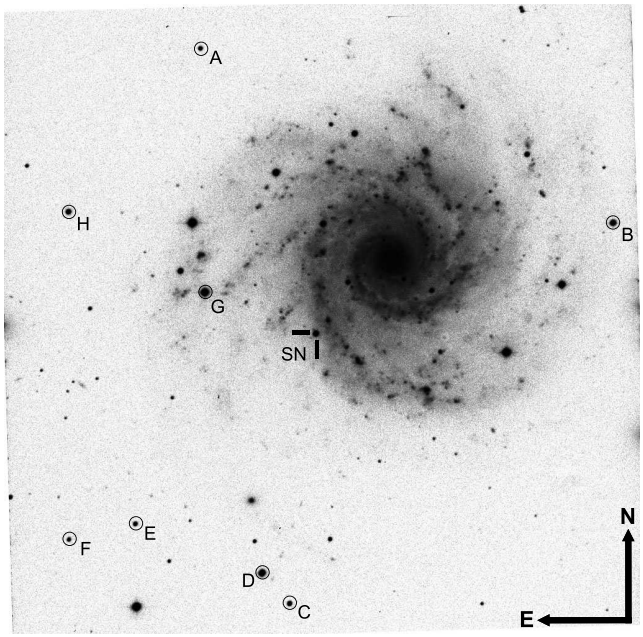

Figure 6.1: SN 2013ej in NGC 0628. The BR-band composite image taken from 104-cm Sampurnanad telescope, covering an area of about $13' \times 13'$ is shown. Eight local field standards and SN are marked in the image.

where u, b, v, r and i are instrumental magnitudes corrected for time, aperture and airmass; U, B, V, R and I are standard magnitude. The standard-deviation of the difference between the calibrated and the standard magnitudes of the observed Landolt stars are found to be $\sim$ 0.03 mag in U, $\sim$ 0.02 mag in BR and $\sim$ 0.01 mag in VI. The transformation coefficients were then used to generate eight local standard stars in the field of SN 2013ej, which are verified to be non-variable and have brightness similar to SN. These stars are identified in Fig.6.1 and the calibrated $UBVRI$ magnitudes are listed in Table 6.1. These selected eight local standards were further used to standardize the instrumental light curve of the SN. One of these stars (star B) is common to that used in the study by Richmond (2014), and its $BVRI$ magnitudes are found to lie within 0.03 mag of our calibrated magnitudes. Our calibrated magnitudes for SN 2013ej are also found to be consistent within errors to that presented in earlier studies of the event (Richmond, 2014; Valenti et al., 2014). The standard photometric magnitudes of SN 2013ej are listed in Table 6.2.

This supernova was also observed with the Ultra-Violet/Optical Telescope (UVOT;

Table 6.1: Eight local standards in the field of SN 2013ej with corresponding coordinates (α, δ) calibrated magnitudes in *UBVRI*. Errors quoted here, include both photometric and calibration errors.

Star ID	α_{J2000} (h m s)	δ_{J2000} (° ′ ″)	U (mag)	B (mag)	V (mag)	R (mag)	I (mag)
A	1:36:57.9	+15:51:19.4	16.773 ± 0.0325	16.867 ± 0.0259	16.297 ± 0.0193	15.939 ± 0.0163	15.567 ± 0.0207
B	1:36:23.0	+15:47:45.3	15.102 ± 0.0289	15.109 ± 0.0302	14.580 ± 0.0234	14.253 ± 0.0183	13.888 ± 0.0260
C	1:36:50.4	+15:40:01.9	16.588 ± 0.0318	16.525 ± 0.0277	15.798 ± 0.0200	15.372 ± 0.0157	14.925 ± 0.0187
D	1:36:52.7	+15:40:39.4	14.811 ± 0.0318	14.561 ± 0.0265	13.817 ± 0.0184	13.384 ± 0.0167	12.976 ± 0.0196
E	1:37:03.4	+15:41:39.2	17.140 ± 0.0386	17.064 ± 0.0251	16.407 ± 0.0200	16.008 ± 0.0160	15.601 ± 0.0206
F	1:37:09.0	+15:41:20.4	18.804 ± 0.1537	17.800 ± 0.0282	16.769 ± 0.0249	16.146 ± 0.0167	15.583 ± 0.0205
G	1:36:57.6	+15:46:22.7	13.934 ± 0.0272	13.756 ± 0.0219	12.991 ± 0.0160	12.555 ± 0.0161	12.155 ± 0.0240
H	1:37:09.0	+15:48:00.6	16.974 ± 0.0434	16.172 ± 0.0249	15.175 ± 0.0157	14.598 ± 0.0170	14.062 ± 0.0194

Table 6.2: Photometric evolution of SN 2013ej. Errors denote 1σ uncertainty.

UBVRI photometry

UT Date (yyyy-mm-dd)	JD 2456000+	Phase[a] (day)	U (mag)	B (mag)	V (mag)	R (mag)	I (mag)	Tel[b]
2013-08-04.82	509.32	12.02	12.026 ± 0.061	12.633 ± 0.020	12.612 ± 0.013	12.434 ± 0.017	12.349 ± 0.018	HCT
2013-08-31.93	536.43	39.13	14.576 ± 0.251	14.208 ± 0.020	13.125 ± 0.011	12.670 ± 0.015	12.436 ± 0.011	HCT
2013-09-29.77	565.27	67.97	16.088 ± 0.027	14.991 ± 0.020	13.569 ± 0.012	13.056 ± 0.016	12.750 ± 0.016	HCT
2013-09-30.72	566.22	68.92	16.207 ± 0.109	14.956 ± 0.020	13.595 ± 0.008	12.992 ± 0.015	12.741 ± 0.016	ST
2013-10-02.87	568.37	71.07	16.223 ± 0.028	15.017 ± 0.020	13.640 ± 0.012	13.053 ± 0.015	12.750 ± 0.017	HCT
2013-10-13.70	579.20	81.90	16.823 ± 0.054	15.291 ± 0.015	13.864 ± 0.010	13.222 ± 0.017	—	ST
2013-10-15.85	581.35	84.05	17.026 ± 0.061	15.365 ± 0.021	13.884 ± 0.012	13.273 ± 0.011	12.978 ± 0.017	ST
2013-10-16.71	582.21	84.91	17.036 ± 0.089	15.406 ± 0.013	13.939 ± 0.010	13.288 ± 0.018	12.986 ± 0.025	ST
2013-10-21.73	587.23	89.93	17.292 ± 0.057	15.611 ± 0.017	14.126 ± 0.017	13.446 ± 0.016	13.147 ± 0.018	ST
2013-10-24.70	590.20	92.90	17.405 ± 0.035	15.743 ± 0.016	14.233 ± 0.021	13.540 ± 0.014	13.253 ± 0.014	ST
2013-10-25.72	591.22	93.92	17.365 ± 0.023	15.732 ± 0.014	14.340 ± 0.008	13.592 ± 0.011	13.322 ± 0.011	DFOT
2013-10-26.74	592.24	94.94	17.442 ± 0.020	15.795 ± 0.014	14.431 ± 0.007	13.672 ± 0.010	13.384 ± 0.011	DFOT

Table 6.2 - continued.

UT Date (yyyy-mm-dd)	JD 2456000+	Phase[a] (day)	U (mag)	B (mag)	V (mag)	R (mag)	I (mag)	Tel[b]
2013-10-27.76	593.26	95.96	17.515 ± 0.033	15.985 ± 0.022	14.453 ± 0.016	13.750 ± 0.016	13.447 ± 0.021	ST
2013-11-09.63	606.13	108.83	18.440 ± 0.039	17.611 ± 0.015	16.108 ± 0.012	15.144 ± 0.015	14.783 ± 0.016	HCT
2013-11-11.72	608.22	110.92	18.655 ± 0.106	17.725 ± 0.020	16.358 ± 0.012	15.357 ± 0.016	14.978 ± 0.016	ST
2013-11-12.67	609.17	111.87	—	17.700 ± 0.021	16.379 ± 0.014	15.358 ± 0.017	15.004 ± 0.014	ST
2013-11-14.65	611.15	113.85	—	17.764 ± 0.031	16.405 ± 0.011	15.402 ± 0.010	15.031 ± 0.013	ST
2013-11-19.69	616.19	118.89	18.515 ± 0.133	17.865 ± 0.023	16.493 ± 0.015	15.480 ± 0.016	15.133 ± 0.019	ST
2013-11-23.69	620.19	122.89	19.144 ± 0.408	17.945 ± 0.021	16.533 ± 0.009	15.529 ± 0.010	15.203 ± 0.011	ST
2013-11-24.62	621.12	123.82	18.973 ± 0.128	17.911 ± 0.019	16.552 ± 0.012	15.544 ± 0.015	15.205 ± 0.016	ST
2013-12-06.72	633.22	135.92	19.292 ± 0.171	18.113 ± 0.028	16.771 ± 0.014	15.719 ± 0.016	15.420 ± 0.017	ST
2013-12-08.73	635.23	137.93	19.286 ± 0.175	18.139 ± 0.018	16.815 ± 0.017	15.766 ± 0.022	15.486 ± 0.024	ST
2013-12-09.69	636.19	138.89	—	18.167 ± 0.022	16.832 ± 0.011	15.779 ± 0.017	15.488 ± 0.017	ST
2013-12-10.61	637.11	139.81	—	18.209 ± 0.034	16.863 ± 0.019	15.796 ± 0.020	15.490 ± 0.022	ST
2013-12-14.74	641.24	143.94	—	18.015 ± 0.093	16.892 ± 0.034	15.856 ± 0.020	15.597 ± 0.023	ST
2013-12-15.63	642.13	144.83	—	18.223 ± 0.041	16.974 ± 0.019	15.914 ± 0.025	15.603 ± 0.026	ST
2013-12-16.70	643.20	145.90	—	18.109 ± 0.053	16.943 ± 0.025	15.903 ± 0.019	15.596 ± 0.126	ST
2013-12-19.61	646.11	148.81	—	18.249 ± 0.043	17.009 ± 0.015	15.932 ± 0.019	15.661 ± 0.023	ST
2013-12-24.62	651.12	153.82	19.474 ± 0.061	18.265 ± 0.027	17.138 ± 0.014	16.003 ± 0.015	15.743 ± 0.016	ST
2013-12-25.66	652.16	154.86	—	18.321 ± 0.016	17.101 ± 0.010	16.012 ± 0.009	15.722 ± 0.012	ST,DFOT
2013-12-28.62	655.12	157.82	19.368 ± 0.058	18.325 ± 0.019	17.161 ± 0.009	16.041 ± 0.015	15.760 ± 0.016	DFOT
2013-12-29.59	656.09	158.79	19.436 ± 0.060	18.315 ± 0.024	17.180 ± 0.011	16.061 ± 0.010	15.791 ± 0.011	DFOT
2014-01-19.62	677.12	179.82	—	18.676 ± 0.025	17.458 ± 0.011	16.370 ± 0.014	16.128 ± 0.015	ST
2014-01-25.62	683.12	185.82	19.703 ± 0.071	18.638 ± 0.013	17.526 ± 0.009	16.424 ± 0.011	16.164 ± 0.012	DFOT
2014-01-30.62	688.12	190.82	19.797 ± 0.596	18.785 ± 0.027	17.602 ± 0.014	16.501 ± 0.013	16.282 ± 0.015	ST
2014-01-31.58	689.08	191.78	—	18.787 ± 0.030	17.618 ± 0.019	16.522 ± 0.017	16.273 ± 0.025	ST
2014-02-02.62	691.12	193.82	—	18.813 ± 0.035	17.623 ± 0.031	16.546 ± 0.020	16.323 ± 0.024	ST
2014-02-17.59	706.09	208.79	—	19.218 ± 0.079	17.814 ± 0.022	16.682 ± 0.012	16.470 ± 0.017	ST

Swift UVOT photometry

UT Date (yyyy/mm/dd)	JD 2456000+	Phase[a] (day)	*uvw2* (mag)	*uvm2* (mag)	*uvw1* (mag)	*uvu* (mag)	*uvb* (mag)	*uvv* (mag)	Tel[b] /Inst
2013-07-30.98	504.48	7.18	12.369 ± 0.040	12.023 ± 0.040	11.711 ± 0.039	—	—	12.689 ± 0.042	Swift
2013-07-31.50	505.00	7.70	12.455 ± 0.040	12.097 ± 0.040	11.755 ± 0.039	—	—	12.614 ± 0.040	Swift
2013-07-31.83	505.33	8.03	12.577 ± 0.035	12.204 ± 0.033	11.814 ± 0.032	—	—	—	Swift
2013-08-03.06	507.56	10.26	13.044 ± 0.037	12.695 ± 0.041	—	11.675 ± 0.029	12.619 ± 0.029	—	Swift
2013-08-03.18	507.68	10.38	13.056 ± 0.035	—	—	—	12.622 ± 0.029	—	Swift
2013-08-04.85	509.35	12.05	13.374 ± 0.040	13.155 ± 0.053	—	11.812 ± 0.029	12.608 ± 0.029	—	Swift
2013-08-04.98	509.48	12.18	13.385 ± 0.037	—	—	—	—	—	Swift
2013-08-07.24	511.74	14.44	13.907 ± 0.041	—	12.948 ± 0.042	—	—	—	Swift
2013-08-07.55	512.05	14.75	13.968 ± 0.050	—	—	—	—	—	Swift
2013-08-08.02	512.52	15.22	14.039 ± 0.052	14.058 ± 0.070	13.131 ± 0.038	12.185 ± 0.031	12.749 ± 0.029	12.477 ± 0.030	Swift
2013-08-08.22	512.72	15.42	14.126 ± 0.045	—	—	12.266 ± 0.029	—	—	Swift
2013-08-09.25	513.75	16.45	14.387 ± 0.055	14.305 ± 0.112	13.379 ± 0.041	12.333 ± 0.029	12.906 ± 0.029	12.535 ± 0.031	Swift
2013-08-09.31	513.81	16.51	—	14.406 ± 0.065	—	—	—	—	Swift
2013-08-11.78	516.28	18.98	15.210 ± 0.118	15.114 ± 0.109	13.907 ± 0.052	12.659 ± 0.029	12.983 ± 0.029	12.581 ± 0.031	Swift
2013-08-13.85	518.35	21.05	15.652 ± 0.082	15.964 ± 0.068	14.446 ± 0.059	12.982 ± 0.031	13.109 ± 0.029	12.599 ± 0.032	Swift
2013-08-15.00	520.50	23.20	16.209 ± 0.090	—	14.905 ± 0.069	13.308 ± 0.033	13.221 ± 0.030	12.573 ± 0.032	Swift
2013-08-17.65	522.15	24.85	16.588 ± 0.098	17.109 ± 0.195	15.201 ± 0.072	13.602 ± 0.035	13.293 ± 0.030	12.656 ± 0.032	Swift
2013-08-19.73	524.23	26.93	16.824 ± 0.105	17.554 ± 0.221	15.493 ± 0.076	13.964 ± 0.039	13.476 ± 0.030	12.692 ± 0.032	Swift
2013-08-22.54	527.04	29.74	17.245 ± 0.120	18.047 ± 0.250	15.890 ± 0.075	14.338 ± 0.045	13.663 ± 0.032	12.816 ± 0.033	Swift
2013-08-23.14	527.64	30.34	17.170 ± 0.117	—	15.866 ± 0.083	14.366 ± 0.045	13.627 ± 0.031	12.892 ± 0.034	Swift
2013-08-27.74	532.24	34.94	17.746 ± 0.146	18.569 ± 0.214	16.356 ± 0.095	14.844 ± 0.058	13.915 ± 0.033	12.965 ± 0.034	Swift
2013-09-06.16	541.66	44.36	18.133 ± 0.124	19.137 ± 0.190	16.793 ± 0.084	15.573 ± 0.067	—	—	Swift
2013-09-06.41	541.91	44.61	—	—	—	15.674 ± 0.087	14.367 ± 0.036	13.231 ± 0.035	Swift
2013-09-16.71	552.21	54.91	18.687 ± 0.158	19.486 ± 0.236	17.292 ± 0.096	16.229 ± 0.090	14.750 ± 0.039	13.470 ± 0.038	Swift
2013-09-26.45	561.95	64.65	18.793 ± 0.166	—	17.562 ± 0.123	16.585 ± 0.128	14.922 ± 0.042	13.604 ± 0.039	Swift
2013-10-06.88	572.38	75.08	19.241 ± 0.231	19.883 ± 0.333	17.919 ± 0.133	17.055 ± 0.094	—	—	Swift
2013-10-16.77	582.27	84.97	19.294 ± 0.247	—	18.127 ± 0.170	17.286 ± 0.164	15.464 ± 0.055	14.029 ± 0.045	Swift
2013-10-26.95	592.45	95.15	—	—	18.248 ± 0.190	17.514 ± 0.171	—	—	Swift
2013-11-06.16	602.66	105.36	—	—	—	18.774 ± 0.304	—	—	Swift
2013-11-13.21	609.71	112.41	—	—	19.523 ± 0.351	19.058 ± 0.306	—	—	Swift

Table 6.2 - continued.

UT Date (yyyy/mm/dd)	JD 2456000+	Phase[a] (day)	$uvw2$ (mag)	$uvm2$ (mag)	$uvw1$ (mag)	uvu (mag)	uvb (mag)	uvv (mag)	Tel[b] /Inst
2013-11-13.68	610.18	112.88	—	—	—	18.816 ± 0.263	17.974 ± 0.210	16.512 ± 0.148	Swift
2013-11-20.43	616.93	119.63	—	—	—	18.977 ± 0.214	17.889 ± 0.090	16.718 ± 0.080	Swift
2013-11-25.40	621.90	124.60	—	—	—	19.162 ± 0.323	—	—	Swift
2013-11-30.43	626.93	129.63	—	—	19.726 ± 0.313	19.342 ± 0.280	18.155 ± 0.101	16.834 ± 0.082	Swift
2013-12-09.75	636.25	138.95	—	—	19.807 ± 0.327	19.343 ± 0.274	18.196 ± 0.102	16.928 ± 0.085	Swift

[a] with reference to the explosion epoch JD 2456497.30

[b] ST : 104-cm Sampurnanand Telescope, ARIES, India; DFOT : 130-cm Devasthal fast optical telescope, ARIES, India; HCT: 2m Himalyan Chandra Telescope, Hanle, India; Swift: *Swift* UVOT

Note: Data observed within 5 Hrs, are represented under single epoch observation.

Roming et al., 2005) in six bands (viz. uvw2, uvm2, uvw1, uvu, uvb, uvv) on the Swift spacecraft (Gehrels et al., 2004). The UV photometry was obtained from the Swift Optical/Ultraviolet Supernova Archive[1] (SOUSA; Brown et al., 2014). The reduction is based on that of Brown et al. (2009), including subtraction of the host galaxy count rates and uses the revised UV zeropoints and time-dependent sensitivity from Breeveld et al. (2011). The UVOT photometry is listed in Table. 6.2. The first month of UVOT photometry was previously presented by Valenti et al. (2014).

6.2.2 Spectroscopy

Spectroscopic observations have been carried out at 10 phases during 12 to 125d. Out of these, nine epochs of low resolution spectra are obtained from Himalaya Faint Object Spectrograph and Camera (HFOSC) mounted on 2.0m HCT. Spectroscopy on the HCT/HFOSC was done using a slit width of 1.92 arcsec, and grisms with resolution $\lambda/\Delta\lambda = 1330$ for Gr7 and 2190 for Gr8, and bandwidth coverage of $0.38 - 0.64\ \mu m$ and $0.58 - 0.84\ \mu m$ respectively. One high resolution spectrum is obtained from the ARC Echelle Spectrograph (ARCES) mounted on 3.5m ARC telescope located at Apache Point Observatory (APO). ARCES is a high resolution cross-dispersion echelle spectrograph, the spectrum is recorded in 107 echelle orders covering a wavelength range of $\lambda \sim 0.32$-1.00μm, at resolution of $R \sim 31500$ (Wang et al., 2003b). Summary of spectroscopic observations is given in Table. 6.3.

Spectroscopic data reduction was done under the `IRAF` environment. Standard reduction procedures are followed for bias subtraction and flat fielding. Cosmic ray rejections are done using a Laplacian kernel detection algorithm for spectra, L.A.Cosmic (van Dokkum, 2001). One dimensional low resolution spectra were extracted using the APALL task. Wavelength calibration was done using the IDENTIFY task applied on FeNe and FeAr (for HCT) arc spectra taken during observation. Wavelength calibration was crosschecked against the [O I] λ5577 sky line in the sky spectrum, and it was found to lie within 0.3 to 4.5 Å of the actual value. Spectra were flux calibrated using STANDARD, SENSFUNC and CALIBRATE tasks in `IRAF`. For flux calibration, spectrophotometric standards were used which were observed

[1] http://swift.gsfc.nasa.gov/docs/swift/sne/swift_sn.html

Table 6.3: Summary of spectroscopic observations of SN 2013ej. The spectral observations are made at 10 phases during 12d to 125d.

UT Date (yy/mm/dd.dd)	JD 2456000+	Phase[a] (days)	Telescope[c]	Range[b] μm	Exposure (s)
2013-08-04.86	509.36	12.1	HCT	0.38-0.68	900
2013-08-27.76	532.26	35.0	HCT	0.38-0.68	1200
			HCT	0.58-0.84	1200
2013-09-03.90	539.40	42.1	HCT	0.38-0.68	1500
			HCT	0.58-0.84	1500
2013-09-29.78	565.28	68.0	HCT	0.38-0.68	1800
			HCT	0.58-0.84	2400
2013-10-02.89	568.39	71.1	HCT	0.38-0.68	1500
			HCT	0.58-0.84	1500
2013-10-11.28	576.78	79.5	APO	0.32-1.00	1200
2013-10-27.87	593.37	96.1	HCT	0.38-0.68	2400
2013-10-28.79	594.29	97.0	HCT	0.58-0.84	2400
2013-11-09.65	606.15	108.9	HCT	0.38-0.68	2100
			HCT	0.58-0.84	3900
2013-11-25.75	622.25	125.0	HCT	0.38-0.68	2400
			HCT	0.58-0.84	2400

[a] With reference to the adopted explosion time JD 2456497.30
[b] For transmission $\geq$50%
[c] HCT : HFOSC on 2 m Himalyan Chandra Telescope, India; APO : Echelle spectrograph on 3.5 m ARC telescope at Apache Point Observatory, U.S.
[d] At 0.6 μm

on the same nights as the SN spectra were recorded. All spectra were tied to absolute flux scale using the observed flux from *UBVRI* photometry of SN. To perform the tying, individual spectrum is multiplied by a wavelength dependent polynomial, which is convolved with *UBVRI* filters and then the polynomial is tuned to match the convolved flux with observations. The one dimensional calibrated spectra were corrected for heliocentric velocity of host galaxy (658 $\mathrm{km\,s^{-1}}$; Table 6.1) using DOPCOR task.

6.3 Distance and Extinction

We adopt a distance of 9.57 ± 0.70 Mpc which is a mean value of four different distance estimation techniques used for NGC 0628, viz., 9.91 Mpc applying Standard Candle Method (SCM) to SN 2003gd by Olivares et al. (2010); 10.19 Mpc using the Tully-Fisher method (`HyperLeda`[1]); 9.59 Mpc using brightest supergiant distance estimate by Hendry et al. (2005); and planetary nebula luminosity function distance 8.59 Mpc (Herrmann et al., 2008). Although for each of these methods number of distance estimates exists in literature, we tried to select only most recent estimates. Richmond (2014) estimated a distance of 9.1 ± 0.4 Mpc by applying Expanding Photosphere Method (EPM) to SN 2013ej, which we find consistent to that we adopted.

One of the most reliable and well accepted method for SNe line-of-sight reddening estimation is using the Na I D absorption feature. The equivalent width (EW) of Na I D doublet ($\lambda\lambda$ 5890, 5896) is found to be correlated with the reddening, estimated from the tail color curves of type Ia SNe (Barbon et al., 1990; Turatto et al., 2003). However, Poznanski et al. (2011) suggested that although Na I D EW is weakly correlated with $E(B-V)$, the EWs estimated from low resolution spectra is a bad estimator of $E(B-V)$. Poznanski et al. (2012b) used a larger sample of data and presented a more precise and rather different functional form of the correlation than that was derived earlier. Our high resolution echelle spectra at 79.5d provided an excellent opportunity to investigate the line-of-sight extinction.

The resolved Na I D doublet for Milky-way is clearly visible in the high-resolution spectra (recorded on 79.5d) as shown in Fig.6.1. Whereas no impression of Na I D for NGC 0628 is detected at the expected redshifted position relative to Milky-way. This indicates that the reddening due to host is negligible, only Galactic reddening will contribute to the total line of sight extinction. A similar conclusion has also been inferred by Valenti et al. (2014) from their high resolution spectra obtained at 31d. Thus, we adopt a total $E(B-V) = 0.060 \pm 0.001$ mag, which is entirely due to Galactic reddening (Schlafly & Finkbeiner, 2011) and assuming total-to-selective extinction at V band as $R_V = 3.1$, it translates into $A_V = 0.185 \pm 0.004$ mag.

[1] http://leda.univ-lyon1.fr/

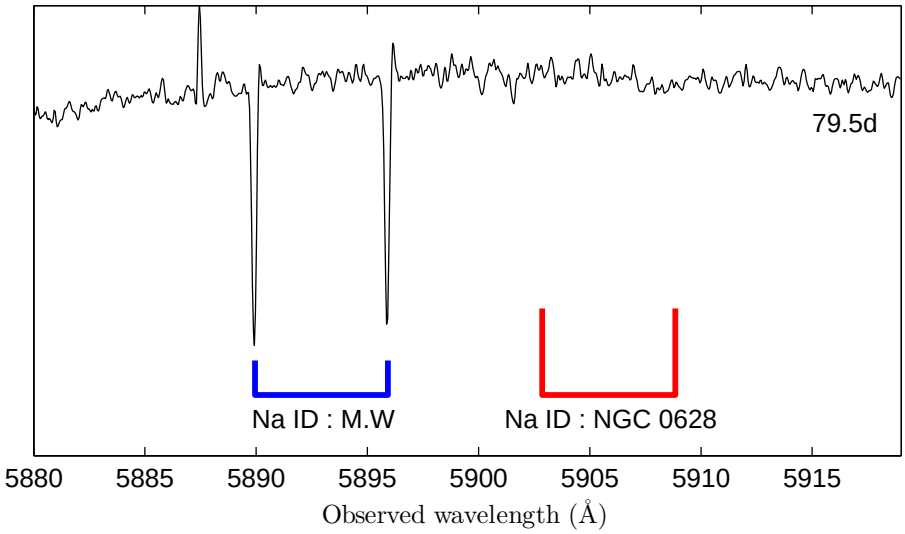

Figure 6.1: Echelle spectra at 79.5d showing the Na I D doublet for Milky-way while no impression for NGC 0628 is detected.

6.4 Light curve

6.4.1 Light curve evolution and comparison

The optical light curves of SN 2013ej in *UBVRI* and six UVOT bands are shown in Fig. 6.1. *UBVRI* photometric observations were done at 38 phases during 12 to 209d (from plateau to nebular phase). The duration of plateau phase is sparsely covered, while denser follow-up initiated after 68d. The plateau phase lasted until $\sim$ 85d with an average decline rate of 6.60, 3.57, 1.74, 1.07 and 0.74 mag (100 d)$^{-1}$ in *UBVRI* bands respectively. Since 95d, the light curve declines very fast until 115d, after which it settles to a relatively slow declining nebular phase. During this phase the decline rates for *UBVRI* bands are 0.98, 1.22, 1.53, 1.42 and 1.55 mag (100 d)$^{-1}$ respectively.

SN 2013ej has been also observed by *Swift* UVOT at 35 phases during 7 to 139d. The UVOT *UV* band light curves declines steeply during the first 30d at a rate of 0.182, 0.213, 0.262 mag d^{-1} in *uvw1, uvw2* and *uvm2* bands respectively, thereafter settling into a slow declining phase until it reaches the end of plateau.

SN 2013ej experience a steeper plateau decline than that observed for SN 1999em

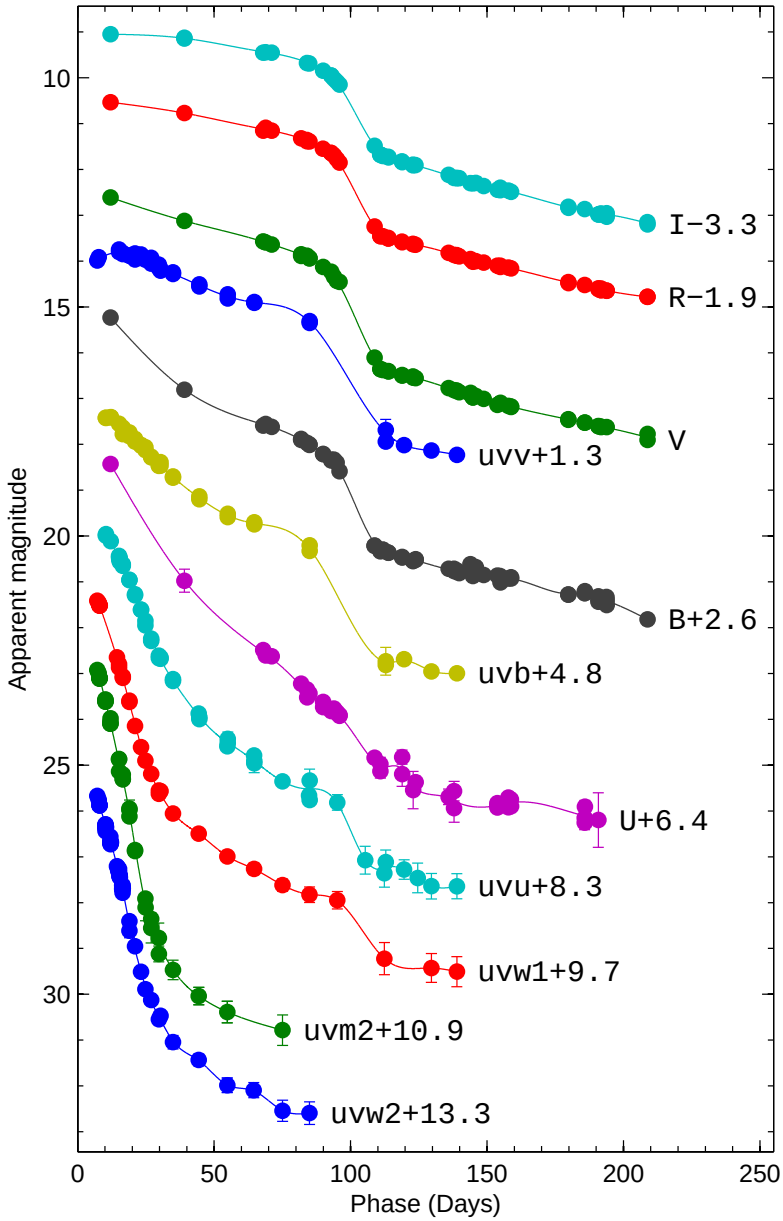

Figure 6.1: The photometric light curves in Johnson-Cousins *UBVRI* and *Swift* UVOT bands. The light curves are vertically shifted for clarity. The line joining the data points of light curves is for visualization purpose only.

(Leonard et al., 2002a), SN 1999gi (Leonard et al., 2002b), SN 2012aw (Bose et al., 2013) and SN 2013ab (Bose et al., 2015a). For example, SN 2012aw plateau declines at a rate of 5.60, 1.74, 0.55 mag (100 d)$^{-1}$ in UBV-bands, similarly for SN 2013ab decline rates in $UBVRI$ are 7.60, 2.72, 0.92, 0.59 and 0.30 mag (100 d)$^{-1}$ and 0.169, 0.236, 0.257 mag d^{-1} in UVOT *uvw1, uvw2* and *uvm2* bands (during first 30d).

The absolute V-band (M_V) light curve of SN 2013ej is plotted in Fig. 6.2 and is compared with other well studied type II SNe (after correcting for extinction and distance). In Table 6.1 we list the plateau slope of all compared type II events. The comparison shows that the decline rate of SN 2013ej during this phase is highest (1.74 mag (100 d)$^{-1}$) among most other SNe, except three type IIL SNe 1980K, 2000dc and 2013by, where SN 1980 is among the very first observed prototypical type IIL event. The early plateau ($<$ 40d) light curve of SN 2013ej is identical to SN 2009bw. However, unlike most other IIP SNe, e.g. 2009bw and 2013ab, which becomes flatter during late plateau, SN 2013ej continues to decline almost at a steady rate until the end of plateau ($\sim$ 85d). The mid-plateau $M_V = -14.7$ mag for SN 2013ej, which places it in the class of normal luminous type II events. SN 2013ej is comparable with fast declining and short plateau SNe in the sample of Anderson et al. (2014b). Following the plateau phase, V-band light drops very fast to reach slow declining nebular phase (1.53 mag (100 d)$^{-1}$), which is powered by the radioactive decay of ^{56}Co to ^{56}Fe. The fall of M_V during the plateau nebular transition is $\sim$ 2.4 mag, which is on the higher side of the compared events. The closest comparison is SNe 2009bw and 2012A which exhibits a drop of $\sim$2.4 mag and $\sim$2.5 mag respectively. This also indicates low amount of ^{56}Ni mass synthesized during the explosion which we shall further discuss in the next section.

Swift UVOT absolute magnitude light curves of SN 2013ej are shown in Fig. 6.3 and compared with other well observed type II SNe. The sample is selected in such a way that SNe have at least a month of observations. Most SNe are not followed for more than a month by *Swift*, mainly because of the large distances or high extinction values. However, both these factors work in favor of SN 2013ej making it possible to have about four months of observations. Moreover, the location of the SN being in the outskirt of a spiral arm of NGC 0628, the background flux contamination is also

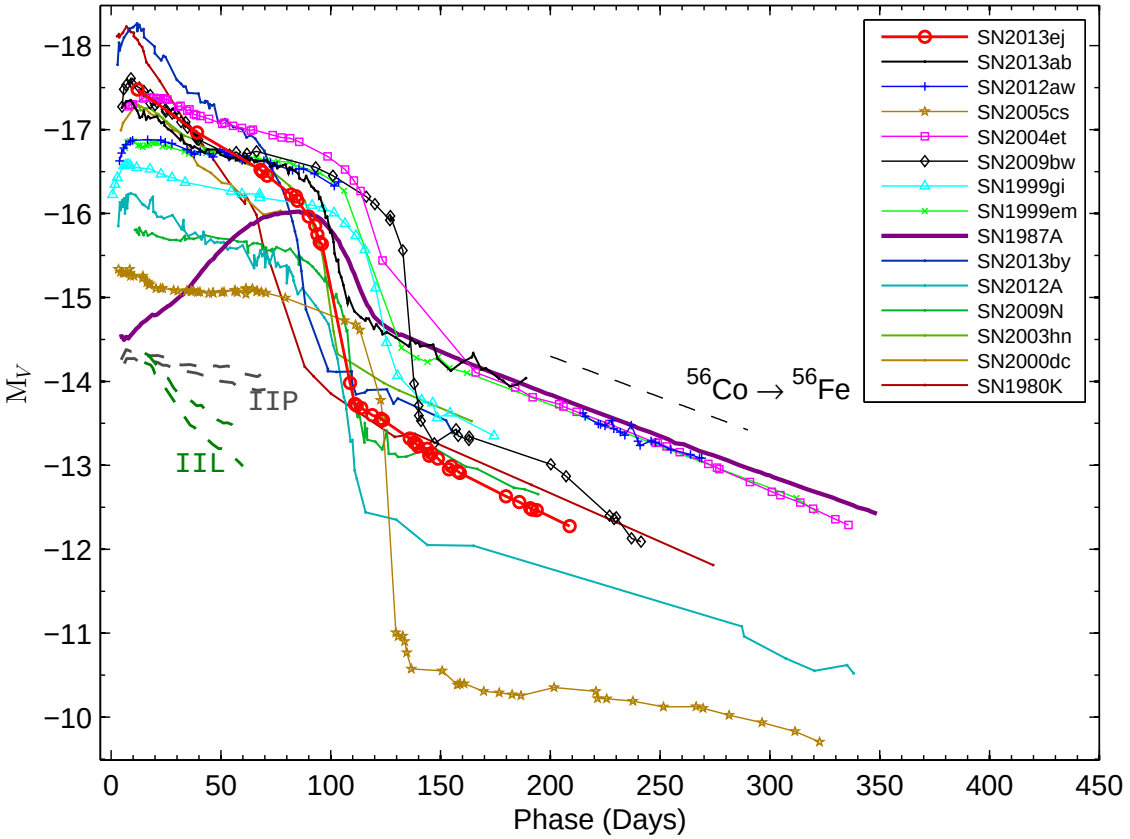

Figure 6.2: The M_V light curve of SN 2013ej is compared with other type II SNe. The exponential decline of the tail light curve following the radioactive decay law for ^{56}Co→^{56}Fe is shown with a dashed line. On the bottom left side, pair of dotted lines in each gray and green colors represent the slope range for type IIP and IIL SNe templates as given by Faran et al. (2014). The adopted explosion time in JD-2400000, distance in Mpc, $E(B-V)$ in mag and the reference for observed V-band magnitude, respectively, are : SN 1980K – 44540.5, 5.5, 0.30; Barbon et al. (1982), NED database; SN 1987A – 46849.8, 0.05, 0.16; Hamuy & Suntzeff (1990); SN 1999em – 51475.6, 11.7, 0.10; Elmhamdi et al. (2003b); Leonard et al. (2002c); SN 1999gi – 51522.3, 13.0, 0.21; Leonard et al. (2002b); SN 2000dc – 51762.4, 49.0, 0.07; Faran et al. (2014), NED database; SN 2003hn – 52866.5, 17.0, 0.19; Anderson et al. (2014b); Krisciunas et al. (2009); SN 2004et – 53270.5, 5.4, 0.41; Sahu et al. (2006); SN 2005cs – 53549.0, 7.8, 0.11; Pastorello et al. (2009); SN 2009N – 54848.1, 21.6, 0.13; Takáts et al. (2014); SN 2009bw – 54916.5, 20.2, 0.31; Inserra et al. (2012b); SN 2012A – 55933.5, 9.8, 0.04; Tomasella et al. (2013); SN 2012aw – 56002.6, 9.9, 0.07; Bose et al. (2013); SN 2013ab – 56340.0, 24.0, 0.04; Bose et al. (2015a); SN 2013by – 56404.0, 14.8, 0.19; Valenti et al. (2015).

Table 6.1: Parameters estimated from V band light cruve

SN Name	Plateau slope[a] mag (100 d)$^{-1}$	Transition drop[b] mag	Transition time[c] days
SN1980K	3.63 ± 0.04	2.0±0.04	37 ± 5
SN2000dc	2.56 ± 0.06[i]	–	–
SN2013by	2.01 ± 0.02	2.2±0.03	19 ± 5
SN 2013ej	1.74 ± 0.08	2.4±0.02	21 ± 3
SN2003hn	1.41 ± 0.04	2.0±0.04	19 ± 4
SN2012A	1.12 ± 0.03	2.5±0.02	23 ± 4
SN2009bw	0.93 ± 0.04	2.4±0.03	14 ± 3
SN2004et	0.73 ± 0.02	2.1±0.04	27 ± 6
SN2013ab	0.54 ± 0.02	1.7±0.02	25 ± 2
SN2012aw	0.51 ± 0.02	–	–
SN1999gi	0.47 ± 0.02	2.0±0.02	29 ± 3
SN2005cs	0.44 ± 0.03	4.0±0.03	24 ± 3
SN2009N	0.36 ± 0.03	2.0±0.04	26 ± 3
SN1999em	0.31 ± 0.02	1.9±0.02	28 ± 4

Note: Objects are sorted in order of plateau slope.
[a] Plateau slope during the linear decline phase, starting after first minima until plateau end.
[b] Drop in magnitude during the plateau to nebular transition.
[c] Duration of plateau to nebular transition.
[i] Slope is calculated up to the available range of data, as plateau end is not observed.

negligible. The comparison shows that the SN 2013ej UV light curves are identical to SN 2012aw. SN 2013ej also shows a similar UV plateau trend as observed in SN 2012aw (Bayless et al., 2013), which is although expected but rarely detected for IIP/L SNe.

Broadband color provides important information to study the temporal evolution of SN envelope. In Fig. 6.4, we plot the intrinsic colors *U-B, B-V, V-R* and *V-I* for SN 2013ej and compare its evolution with type II-pec SN 1987A, and type IIP SNe 1999em, 2004et, 2012aw and 2013ab. All the colors show generic signature of fast cooling ejecta until the end of plateau ($\sim$ 110d). With the start of the nebular phase it continues to cool at a much slower rate in *V-I* and *V-R* colors, whereas

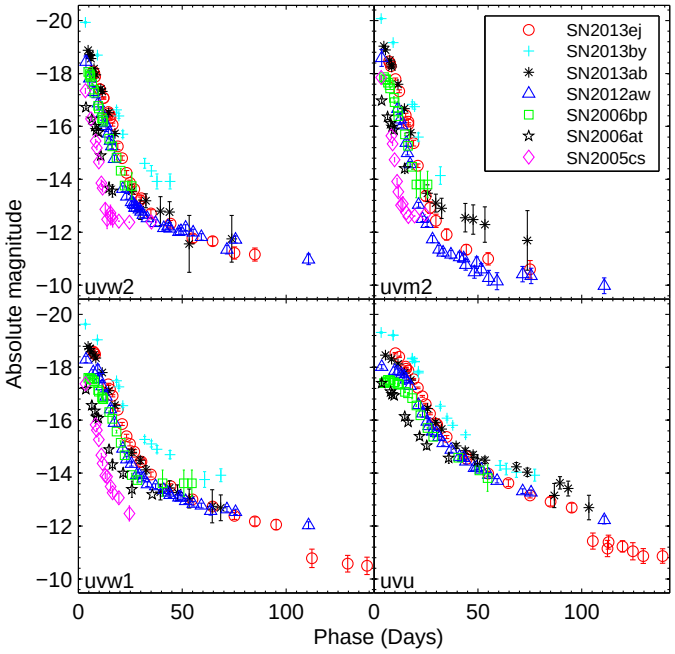

Figure 6.3: Comparison of the *Swift* UVOT UV absolute light curves of SN 2013ej, with other well observed II SNe from UVOT. For the compared SNe, references for UVOT data, extinction and distance are: SN 2005cs – Brown et al. (2009); Pastorello et al. (2009), SN 2006at – Brown et al. (2009); Distance 65 Mpc; $E(B-V) = 0.031$ mag (only Galactic reddening Schlafly & Finkbeiner, 2011), SN 2006bp – Dessart et al. (2008), SN 2012aw – Bayless et al. (2013); Bose et al. (2013), SN 2013ab – Bose et al. (2015a), SN 2013by – Brown et al. (2014); Valenti et al. (2015). Some late data points for SN 2013ab with large errors has been omitted from the plot.

U-*V* and *B*-*V* shows a bluer trend. This is because, as the SN enters the nebular phase, the ejecta become depleted of free electrons, thereby making the envelope optically thin, and so unable to thermalize the photons from radioactive decay of ^{56}Co to ^{56}Fe.

6.4.2 Bolometric light-curve

We compute the pseudo-bolometric luminosities following the method described in Bose et al. (2013); which include SED integration over the semi-deconvolved photometric fluxes after correcting for extinction and distance. Supernova bolomet-

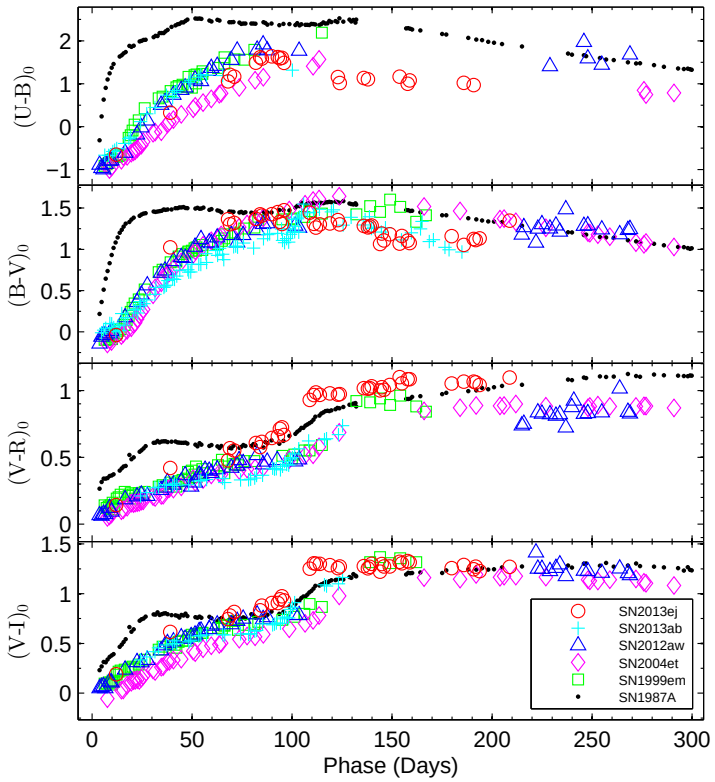

Figure 6.4: The intrinsic colors evolution of SN 2013ej is compared with other well-studied type IIP SNe 1987A, 1999em, 2004et, 2012aw and 2013ab. The reference for the data is same as in Fig. 6.2.

ric luminosities during early phases ($\leq$ 30d) are dominated by ultraviolet fluxes, while after mid-plateau ($\sim$ 50d) UV contribution becomes insignificant as compared to optical counterpart (e.g., as seen in SNe 2012aw, 2013ab; Bose et al., 2013, 2015a). Similarly, during late phases $>$ 100d NIR becomes dominant over optical fluxes. However, during most of the light curve evolution, optical fluxes still provide significant contribution. We compute pseudo-bolometric luminosities in the wavelength range of U to I band (3335-8750Å). We also computed UV-optical pseudo-bolometric light curve with wavelength starting from *uvw2* band (wavelength range of 1606-8750Å). The UV contribution enhances the luminosity significantly during early phases, whereas it is almost negligible after mid-plateau.

In Fig. 6.5, we plot pseudo bolometric light curve for SN 2013ej and compare it with other SNe light curves computed using the same technique. We also include UV-

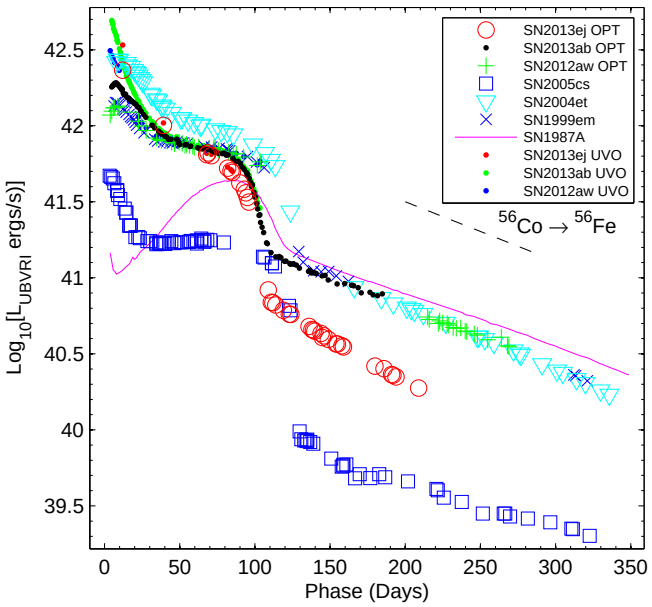

Figure 6.5: The *UBVRI* bolometric light-curve of SN 2013ej is compared with other well studied supernovae. Light curves with added UVOT UV contributions are also shown for SNe 2013ej, 2013ab and 2012aw (labeled as UVO). The adopted values of distances, reddening and explosion time are same as in Fig. 6.2. The exponential decline of the tail light curve following the radioactive decay law is shown with a dashed line.

optical bolometric light curve for SNe 2012aw and 2013ab along with SN 2013ej for comparison. Although the UV-optical light curve is initially brighter than the optical light curve, they completely coincide by the end of plateau phase (85d). It is evident from the comparison that SN 2013ej experienced a steep decline during the plateau phase, but with a much shorter duration. This is consistent with the anti-correlation observed between plateau slope and duration for type II SNe (Anderson et al., 2014b; Blinnikov & Bartunov, 1993). The UV-optical bolometric light decreases by 0.83 dex during plateau phase (from 12 to 85d), followed by an even faster drop by 0.76 dex in a short duration of 21 days (from 90 to 111d). Thereafter, the SN settles in a slow declining nebular phase. The tail luminosities are significantly lower than other normal luminosity IIP events, e.g., SN 2013ej luminosities are lower by ~ 0.5 dex (at 200d) than that of type II SNe 1987A, 1999em, 2004et and 2012aw, but higher than subluminous events like SN 2005cs. Another noticeable dissimilarity of

the tail light curve is its high decline rate. SN 2013ej tail luminosity declines at a rate of 0.55 dex 100 d^{-1}, which is much higher than that expected from radioactive decay of ^{56}Co to ^{56}Fe. This is possibly because of inefficient gamma-ray trapping in the ejecta, and thus incomplete thermalization of the photons. We shall further explore this in §6.7 in context of modeling the light curve.

6.4.3 Mass of nickel

During the explosive nucleosynthesis of silicon and oxygen, at the time of shock-breakout in CCSNe, radioactive ^{56}Ni is produced. The nebular-phase light-curve is mainly powered by the radioactive decay of ^{56}Ni to ^{56}Co and ^{56}Co to ^{56}Fe with half-life times of 6.1d and 77.1d respectively emitting γ-rays and positrons. Thus the tail luminosity will be proportional to the amount of radioactive ^{56}Ni synthesized at the time of explosion. We determine the mass of ^{56}Ni using following two methods.

For SN 1987A, one of the most well studied and well observed event, the mass of ^{56}Ni produced in the explosion has been estimated quite accurately, to be 0.075 ± 0.005 $M_\odot$ (Arnett, 1996). By comparing the tail luminosities of SN 2013ej and SN 1987A at similar phases, it is possible to estimate the ^{56}Ni mass for SN 2013ej. In principle true bolometric luminosities (including UV, optical and IR) are to be used for this purpose, which are available for SN 1987A, whereas for SN 2013ej we have only UV and optical observations. Thus, in order to have uniformity in comparison, we used only the *UBVRI* bolometric luminosities for both SNe and computed using the same method and wavelength range. We estimate the tail *UBVRI* luminosity at 175d, by making a linear fit over 155 to 195d, to be $2.90 \pm 0.43 \times 10^{40}$ erg s^{-1}. Likewise, SN 1987A luminosity is estimated to be $9.60 \pm 0.06 \times 10^{40}$ erg s^{-1} at similar phase. Thus, the ratio of SN 2013ej to SN 1987A luminosity is 0.302 ± 0.044, which corresponds to a ^{56}Ni mass of $0.023 \pm 0.003 M_\odot$ for SN 2013ej.

Assuming the γ-photons emitted from radioactive decay of ^{56}Co thermalize the ejecta, ^{56}Ni mass can be independently estimated from the tail luminosity as described by Hamuy (2003).

$$M_{\rm Ni} = 7.866 \times 10^{-44} \times L_t \exp\left[\frac{(t_t - t_0)/(1+z) - 6.1}{111.26}\right] M_\odot$$

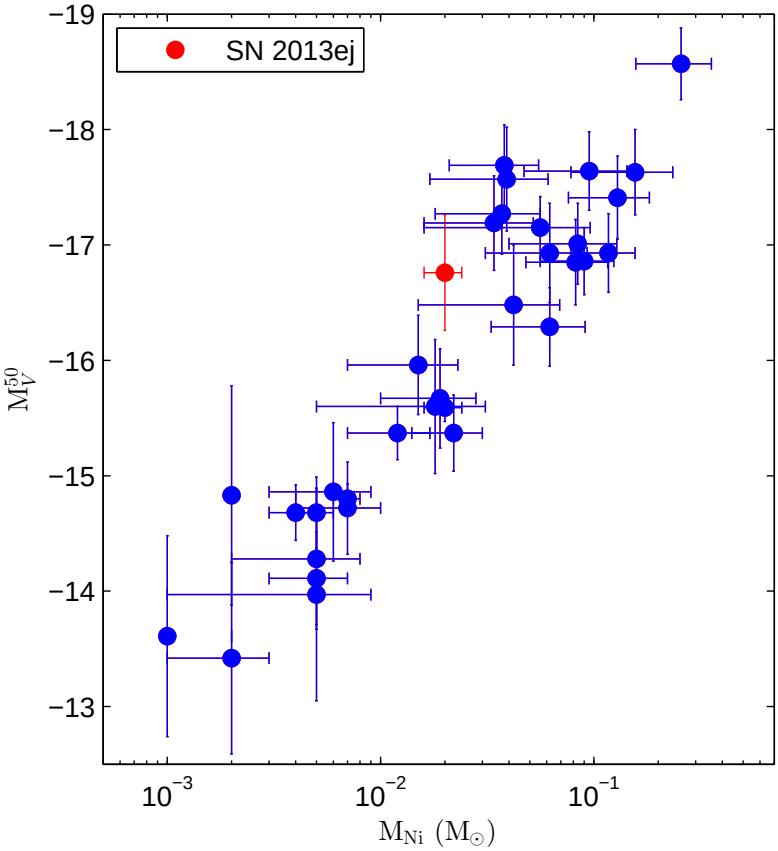

Figure 6.6: The plot of absolute V band magnitude at 50 day versus ^{56}Ni mass for 34 type II SNe. Data taken from Hamuy (2003) and Spiro et al. (2014). The position of SN 2013ej on the correlation is shown with filled red circle.

where t_0 is the explosion time, 6.1d is the half-life time of ^{56}Ni and 111.26d is the e-folding time of the ^{56}Co decay. We compute tail luminosity L_t at 6 epochs within 153 to 185d from the V band data corrected for distance, extinction and bolometric correction factor of 0.26 ± 0.06 mag during nebular phase (Hamuy, 2003). The weighted mean value of L_t is found to be $5.45 \pm 0.35 \times 10^{40}$ erg s^{-1}corresponding to mean phase of 170d. This tail luminosity corresponds to a value of $M_{Ni} = 0.019 \pm 0.002 M_\odot$.

We take the weighted mean of the estimated values from above two methods, and adopt a ^{56}Ni mass of $0.020 \pm 0.002 M_\odot$ for SN 2013ej.

Hamuy (2003) found a strong correlation between the ^{56}Ni mass and the mid

plateau (at 50d) V band absolute magnitude for type II SNe and this correlation was further confirmed by Spiro et al. (2014) specifically for low luminous events. Fig. 6.6 shows the correlation of mid plateau M_V versus ^{56}Ni mass for 34 events, including SN 2013ej. The SN lies within the scatter relation, but towards the lower mass range of ^{56}Ni than where most of the events cluster around (top right).

6.5 Optical spectra

6.5.1 Key spectral features

The spectroscopic evolution of SN 2013ej is presented in Fig. 6.1. Preliminary identifications of spectral features has been done as per previously studied type IIP SNe (e.g., Bose et al., 2013; Leonard et al., 2002c). The spectrum at 12d shows broad Hα, Hβ and He I features on top of a hot blue continuum. The 35d spectrum shows a relatively flat continuum with well developed features of Hα, Hβ, Fe II along with blends of other heavier species Ti II and Ba II. He I line is no longer detectable, instead Na I D features start to appear at similar location. The spectra from 35 to 80d represent the cooler photospheric phase, where the photosphere starts to penetrate deeper layers rich in heavier elements like Fe II and Sc II. During these phases we see the emergence and development of various other heavy atomic lines and their blends like Ti II, Ba II, Na I D and Ca II. Fig. 6.2 shows the comparison of three plateau phase spectra, viz. 12, 35 and 68d with other well studied type IIP SNe at similar epochs. The comparison shows the spectra of SN 2013ej is broadly identical to others in terms of observable line features and their evolution. A notable feature during early spectrum (12d) is the dip on the bluer wing of Hα profiles near 6170 Å which can be attributed as the Si II feature. Leonard et al. (2013) also identified this feature at $\sim$ 9d spectra of SN 2013ej however, due to unlikeliness of such a strong Si II feature at such early epochs, a possiblity of non-standard red supergiant envelope or CSM interaction was suggested. However, such dips are detectable in 35 and 42d spectra, which we identify as Si II feature in SYNOW modeling.

The spectra at 96 and 97d represents the plateau-nebular transition phase.

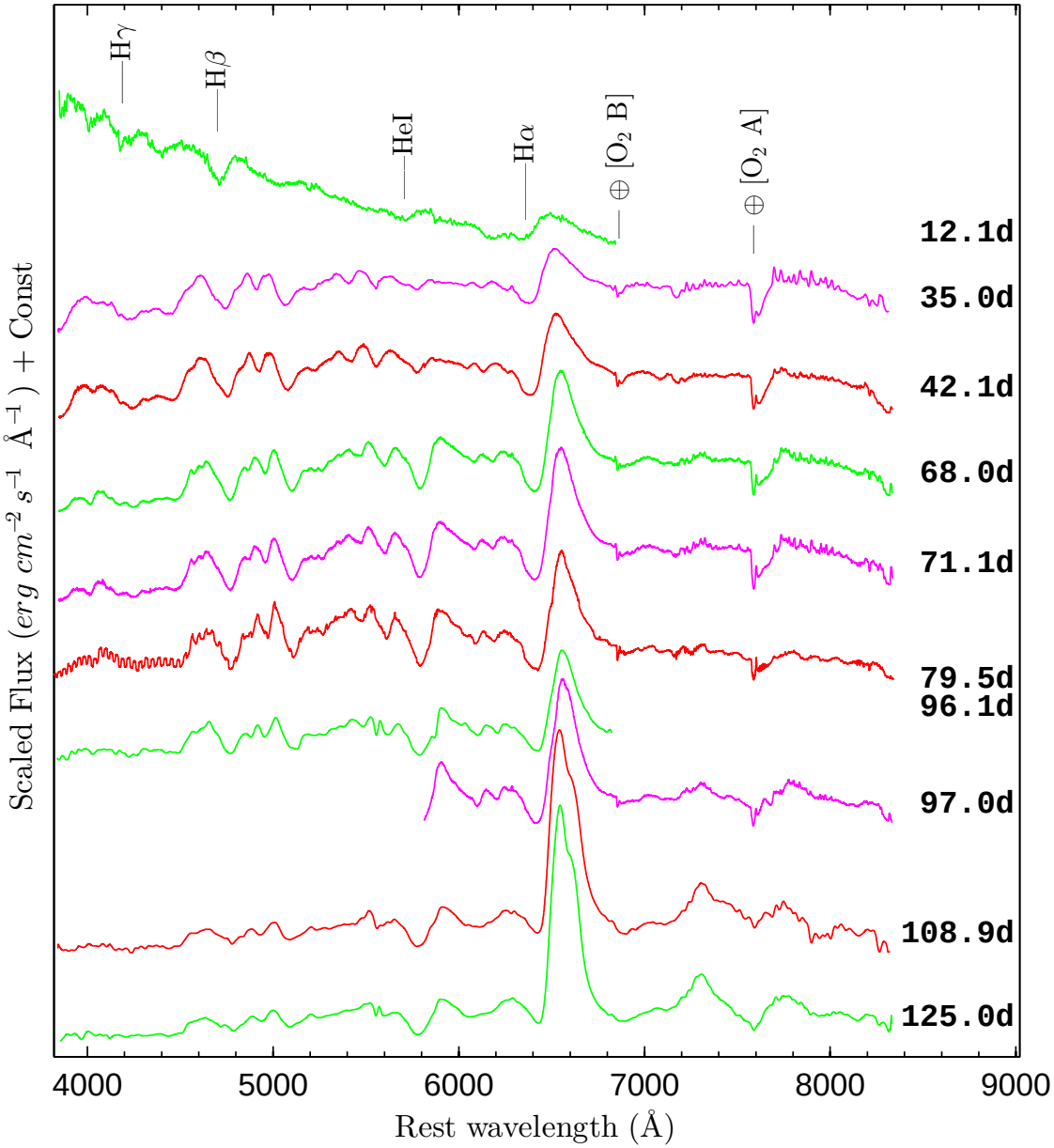

Figure 6.1: The redshift corrected spectra of SN 2013ej are plotted for 10 phases during 12d to 125d. The prominent P-Cygni profiles of hydrogen (Hα, Hβ, Hγ) and helium (He I λ5876) are marked. The telluric absorption features of O_2 are marked with $\oplus$, symbol. Portion of spectra in extreme blue or red ends have low SNR. Individual spectra with with overall low SNR has been binned for better visualization.

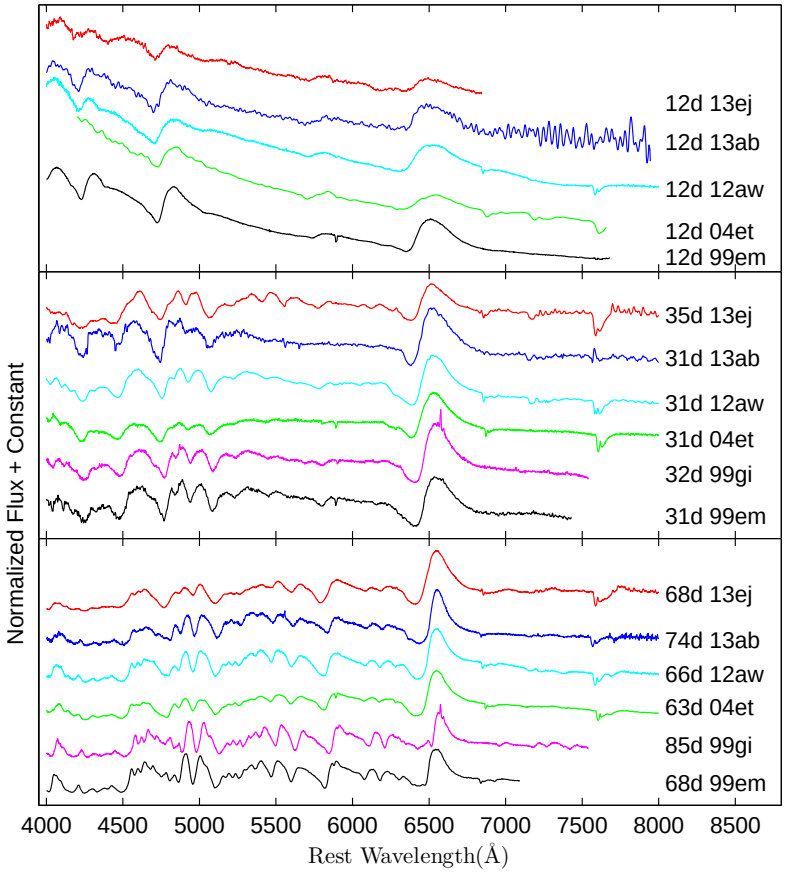

Figure 6.2: Comparison of early (12d) and plateau (35d, 68d) phase spectra of SN 2013ej with other well-studied type IIP SNe 1999em (Leonard et al., 2002c), 1999gi (Leonard et al., 2002b), 2004et (Maguire et al., 2010; Sahu et al., 2006), 2012aw (Bose et al., 2013) and 2013ab (Bose et al., 2015a). All comparison spectra are corrected for extinction and redshift (adopted values are same as in Fig. 6.2).

Thereafter, spectra at 109 and 125d represents the nebular phase, where the ejecta has become optically thin. These spectra shows the emergence of some emission features from forbidden lines of [O I] $\lambda\lambda$ 6300, 6364 and [Ca II] $\lambda\lambda$ 7291, 7324Å, as well as previously evolved permitted lines of H I, and the Na I λ5893 doublet (see Fig. 6.3).

Gutiérrez et al. (2014) found correlations between Hα absorption to emission strengths and light curve parameters, i.e. plateau slope and duration of optically thick phase. Following their selection criteria for choosing phase of SN spectra,

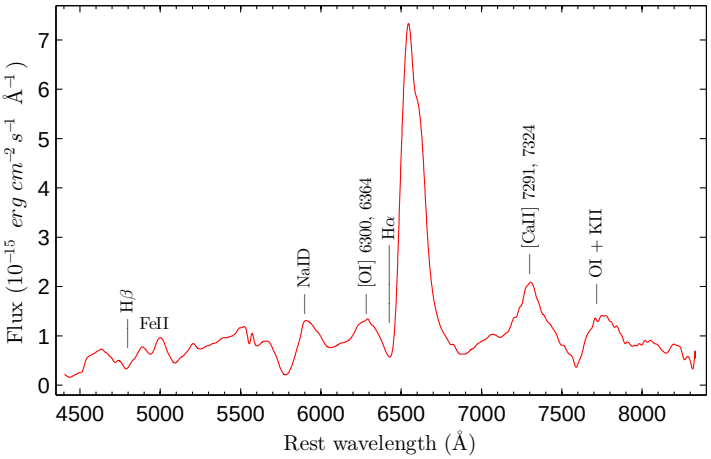

Figure 6.3: The nebular phase spectrum of SN 2013ej at 125d. Prominent emission and absorption features are marked and labeled.

i.e. ten days after start of recombination, we selected 42d spectrum as the closet available phase to the criteria. The Hα absorption to emission ratio of equivalent widths for SN 2013ej is found to be 0.23 ± 0.02, the optically thick phase is $\sim$ 85d and B-band late plateau (40 to 85d) slope is ~ 0.27 mag (100 d)$^{-1}$. The correlation for optically thick phase duration is found to follow that presented by Gutiérrez et al. (2014). For the plateau slope, the correlation also hold true, but here SN 2013ej lies in the border line position of the scattered relation. However, it may be noted that Hα profiles are possibly contaminated by high velocity features as we describe in next sections, which may result in deviation from correlation.

6.5.2 SYNOW modelling of spectra

SN 2013ej spectra has been modeled with SYNOW[1] (Branch et al., 2002; Fisher et al., 1999, 1997) for line identification and its velocity estimation. SYNOW is a highly parametrized spectrum synthesis code which employs the Sobolev approximation to simplify radiation transfer equations assuming a spherically symmetric supernova expanding homologously. The strength of the SYNOW code is its capability to reproduce P-Cygni profiles simultaneously in synthetic spectra for a given set of atomic

[1]https://c3.lbl.gov/es/#id22

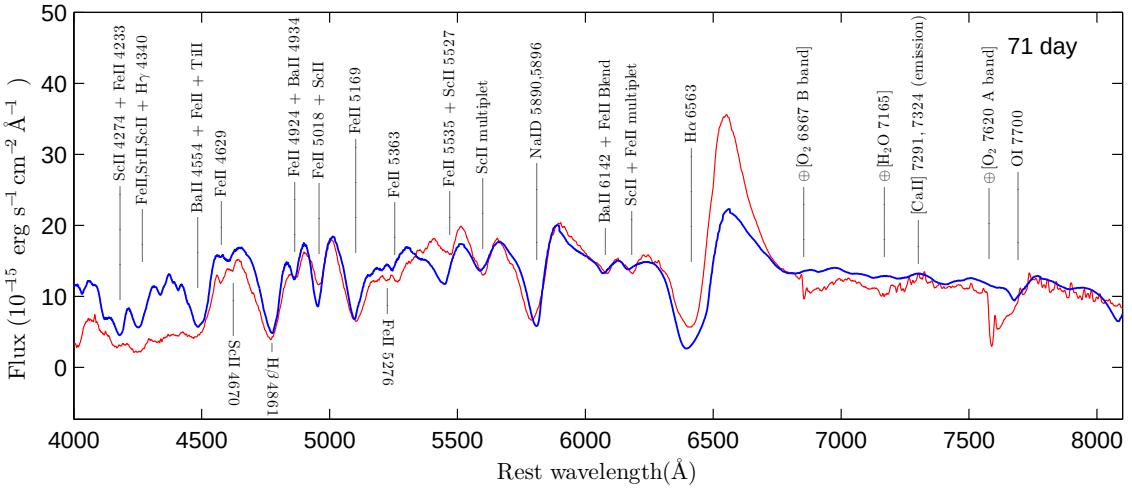

Figure 6.4: SYNOW modelling of SN 2013ej spectrum at 71d. Model spectrum is shown with thick solid line (blue), while the observed one is shown with thin solid line (red). Observed fluxes are corrected for extinction.

species and ionization states. The applicability of SYNOW is well tested in various core-collapse SNe studies (e.g. Bose & Kumar, 2014a; Bose et al., 2013; Inserra et al., 2012a; Marion et al., 2014; Milisavljevic et al., 2013; Takáts et al., 2014) for velocity estimation and analysis of spectral lines.

To model the spectra we tried various optical depth profiles (viz. gaussian, exponential and power law) with no significant difference among them, however we find exponential profile ($\tau \propto exp[-v/v_e]$) marginally better suited to match the absorption trough of observed spectra, where v_e the e-folding velocity, is a fitted parameter. While modeling spectra, H I lines are always dealt as detached scenario. This implies the velocity of hydrogen layer is significantly higher and is thus detached from photospheric layer, close to which most heavier atomic lines form, as assumed in SYNOW code. As a consequence to this, the Hα lines in synthetic spectrum, which are highly detached, has flat topped emissions with blue shifted absorption counter parts.

SN 2013ej spectra are dereddened and approximate blackbody temperature is supplied in the model to match the spectral continuum. For early spectrum (12d), local thermodynamic equilibrium (LTE) assumption holds good and thus SYNOW

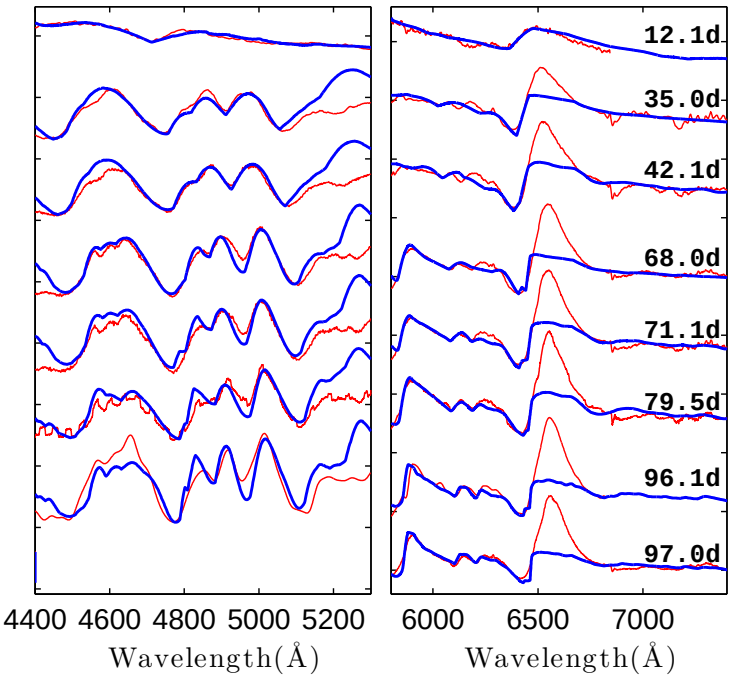

Figure 6.5: SYNOW modelling of SN 2013ej spectra at 8 phases during 12d to 97d for Hβ, Fe II multiplet (left) and Hα (right) profiles. Model spectra are shown with thick solid line (blue), while the observed ones are shown with thin solid line (red). In the model, H I lines are treated as detached to fit the absorption troughs. Along with Fe II and H I; other ions (Sc II, Ba II, Si II and Na I, Ti II) are also incorporated in model to fit some weaker features, specially at later phases. In addition to this, high-velocity H I lines are also incorporated (42d onwards) to fit the extended Hα and Hβ absorption troughs. The 97d spectrum do not have Hβ and Fe II wavelength region, hence it is not shown here.

could fit the continuum well, whereas at later epochs it fails to fit properly. The set of atomic species incorporated to generate the synthetic model spectrum are H I, He I; Fe II; Ti II; Sc II; Ca II; Ba II; Na I and Si II. The photospheric velocity $v_{\rm ph}$ is optimized to simultaneously fit the Fe II ($\lambda\lambda$ 4924, 5018, 5169) P-Cygni profiles and H I lines are treated as detached. The optical depths and optical depth profile parameters, e-folding velocity are varied for individual species to fit respective line profiles. In Fig. 6.4 we show the model fit of 71d spectrum. Most of the observable spectral features are reproduced well and are identified in the figure.

Similarly all spectra during 12 to 97d are modeled with SYNOW. The model

fits for Fe II ($\lambda\lambda$ 4924, 5018, 5169), Hβ and Hα spectral sections are shown in Fig. 6.5. The atomic species which are important to model these features are H I, Fe II, Ba II, Ti II, Sc II and Na I. In addition to these Si II is also used to model the dips in the blue wing of Hα P-Cygni during 12 to 42d. While modeling the Hα and Hβ profiles, SYNOW was unable to properly fit the broad and extended P-Cygni absorption troughs with single regular component. In order to fit these extended troughs, we invoke high-velocity (HV) component of H I. Although no separate dip is seen, possibly due to low spectral resolution and overlapping of broad P-Cygni profiles, the HV component can well reproduce the observed features in synthetic model spectrum. The implication and interpretation of these HV components are further discussed in §6.5.4. The SYNOW-derived velocities for Fe II, Hα, Hβ lines and corresponding HV components are listed in Table 6.1. The nebular spectra during 109 to 125d have not been modeled primarily due to limitations of the LTE assumption of SYNOW, and also because nebular phase spectra are dominated by emission lines rather than P-Cygni profiles.

6.5.3 Evolution of spectral lines

Investigation of the spectral evolution sheds light on various important aspects of the SN, like interaction of ejecta with the circumstellar material, geometrical distribution of expanding shell of ejecta and formation of dust during late time. SN spectra are dominated by P-Cygni profiles which are direct indicators of expansion velocities and they evolve with the velocity of photosphere. As ejecta expands and opacity decreases allowing photons to escape from deeper layers rich in heavier elements, we are able to see emergence and growth of various spectral lines.

To illustrate the evolution of Hα line, in Fig. 6.6 partial region of spectra is plotted in velocity domain corresponding to rest wavelengths of Hα. At 12d broad P-Cygni profile (FWHM $\sim$ 9500 km s^{-1}) is visible which becomes narrower with time as the expansion slows down. The blue-shifted absorption troughs are direct estimator of expansion velocity of the associated line forming layer. The emission peaks are found to be blue-shifted (by $\sim$ 3200 km s^{-1}at 12d), which progressively decreases with decrease in expansion velocity and almost settling to zero velocity

Table 6.1: The line velocities of Hα, Hβ, Fe II ($\lambda\lambda$ 4924, 5018, 5169) and He I λ5876 as estimated by modelling the observed spectra of SN 2013ej with SYNOW. Fe II or He I lines velocities are taken to represent photospheric velocity ($v_{\rm phm}$).

UT Date	Phase[a]	v(He I)	v(Fe II)	v(H$_\alpha$)	v(H$_\alpha$) HV[b]	v(H$_\beta$)	v(H$_\beta$) HV[b]
(yyyy-mm-dd)	(day)	10^3 km s^{-1}	10^3 km s^{-1}	10^3 km s^{-1}	10^3 km s^{-1}	10^3 km s^{-1}	10^3 km s^{-1}
2013-08-04.86	12.1	8.8	–	9.6	–	9.7	–
2013-08-27.76	35.0	–	6.7	7.9	–	6.6	–
2013-09-03.90	42.1	–	5.8	7.2	8.5	5.4	6.4
2013-09-29.78	68.0	–	3.6	5.8	7.4	4.0	5.8
2013-10-02.89	71.1	–	3.3	5.4	7.3	3.8	5.8
2013-10-11.28	79.5	–	3.3	5.2	6.3	3.6	4.8
2013-10-27.87	96.1	–	2.7	4.9	6.3	3.5	4.8
2013-10-28.79	97.0	–	2.7	4.8	6.3	–	–

[a] With reference to the time of explosion JD 2456497.30

[b] High velocity component used to fit the broad Hα and Hβ profile.

when the SN starts to enter nebular phase (97d). Such blue-shifted emission peaks, especially during early phases are generic features observable in SN spectra, e.g., SNe 1987A (Hanuschik & Dachs, 1987), 1998A (Pastorello et al., 2005), 1999em (Elmhamdi et al., 2003b), 2004et (Sahu et al., 2006), 2012aw (Bose et al., 2013), 2013ab (Bose et al., 2015a). These features are tied with the density structure of the ejecta, which in turn controls the amount of occultation of the receding part of ejecta, resulting in biasing of the emission peak (Anderson et al., 2014a), which are not limited to Hα but applicable to all spectral lines. However, such a blue-shift is clearly detected for Hα whereas for most other lines, emission profiles are weak and peaks are contaminated by adjacent P-Cygni profiles. Detailed SN spectral synthesis code like CMFGEN (Dessart & Hillier, 2005c) is capable of reproducing such blue-shifted emission peaks.

As inferred from Fig. 6.2, the spectral evolution of SN 2013ej is almost identical to other typical IIP SNe. However, the comparison of 35 and 68d spectra indicates Fe II lines are somewhat under developed as compared to other SNe at similar phase. As seen in the 68d comparison, the Fe II ($\lambda\lambda$ 4924, 5018, 5169) absorption dips are significantly weaker in comparison to that seen in other SNe.

Another prominent and unusual feature is seen in nebular spectra at 109d and 125d, on top of Hα emission, and the same is marked as feature A in Fig. 6.6. This unusual dip is resulting into an apparent blue-shift of the emission peak, which is in fact larger than that seen in the last plateau spectra at 97d. Such evolution is unexpected and against the general trend of emission peak evolution in SNe. The low resolution of these spectra prohibits us from investigating this feature in detail. The feature can be described as a superimposition of two emission profiles. Fig. 6.7 shows the observed Hα profile at 125d which is fitted by two component Gaussian profiles. These two profiles are separated by 55 Å ($\sim$ 2500 km s^{-1}), one being blue shifted by -1300 km s^{-1} while the other is red shifted at 1200 km s^{-1} with respect to rest Hα position. The FWHM for the blue component is 54Å and for red component is 146Å. The redshifted component is dominant in strength over the blue one, having their ratio of equivalent widths to be 4.5. It may be noted that for the sake of simplicity and only for the purpose of illustration we used Gaussian

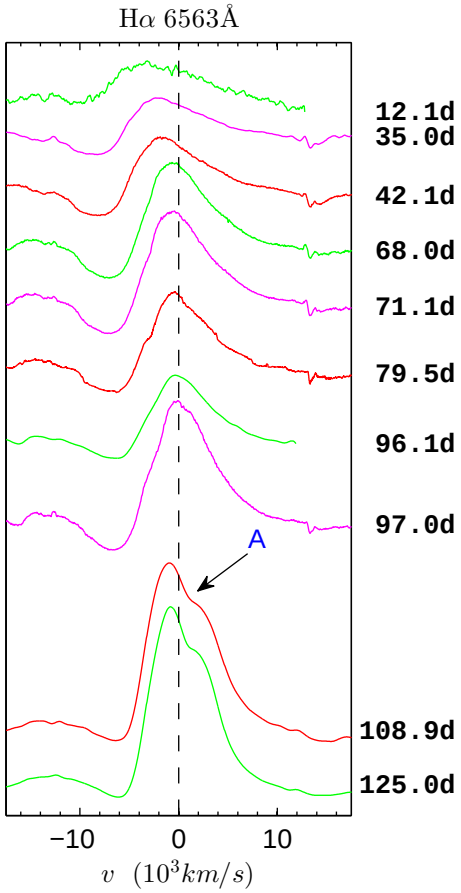

Figure 6.6: Evolution of Hα line profile at 10 phases during 12d to 125d. A zero-velocity line is plotted with a dashed line corresponding to the rest wavelength of Hα λ6563.

profiles, which does not account for the P-Cygni absorption troughs as we see on bluer wings of line profiles in observed SN spectrum.

Such an asymmetric or double peaked Hα nebular emission has been observed in a number of SNe, e.g. SN 1999em (Leonard et al., 2002c) and SN 2004dj (Chugai et al., 2005). Leonard et al. (2002c) identified such a dip or notch in Hα emission profile only during nebular phase of SN 1999em, which they suggested as possible ejecta-CSM interaction or asymmetry in line emitting region. In SN 2004dj, the asymmetry in nebular Hα spectra identified by Chugai et al. (2005) has been explained by bipolar distribution of ^{56}Ni with a spherical hydrogen envelope (Chugai, 2006).

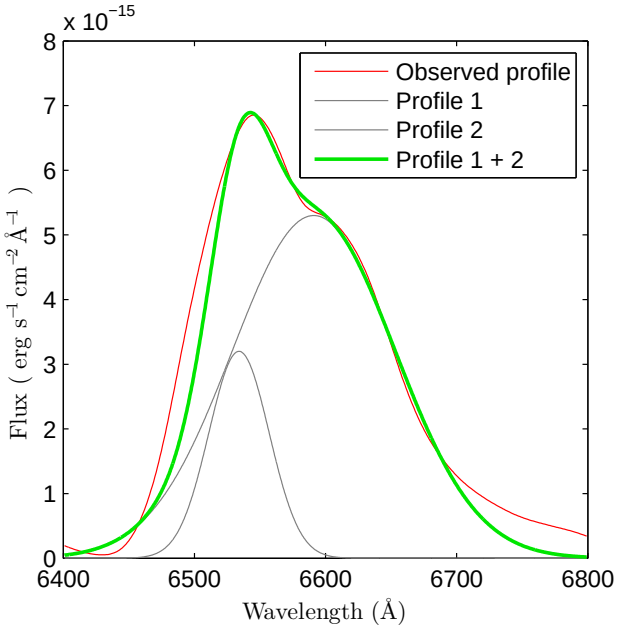

Figure 6.7: Continuum subtracted Hα profile of 125d spectrum fitted by two component gausian profile seperated by $\sim$2500 km s^{-1}.

6.5.4 Ejecta velocity

Progenitor stars prior to explosion develop stratified layers of different elements, which are generally arranged in an elemental sequence, hydrogen being abundant in the outermost shell, whereas heavier metals like iron predominate at deeper layers. However at the time of shock breakout significant mixing of layers may occur. Spectral lines originating from different layers of the ejecta attains different characteristic velocities. Thus study of velocity evolution provides important clues to the explosion geometry and the characteristics of various layers. Evolution of photospheric layer is of special interest as it is directly connected to the kinematics and other related properties. Photosphere represents the layer of SN atmosphere where optical depth attains a value of $\sim$ $^2/_3$ (Dessart & Hillier, 2005b). Due to complex mixing of layers and continuous recession of the recombination front, no single spectral line can represent the true photospheric layer. During the plateau phase, Fe II or Sc II lines are the best estimator of photospheric velocity ($v_{\rm ph}$). In early phases when Fe II lines are not strongly detectable, the best proxy for $v_{\rm ph}$ is He I, or Hβ (Takáts

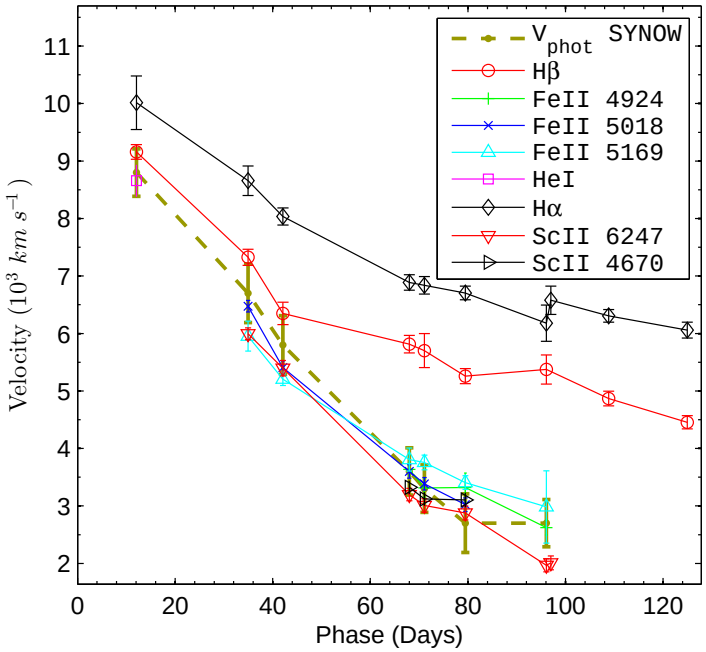

Figure 6.8: Velocity evolution of Hα, Hβ, He I, Sc II and Fe II lines. The velocities are estimated using blueshift of the absorption minima. The expansion velocity of photosphere ($v_{\rm phm}$) estimated from SYNOW modeling of He I line at 12d and Fe II lines at later phases (see Table 6.1) are also overplotted for comparison.

& Vinkó, 2012) in even earlier phases.

Line velocities can either be estimated by directly locating the P-Cygni absorption troughs, as done using SPLOT task of `IRAF`, or by by modeling the line profiles with velocity as one of the input, as we do in SYNOW. In Fig. 6.8, we plot the line velocities of Hα, Hβ, Fe II ($\lambda\lambda$ 4924, 5018, 5169) and Sc II ($\lambda\lambda$ 4670, 6247), using the absorption minima method. It is evident that Fe II and Sc II line velocities are very close to each other and they are formed at deeper layers, whereas Hα and Hβ line velocities are consistently higher at all phases as they form at larger radii. The SYNOW estimated photospheric velocities are also plotted for comparison, which is very close to the Fe II and Sc II velocities estimated from absorption minima method. Here the SYNOW-derived photospheric velocities are estimated by modelling He I line for 12d spectrum and Fe II lines for rest of the spectra. Velocities for various lines estimated using SYNOW are tabulated in Table 6.1.

Fig. 6.10 shows the comparison of photospheric velocity of SN 2013ej with other well-studied type II SNe 1987A, 1999em, 1999gi, 2004et, 2005cs, 2012aw and 2013ab. For the purpose of comparison the absorption trough velocities have been used, taking the mean of Fe II line triplet, or He I lines at early phases where Fe II lines are not detectable. The velocity profile of SN 2013ej is very similar to other normal IIP SNe 1999em, 1999gi, 2004et, 2012aw and 2013ab, on the other hand velocities of SN 2005cs and 1987A are significantly lower. The velocity profile of SN 2013ej is almost identical with SNe 2004et, 2012aw and 2013ab, whereas it is consistently higher than SNe 1999gi and 1999em by $\sim 800 - 900\,\mathrm{km\,s^{-1}}$. For comparison of H I (Hα and Hβ) velocities, we have chosen all those events which are at least photometrically and spectroscopically similar to SN 2013ej. Comparison reveals that, H velocities during later phases (60-100 d) are consistently higher than all comparable events. SNe 2012aw and 2013ab, have photospheric velocities identical to SN 2013ej, but their H velocities are significantly lower by large values, e.g., for SN 2013ej the Hα velocity at 80d is higher by 1500 $\mathrm{km\,s^{-1}}$ and Hβ is higher by 2400 $\mathrm{km\,s^{-1}}$. Likewise, H velocities for SNe 1999em and 1999gi are even lower at similar phases. Although SN 2004et H I velocities are somewhat on higher end, they are still significantly less than those of SN 2013ej. It is also to be noted that, at 12d SN 2013ej H I velocities are consistent and similar to those of other normal SNe, but as it evolves these velocities decline relatively slowly, ultimately turning out into a higher velocity profile after $\sim$ 40d.

6.5.5 High velocity components of H I and CSM interaction

As discussed in §6.5.2, the broad and extended Hα or Hβ absorption profiles are not properly reproduced using single H I velocity component in SYNOW, and those profiles can only be fitted by incorporating a high-velocity (HV) components along with the regular one. Fig. 6.9 shows the comparison of SYNOW fits for 68d Hβ profile with various single velocity as well as for combined two velocity components. A single velocity component at 5600 $\mathrm{km\,s^{-1}}$ can match the blue wing well and partially the trough, whereas, it does not match the red side at all. Similarly, with a single velocity component at 4000 $\mathrm{km\,s^{-1}}$ can partially match the red slope of the

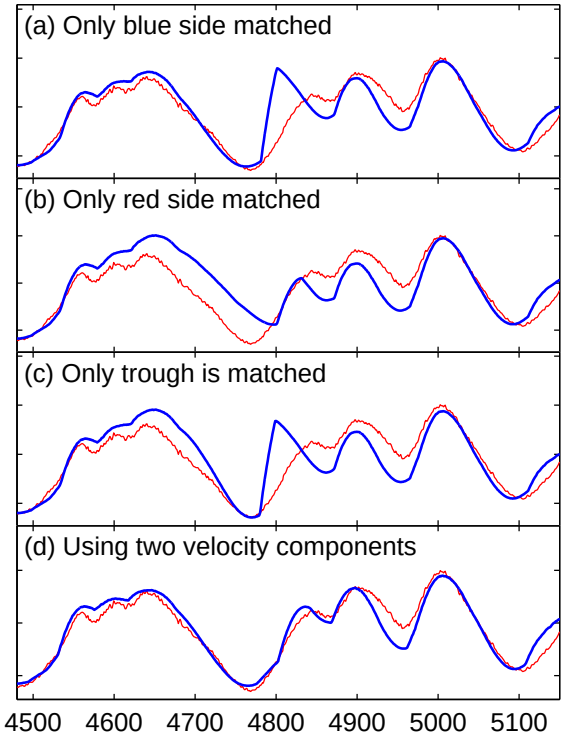

Figure 6.9: For 68d spectrum, the Hβ profile is fitted using SYNOW with various velocity components. (a) The fit only with a single high velocity component to match the blue wing of the absorption dip, (b) with a single low velocity component to match the red wing, (c) with single velocity to only fit the trough, (d) with two velocity components to fit entire absorption profile.

trough, but does not include the trough as well as the extended blue wing. By only matching the trough position, the model fits for a single velocity of 5300 km s^{-1}, which does not fit either of the blue or red wing. Even-though the 'detachment' of H I from photosphere in SYNOW model makes the fit of red wing worse by steepening it further, but it is still conclusive that none of these single velocity component can properly reproduce the absorption profile. It is only by including two velocity components together in the model could reproduce the entire Hβ profile. Such a scenario start to appear from 42d spectrum which only becomes stronger as the line evolves until 97d. The Hα troughs are also reproduced in a similar fashion. However, it may be noted, that such an extended H I feature may also be explained as a possible outcome of a different (complex and extended) density profile which

SYNOW can not reproduce.

The comparison of Hα and Hβ velocities with other normal IIP SNe (see Fig. 6.10), estimated by directly locating the P-Cygni absorption troughs, shows that SN 2013ej velocities are significantly higher and declines relatively slowly (especially during later phases; 60-100d) as compared to those seen in typical IIP SNe, e.g., 1999em, 1999gi, 2012aw or 2013ab. On the other hand the photospheric velocity comparison with other IIP SNe does not show any such anomaly. This, we suggest as the effect of blending with H I HV components in Hα and Hβ, which we could separate out while modeling these broad features with SYNOW having two velocity components. The regular Hα and Hβ velocities estimated from SYNOW declines at a normal rate consistent to that seen in other SNe (see Fig.6.10), whereas the HV components remains at higher velocities by $1000 - 2000$ km s^{-1}, declining at relatively slower rate. It is also interesting to note that the velocity difference between the regular and HV component for Hα and Hβ is similar at same epochs. Chugai et al. (2007) identified similar HV absorption features associated close to Hα and Hβ troughs in SNe 1999em and 2004dj, which remained constant with time. Presence of such HV features has also been detected in SN 2009bw (Inserra et al., 2012b) and SN 2012aw (Bose et al., 2013) which is suggestive of interaction of SN ejecta with pre-existent CSM. Similar to SN 2013ej, HV signatures has been detected all throughout the plateau phase evolution of SN 2009bw, while in SN 2012aw such features were only detected at late plateau phase (55 to 104d). Although, we found HV components in SN 2013ej by modeling the extended P-Cygni troughs, we are unable to visually detect such two individual velocity components, this is possibly because of our signal-to-noise-ratio limited spectra and weaker strength of HV components. Chugai et al. (2007) argued that SN ejecta can interact with the cooler dense shell of CMS material, which might have originated from the pre-supernova mass loss in the form of stellar winds. Their analysis showed that such interaction can led to the detection of HV absorption features on bluer wings of Balmer lines due to enhanced excitation of the outer layers of unshocked ejecta. We, therefore suggest weak or moderate ejecta-CSM interaction in SN 2013ej. X-ray emission from SN 2013ej has also been reported by Margutti et al. (2013), which they measured a 0.3-10 keV count-rate of

2.7±0.5 cps, translating into a flux of $\sim 1.1 \times 10^{-13}$ erg s^{-1}cm^{-2} (assuming simple power-law spectral model with photon index Gamma = 2). Such X-ray emission may also indicate ejecta-CSM interaction suffered by SN 2013ej.

6.6 Status of SN 2013ej in type II diversity

6.6.1 Factors favoring SN 2013ej as type IIL

Having characterized the event both photometrically and spectroscopically, we may now revisit the aspects which favor SN 2013ej as type IIL event. The SN was originally classified as type IIP (Valenti et al., 2013) based on spectroscopic similarity to SN 1999gi. Due to same underlying physical mechanisms which govern both type IIP and IIL SNe, early spectra may not clearly distinguish these sub classes of SN type II. The distinguishing factor among IIP and IIL is nominal and mainly depend upon light curve characteristics. SN 2013ej shows a decline of 1.74 mag (100 d)$^{-1}$ (see Table 6.1) or $\sim$ 0.87 mag in 50 days, which definitely falls in the criteria of type IIL SNe as proposed by Faran et al. (2014). In Fig. 6.2, the spread of template light curves for type IIP and IIL (Faran et al., 2014) is shown along with M_V light curves of SNe sample. It is evident that under this scheme of classification, SN 2013ej is not a type IIP, rather it is marginally within the range of type IIL template light curves. This is also justified from the point of basic idea behind these classifications, that type IIP must show a 'plateau' of almost constant brightness for some time ($\sim$ 90d), which is not the case with SN 2013ej. Due to the very fact that SN type II light curves and physical properties exhibit a continuum distribution rather than a bi-modality (Anderson et al., 2014b), SN 2013ej shows intermediate characteristic in the SN type II diversity.

One distinguishing spectroscopic property Faran et al. (2014) found for type IIL SNe is the overall higher photospheric (Fe II λ5196) velocity and flatter H I (Hβ and Hα) velocity profiles as compared to type IIP counterpart. Although Fe II velocities are on the higher end as compared to typical IIP SNe velocities, we do not find it as a remarkable deviation to distinguish SN 2013ej from IIP sample. However, we do see a anomaly in Hα, Hβ absorption minima velocity profiles, as they start off

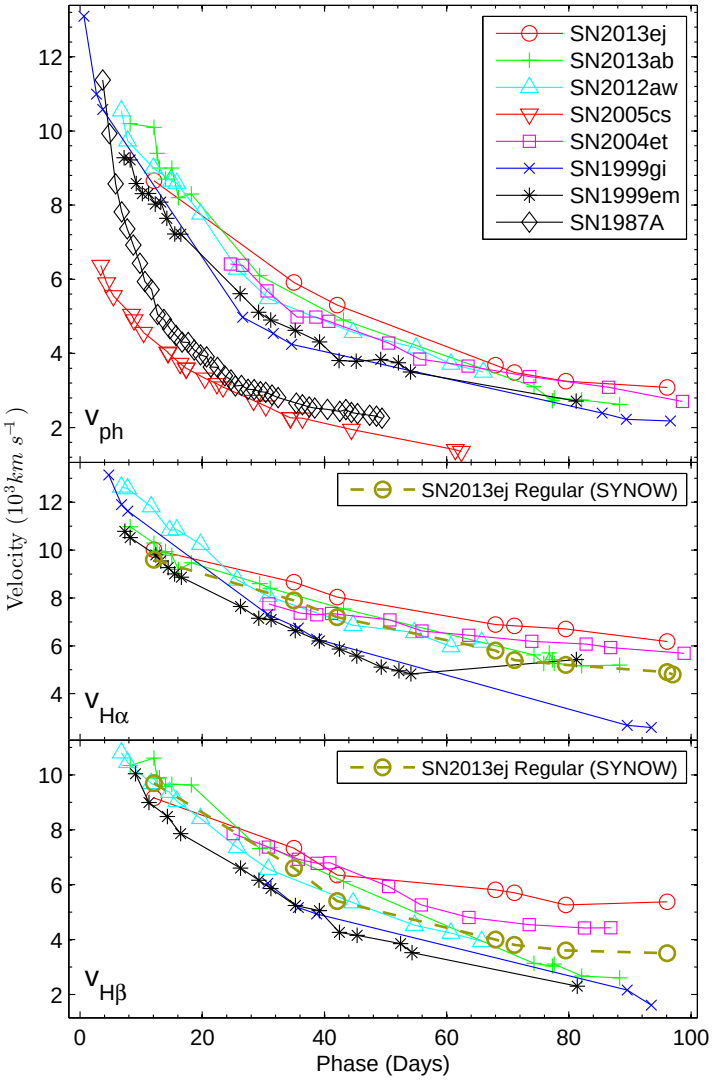

Figure 6.10: The photospheric velocity (top) evolution ($v_{\rm ph}$) of SN 2013ej is compared with other well-studied type II SNe. The $v_{\rm ph}$ plotted here are the absorption trough velocities (average of Fe II lines at late phases and He I at early phases). Similar comparison of P-Cygni absorption velocities, but for Hα and Hβ are shown in middle and bottom panels respectively. The regular velocity component for Hα and Hβ estimated from SYNOW (without HV components; see Table. 6.1) are also plotted for comparison.

with velocities consistent with those of type IIP but declines relatively slowly (see §6.5.4 for more description of this feature) ultimately surpassing faster declining IIP velocity profiles after 50 days. This characteristic feature of H I velocities for SN 2013ej is typical for most IIL SNe as found by Faran et al. (2014).

6.6.2 CSM interaction and type IIL

Faran et al. (2014) proposed a possible explanation for the flatter velocity profiles in IIL SNe, which is due the lack of hydrogen in deeper and slow expanding layers of ejecta, resulting into higher H I absorption velocities arising mostly from outer layer. However, for SN 2013ej we suggest the flattening of Hα and Hβ velocity profiles are due to the contamination of HV component of H I (see §6.5.5). Indication of CSM interaction in SN 2013ej may also be inferred from X-ray detection by Margutti et al. (2013). Valenti et al. (2015) found SN 2013by, a type IIL SN, to be moderately interacting with CSM. This led them to ask the prevalence of CSM interaction among IIL SNe in general. Type IIL SNe originate from progenitors similar to IIPs, but have lost a significant fraction of hydrogen before explosion during pre SN evolution. Hence it may not be usual to detect HV H I signatures in Hα, Hβ absorption profiles as a consequence of ejecta-CSM interaction. A moderate or weak interaction may produce a HV component blending with Hα, Hβ profiles, which may result into shift in absorption minima, rather than a prominent secondary HV dip. Such a scenario may perfectly explain the relatively higher and flatter H I velocity profiles of most type IIL SNe as compared to IIP counterparts, found by Faran et al. (2014) based on direct velocity estimates of absorption minima.

Another example of CSM interaction in type IIL is SN 2008fq, which does show strong interaction signature like a type IIn (Taddia et al., 2013), but also shows a steep decline like IIL during first 60 days (Faran et al., 2014). Supernova PTF11iqb (Smith et al., 2015) is also a type IIn SN, having prominent CSM interaction signatures, but with IIL like steeper light curve. Initial spectra of this SN showed IIn characteristics, however late plateau spectra revealed features similar to type IIL. PTF11iqb originated from a progenitor identical to type IIP/L, instead of a LBV as expected for a typical IIn. However, because of rare detection of type IIL events and

its fast decline in magnitudes we do not have sufficient information to investigate CSM interaction in all such objects. Thus, the question still remains open if all or most IIL SNe interact with CSM and whether the flatter H I absorption minima velocity profiles is a consequence of interaction.

6.7 Light curve modelling

To determine the explosion parameters of SN 2013ej, the observed light curve is modeled following the semi-analytical approach originally developed by Arnett (1980) and further refined in Arnett & Fu (1989). More appropriate and accurate approach would have been detailed hydrodynamical modeling (e.g. Bersten et al., 2011; Falk & Arnett, 1977; Pumo & Zampieri, 2011; Utrobin, 2007) to determine explosion properties, however application of simple semi-analytical models (Arnett, 1980, 1982; Arnett & Fu, 1989; Chatzopoulos et al., 2012; Popov, 1993; Zampieri et al., 2003) can be useful to get preliminary yet reliable estimates of the parameters without running resource intensive and time consuming hydrodynamical codes. Nagy et al. (2014) also followed the original semi-analytical formulation presented by Arnett & Fu (1989) and modeled a few well studied II SNe. The results are compared with hydrodynamical models from the literature and are found to be in good agreement. The model light-curve is computed by solving the energy balance of the spherically symmetric supernova envelope, which is assumed to be in homologous expansion having spatially uniform density profile.

The temperature evolution is given as (Arnett, 1980),

$$T(x,t)^4 = T_0^4 \psi(x) \phi(t) \left(\frac{R_0}{R(t)} \right)^4,$$

where x is defined as dimensionless co-moving radius relative to the mass of the envelope and, $\psi(x)$ is the radial component of temperature profile which falls off with radius as $sin(\pi x)/\pi x$. Here we incorporate the effect of recombination, as shock heated and ionized envelope expands and cools down to recombine at temperature T_{rec}. We define x_i as the co-moving radius of the recombination front and the

opacity (κ) changes very sharply at this layer such that $\kappa \approx 0$ for the ejecta above x_i. Following the treatment of Arnett & Fu (1989) the temporal component of temperature, $\phi(t)$ can be expressed as (Nagy et al., 2014),

$$\frac{d\phi(t)}{dz} = \frac{R(t)}{R_0 x_i^3}\left[p_1\zeta(t) - p_2\phi(t)x_i - 2x_i^2\phi(t)\frac{R_0}{R(t)}\frac{dx_i}{dz}\right],$$

here $\zeta(t)$ is the total radioactive energy input from decay chain of unit mass of ^{56}Ni, which is normalized to the energy production rate of ^{56}Ni. The rest of the parameters in the equation have usual meaning and can be found in aforementioned papers. From this ordinary differential equation we can find out the solution of $\phi(t)$ using Runge-Kutta method. The treatment adopted to determine x_i is somewhat similar to Nagy et al. (2014), where we numerically determine the radius x_i (to an accuracy of 10^{-12}) for which the temperature of the layer reaches T_{rec}. Once we find out the solution of $\phi(t)$ and x_i, the total bolometric luminosity is calculated as the sum of radioactive heating and rate of energy released due to recombination,

$$L(t) = x_i\frac{\phi(t)E_{th}(0)}{\tau_d}\left(1 - e^{-A_g/t^2}\right) + 4\pi r_i^2 Q\rho(x_i,t)R(t)\frac{dx_i}{dt},$$

here, $d(x_i)/dt$ is the inward velocity of co-moving recombination front and the term $[1 - exp(-A_g/t^2)]$, takes into account of gamma-ray leakage from the ejecta. The factor A_g is the effectiveness of gamma ray trapping (see e.g., Chatzopoulos et al., 2012; Clocchiatti & Wheeler, 1997), where large A_g means full trapping of gamma rays, this factor is particularly important to model the SN 2013ej tail light curve. In this relation we also modified the second term to correctly account for the amount of envelope mass being recombined.

To model SN light curves it is essential to obtain the true bolometric luminosity from observations. Since our data is limited only to optical and UV bands, we adopt the prescription for color dependent bolometric corrections by Bersten & Hamuy (2009) to obtain bolometric light curve for SN 2013ej. Figure 6.1 shows the model fit with the observed bolometric light curve of the SN. We estimate an ejecta mass of 12 $M_\odot$, progenitor radius of 450 $R_\odot$ and explosion energy (kinetic + thermal) of 2.3 foe (10^{51} erg). The uncertainty in mass and radius is about 25%. We find that the

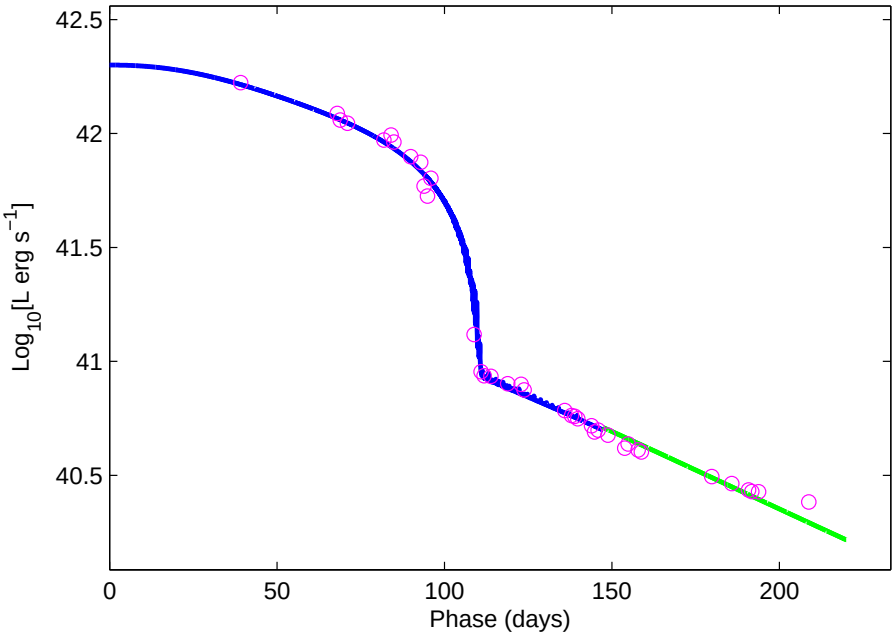

Figure 6.1: Model fit (solid line) on the observed bolometric light curve (open circles) of SN 2013ej. The green solid line follows only the radioactive decay law, where the recombination front has completely disappeared.

plateau duration is strongly correlated with explosion energies (especially kinetic), and also with κ and T_{rec}. Thus depending upon these parameters our model is consistent with a wide range of explosion energies, with 2.3 foe towards the lower end and energies up to 4.5 foe at higher end. Assuming the mass of the compact remnant to be 1.5-2.0 $M_{\odot}$, the total progenitor mass adds up to be $14M_{\odot}$.

The mass of radioactive ^{56}Ni estimated from the model is $0.018M_{\odot}$, which primarily governs the tail light curve of the SN. As discussed in §6.4.2, the slope of the tail light curve observed for SN 2013ej is significantly higher than other typical IIP SNe and also to that expected from radioactive decay of ^{56}Co to ^{56}Fe. The light curve powered by full gamma-ray trapping from radioactive decay chain of $^{56}\mathrm{Ni} \rightarrow {}^{56}\mathrm{Co} \rightarrow {}^{56}\mathrm{Fe}$ results in a slower decline and does not explain the steeper tail observed in SN 2013ej. In the model we decreased the gamma-ray trapping effectiveness parameter A_g to 3×10^4 day^2, which matches the steeper radioactive tail. The gamma-ray optical depth can be related to this parameter as $\tau_g \sim A_g/t^2$.

This implies that the gamma-ray leakage in SN 2013ej is significantly higher than other typical type IIP SNe.

Valenti et al. (2014) using early temperatures (< 5 days) of SN 2013ej provided a preliminary estimate of the progenitor radius as $400 - 600$ $R_{\odot}$, which is in good agreement with our result. Our progenitor mass estimate is also consistent with that reported by Fraser et al. (2014) from direct observational identification of the progenitor using *HST* archival images, which is $8 - 15.5$ $M_{\odot}$.

6.8 Summary

We present photometric and spectroscopic observations of SN 2013ej. Despite low cadence optical photometric follow up during photospheric phase, we are able to cover most of the important phases and features of light curve.

Our high resolution spectrum at 80d shows the presence of Na I D ($\lambda\lambda$ 5890, 5896) doublet for Milky Way, while no impression for host galaxy NGC 0628. This indicates that SN 2013ej suffers minimal or no reddening due to its host galaxy.

The optical light curves are similar to type IIL SNe, with a relatively short plateau duration of 85d and steeper decline rates of 6.60, 3.57, 1.74, 1.07 and 0.74 mag 100 day^{-1} in *UBVRI* bands respectively. The comparison of absolute V band light curves shows that SN 2013ej suffers the higher decline rate than all type IIP SNe, but similar to type IIL SNe 1980k, 2000dc and 2013by. The drop in luminosity during the plateau-nebular transition is also higher than most type II SNe in our sample, which is 2.4 mag in V band.

The UVOT UV optical light curves shows steep decline during first 30 days at a rate of 0.182, 0.213, 0.262 mag d^{-1} in *uvw1, uvw2* and *uvm2* bands respectively. The absolute UV light curves are identical to SN 2012aw and also shows a similar UV-plateau trend as observed in SN 2012aw.

Owing to the large drop in luminosity during plateau-nebular transition, the light curve settles to a significantly low luminous tail phase as compared to other normal IIP SNe. The mass of radioactive ^{56}Ni estimated from the tail bolometric luminosity is 0.020 ± 0.002 $M_{\odot}$, which is in between normal IIP SNe (e.g., 1999em,

2004et, 2012aw) and subluminous events, like SN 2005cs.

The spectroscopic features and their evolution is similar to normal type II events. Detailed SYNOW modelling has been performed to identify spectral features and to estimate velocities for Hα, Hβ, Fe II ($\lambda\lambda$ 4924, 5018, 5169) and Sc II ($\lambda\lambda$ 4670, 6247) lines. The photospheric velocity profile of SN 2013ej, which is represented by Fe II lines and He I line at 12d, is almost identical to SNe 2004et, 2012aw and 2013ab. The Hα, Hβ velocities estimated by directly locating the absorption troughs are significantly higher and slow declining as compared to other normal IIP events. However, such H I velocity profiles are typical for type IIL SNe.

The P-Cygni absorption troughs of Hα and Hβ are found to be broad and extended which a single H I component in SYNOW model could not fit properly. However, these extended features are fitted well with SYNOW by incorporating a high velocity H I component. These HV components can be traced throughout the photospheric phase which may indicate possible ejecta-CSM interaction. Our inference is also supported by the detection of X-ray emission from the SN 2013ej (Margutti et al., 2013) indicating possible CSM interaction, and the unusually high polarization reported by Leonard et al. (2013) may also further indicate asymmetry in environment or ejecta of the SN. Such CSM interaction and their signature in Hα, Hβ profiles has also been reported for SNe 2009bw (Inserra et al., 2012b) and 2012aw (Bose et al., 2013).

Nebular phase spectra during 109 to 125d phases are dominated by characteristic emission lines, however the Hα line shows an unusual notch, which may be explained by superposition of HV emission on regular Hα profile. Although, the origin of the feature is not fully explained, it may indicate bipolar distribution of ^{56}Ni in the core.

We modeled the bolometric light curve of SN 2013ej and estimated a progenitor mass of $\sim$ 14M$_{\odot}$, radius of $\sim$ 450R$_{\odot}$ and explosion energy of $\sim$ 2.3 foe. These progenitor property estimates are consistent to those given by Fraser et al. (2014) and Valenti et al. (2014) for mass and radius respectively. The tail bolometric light curve of SN 2013ej, is found to be significantly steeper than that expected from decay chain of radioactive ^{56}Ni. Thus, in the model we decreased the effectiveness of gamma ray trapping, which could explain the steeper slope of tail light curve.

Chapter 7

Photometric and polarimetric observations of fast declining Type II SNe 2013hj and 2014G

7.1 Introduction

According to historical classification based on the light curve properties (Barbon et al., 1979), fast declining counterpart of type IIPs are SNe IIL, which are supposed to show almost a linear decline in the light curve until it reaches the tail phase, without any sort of flattening during early phases of light curve. Over time it has been realized that such events are extremely rare that could fit in the criteria of SNe IIL. Studies by Anderson et al. (2014b) and Sanders et al. (2015) on a large sample of SNe II disapprove existence of any bimodality in light curve properties which can be grouped into distinct subclasses. Rather they found a continuum in light curve slopes and physical parameters. Moreover now it is also believed that a steep declining plateau-nebular transition like phase can be detected even in typical SNe IIL if they are observed long enough. The plateau slope of SNe II light curves are primarily governed by the amount of hydrogen present in the ejecta. As in the case of SNe IIP where the hydrogen content is high enough with an extended envelope, the energy deposited instantaneously from shock and also from the initial decay of

^{56}Ni is released slowly over a longer period of time, which sustain the flat plateau phase. On the contrary, if the amount of intact hydrogen is relatively less, then energy will be released at a faster rate resulting into a fast declining light curve but with a brighter initial peak luminosity. Considering vast diversity of progenitor properties (Smartt, 2009), variable amount of hydrogen mass intact in the ejecta would give rise to a continuum distribution of light curve slopes. Faran et al. (2014) proposed a criteria to reestablish SNe IIL classification, according to which a SN with a decline of 0.5 mag in V-band light curve during first 50 days would qualify as a type IIL. However this criteria is too rigid for IIL classification as it will classify more than 50% of all Type II SNe as Type IIL considering the sample of Anderson et al. (2014b). Rather we use the presented SNe IIL light curve template (Faran et al., 2014) for the said purpose. Following this criteria of classification, many earlier studies which comprises of collective sample of SNe IIP may also include some reclassified SNe IIL as well.

Extensive theoretical and numerical attempts have been made to understand progenitor properties and relate them with other observable parameters of explosion (Arnett & Fu, 1989; Hamuy, 2003; Litvinova & Nadezhin, 1985). Stellar evolutionary models suggest that these SNe can originate from red supergiant (RSG) stars of masses $\sim 9-25 M_{\odot}$ (e.g. Heger et al., 2003). However, progenitors directly identified from pre-SN archival *HST* images for a decent number of IIP SNe suggest an upper mass limit of 16.5 ± 1.5 $M_{\odot}$ (Smartt et al., 2009). One of the many proposed explanation for the lack of high mass RSG progenitors is that stars above $17 M_{\odot}$ may end up into IIL or IIn SNe (Smartt, 2009).

Extragalactic SNe are spatially unresolvable and hence its difficult to address structure and geometry of explosion. Polarimetric observations have proved to be a unique probe in investigating asymmetry of SN explosion. In SNe the source of polarization is primarily the geometry of electron scattering atmosphere within the ejecta. Any asymmetry in this envelope would give rise to net polarization of observed light. CCSNe are often found to show significant degree of polarization in optical and IR wavelengths (Leonard & Filippenko, 2001; Leonard et al., 2001; Pereyra et al., 2006; Wang et al., 2002a; Wang & Wheeler, 1996). SNe with hydro-

gen envelope stripped (Type Ib/c) or partially stripped (Type IIb or IIn) exhibit higher level of polarization as compared to SNe with intact H envelope like SNe IIP (typically about 0.5 – 0.8% polarization). The thick H envelope suppresses the observed asymmetry, whereas probing deeper towards the central part of the explosion, more polarization is observed implying higher degree of asymmetry in electron scattering atmosphere (Leonard & Filippenko, 2005). However, in IIP SNe polarization enhancement is observed towards the end of plateau as SN starts to enter the nebular phase, where the hydrogen recombination is close to completion, and with decreasing opacity the inner asymmetric core is being revealed (e.g. SN 2004dj; Leonard et al., 2006). Generally a moderate asphericity of $\sim$ 20% would result in a linear polarization of $\sim$ 1% (Leonard & Filippenko, 2005). Besides asphericity in electron scattering atmosphere, some amount of polarization may also originate from scattering by dust environment (Wang & Wheeler, 1996), clumps in ejecta, asymmetric distribution of radioactive ^{56}Ni (Chugai, 2006) or asymmetric ionization of outer envelope due to shock produced in CSM interaction.

The first broadband polarimetric observation was done for SN 1987A (Barrett, 1988) demonstrating significant polarization and its time evolution. Late time *HST* observations of spatially resolved ejecta revealed elongation in a direction consistent to the polarization angle inferred from polarimetry (Wang et al., 2002b), which validated our understanding to use polarimetry as a probe for SN explosion geometry. SNe 1999em and 2004dj are extremely well studied and observed spectropolarimetrically, which provided detailed insight on the nature of these explosions (Leonard et al., 2001, 2006). While spectropolarimetry has advantage of wavelength resolved polarization information, on the other hand broadband polarimetry is useful to extract overall polarimetric information and infer any asymmetry without the requirement of bright SN or powerful observational resources.

In this work we present broadband photometric and polarimetric observations of two fast declining type II SNe 2013hj and 2014G. A brief introduction of these events is given in Section 7.1.1. This chapter is organized as follows. In Section. 7.2 we describe photometric and polarimetric observations and data reduction procedure. Adopted distance and estimated extinction values for both the SNe are discussed

in Section 7.3. In Section 7.4 we analyze photometric light curve properties of SNe 2013hj and 2014G and compare with other SNe II to establish its position in Type II diversity. In this section we also estimate ^{56}Ni mass from computed bolometric light curves. The explosion parameters and progenitor properties are estimated by modelling the light curve, which are described in Section 7.5. Polarimetric analysis and its temporal evolution is discussed in Section 7.6. Finally in Section 7.7 we summarize the results obtained in this work.

7.1.1 SNe 2013hj and 2014G

SNe 2013hj and 2014G, both are moderately bright events which have been detected very young. SN 2013hj was discovered on December 12.3 UTC, 2013 by Antezana et al. (2013) in the galaxy MCG -02-24-3 ($\sim$ 30 Mpc). Unfortunately there is no reported non-detection prior to SN explosion, which can be used to observationally constrain the explosion epoch. The classification spectrum from ASIAGO on December 13.1 UTC shows broad and very shallow Hα and Hβ P-Cygni profiles on top of featureless blue continuum. Comparison of this spectrum with well studied SNe templates, using GELATO (Harutyunyan et al., 2008) and SNID (Blondin & Tonry, 2007), is found similar to type II SNe and matches best with SN 2012A spectrum at 2.6 day after explosion. Moreover, from visual comparison with other SNe II spectra (e.g., Bose et al., 2015a; Valenti et al., 2014) at early epochs, the December 13 spectrum looks no older than 4 days. Therefore, we adopt an explosion epoch (0d) of December 10.5 UTC, 2013 (JD = 2456637.0 $\pm$ 1.5 days) for SN 2013hj.

SN 2014G was discovered on January 14.5 UTC, 2014 in NGC 3448 ($\sim$ 24 Mpc) and was reported in *CBAT Transient Object Followup Reports*[1]. They also reported an earlier faint detection ($\sim$ 17.4 mag) in CCD image taken on January 13.6 UTC with limiting magnitude of 18.5. Denisenko et al. (2014) reported last confirmed non-detection of the SN on January 10.9 UTC, 2014 up to a limiting magnitude of 19.4. Thus we adopt mid time between the first faintest detection and last non-detection as the explosion epoch (0d) for SN 2014G, which is January 12.2 UTC, 2014 (JD = 2456669.7 $\pm$ 1.4 days). Ochner et al. (2014) reported optical spectrum

[1]http://www.cbat.eps.harvard.edu/unconf/tocp.html

taken on January 15.1 UTC, showing H I line with narrow Hα emission and unusually strong He II line, which was found similar to type IIn SN 2013cj. However, it was again reclassified as type IIL by Eenmae et al. (2014) from spectrum taken several weeks after peak. The basic parameters of these two SNe and their host galaxies are tabulated in Table. 7.1.

7.2 Observation and Data reduction

7.2.1 Photometry

Broadband photometric observations of SNe 2013hj and 2014G have been carried out in *UBVRI* bands. Rigorous follow up observations for both the SNe was initiated soon after their discovery. The observations in the nebular phase continued until the objects went behind the Sun. High cadence monitoring was done using ARIES 104cm Sampurnanand Telescope (ST) and 130cm Devasthal Fast Optical Telescope (DFOT) located at Nainital, India. Additional *BVRI* data of SN 2013hj was also collected from 50cm telescope at Osaka Kyoiku University, Japan. *Swift* Ultraviolet optical telescope (UVOT) also observed SN 2014G for nearly a month in all six UVOT bands.

The routine data cleaning, reduction, extraction of light curve and field calibration to generate local standards follows the same procedure as outlined in Bose et al. (2013). Fig. 7.1 and Fig. 7.2 shows the field of SNe 2013hj and 2014G respectively. As seen in the figures both the SNe are fairly embedded in their host galaxies and the estimated SN flux measurements will be contaminated by the background specially during late phases. It is therefore necessary to correct for the host galaxy fluxes and in order to do so galaxy templates have been observed. Template images of the host galaxies in all five photometric bands were taken during 7 to 10 May 2015 when the SNe have fainted much below the detection limit (at an age of $\sim$ 515 and $\sim$ 480 days for SN 2013hj and SN 2014G respectively). In order to do the template correction, we adopted aperture flux subtraction method, in which the SN flux and host galaxy background flux (from the template image) is extracted using the same aperture and at the same exact same location. The SN fluxes are

Table 7.1: Parameters of SNe and their host galaxies.

Parameters	Value	Ref.
	SN 2013hj	
MCG -02-24-3:		
Alternate name	PGC 025938	2
Type	SBcd	2
RA (J2000)	$\alpha = 09^{\rm h}12^{\rm m}06\overset{\rm s}{.}7$	2
DEC (J2000)	$\delta = -15°25'51\overset{''}{.}9$	2
Abs. Magnitude	$M_B = -18.26$ mag	2
Distance	$D = 28.2 \pm 2.0$ Mpc	2
Distance modulus	$\mu = 32.25 \pm 0.15$ mag	
Heliocentric Velocity	$cz_{\rm helio} = 2060 \pm 7\,{\rm km\,s^{-1}}$	2
SN 2013hj:		
RA (J2000)	$\alpha = 09^{\rm h}12^{\rm m}06\overset{\rm s}{.}3$	3
DEC (J2000)	$\delta = -15°25'46\overset{''}{.}0$	
Galactocentric Location	$6\overset{''}{.}5$ W, $5\overset{''}{.}9$ N	3
Time of explosion	$t_0 = 10.5$ December 2013 (UTC) (JD 2456637.0 ± 1.5 day)	1
Total reddening	$E(B-V) = 0.100 \pm 0.069$ mag	1
	SN 2014G	
NGC 3448:		
Type	Sab	2
RA (J2000)	$\alpha = 10^{\rm h}54^{\rm m}39\overset{\rm s}{.}4$	2
DEC (J2000)	$\delta = 54°18'18\overset{''}{.}8$	2
Abs. Magnitude	$M_B = -20.07$ mag	2
Distance	$D = 24.4 \pm 9.0$ Mpc	2
Distance modulus	$\mu = 31.94 \pm 0.80$ mag	
Heliocentric Velocity	$cz_{\rm helio} = 1372 \pm 8\,{\rm km\,s^{-1}}$	4
SN 2014G:		
RA (J2000)	$\alpha = 10^{\rm h}54^{\rm m}34\overset{\rm s}{.}1$	5
DEC (J2000)	$\delta = 54°17'56\overset{''}{.}9$	
Galactocentric Location	$44''$W, $20''$N	5
Time of explosion	$t_0 = 12.2$ January 2014 (UTC) (JD 2456669.7 ± 1.4 day)	1
Total reddening	$E(B-V) = 0.254 \pm 0.072$ mag	1

(1) This work; (2) HyperLEDA - http://leda.univ-lyon1.fr (Makarov et al., 2014); (3) Antezana et al. (2013); (4) Tully & Fisher (1988); (5) Denisenko et al. (2014)

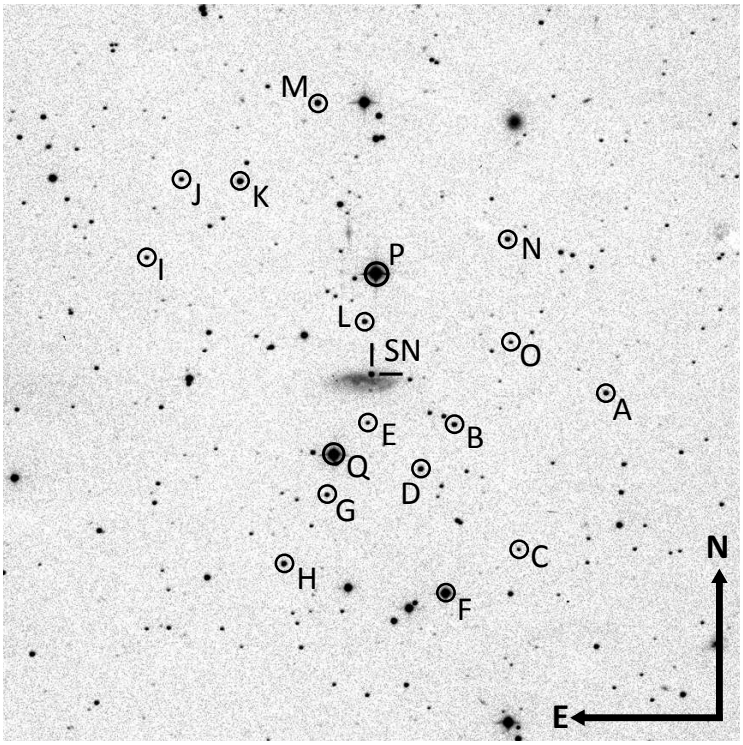

Figure 7.1: SN 2013hj in MCG -02-24-3. The V-band image taken from 104-cm ST covering a subsection of about $11' \times 11'$ is shown.

then subtracted by estimated background flux resulting into true SN flux free from galaxy contamination. This entire process is achieved with set of self written scripts which employs DAOPHOT within it. In principle, the technique of template image subtraction should be adopted for best results (Alard, 2000; Alard & Lupton, 1998). However, in this technique there are number of shortcoming with data obtained from small ground based telescopes. Stellar point spread function (PSF) may often be degraded in terms of minor elongation and skewness due to defect in passive telescope optics, which may further vary depending on telescope's altitude-azimuth. In such cases, PSF matching becomes non trivial and may leave behind significant and arbitrary residual in flux. In our case, such defects are prevailing in several images when the SNe were observed at high zenith angles.

To standardize both the SNe fields, four Landolt (2009) standard fields (PG 1323, PG 1633, SA 104 and SA 107) were observed on March 08 2014 from 104-cm

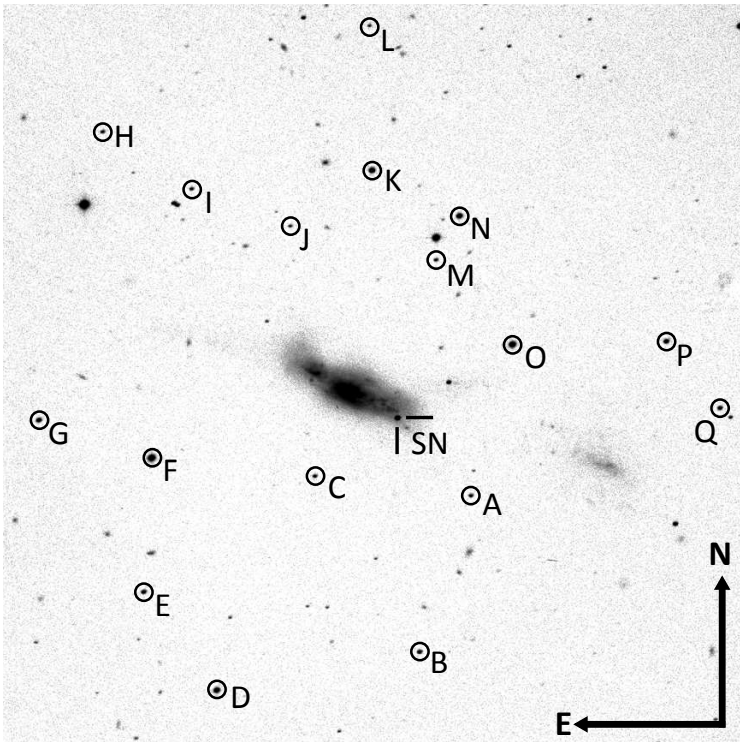

Figure 7.2: SN 2014G in NGC 3448. The V-band image taken from 104-cm ST covering a subsection of about $11' \times 11'$ is shown.

ST under good photometric night and seeing (FWHM $\sim 2''$ in V band) conditions. For determination of atmospheric extinction, multiple standard fields were observed with varying air masses. SNe fields were also observed during the same night, so that the derived transformation can be used to calibrate instrumental magnitudes of SNe. The obtained transformation equations with zero-point, color and atmospheric extinction coefficients are given as,

$$
\begin{aligned}
u &= U + (7.841 \pm 0.012) - (0.071 \pm 0.013) \cdot (U - B) + (0.660 \pm 0.034) \cdot X \\
b &= B + (5.319 \pm 0.010) - (0.072 \pm 0.010) \cdot (B - V) + (0.402 \pm 0.020) \cdot X \\
v &= V + (4.715 \pm 0.007) - (0.063 \pm 0.006) \cdot (B - V) + (0.247 \pm 0.014) \cdot X \\
r &= R + (4.429 \pm 0.007) - (0.057 \pm 0.010) \cdot (V - R) + (0.259 \pm 0.024) \cdot X \\
i &= I + (4.892 \pm 0.010) - (0.050 \pm 0.010) \cdot (V - I) + (0.117 \pm 0.015) \cdot X
\end{aligned}
$$

where *ubvri* are instrumental magnitudes corrected for time and aperture, *UBVRI* are standard magnitudes and X is the airmass. These transformation equations are applied to the SNe fields to calibrate 17 secondary standard stars in each of the fields of SNe 2013hj and 2014G. The secondary standards are marked in Fig. 7.1 and Fig. 7.2, and their calibrated magnitudes are listed in Table 7.A.1. The final photometry of SN 2013hj and SN 2014G are tabulated in Tables 7.A.2 and 7.A.3 respectively.

SN 2014G was also observed with UVOT (Roming et al., 2005) on board *Swift* spacecraft (Gehrels et al., 2004), in all six UVOT bands (*uvw2, uvm2, uvw1, uvu, uvb, uvv*). The UVOT photometry was obtained from *Swift* Optical/Ultraviolet Supernova Archive (SOUSA; Brown et al., 2014). The reduction procedure for UVOT photometry is based on Brown et al. (2009), which include subtraction of background galaxy counts, and adopting the revised zero-points and time dependent sensitivity from Breeveld et al. (2011). The UVOT photometry for SN 2014G is presented in Table 7.A.3.

7.2.2 Polarimetry

Broadband polarimetric observations in R-band have been carried out for SNe 2013hj and 2014G using ARIES Imaging Polarimeter (AIMPOL; Rautela et al., 2004) mounted at 104cm ST telescope. The unvignetted field of view of the CCD image is $\sim 8'$. Stellar FWHM is found to vary within 2 to 3 pixels, CCD read-noise and gain are 7.0e$^-$and 11.98 e$^-$/ADU respectively.

Bias correction and cosmic ray removal is done following usual procedure. The Wollaston prism splits light into ordinary and extraordinary rays and make it incident on the CCD. The corresponding stellar images are separated by $\sim$ 28 pixels along the north-south direction on the sky plane. Images are taken in four positions by rotating the half-wave plate through an angle $\alpha = 0°$, $22.5°$, $45°$ and 67.5 and the corresponding reduced stokes parameters are designated as $q1$, $u1$, $q2$ and $u2$ respectively and are determined as,

$$R(\alpha) = \frac{I_e(\alpha)/I_o(\alpha) - 1}{I_e(\alpha)/I_o(\alpha) + 1} = P\cos(2\theta - 4\alpha). \tag{7.1}$$

Here, I_o and I_e are the intensities of ordinary and extraordinary stellar images determined from standard aperture photometry. P is the fraction of linear polarization and θ is the angle of polarization plane. Correction factor for nonuniform responsivity of (i) CCD pixels and (ii) system to orthogonal polarized beams, is also introduced as a ratio described by Ramaprakash et al. (1998),

$$\frac{F_o}{F_e} = \left[\frac{I_o(0^\circ)}{I_e(45^\circ)} \times \frac{I_o(45^\circ)}{I_e(0^\circ)} \times \frac{I_o(22.5^\circ)}{I_e(67.5^\circ)} \times \frac{I_o(67.5^\circ)}{I_e(22.5^\circ)}\right]^{0.25}, \tag{7.2}$$

which are multiplied with I_e/I_o ratios in Eq. 7.1. The obtained $q1, u1, q2, u2$ values are fitted with *cosine* function to obtain P and θ. In principle, a single set of q and u value is sufficient to determine polarization parameters, but all four stokes parameters are used as a redundancy check. The errors associated with stokes parameters are dominated primarily by photon statistics and is expressed as (Ramaprakash et al., 1998),

$$\sigma_{R(\alpha)} = (\sqrt{N_e + N_o + N_{Be} + N_{Bo}})/(N_e + N_o), \tag{7.3}$$

which are further propagated appropriately in deriving polarization parameters. Here N_o, N_e are ordinary and extraordinary counts and N_{Bo}, N_{Be} are ordinary and extraordinary background counts respectively for a position α.

Along with SNe, a number of polarized and unpolarized standards (Schmidt et al., 1992b) have been also observed to estimate instrumental polarization and correct the zero-point polarization angle which mainly originate from imperfection in manual alignment of the instrument. For the polarized standards, the degree of polarization P measured from the instrument is found consistent within limit of errors and any offset found in the measured and standard values of polarization angle θ is corrected in the measurements for SNe. Using unpolarized standards, the instrumental polarization is found to vary within 0.03 to 0.10%, which is consistent to that found by other authors for AIMPOL (see e.g., Eswaraiah et al., 2013; Rautela et al., 2004). Since the direction of polarization is not confined to any particular plane and the value itself is very small (within error limits), we have not subtracted this from our observational measurements.

To have an estimate of the polarization towards the direction of SNe 2013hj

and 2014G due to Galactic dust,we also observed a number of bright field stars (on April 22 2015) within a average radius of $\sim 5^{\circ}$ around corresponding targets. The V-band polarization observations of these bright field stars are also presented in Heiles (2000). We have observed 11 and 3 field stars in the direction of SNe 2013hj and 2014G respectively.

The observed polarization measurements for SNe 2013hj and 2014G are listed in Table 7.B.1 and those for field stars are tabulated in Table 7.B.2.

7.3 Distance and extinction

Distance and total line-of-sight extinction are the two parameters which are important to study the intrinsic properties of SNe. Thus it is essential to determine these parameters for each of the SNe, before we characterize and analyze them.

SN 2013hj

MCG -02-24-3 hosts SN 2013hj at the edge of the projected view of the diffused spiral galaxy. As there is no redshift independent distance available in the literature, we adopt a redshift distance of 28.2 ± 2.0 Mpc from `Hyperleda`[1] (Makarov et al., 2014) corrected for Virgo infall velocity and assuming $H_0 = 70$ km s^{-1}Mpc^{-1}, $\Omega_m = 0.27$, $\Omega_\Lambda = 0.73$. However there are well accepted techniques which utilizes observations of type II SN itself to determine its distance. EPM (Bose & Kumar, 2014a; Jones et al., 2009; Kirshner & Kwan, 1974) and SCM (Hamuy & Pinto, 2002; Olivares et al., 2010) are two such methods which has been successfully implemented on several SNe II to estimate redshift independent distances, but requires extensive spectroscopic information as well which restricts us from implementing these methods on both of these SNe.

The most widely adopted method to estimate line-of-sight extinction is from correlation of narrow Na I D absorption line equivalent width with the reddening $E(B-V)$ (see Barbon et al., 1990; Poznanski et al., 2012b; Turatto et al., 2003). Since our dataset is only limited to photometry, we can not adopt this method which

[1] http://leda.univ-lyon1.fr/

requires SN spectrum of good resolution and high SNR. In order to determine total extinction we need estimates for both Milky way and host galaxy extinction. Using the all-sky Galactic extinction map by Schlafly & Finkbeiner (2011), we adopt a reddening value of $E(B-V)_{\rm MW} = 0.045 \pm 0.002$ mag due to Milky Way. To have an estimate of extinction due to host galaxy we implement the "color-method" (Olivares et al., 2010), which assumes that intrinsic $(V-I)$ color towards the plateau end is constant. Olivares et al. (2010) found an empirical relation between color and visual extinction as,

$$\begin{aligned} A_V(V-I) &= 2.518[(V-I)-0.656] \\ \sigma_{(A_V)} &= 2.518\sqrt{\sigma^2_{(V-I)} + 0.053^2 + 0.059^2} \end{aligned} \tag{7.4}$$

Putting a $(V-I)$ color of 0.725 ± 0.031 mag, which is a low-order cubic interpolated value at 75d and corrected for Galactic extinction, we derive the host galaxy visual extinction of $A_{V_{host}} = 0.172 \pm 0.069$ mag. Therefore, the adopted total line-of-sight visual extinction is $A_V = 0.312 \pm 0.214$ mag, which translates to $E(B-V) = 0.100 \pm 0.069$ mag assuming the ratio of total to selective extinction $R_V = 3.1$.

SN 2014G

SN 2014G is hosted in the galaxy NGC 3448. From previous studies, only a single redshift independent distance estimate is available using Tully-Fisher method (Tully & Fisher, 1988) for the galaxy, which is 24.4 ± 9.0 Mpc. We adopt this distance for SN 2014G throughout the chapter.

The value of reddening due to Milky Way towards NGC 3448 is found to be $E(B-V)_{\rm MW} = 0.010 \pm 0.000$ mag from the all-sky Galactic dust-extinction survey (Schlafly & Finkbeiner, 2011). To estimate the host galaxy extinction for SN 2014G, we implement the color-method (Olivares et al., 2010) as described in the case of SN 2013hj. Following their prescription, using $(V-I) = 0.956 \pm 0.038$ mag (interpolated at 56 day after correcting for Galactic extinction) in Eq. 7.4, we obtain host visual extinction $A_{V_{host}} = 0.755 \pm 0.222$ mag. Thus summing up, we adopt a total extinction of $A_V = 0.787 \pm 0.222$ mag, corresponding to a reddening value

$E(B-V) = 0.254 \pm 0.072$ mag.

7.4 Optical light curve

7.4.1 Apparent magnitude light curves

SN 2013hj

UBVRI broadband photometric observations of SN 2013hj are available at 117 phases from 3 to 170d. The data coverage is dense and almost continuous during this span. The resultant light curves are shown in Fig. 7.1.

The early light curves show a sharp rise in *RI* bands, which is also visible in *BV* bands but relatively much flatter. After the initial peak the light curves decline slowly until the plateau end. SN 2013hj does not show very sharp transition in slope at the end of plateau as is seen in generic SNe IIP, e.g., SNe 1999em (Leonard et al., 2002c), 1999gi (Leonard et al., 2002b), 2004et (Sahu et al., 2006), 2013ab (Bose et al., 2015a). Rather the light curve shows linearity only up to $\sim$ 80d, thereafter it shows a gradual increase in slope until it reaches the end of plateau at around $\sim 96-100$d. At the end of plateau, the light curve declines steeply to settle onto a relatively slow declining radioactive tail at $\sim$ 118d, which continues till the end of our observations.

The light curve parameters of SN 2013hj are listed in Table 7.1 (Rows:1–3). The time of peak in early light curves (Tab. 7.1, Row:1) are consistent with most typical and common fast-rising SNe IIP like 2005cs (Pastorello et al., 2009), 2004et (Sahu et al., 2006) and 2013ab (Bose et al., 2015a), which is significantly faster than slow-rising SNe e.g. SNe 2006bp (Quimby et al., 2007), 2009bw (Inserra et al., 2012b) and 2012aw (Bose et al., 2013). After the initial peaks the light curves continue to decline during the entire plateau phase, however in *R* and *I* bands a break in slope is visible at 23 and 24 days respectively. This break is possibly the mark of emergence of recombination phase, as the shock heated ejecta is cooling down and recombination starts to power the light curve. Such a feature, but more prominent, was also seen in *VRI* bands of type IIP SN 2012aw (Bose et al., 2013).

Since the initial peak SN 2013hj continues to decline, but does not show a constant slope towards the plateau end. During 80 to 100d light curve slope increase gradually, the plateau slope for the linear part is listed in Tab. 7.1 (Row:2). This is steeper than the values reported for generic type IIP SNe 1999em (Leonard et al., 2002c), 1999em (Leonard et al., 2002b), 2012aw (Bose et al., 2013) and 2013ab (Bose et al., 2015a), but flatter than the fast declining SNe like SN 2013by (Valenti et al., 2015), SN 2013ej (Bose et al., 2015b) and 2014G (this work). For example, decline rates for SN 2012aw are 5.60, 1.74, 0.55 mag (100 d)$^{-1}$ in UBV-bands and for SN 2013ab decline rates are 7.60, 2.72, 0.92, 0.59 and 0.30 mag (100 d)$^{-1}$ in $UBVRI$ bands, whereas SN 2013ej decline rates are 6.60, 3.57, 1.74, 1.07 and 0.74 mag (100 d)$^{-1}$. Decline rates for radioactive tail phase in VRI bands are listed in Tab. 7.1 (Row:3), where U and B band slopes were not computed due to large errors in tail data points.

SN 2014G

Photometric measurements in $UBVRI$ bands for SN 2014G were made at 63 phases during 4 to 319d, where continuous and high-cadence observation were only during 4 to 166d, with a late nebular data point at 319d recovered only after galaxy background subtraction. Additionally 15 phases of UVOT observations during 2 to 27d is also available in all six UVOT bands (*uvw1, uvw2, uvm2, uvu, uvb* and *uvv*). The light curves are shown in Fig. 7.2.

The early part of light curves show a sharp rise in most of the optical bands ($BVRI$ and *uvb, uvv*). The rising is detectable in UV bands as well except for *uvm2* and *uvw2* bands. After the initial peak all the light curves decline linearly until plateau end ($\sim$ 77d), like a generic SNe IIL (SN 1980K; Barbon et al. 1982 and SN 2013by; Valenti et al. 2015). From $\sim$ 77d, the light curve decline steeply to enter relatively slow declining radioactive tail phase starting from $\sim$ 90d.

The light curve parameters for SN 2014G are tabulated in Table 7.1 (Rows:4–6). Early rising of SN 2014G light curve (Tab. 7.1, Rows:4) is consistent with slow rising SNe, e.g, the V-band maximum is delayed to 16d in SN 2006bp (Quimby et al., 2007), 13d in SN 2009bw (Inserra et al., 2012b) and 15d in SN 2012aw (Bose

Table 7.1: Light curve parameters of SN 2013hj and SN 2014G.

	Row No.	Parameter	*U*	*B*	*V*	*R*	*I*	*uvw2*	*uvm2*	*uvw1*	*uvu*	*uvb*	*uvv*
SN 2013hj	1	Rise time of early peak (days)	–	6	8	11	12	–	–	–	–	–	–
	2	Plateau slope [mag (100 d)$^{-1}$]	5.81	3.38	1.50	0.89	0.77	–	–	–	–	–	–
	3	Nebular slope [mag (100 d)$^{-1}$]	–	–	0.72	0.81	0.76	–	–	–	–	–	–
SN 2014G	4	Rise time of early peak (days)	6	10	13	15	17	–	–	5	6	10	11
	5	Plateau slope [mag (100 d)$^{-1}$]	6.66	4.09	2.55	1.97	1.83	18.63	20.40	15.33	–	–	–
	6	Nebular slope [mag (100 d)$^{-1}$]	–	1.40	1.57	1.52	1.78	–	–	–	–	–	–

et al., 2013). This is significantly slower than most typical type II SNe, like SNe 2005cs, 2004et, 2013ab or the other SN which we present here - SN 2013hj.

After reaching maxima, SN 2014G light curves in all bands shows linear decline throughout the plateau and their decline rates are listed in Tab. 7.1 (Rows:5). These values are similar to that of type IIL SNe like SN 1980K and SN 2013by, but much steeper than all type IIP SNe (decline rates as mentioned above for SNe 2012aw and 2013ab). For example, SN 2013by (Valenti et al., 2015) shows a recline rate of 3.62, 2.01, 1.42 and 1.26 mag (100 d)$^{-1}$ in *BVri* bands and 19.53, 20.54 and 15.26 mag (100 d)$^{-1}$ in *uvw2, uvm2, uvw1* bands. The decline rates for radioactive tail light curves are also listed Tab. 7.1 (Rows:6). The slope of radioactive tail light curve is also found to be steeper than normal IIP SNe (e.g. SN 2013ab tail slopes are 0.36, 0.97, 0.66, 1.16 mag (100 d)$^{-1}$ in *BVri* or in SN 2012aw tail slopes are 0.88, 0.88, 0.81, 0.95 mag (100 d)$^{-1}$ in *BVRI*) but very similar to that found in SN 2013ej (Bose et al., 2015b, tail slopes are 1.22, 1.53, 1.42, 1.55 mag (100 d)$^{-1}$ in *BVRI* bands).

7.4.2 Absolute magnitude light curves

Absolute V-band (M_V) light curves of SNe 2013hj and 2014G are shown in Fig. 7.3 and are compared with a moderately sized sample of SNe II. In order to determine light curve characteristics of these two SNe and mark their position in the type II diversity, we selected the comparison sample with diverse range of properties, comprising of archetypal type IIP SNe 1999em, 1999gi, 2012aw to prototypical type IIL SN 1980K. The plateau slopes for all SNe II sample shown in Fig. 7.3 are listed in Table. 7.2. This table and figure is primarily an adaptation from Bose et al. (2015b).

The mid plateau absolute magnitude for SN 2013hj is highest amongst the compared sample of events. However, it may be noted that uncertainty in adopted reddening and distance values may alter this inference to some extent. The plateau decline rate of SN 2013hj is higher than most generic IIP SNe (e.g., SN 1999em, SN 2005cs, SN 2012aw) but lower than IIL SNe 1980K or 2000dc. According to Faran et al. (2014), type II SN with plateau decline of at least 0.5 mag in first 50 days

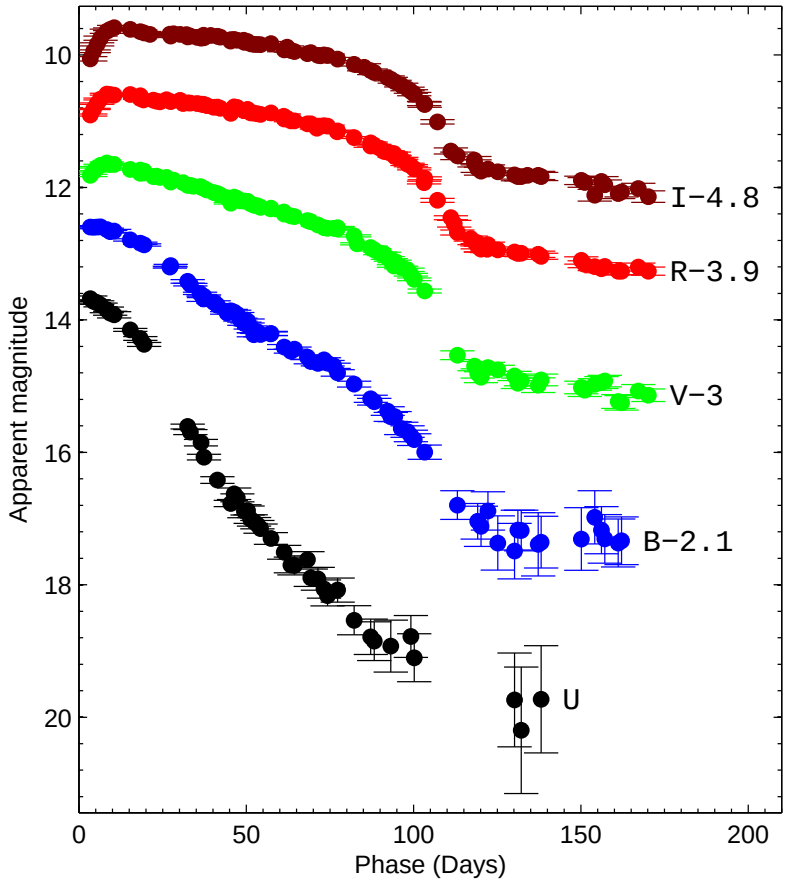

Figure 7.1: The photometric light curve of SN 2013hj in Johnson-Cousins *UBVRI* bands. The light curves are shifted arbitrarily for clarity.

would be classified as type IIL, which would definitely classify SN 2013hj as type IIL. However, this criteria proposed by Faran et al. (2014) is a bit too rigid, as it would reclassify all SNe up to slopes of SN 2012A (see Table 7.2) as type IIL. Faran et al. (2014) also presented template light curve range for SNe IIP and IIL, which is shown in Fig. 7.3. SN 2013hj lies marginally outside the lower slope range of SNe IIL templates, whereas it is very much lower than the IIP template presented in the figure. Thus, if SN 2013hj has to be classified either between type IIP or IIL, it would fit best in the class of type IIL rather than type IIP. The closest comparison to SN 2013hj in terms of plateau slope, shape and duration is SN 2013ej. However, plateau decline of SN 2013ej is a bit more steep than SN 2013hj making it compatible

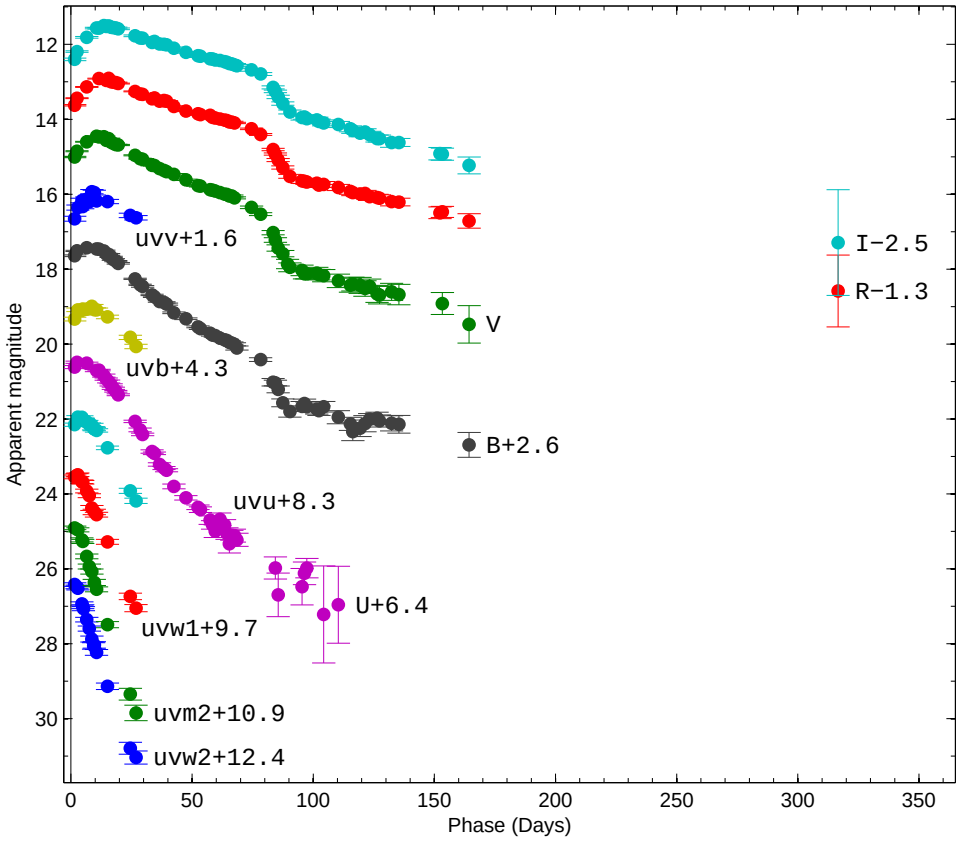

Figure 7.2: The photometric light curve of SN 2014G in Johnson-Cousins *UBVRI* and *Swift* UVOT bands. The light curves are shifted arbitrarily for clarity.

to SNe IIL light curve templates.

On the other hand, owing to the fast decline of SN 2014G, its mid-plateau magnitude is lower than SN 2013hj, but the peak luminosity is highest amongst the compared sample. The decline rate is higher than all SNe II in the sample, except for prototypical type IIL SN 1980K and SN 2000dc. The plateau slope of SN 2014G is marginally over the SNe IIL template, thus clearly qualifying as a type IIL SN. SN 2013by is the closest comparison to SN 2014G in terms of light curve shape and magnitudes except for the fact that SN 2014G plateau is steeper and the nebular tail is brighter. The decline rate of tail light curve is 1.57 mag $(100\ \mathrm{d})^{-1}$, which is higher than that expected for light curve powered from radioactive decay of ^{56}Co to ^{56}Fe. However, such steepening of tail light curve was also seen in other type IIL SNe as

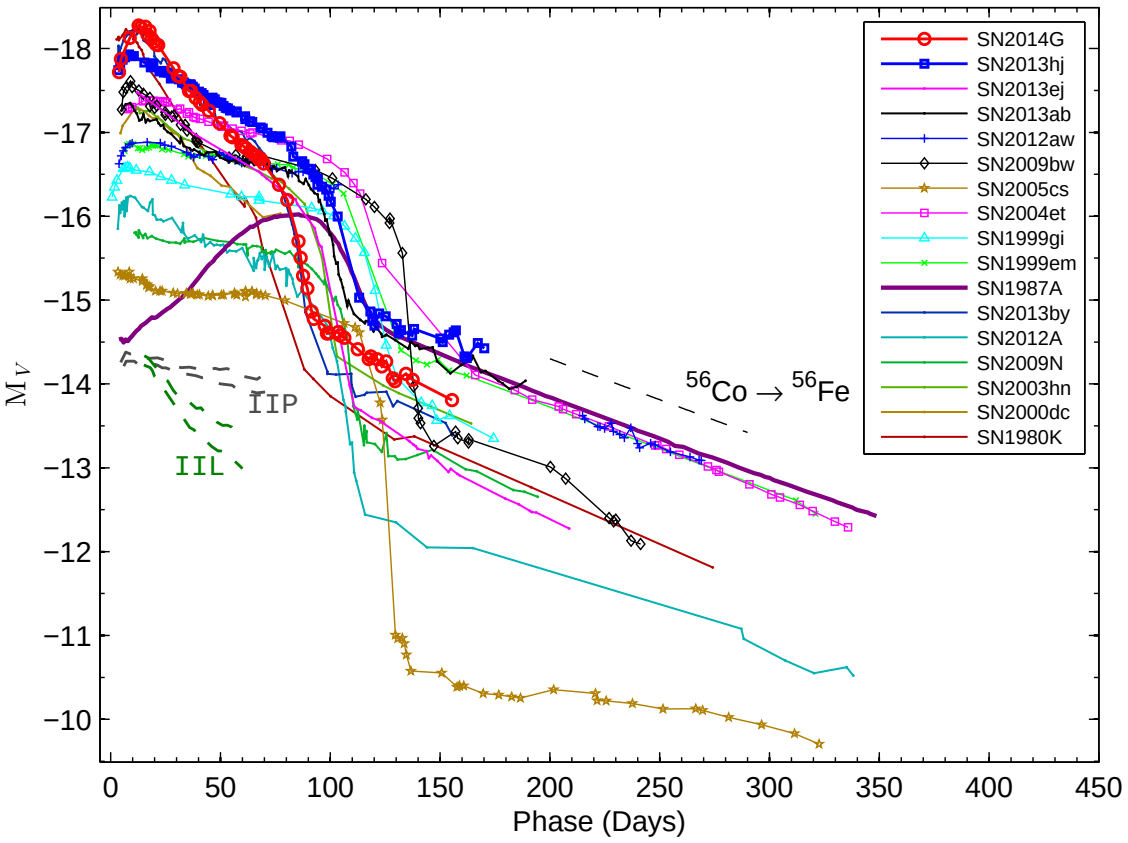

Figure 7.3: Absolute V band light curves of SNe 2013hj and 2014G are compared with other type II SNe. The exponential decline of the tail light curve following the radioactive decay of ^{56}Co→^{56}Fe is shown with a dashed line. On the bottom left side, two pair of dotted lines in gray and green colors represent the slope range for type IIP and IIL SNe templates as presented by Faran et al. (2014). The adopted explosion time in JD-2400000, distance in Mpc, $E(B-V)$ in mag and the reference for observed V-band magnitude, respectively, are : SN 1980K – 44540.5, 5.5, 0.30; Barbon et al. (1982), NED database; SN 1987A – 46849.8, 0.05, 0.16; Hamuy & Suntzeff (1990); SN 1999em – 51475.6, 11.7, 0.10; Elmhamdi et al. (2003b); Leonard et al. (2002c); SN 1999gi – 51522.3, 13.0, 0.21; Leonard et al. (2002b); SN 2000dc – 51762.4, 49.0, 0.07; Faran et al. (2014), NED database; SN 2003hn – 52866.5, 17.0, 0.19; Anderson et al. (2014b); Krisciunas et al. (2009); SN 2004et – 53270.5, 5.4, 0.41; Sahu et al. (2006); SN 2005cs – 53549.0, 7.8, 0.11; Pastorello et al. (2009); SN 2009N – 54848.1, 21.6, 0.13; Takáts et al. (2014); SN 2009bw – 54916.5, 20.2, 0.31; Inserra et al. (2012b); SN 2012A – 55933.5, 9.8, 0.04; Tomasella et al. (2013); SN 2012aw – 56002.6, 9.9, 0.07; Bose et al. (2013); SN 2013ab – 56340.0, 24.0, 0.04; Bose et al. (2015a); SN 2013by – 56404.0, 14.8, 0.19; Valenti et al. (2015); SN 2013ej – 56497.3, 9.6, 0.06; Bose et al. (2015b).

Table 7.2: Parameters estimated from V band light cruve

SN Name	Plateau slope[a] mag (100 d)$^{-1}$	Transition drop[b] mag	Transition time[c] days
SN1980K	3.63 ± 0.04	2.0±0.2	37 ± 5
SN2000dc	2.56 ± 0.06[i]	–	–
SN2014G	2.55 ± 0.02	1.6±0.2	17 ± 2
SN2013by	2.01 ± 0.02	2.2±0.2	19 ± 5
SN2013ej	1.74 ± 0.08	2.4±0.1	21 ± 3
SN2013hj	1.50 ± 0.02	1.5±0.2	22 ± 5
SN2003hn	1.41 ± 0.04	2.0±0.2	19 ± 4
SN2012A	1.12 ± 0.03	2.5±0.1	23 ± 4
SN2009bw	0.93 ± 0.04	2.4±0.2	14 ± 3
SN2004et	0.73 ± 0.02	2.1±0.2	27 ± 6
SN2013ab	0.54 ± 0.02	1.7±0.1	25 ± 2
SN2012aw	0.51 ± 0.02	–	–
SN1999gi	0.47 ± 0.02	2.0±0.1	29 ± 3
SN2005cs	0.44 ± 0.03	4.0±0.1	24 ± 3
SN2009N	0.36 ± 0.03	2.0±0.2	26 ± 3
SN1999em	0.31 ± 0.02	1.9±0.1	28 ± 4

Note: Objects are sorted in order of descending plateau slope.
[a] Plateau slope during the linear decline phase, starting after first minima until plateau end.
[b] Drop in magnitude during the plateau to nebular transition.
[c] Duration of plateau to nebular transition.
[i] Slope is calculated up to the available range of data, as plateau end is not observed.

well. For example, SN 2013ej exhibits a steeper decline rate of 1.53 mag (100 d)$^{-1}$ (Bose et al., 2015b), similarly other IIL SNe 1980K and 2013by also show steeper declines like SN 2014G (see Fig. 7.3). In Fig. 7.4 we show the *Swift* UVOT absolute magnitude light curves for SN 2014G in UV bands and are compared with other SNe II which are well observed by UVOT. UV light curve evolution of SN 2014G is found similar to other SNe. The peak brightness closely matches to that of SN 2013by but is higher than most other SNe in the sample.

Based on the light curve parameters, SN 2014G is a perfect example of generic type IIL SN whereas SN 2013hj belongs to an intermediate class with plateau slope

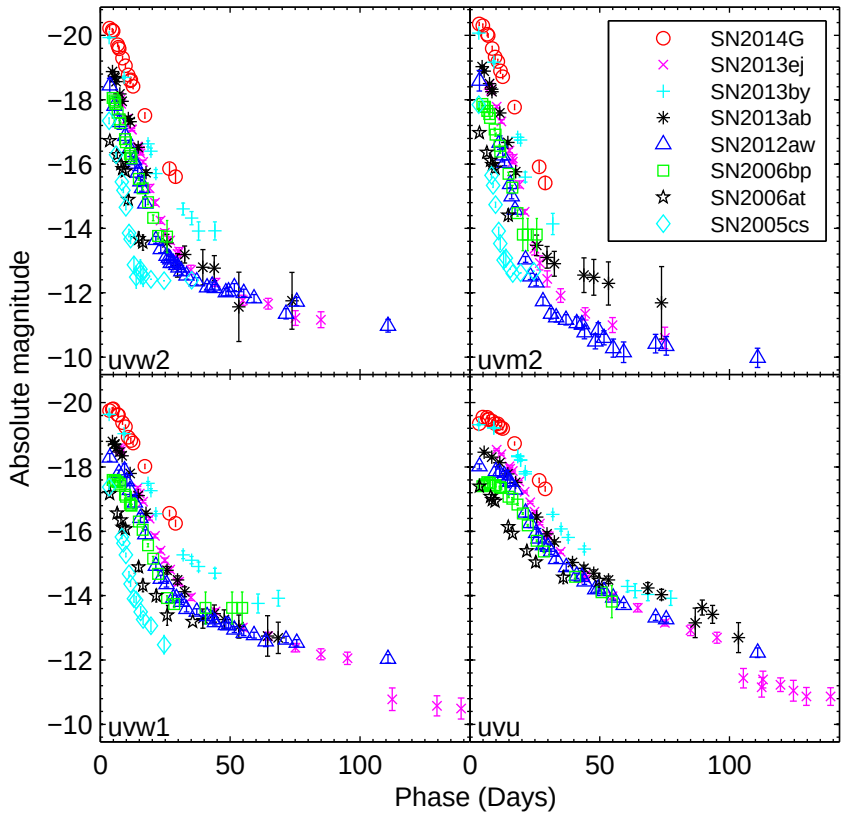

Figure 7.4: *Swift* UVOT UV absolute light curves of SN 2014G is compared with other well observed SNe II from UVOT. For the compared SNe, references for UVOT data, extinction and distance are: SN 2005cs – Brown et al. (2009); Pastorello et al. (2009), SN 2006at – Brown et al. (2009); Distance 65 Mpc; $E(B-V) = 0.031$ mag (only Galactic reddening Schlafly & Finkbeiner, 2011), SN 2006bp – Dessart et al. (2008), SN 2012aw – Bayless et al. (2013); Bose et al. (2013), SN 2013by – Valenti et al. (2015), SN 2013ej – (Bose et al., 2015b).

close but lower than typical SNe IIL. With the adopted reddening and distance values, both the SNe lie on the luminous end of the comparison sample, which may eventually fall in the range of normal luminosity if reddening or distance values are lowered. Anderson et al. (2014b) found an anti-correlation between the plateau slope and duration, which is consistent with the trend as we see for SNe 2013hj and 2014G as well as other SNe in the sample.

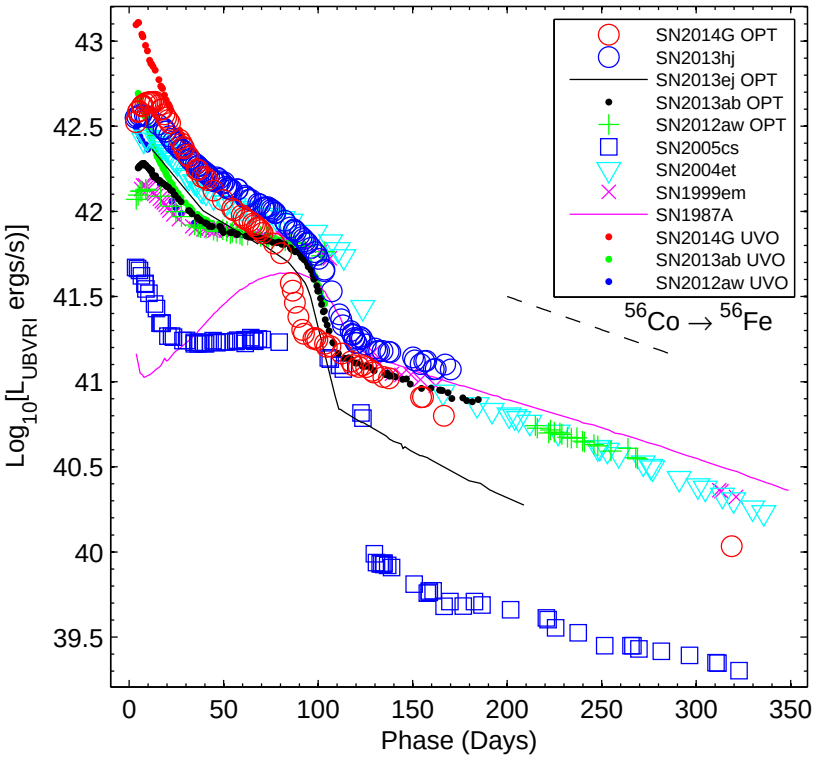

Figure 7.5: The *UBVRI* pseudo-bolometric light curves of SNe 2013hj and 2014G are compared with those of other well studied SNe. Light curves with added *Swift* UVOT UV contributions are also shown for SN 2013ej, SN 2013ab and SN 2012aw (labeled as UVO). The adopted distances, reddening and time of explosion values are same as in Fig. 7.3. The exponential decline of the radioactive ^{56}Co decay law is shown with a dashed line.

7.4.3 Bolometric light curve

Pseudo-bolometric light curves for SNe 2013hj and 2014G are computed using photometric fluxes corrected for adopted reddening and distance values. We follow the same method as outlined in Bose et al. (2013) to compute bolometric luminosities, which involves semi-deconvolution of broadband filter response from photometric fluxes. Thermal emission from SNe mostly peaks in optical and near-optical wavelengths depending on the phase of SN evolution. At early phases ($<$ 30d) when the SN is hot, UV wavelengths dominate bolometric luminosity. Likewise, at late phases ($>$ 100d) when the SN is cool enough, bolometric light is dominated by in-

frared fluxes. We compute pseudo-bolometric luminosity for both the SNe in the optical domain, which include *UBVRI* fluxes. For SN 2014G we also computed bolometric luminosity by taking UV fluxes into account, which include fluxes from *uvw2* to I bands. The UV+Optical luminosity yields a significantly higher value at early times. In Fig. 7.5 we compare bolometric light curves of SNe 2013hj and 2014G with other well-studied SNe. The bolometric light curves of the comparison sample were also computed using the same method and within the same wavelength range.

Bolometric light of SN 2013hj suffers almost a linear decline during 6 to 100d with a luminosity drop of ~ 0.85 dex. This decline rate is similar to SN 2013ej, but higher than most generic IIP SNe in the sample. An additional drop of 0.47 dex is seen at the end of plateau while light curve settles onto the radioactive nebular tail phase since 118d. The slope of tail light curve is similar to those of SNe 1987A, 1999em, 2004et and 2013ab which is consistent to that expected for ^{56}Co to ^{56}Fe radioactive decay rate.

SN 2014G shows a decline rate higher than all compared SNe including SN 2013hj. SN 2014G shows a linear decline throughout the plateau phase and experiences a drop of 0.89 dex in bolometric luminosity during 13 to 80d. A drop of 0.49 dex in luminosity is seen during the transition from plateau to nebular phase. SN 2014G light curve settles onto relatively slow declining radioactive tail phase after 92d. The slope during this phase is found to be somewhat steeper (0.39 dex $(100)^{-1}$d) than other generic IIP SNe (e.g. SNe 1987A, 1999em, 2004et, 2013ab), and also that expected for a light curve powered by radioactive decay of ^{56}Co to ^{56}Fe. On carefully examination of the absolute V-band and bolometric light curve (see Figs. 7.3 and 7.5), such steepening of tail light curve is also seen in other type IIL SNe 1980K, 2013by and 2013ej. Steepening of tail light curve would indicate inefficient trapping of gamma rays in the ejecta. In type IIL SNe, the hydrogen envelope is relatively more depleted than IIP counterpart, resulting into lower gamma ray optical depth causing leakage of gamma photons. Such a scenario may explain steeper tail light curve in SN 2014G, and this may also to true for all other fast declining SNe IIL as well. However, due to fast decaying brightness, there are only

a handful of SNe IIL with observations extending up to the tail phase and SN 2014G is the newest among such candidates.

7.4.4 Mass of nickel

In CCSNe, radioactive ^{56}Ni is produced by explosive nucleosynthesis at the time of explosion. The nebular phase light curve is mainly powered by the radioactive decay chain of ^{56}Ni to ^{56}Co and ^{56}Co to ^{56}Fe, with e-folding life time of 8.8 and 111.26 d respectively. Thus, the tail luminosity would be proportional to the amount of radioactive nickel synthesized at the time of explosion.

SN 1987A is one of the most well studied SN with a fair degree of accuracy in the estimation of ^{56}Ni mass ($0.075 \pm 0.005 M_\odot$; Arnett, 1980). By comparing the tail luminosity of a SN with that of SN 1987A, we can estimate the mass of ^{56}Ni for that SN as well. Although in principle true bolometric luminosities (including UV, optical and IR) are to be used to compute ^{56}Ni mass, but we do not have IR fluxes for either of SN 2013hj or SN 2014G. For the uniformity in comparison we also use *UBVRI* bolometric luminosity for SN 1987A, computed using the same method and wavelength range. We compute the ratio of SN 2013hj to SN 1987A luminosity at 150d to be 1.152 ± 0.168. This corresponds to a ^{56}Ni mass of M_{Ni}(2013hj) = 0.086 ± 0.013 M$_\odot$. Similarly, the ratio of SN 2014G to SN 1987A luminosity at 150d is 0.735 ± 0.552, which corresponds to M_{Ni}(2014G) = 0.055 ± 0.041 M$_\odot$.

The gamma photons emitted from the radioactive decay of ^{56}Co to ^{56}Fe are assumed to thermalize the ejecta powering the tail light curve, which in turn depends on the initial mass of synthesized ^{56}Ni. Hamuy (2003) related these parameters as,

$$M_{\rm Ni} = 7.866 \times 10^{-44} \times L_t \exp\left[\frac{(t_t - t_0)/(1+z) - 6.1}{111.26}\right] M_\odot,$$

where t_0 is the explosion time, 6.1d is the half-life of ^{56}Ni and 111.26d is the e-folding time of the ^{56}Co decay. Using the bolometric correction factor for tail phase as given by Hamuy (2003), we compute a tail luminosity of $2.71 \pm 0.20 \times 10^{41}$ erg at 150d for SN 2013hj, which correspond to ^{56}Ni mass of M_{Ni}(2013hj) = 0.077 ± 0.010 M$_\odot$. Likewise, tail luminosity of SN 2014G at 140d is $1.78 \pm 1.01 \times 10^{41}$ erg corresponding

to $M_{Ni}(2014G) = 0.045 \pm 0.035$ $M_{\odot}$.

The amount of ^{56}Ni masses estimated from both the methods are consistent with each other within errors. Thus we adopt a mean value of both the results, which is $M_{Ni}(2013hj) = 0.080 \pm 0.008$ $M_{\odot}$ for SN 2013hj, and $M_{Ni}(2014G) = 0.050 \pm 0.027$ $M_{\odot}$ for SN 2014G. Although the quoted errors in ^{56}Ni mass include uncertainty from adopted reddening and distance values, but does not take care of selection bias involved in these parameters. Estimated ^{56}Ni masses may be lowered if lower values of reddening or distance is assumed.

7.5 Light curve modelling

We model the bolometric light curves of SNe 2013hj and 2014G following the semi-analytical approach originally developed by Arnett (1980) and further refined in Arnett & Fu (1989). Such simplistic models (e.g. Arnett, 1980, 1982; Arnett & Fu, 1989; Chatzopoulos et al., 2012; Popov, 1993; Zampieri et al., 2003) are useful to get a preliminary yet reliable estimate of explosion parameters without running more accurate but resource intensive hydrodynamical models (e.g. Bersten et al., 2011; Falk & Arnett, 1977; Pumo & Zampieri, 2011; Utrobin, 2007). The model has been implemented by Nagy et al. (2014) and Bose et al. (2015b) for several type II SNe to estimate explosion parameters and are found to be fairly consistent with results from hydrodynamical models.

Description of model formulation and algorithm is presented in Bose et al. (2015b) and references therein. The temporal component of temperature evolution in a co-moving frame of expansion is given (Arnett & Fu, 1989; Nagy et al., 2014) as,

$$\frac{d\phi(t)}{dz} = \frac{R(t)}{R_0 x_i^3}\left[p_1\zeta(t) - p_2\phi(t)x_i - 2x_i^2\phi(t)\frac{R_0}{R(t)}\frac{dx_i}{dz}\right], \tag{7.5}$$

which is numerically solved with appropriate treatment of dimensionless recombination front x_i. After finding the solution for $\phi(t)$ and x_i, the model luminosity is

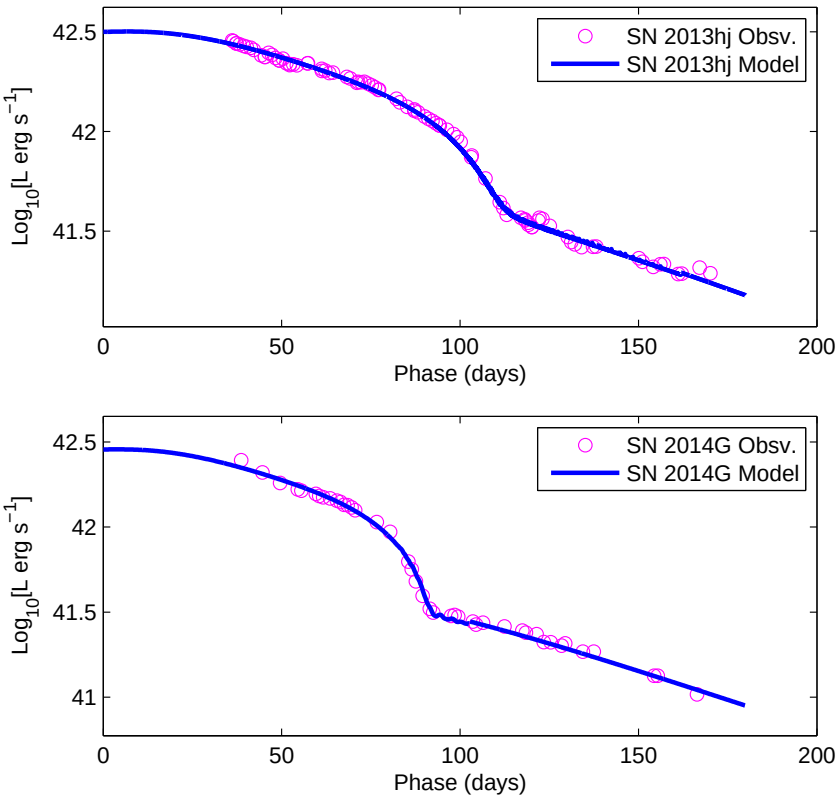

Figure 7.1: The observed bolometric light curves of SNe 2013hj and 2014G are shown with the best fit model.

computed as (Arnett & Fu, 1989; Bose et al., 2015b; Nagy et al., 2014),

$$L(t) = x_i \frac{\phi(t) E_{th}(0)}{\tau_d} \left(1 - e^{-A_g/t^2}\right) + 4\pi r_i^2 Q \rho(x_i, t) R(t) \frac{dx_i}{dt}. \tag{7.6}$$

The parameters in these equations have standard meaning as referred in aforementioned papers. A_g is the effectiveness of gamma ray trapping (see e.g., Chatzopoulos et al., 2012; Clocchiatti & Wheeler, 1997) which is an important parameter to model the steepened radioactive tail.

To implement the model, we require true bolometric luminosities for the SNe. Since our data is limited only to UV and optical, we add IR flux contribution assuming SNe 2013hj and 2014G have similar optical to IR flux ratio as observed for SN 1999em at similar phases. Fig. 7.1 shows the computed bolometric light curves

of SNe 2013hj and 2014G fitted with our model. Since these models are inefficient to reproduce post-breakout peaks of early light curves, we restricted the data only from later phase of plateau.

From the best fit model of SN 2013hj we estimate an ejecta mass of 9.6 $M_\odot$, progenitor radius of 700 $R_\odot$ and total explosion energy $\sim$ 2.1 foe. The mass of radioactive ^{56}Ni incorporated in the model is 0.075 $M_\odot$, which is consistent to the value estimated in Section 7.4.4. Assuming the mass of compact remnant to be 1.5–2.0 $M_\odot$, the total progenitor mass adds up to $\sim$ 11 $M_\odot$.

Similarly for SN 2014G, model estimated ejecta mass is 7.0 $M_\odot$, progenitor radius is 630 $R_\odot$ and total explosion energy is $\sim$ 2.1 foe. ^{56}Ni mass determined from model is 0.052 $M_\odot$ which is almost equal to the value estimated in Section 7.4.4. Adding up a mass of 1.5 – 2.0 $M_\odot$for the compact remnant, the total progenitor mass is $\sim$ 9 $M_\odot$. To fit the steepened tail light curve of SN 2014G, as already discussed in Sections 7.4.1 and 7.4.3, we increased the gamma ray leakage in the model by lowering the effectiveness of gamma ray trapping parameter A_g to 4×10^4day^2. This parameter is related to gamma-ray optical depth as $\tau_g \sim A_g/t^2$.

7.6 Broadband polarimetry

Broadband polarimetric observations in R-band has been carried out for SN 2013hj at 5 phases during 23 to 86d, whereas for SN 2014G only 3 phases of observation during 12 to 25d are available. The observed temporal evolution of P and θ for both the SNe, along with R-band absolute light curve is plotted (P and θ in dashed lines) in Fig. 7.1 (data is tabulated in Table. 7.B.1).

7.6.1 Estimation of interstellar polarization

The observed polarization in supernova light primarily has three components, intrinsic polarization due to SN itself, interstellar polarization due to Milk Way (ISP_{MW}) and interstellar polarization due to host galaxy (ISP_{HG}). Thus, in order to interpret the intrinsic polarization of SN, we need to subtract ISP components from the observed polarization. However, there is no completely reliable method to derive

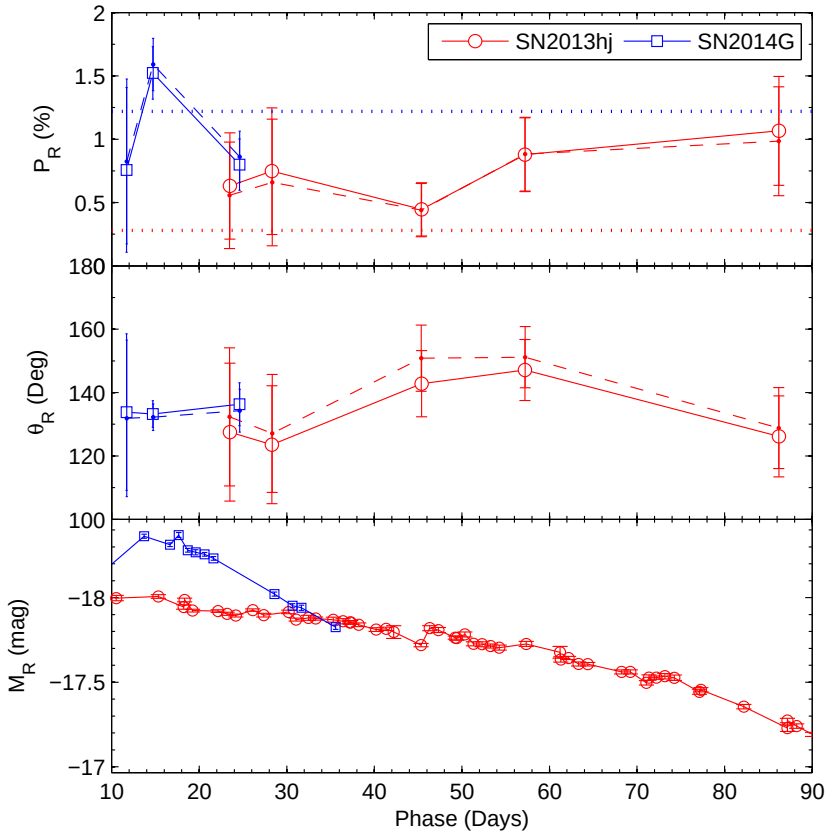

Figure 7.1: The degree of polarization P, polarization angle θ and absolute R-band magnitude M_R is plotted in three panels for SNe 2013hj and 2014G. The dashed lines in polarization plots represent the observed polarization parameters, whereas the solid connected plots represent polarization parameters after subtracting for $\mathrm{ISP_{MW}}$. The horizontal dotted lines in top panel represents maximum amount of mean host galaxy polarization component that could be present in SN polarization values (0.28 and 1.22 % for SNe 2013hj and 2014G respectively; see Sec. 7.6.1.2) which may be linearly subtracted if the polarization angles of host and SN are co-aligned. R-band light curves are truncated to only show phases where polarimetric data exists.

ISP and thus posses an issue in SN polarimetric studies. Number of methods have been proposed to estimate ISP (Trammell et al., 1993; Tran et al., 1997; Wang et al., 2001), but all involve some assumptions which are not always valid (Wang & Wheeler, 2008). Having this limitation, best possible attempt has been made to have a reasonable estimate of ISPs which are discussed in following sections.

7.6.1.1 Milky way

To get an estimate of $\mathrm{ISP_{MW}}$, we observed 11 bright stars towards the direction of SN 2013hj, within a maximum radius of 8° around the SN. The V-band polarization measurements of these stars are available in Heiles (2000) catalog. Similarly, field stars have also been observed towards the direction of SN 2014G, but due to scarcity of bright stars only 3 have been selected (within a maximum radius of 13°) also having polarization measurements in Heiles (2000). All these selected stars have very low V-band polarization values listed (Heiles, 2000). The measured R-band polarization (see Table 7.B.2) for these stars was also found to be low and of similar order as that of the V-band. To compute the median ISP from observed stars, averaging is done on stokes components and which is then converted back to polarization parameters. The median of stokes components are computed as,

$$\begin{aligned} \langle Q \rangle &= \langle\, P_i \cos(2\theta_i) \,\rangle_{i=1..n} \\ \langle U \rangle &= \langle\, P_i \sin(2\theta_i) \,\rangle_{i=1..n} \end{aligned} \tag{7.7}$$

which are then converted back to polarization parameters,

$$\begin{aligned} P_{\mathrm{MW}} &= \sqrt{\langle Q \rangle^2 + \langle U \rangle^2} \\ \theta_{\mathrm{MW}} &= \frac{1}{2} \tan^{-1} \left(\frac{\langle U \rangle}{\langle Q \rangle} \right). \end{aligned} \tag{7.8}$$

Thus, we obtain median $\mathrm{ISP_{MW}}$ as $P_{\mathrm{MW}} = 0.13 \pm 0.06\%$ and $\theta_{\mathrm{MW}} = 12.4 \pm 10.3°$ for SN 2013hj, while for SN 2014G, $P_{\mathrm{MW}} = 0.08 \pm 0.22\%$ and $\theta_{\mathrm{MW}} = 106.6 \pm 68.5°$. These $\mathrm{ISP_{MW}}$ values are then vectorially subtracted from the observed SN polarization which are also listed in Table 7.B.1 and plotted in (connected solid lines) Fig. 7.1.

According to Serkowski et al. (1975) the interstellar polarization efficiency due to Galactic dust is highly correlated to line-of-sight reddening, which may vary from 3 to 9 times the reddening value. As a reasonable approximation we adopt the mean polarization efficiency as $P_{\mathrm{mean}} = 5 \times E(B-V)$. Using this relation and Galactic reddening values adopted (refer Section 7.3) towards the direction each SN, we get

$P_{\rm mean}$ value of $\sim 0.23\%$ and $\sim 0.05\%$ for SNe 2013hj and 2014G respectively. These are roughly consistent with the $\rm ISP_{MW}$ values we computed from observations of field stars, which implies that Galactic ISM follows the mean polarization efficiency.

7.6.1.2 Host galaxy

For an accurate estimation of $\rm ISP_{HG}$, one needs to know dust grain properties and magnetic field orientation along the line of sight within the host galaxy. In context to few SNe studies, it has been found that size of dust grains in respective host galaxy were dissimilar to Galactic dust grains (see e.g. SN 1986G; Hough et al. 1987 and SN 2001el; Wang et al. 2003a). Due to very diverse nature of dust grains in various galaxies, it is non trivial to adopt mean polarization efficiency without the knowledge of grain properties. However, in order to get an idea of $\rm ISP_{HG}$ and for the sake of understanding its possible implication in SN polarization measurements, we assume dust grain properties of galaxies MCG -02-24-3 (for SN 2013hj) and NGC 3448 (for SN 2014G) are similar to Galactic dust. Now, we may estimate $P_{\rm mean}$ due to host galaxies following the same Serkowski et al. (1975) relation as mentioned above. In Section 7.3 we estimated host galaxy extinctions for both the SNe using color-method, which translates to $E(B-V)_{\rm host}$ values of 0.055 and 0.244 mag for SNe 2013hj and 2014G respectively, assuming $R_V = 3.1$. On applying the mean polarization relation $P_{\rm mean} = 5 \times E(B-V)$ (Serkowski et al., 1975), corresponding $P_{\rm mean}$ (for host) values are $\sim 0.28\%$ and $\sim 1.22\%$ for SNe 2013hj and 2014G respectively.

To vectorially remove ISP components from SN polarization one need to know the direction information as well. It is generally believed and also found to be true that galactic magnetic fields run along the spiral arms (Han, 2009; Scarrott et al., 1990, 1991), which is roughly perpendicular to the line joining galactic center and position of spiral arm (see e.g., Kumar et al., 2014; Leonard et al., 2001; Maund et al., 2007). However, in case of both SNe 2013hj and 2014G the host galaxies are almost irregular, not in face-on projection and SN location is not well resolved, this makes it difficult to make any reasonable estimate of the magnetic field orientation and effective line of sight polarization angle at SN locations.

Despite emphasizing all the critical aspects of ISP_{HG}, we do not subtract it from SN polarization measurements and make any speculative inference based on that. This was done mainly because of three uncertainties, (a) the reddening estimation of host galaxy is quite uncertain and may suffer systematic bias due to the method itself (see Section 7.3), (b) unknown grain properties in host galaxy may significantly vary the mean polarization efficiency we are adopting and (c) without knowing the polarization angle of host galaxy vectorial subtraction will not be possible as a subtraction of ISP component may increase or decrease polarization values depending on θ. Thus, we caution the reader while interpreting the quoted polarization values as well as Figures 7.1 and 7.2 in this chapter.

7.6.2 Intrinsic polarization and its evolution

The evolution of degree of polarization and the polarization angle of SNe 2013hj and 2014G are represented in Fig. 7.1. The evolution of polarimetric parameters of both the events are also compared with other well sampled SNe IIP as shown in Fig. 7.2. Here SN 1999em observations are V-band polarimetry, however temporal evolution in R-band is expected to be similar. In both the figures the polarization values for SNe 2013hj and 2014G are subtracted for ISP_{MW} only, thus these measurements have components for intrinsic SN polarization as well as ISP_{HG}. In Fig. 7.1 horizontal dotted lines are shown to represent the maximum degree of host polarization component which may be removed if orientation of host and measured SN polarization are assumed to be co-aligned. For any other θ of ISP_{HG}, the component of P in SN light will be lower than this level. It is to be noted that this level represents maximum possible subtraction of mean ISP_{HG} component as computed in Section 7.6.1.2, but does not represent the maximum possible ISP_{HG}.

It is clear from Fig. 7.1 that there is significant amount of intrinsic polarization is left ($\sim 0.3 - 0.8\%$) in SN 2013hj even after considering maximum subtraction of mean ISP_{HG}. The P and θ evolution does not show a significant relative variation among individual data points and is all within the limit of errors. However, a subtle increasing trend is noticed in overall P evolution, but θ remains almost constant throughout. This may imply that there is some asymmetry in electron scattering SN

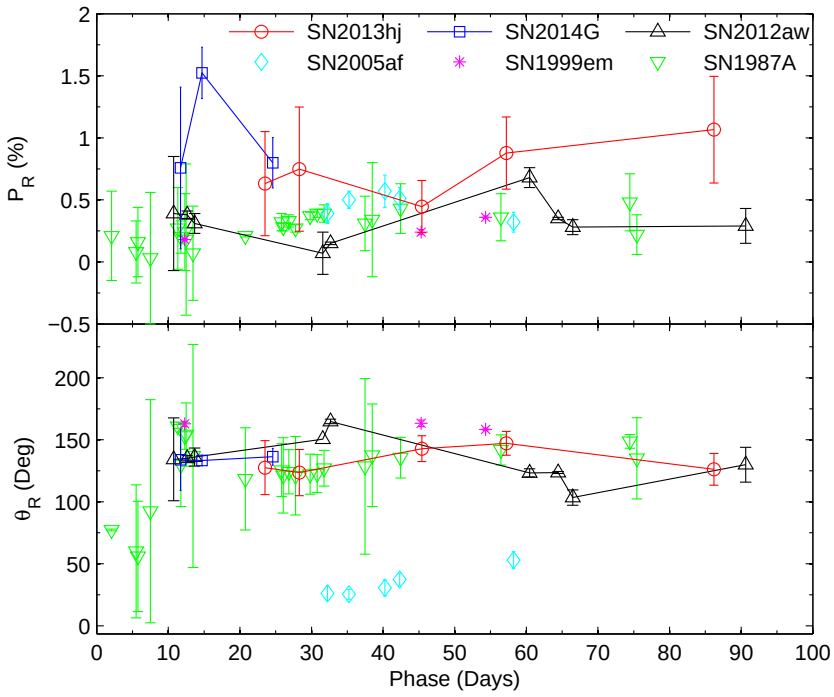

Figure 7.2: Broadband polarimetric evolution of SNe 2013hj and 2014G (only ISP_{MW} subtracted values) are compared with other type IIP SNe. The references for data and explosion epochs are: SN 1987A – Barrett (1988), SN 1999em – Leonard et al. (2001, 2002c), SN 2005af – Filippenko & Foley (2005); Pereyra et al. (2006) and SN 2012aw – Kumar et al. (2014).

envelope, which is increasing according to envelope size and decrease in optical depth revealing the asymmetric central part of explosion, but its geometrical orientation remains constant over time. It may be noted that the increase in polarization is almost linearly anti-correlated with the decline of SN brightness. Such monotonic increase in polarization without change in polarization angle has been also observed in SN 1999em (see Fig. 7.2) which was reported by Leonard & Filippenko (2005); Leonard et al. (2001) and also for SN 2004dj from spectropolarimetric observations (Leonard et al., 2006).

SN 2014G has only three measurements within first 25d. If maximum subtraction of ISP_{HG} is considered then almost no residual intrinsic polarization would be left (see Fig. 7.1). The polarization angle for ISP_{HG} would play an important role in this case, only after knowing which we may conclude on the intrinsic polarization

or asymmetry in SN envelope or CSM. Any favorable misalignment of ISP_{HG} angle may lead to significant residual SN polarization. A sudden and unusual increase in polarization in noticed at 15d which is coincident with the peak R-band light, although no change in polarization angle is observed. However, considering the large errors and low density of observations, we restrict ourselves from making any conclusive inference based on a single measurement which may be resulting from a spurious detection.

7.7 Summary

In this chapter we present high-cadence photometric observation and a few epochs of broadband polarimetric observation of two fast declining type II SNe 2013hj and 2014G.

Due to lack of reliable handle on distance and reddening estimation, we adopted distance from single Tully fisher measurement or redshift distance available in literature, whereas host galactic reddening is estimate using 'color-method' which itself is not very reliable. Details of these methods and adapted values are discussed in Section 7.3. Implications of these uncertainties on the derived parameters and properties must be considered while making any interpretation. Although the derived parameters include the uncertainty from reddening and distance values, but it does not take care of the possible selection bias which might have been introduced while adopting those values.

The plateau slope of SN 2013hj is significantly steeper (1.5 mag $(100\ \mathrm{d})^{-1}$ in V) than typical SNe IIP, but is similar to generic SNe IIL templates (Faran et al., 2014). SN 2013hj is found to lie at an intermediate position in the broad continuum of light curve properties of SNe II diversity (see Anderson et al., 2014b). If at all SN 2013hj has to be classified in IIP/L taxonomy, then it will qualify better as a type IIL. SN 2013hj does not show a sharp change in slope at plateau end ($\sim$ 98d) as we see in typical SNe IIP/L, rather a gradual increase of slope is observed. On the other hand, SN 2014G is a perfect IIL candidate showing high initial peak brightness and steep plateau slope (2.55 mag $(100\ \mathrm{d})^{-1}$ in V) which lies at the higher end of SNe

IIL light curve template. A sharp end of plateau phase is visible at $\sim$ 77d for SN 2014G.

Owing to fast decline of brightness, most IIL SNe do not have post-plateau observations. SN 2014G is among the very few SNe IIL which has extensive observations covering all the light curve phases until nebular tail. The plateau-nebular transitional drop in luminosity is also prominent for the SN which is although expected but rarely detected for SNe IIL (Anderson et al., 2014b). Radioactive tail of SN 2014G is found to be steeper than that expected for a light curve powered by radioactive decay chain of ^{56}Ni$\rightarrow^{56}$Co$\rightarrow^{56}$Fe. Such steepening is explained by inefficient trapping of gamma rays in the ejecta. The tail light curves of type IIL SNe 1980K, 2013by and 2013ej also shows a significant steepening. This possibly implies that all type IIL SNe may exhibit such steepening of tail light curve, as SNe IIL has thinner hydrogen envelope which is responsible for gamma ray leakage and incomplete thermalization of photons. More type IIL SNe are needed to be observed rigorously until nebular phase to confirm whether steepening of tail is generic feature to all SNe IIL. The mass of synthesized radioactive ^{56}Ni estimated from tail bolometric light curves are $0.08 \pm 0.01 M_{\odot}$ and $0.05 \pm 0.03 M_{\odot}$ for SNe 2013hj and 2014G respectively.

We performed semi-analytical modelling of bolometric light curves of SNe 2013hj and 2014G to estimate explosion and progenitor properties. For SN 2013hj we estimate a progenitor mass of $\sim 11 M_{\odot}$ with a radius of $\sim 700 R_{\odot}$, whereas for SN 2014G progenitor mass is estimated to $\sim 9 M_{\odot}$ with radius $\sim 630 M_{\odot}$. The total explosion energy (kinetic + thermal) for both the SNe is approximately $\sim$ 2 foe. The steepened tail light curve of SN 2014G is fitted by reducing the effectiveness of gamma ray trapping parameter A_g in the model.

Broadband polarimetric observations of SNe 2013hj and 2014G are also presented in this chapter. SN 2013hj reveal some intrinsic polarization in its light, which shows subtle but monotonic increment as SN evolves towards plateau end. It is generally expected for stripped or partially stripped SNe, namely Type Ib/c or IIb, to exhibit higher degree of polarization as compared to SNe with hydrogen envelope intact as in IIPs. As both of our studied SNe are fast declining Type II events, some fraction of

H envelope may have already been shredded during pre-SN evolution in the form of stellar winds, thus the explosion will have relatively less amount of hydrogen retained which will quickly start to reveal the central part having higher degree of asymmetry (Leonard & Filippenko, 2005). Evidence of similar polarization enhancement in SNe IIP during plateau to early nebular phase has been also reported by Leonard et al. (2001, 2006) for SNe 1999em and 2004dj. On the other hand, polarization detected for SN 2014G in our observations is of very low significance, and it may be within the level of interstellar polarization due to the host galaxy.

APPENDIX

7.A Tables of photometry

Table 7.A.1: Calibrated secondary standards in the fields of SNe 2013hj and 2014G with corresponding coordinates (α, δ) and calibrated magnitudes in *UBVRI* bands are listed. Errors quoted here include both photometric and calibration errors.

SN 2013hj field standards

Star ID	α_{J2000} (h m s)	δ_{J2000} ($^\circ\,'\,''$)	U (mag)	B (mag)	V (mag)	R (mag)	I (mag)
A	9:11:51.9	-15:26:02.4	18.116 ± 0.071	17.272 ± 0.021	16.355 ± 0.012	15.824 ± 0.007	15.399 ± 0.024
B	9:12:01.2	-15:26:30.1	16.972 ± 0.032	17.011 ± 0.009	16.455 ± 0.010	16.136 ± 0.018	15.831 ± 0.022
C	9:11:57.3	-15:28:20.6	18.496 ± 0.114	18.896 ± 0.023	18.285 ± 0.021	17.934 ± 0.013	17.607 ± 0.030
D	9:12:03.3	-15:27:09.8	16.320 ± 0.013	16.414 ± 0.007	16.003 ± 0.009	15.742 ± 0.009	15.509 ± 0.017
E	9:12:06.5	-15:26:28.6	—	19.144 ± 0.065	17.857 ± 0.021	17.056 ± 0.027	16.380 ± 0.022
F	9:12:01.8	-15:29:00.0	13.942 ± 0.010	13.615 ± 0.013	12.833 ± 0.015	12.311 ± 0.015	11.917 ± 0.062
G	9:12:09.0	-15:27:32.0	18.843 ± 0.110	18.105 ± 0.019	17.144 ± 0.009	16.551 ± 0.009	16.084 ± 0.034
H	9:12:11.7	-15:28:33.6	17.775 ± 0.065	16.867 ± 0.006	15.870 ± 0.010	15.308 ± 0.008	14.872 ± 0.018
I	9:12:20.0	-15:24:01.5	17.886 ± 0.085	17.959 ± 0.025	17.459 ± 0.023	17.090 ± 0.023	16.804 ± 0.019
J	9:12:17.9	-15:22:52.8	18.224 ± 0.095	17.938 ± 0.012	17.154 ± 0.015	16.727 ± 0.008	16.390 ± 0.017
K	9:12:14.3	-15:22:54.7	16.526 ± 0.017	16.024 ± 0.008	15.135 ± 0.010	14.620 ± 0.024	14.194 ± 0.014
L	9:12:06.7	-15:24:58.8	17.013 ± 0.027	17.041 ± 0.011	16.406 ± 0.012	16.043 ± 0.007	15.711 ± 0.021
M	9:12:09.6	-15:21:45.3	15.877 ± 0.010	15.860 ± 0.006	15.300 ± 0.012	14.944 ± 0.008	14.630 ± 0.013
N	9:11:57.9	-15:23:46.1	17.402 ± 0.028	17.060 ± 0.010	16.328 ± 0.014	15.901 ± 0.007	15.533 ± 0.029
O	9:11:57.7	-15:25:17.1	—	18.942 ± 0.026	18.008 ± 0.027	17.399 ± 0.009	16.920 ± 0.023

Table 7.A.1 - continued.

Star ID	α_{J2000} (h m s)	δ_{J2000} ($^\circ\,'\,''$)	U (mag)	B (mag)	V (mag)	R (mag)	I (mag)
P	9:12:06.0	-15:24:15.8	11.697 ± 0.006	11.660 ± 0.006	11.060 ± 0.031	—	—
Q	9:12:08.6	-15:26:57.0	12.162 ± 0.004	12.063 ± 0.005	11.796 ± 0.022	11.606 ± 0.015	11.442 ± 0.062
SN 2014G field standards							
A	10:54:26.8	54:16:47.1	19.934 ± 0.456	18.943 ± 0.020	17.862 ± 0.020	17.238 ± 0.035	16.722 ± 0.042
B	10:54:32.0	54:14:28.0	17.940 ± 0.044	17.854 ± 0.020	17.253 ± 0.016	16.880 ± 0.026	16.496 ± 0.030
C	10:54:42.6	54:17:03.7	19.067 ± 0.080	18.648 ± 0.019	17.787 ± 0.023	17.284 ± 0.033	16.818 ± 0.041
D	10:54:52.6	54:13:53.8	16.133 ± 0.022	16.106 ± 0.015	15.500 ± 0.018	15.144 ± 0.028	14.839 ± 0.031
E	10:54:59.9	54:15:21.2	17.539 ± 0.024	17.626 ± 0.012	17.067 ± 0.014	16.714 ± 0.027	16.402 ± 0.039
F	10:54:58.9	54:17:19.9	15.753 ± 0.009	15.141 ± 0.011	14.274 ± 0.016	13.754 ± 0.028	13.382 ± 0.039
G	10:55:10.7	54:17:52.9	18.910 ± 0.097	17.656 ± 0.027	16.502 ± 0.017	15.796 ± 0.032	15.199 ± 0.025
H	10:55:04.1	54:22:09.0	18.734 ± 0.107	18.595 ± 0.042	17.850 ± 0.019	17.445 ± 0.033	17.061 ± 0.023
I	10:54:55.1	54:21:18.4	18.482 ± 0.062	18.552 ± 0.024	17.894 ± 0.020	17.533 ± 0.021	17.200 ± 0.023
J	10:54:45.1	54:20:45.1	—	19.994 ± 0.099	18.608 ± 0.031	17.746 ± 0.024	16.995 ± 0.024
K	10:54:36.8	54:21:35.4	16.861 ± 0.013	16.252 ± 0.021	15.395 ± 0.017	14.899 ± 0.025	14.491 ± 0.024
L	10:54:37.0	54:23:42.9	18.337 ± 0.060	18.915 ± 0.026	18.633 ± 0.045	18.191 ± 0.038	17.843 ± 0.038
M	10:54:30.3	54:20:16.0	—	19.328 ± 0.025	17.987 ± 0.026	17.215 ± 0.024	16.566 ± 0.035
N	10:54:28.0	54:20:54.3	16.065 ± 0.018	16.137 ± 0.013	15.637 ± 0.016	15.309 ± 0.026	15.023 ± 0.028
O	10:54:22.6	54:19:00.3	15.632 ± 0.014	15.407 ± 0.013	14.750 ± 0.014	14.362 ± 0.030	14.048 ± 0.034
P	10:54:07.0	54:19:03.0	17.292 ± 0.024	17.089 ± 0.012	16.409 ± 0.023	15.976 ± 0.027	15.590 ± 0.032
Q	10:54:01.6	54:18:04.5	18.828 ± 0.169	18.030 ± 0.035	17.049 ± 0.020	16.454 ± 0.030	15.865 ± 0.034

Table 7.A.2: Photometric evolution of SN 2013hj in *UBVRI* bands.

UT Date (yyyy-mm-dd)	JD 2456000+	Phase[a] (day)	U (mag)	B (mag)	V (mag)	R (mag)	I (mag)	Tel[b]
2013-12-13.88	640.38	3.38	13.681 ± 0.041	14.700 ± 0.024	14.819 ± 0.016	14.806 ± 0.016	14.858 ± 0.034	ARIES
2013-12-14.84	641.34	4.34	13.721 ± 0.025	14.702 ± 0.014	14.757 ± 0.010	14.716 ± 0.010	14.743 ± 0.020	ARIES
2013-12-15.92	642.42	5.42	13.739 ± 0.028	14.699 ± 0.017	14.696 ± 0.011	14.633 ± 0.011	14.639 ± 0.023	ARIES
2013-12-16.93	643.43	6.43	13.775 ± 0.028	14.694 ± 0.024	14.667 ± 0.016	14.565 ± 0.015	14.546 ± 0.031	ARIES
2013-12-18.79	645.29	8.29	13.849 ± 0.042	14.738 ± 0.024	14.632 ± 0.016	14.492 ± 0.015	14.441 ± 0.031	ARIES
2013-12-19.80	646.30	9.30	13.899 ± 0.030	14.769 ± 0.018	14.653 ± 0.012	14.496 ± 0.011	14.412 ± 0.021	ARIES
2013-12-21.01	647.51	10.51	13.924 ± 0.047	14.758 ± 0.026	14.652 ± 0.018	14.505 ± 0.016	14.388 ± 0.034	ARIES
2013-12-25.83	652.33	15.33	14.151 ± 0.021	14.892 ± 0.017	14.730 ± 0.010	14.496 ± 0.011	14.412 ± 0.023	ARIES
2013-12-28.72	655.22	18.22	—	—	14.785 ± 0.012	14.558 ± 0.013	—	OKU
2013-12-28.83	655.33	18.33	14.281 ± 0.029	14.943 ± 0.017	14.738 ± 0.012	14.516 ± 0.011	14.447 ± 0.023	ARIES
2013-12-29.73	656.23	19.23	—	—	14.783 ± 0.008	14.579 ± 0.008	—	OKU
2013-12-29.91	656.41	19.41	14.371 ± 0.029	14.969 ± 0.017	14.753 ± 0.011	—	14.467 ± 0.023	ARIES
2013-12-31.69	658.19	21.19	—	—	—	—	14.490 ± 0.033	OKU
2014-01-01.66	659.16	22.16	—	—	14.835 ± 0.008	14.582 ± 0.008	—	OKU
2014-01-02.69	660.19	23.19	—	—	14.829 ± 0.008	14.598 ± 0.009	—	OKU
2014-01-03.68	661.18	24.18	—	—	14.848 ± 0.008	14.608 ± 0.009	—	OKU
2014-01-05.61	663.11	26.11	—	—	14.849 ± 0.009	14.576 ± 0.007	—	OKU
2014-01-06.61	664.11	27.11	—	15.304 ± 0.015	—	—	14.487 ± 0.015	OKU
2014-01-06.86	664.36	27.36	—	15.280 ± 0.018	14.919 ± 0.012	14.606 ± 0.011	14.515 ± 0.023	ARIES
2014-01-07.73	665.23	28.23	—	—	14.890 ± 0.014	—	14.481 ± 0.022	OKU
2014-01-09.72	667.22	30.22	—	—	—	14.587 ± 0.010	14.489 ± 0.026	OKU
2014-01-10.56	668.06	31.06	—	—	14.928 ± 0.010	14.632 ± 0.009	—	OKU
2014-01-11.59	669.09	32.09	—	—	—	—	14.491 ± 0.012	OKU
2014-01-11.97	669.47	32.47	15.610 ± 0.037	15.519 ± 0.026	14.969 ± 0.016	14.622 ± 0.015	14.527 ± 0.032	ARIES
2014-01-12.79	670.29	33.29	15.695 ± 0.037	15.568 ± 0.020	14.969 ± 0.012	14.626 ± 0.009	14.516 ± 0.023	ARIES
2014-01-13.66	671.16	34.16	—	—	14.981 ± 0.007	—	—	OKU
2014-01-14.80	672.30	35.30	—	—	—	14.633 ± 0.015	14.533 ± 0.031	ARIES
2014-01-15.64	673.14	36.14	—	15.700 ± 0.017	14.989 ± 0.009	—	—	OKU
2014-01-15.93	673.43	36.43	15.854 ± 0.048	—	14.995 ± 0.017	14.642 ± 0.015	14.547 ± 0.032	ARIES
2014-01-16.71	674.21	37.21	—	15.782 ± 0.039	—	14.650 ± 0.009	14.503 ± 0.020	OKU

Table 7.A.2 - continued.

UT Date (yyyy-mm-dd)	JD 2456000+	Phase[a] (day)	U (mag)	B (mag)	V (mag)	R (mag)	I (mag)	Tel[b]
2014-01-16.82	674.32	37.32	16.073 ± 0.042	15.744 ± 0.021	15.017 ± 0.012	14.649 ± 0.011	14.541 ± 0.023	ARIES
2014-01-17.71	675.21	38.21	—	—	15.038 ± 0.011	14.663 ± 0.011	—	OKU
2014-01-18.83	676.33	39.33	—	—	—	—	14.504 ± 0.021	OKU
2014-01-19.71	677.21	40.21	—	15.833 ± 0.021	15.077 ± 0.011	14.691 ± 0.011	—	OKU
2014-01-20.85	678.35	41.35	16.418 ± 0.051	15.879 ± 0.019	15.092 ± 0.010	14.687 ± 0.010	14.517 ± 0.015	ARIES
2014-01-21.71	679.21	42.21	—	—	15.116 ± 0.021	14.706 ± 0.038	14.532 ± 0.021	OKU
2014-01-23.75	681.25	44.25	—	15.995 ± 0.020	15.155 ± 0.010	—	—	OKU
2014-01-24.80	682.30	45.30	—	—	—	—	14.590 ± 0.017	OKU
2014-01-24.84	682.34	45.34	16.774 ± 0.047	15.963 ± 0.022	15.237 ± 0.013	14.783 ± 0.010	14.568 ± 0.023	ARIES
2014-01-25.83	683.33	46.33	16.627 ± 0.087	15.982 ± 0.029	15.148 ± 0.016	14.683 ± 0.015	14.566 ± 0.031	ARIES
2014-01-26.82	684.32	47.32	16.687 ± 0.061	16.018 ± 0.028	15.168 ± 0.016	14.694 ± 0.015	14.577 ± 0.031	ARIES
2014-01-27.74	685.24	48.24	—	16.095 ± 0.022	15.202 ± 0.010	—	—	OKU
2014-01-28.75	686.25	49.25	—	—	—	14.739 ± 0.009	14.579 ± 0.017	OKU
2014-01-28.90	686.40	49.40	16.890 ± 0.098	16.157 ± 0.024	15.207 ± 0.013	14.742 ± 0.013	14.611 ± 0.020	ARIES
2014-01-29.84	687.34	50.34	16.879 ± 0.068	16.118 ± 0.030	15.210 ± 0.016	14.720 ± 0.015	14.596 ± 0.031	ARIES
2014-01-30.82	688.32	51.32	17.009 ± 0.065	16.215 ± 0.025	15.247 ± 0.011	14.775 ± 0.012	14.633 ± 0.023	ARIES
2014-01-31.73	689.23	52.23	—	16.324 ± 0.033	—	—	—	OKU
2014-01-31.80	689.30	52.30	17.049 ± 0.064	16.266 ± 0.031	15.270 ± 0.016	14.778 ± 0.015	14.641 ± 0.031	ARIES
2014-02-01.78	690.28	53.28	17.093 ± 0.064	16.279 ± 0.026	15.276 ± 0.013	14.788 ± 0.012	14.642 ± 0.023	ARIES
2014-02-02.76	691.26	54.26	17.152 ± 0.070	16.322 ± 0.033	15.300 ± 0.016	14.798 ± 0.015	14.645 ± 0.031	ARIES
2014-02-05.76	694.26	57.26	—	16.310 ± 0.027	15.323 ± 0.012	—	—	OKU
2014-02-05.84	694.34	57.34	17.300 ± 0.089	16.306 ± 0.032	15.313 ± 0.017	14.776 ± 0.015	14.628 ± 0.032	ARIES
2014-02-09.71	698.21	61.21	—	—	15.370 ± 0.013	14.826 ± 0.035	—	OKU
2014-02-09.79	698.29	61.29	17.510 ± 0.104	16.510 ± 0.036	15.403 ± 0.013	14.868 ± 0.016	14.722 ± 0.031	ARIES
2014-02-10.69	699.19	62.19	—	—	—	14.859 ± 0.009	14.682 ± 0.019	OKU
2014-02-11.82	700.32	63.32	17.701 ± 0.118	16.573 ± 0.030	15.430 ± 0.011	14.895 ± 0.012	14.734 ± 0.024	ARIES
2014-02-12.87	701.37	64.37	17.708 ± 0.144	16.543 ± 0.031	15.439 ± 0.011	14.896 ± 0.010	14.748 ± 0.020	ARIES
2014-02-16.75	705.25	68.25	17.619 ± 0.120	16.664 ± 0.035	15.502 ± 0.014	14.941 ± 0.012	14.779 ± 0.024	ARIES
2014-02-17.74	706.24	69.24	17.894 ± 0.132	16.728 ± 0.035	15.515 ± 0.013	14.941 ± 0.012	14.764 ± 0.024	ARIES
2014-02-19.57	708.07	71.07	—	—	—	15.006 ± 0.013	—	OKU
2014-02-19.86	708.36	71.36	17.910 ± 0.173	16.757 ± 0.037	15.567 ± 0.018	14.975 ± 0.016	14.807 ± 0.033	ARIES
2014-02-20.72	709.22	72.22	—	—	—	14.975 ± 0.010	14.813 ± 0.019	OKU

Table 7.A.2 - continued.

UT Date (yyyy-mm-dd)	JD 2456000+	Phase[a] (day)	U (mag)	B (mag)	V (mag)	R (mag)	I (mag)	Tel[b]
2014-02-21.69	710.19	73.19	18.064 ± 0.138	16.705 ± 0.032	15.607 ± 0.018	14.967 ± 0.016	14.798 ± 0.024	ARIES
2014-02-22.75	711.25	74.25	18.163 ± 0.156	16.754 ± 0.040	15.619 ± 0.018	14.976 ± 0.016	14.808 ± 0.024	ARIES
2014-02-23.75	712.25	75.25	—	—	—	—	—	OKU
2014-02-24.61	713.11	76.11	—	16.793 ± 0.039	15.619 ± 0.013	—	—	OKU
2014-02-25.64	714.14	77.14	—	—	15.627 ± 0.018	15.059 ± 0.015	—	OKU
2014-02-25.80	714.30	77.30	18.080 ± 0.181	16.901 ± 0.050	15.608 ± 0.018	15.047 ± 0.013	14.862 ± 0.024	ARIES
2014-03-02.70	719.20	82.20	18.537 ± 0.220	17.071 ± 0.045	15.732 ± 0.015	15.147 ± 0.013	14.943 ± 0.024	ARIES
2014-03-03.62	720.12	83.12	—	—	15.851 ± 0.016	—	—	OKU
2014-03-05.69	722.19	85.19	—	—	—	—	14.985 ± 0.054	OKU
2014-03-07.68	724.18	87.18	—	—	15.907 ± 0.019	15.274 ± 0.019	—	OKU
2014-03-07.69	724.19	87.19	18.786 ± 0.266	17.292 ± 0.053	15.910 ± 0.016	15.229 ± 0.013	15.037 ± 0.025	ARIES
2014-03-08.73	725.23	88.23	18.852 ± 0.293	17.336 ± 0.052	15.942 ± 0.017	15.262 ± 0.013	15.064 ± 0.034	ARIES
2014-03-10.55	727.05	90.05	—	—	15.995 ± 0.020	15.311 ± 0.012	—	OKU
2014-03-11.67	728.17	91.17	—	—	16.003 ± 0.025	15.358 ± 0.019	—	OKU
2014-03-12.76	729.26	92.26	—	17.478 ± 0.065	16.065 ± 0.022	15.365 ± 0.018	15.143 ± 0.027	ARIES
2014-03-13.68	730.18	93.18	18.927 ± 0.393	17.565 ± 0.069	16.095 ± 0.018	15.381 ± 0.015	15.165 ± 0.026	ARIES
2014-03-14.62	731.12	94.12	—	—	16.187 ± 0.019	15.388 ± 0.023	—	OKU
2014-03-14.83	731.33	94.33	—	17.561 ± 0.076	16.116 ± 0.019	15.434 ± 0.013	15.204 ± 0.023	ARIES
2014-03-16.80	733.30	96.30	—	17.740 ± 0.094	16.209 ± 0.020	15.460 ± 0.014	15.254 ± 0.028	ARIES
2014-03-18.67	735.17	98.17	—	17.787 ± 0.086	16.244 ± 0.024	15.551 ± 0.018	15.313 ± 0.028	ARIES
2014-03-19.67	736.17	99.17	18.781 ± 0.317	17.853 ± 0.088	16.319 ± 0.021	15.572 ± 0.017	15.351 ± 0.028	ARIES
2014-03-20.67	737.17	100.17	19.102 ± 0.361	17.909 ± 0.089	16.388 ± 0.021	15.620 ± 0.015	15.390 ± 0.025	ARIES
2014-03-23.62	740.12	103.12	—	—	—	15.827 ± 0.021	15.532 ± 0.031	OKU
2014-03-23.79	740.29	103.29	—	18.099 ± 0.107	16.564 ± 0.030	15.761 ± 0.022	15.550 ± 0.039	ARIES
2014-03-27.63	744.13	107.13	—	—	—	16.095 ± 0.030	15.811 ± 0.033	OKU
2014-03-31.63	748.13	111.13	—	—	—	16.357 ± 0.030	16.250 ± 0.046	OKU
2014-04-01.61	749.11	112.11	—	—	—	16.448 ± 0.050	—	OKU
2014-04-02.59	750.09	113.09	—	18.897 ± 0.217	17.533 ± 0.066	16.581 ± 0.038	16.324 ± 0.057	ARIES
2014-04-06.60	754.10	117.10	—	—	—	16.672 ± 0.038	—	OKU
2014-04-07.62	755.12	118.12	—	—	—	—	16.387 ± 0.053	OKU
2014-04-07.73	755.23	118.23	—	—	17.699 ± 0.070	16.723 ± 0.041	16.438 ± 0.054	ARIES
2014-04-08.57	756.07	119.07	—	—	—	16.737 ± 0.046	—	OKU

Table 7.A.2 - continued.

UT Date (yyyy-mm-dd)	JD 2456000+	Phase[a] (day)	U (mag)	B (mag)	V (mag)	R (mag)	I (mag)	Tel[b]
2014-04-08.63	756.13	119.13	—	19.141 ± 0.268	17.809 ± 0.071	16.789 ± 0.039	16.516 ± 0.056	ARIES
2014-04-09.57	757.07	120.07	—	—	—	16.829 ± 0.047	—	OKU
2014-04-09.62	757.12	120.12	—	19.218 ± 0.303	17.866 ± 0.081	16.831 ± 0.044	16.555 ± 0.061	ARIES
2014-04-11.47	758.97	121.97	—	—	—	16.833 ± 0.052	—	OKU
2014-04-11.72	759.22	122.22	—	18.986 ± 0.289	17.722 ± 0.079	16.765 ± 0.039	16.522 ± 0.061	ARIES
2014-04-12.56	760.06	123.06	—	—	—	—	—	OKU
2014-04-14.65	762.15	125.15	—	19.470 ± 0.409	17.755 ± 0.070	16.842 ± 0.043	16.563 ± 0.055	ARIES
2014-04-19.68	767.18	130.18	19.739 ± 0.707	19.592 ± 0.418	17.847 ± 0.071	16.875 ± 0.044	16.612 ± 0.061	ARIES
2014-04-20.65	768.15	131.15	—	19.274 ± 0.301	17.958 ± 0.080	16.897 ± 0.043	16.636 ± 0.063	ARIES
2014-04-21.64	769.14	132.14	20.197 ± 0.955	19.281 ± 0.307	17.920 ± 0.077	16.894 ± 0.049	16.638 ± 0.061	ARIES
2014-04-23.55	771.05	134.05	—	—	—	—	16.617 ± 0.063	OKU
2014-04-26.74	774.24	137.24	—	19.490 ± 0.477	17.986 ± 0.112	16.910 ± 0.047	16.619 ± 0.063	ARIES
2014-04-27.63	775.13	138.13	19.730 ± 0.809	19.457 ± 0.390	17.906 ± 0.089	16.941 ± 0.046	16.635 ± 0.063	ARIES
2014-05-09.63	787.13	150.13	—	19.409 ± 0.473	18.021 ± 0.095	17.003 ± 0.055	16.693 ± 0.064	ARIES
2014-05-10.63	788.13	151.13	—	—	18.063 ± 0.093	17.061 ± 0.052	16.724 ± 0.073	ARIES
2014-05-13.63	791.13	154.13	—	19.081 ± 0.401	17.975 ± 0.086	17.096 ± 0.061	16.917 ± 0.089	ARIES
2014-05-15.64	793.14	156.14	—	19.276 ± 0.355	17.947 ± 0.089	17.128 ± 0.061	16.709 ± 0.072	ARIES
2014-05-16.62	794.12	157.12	—	19.408 ± 0.366	17.923 ± 0.087	17.093 ± 0.057	16.759 ± 0.072	ARIES
2014-05-20.62	798.12	161.12	—	19.469 ± 0.362	18.233 ± 0.104	17.165 ± 0.056	16.894 ± 0.076	ARIES
2014-05-21.63	799.13	162.13	—	19.436 ± 0.361	18.253 ± 0.108	17.165 ± 0.056	16.868 ± 0.076	ARIES
2014-05-26.63	804.13	167.13	—	—	18.075 ± 0.098	17.103 ± 0.060	16.818 ± 0.079	ARIES
2014-05-29.63	807.13	170.13	—	—	18.138 ± 0.095	17.165 ± 0.061	16.939 ± 0.086	ARIES

[a] with reference to the explosion epoch JD=2456637.0d

[b] ARIES: 104cm Sampurnanand telescope and 130cm Devasthal fast optical telescope at ARIES, Nainital, India; OKU: 51cm telescope at Osaka Kyoiku University, Japan

Note: Data observed within 5 Hrs, are represented under single epoch observation.

Table 7.A.3: Photometric evolution of SN 2014G.

UBVRI photometry

UT Date (yyyy-mm-dd)	JD 2456000+	Phase[a] (day)	U (mag)	B (mag)	V (mag)	R (mag)	I (mag)	Tel[b]
2014-01-15.97	673.47	3.74	14.215 ± 0.040	15.043 ± 0.023	15.007 ± 0.017	14.924 ± 0.017	14.900 ± 0.033	ARIES
2014-01-16.88	674.38	4.65	14.085 ± 0.028	14.911 ± 0.016	14.851 ± 0.013	14.738 ± 0.012	14.693 ± 0.020	ARIES
2014-01-20.92	678.42	8.69	14.110 ± 0.029	14.829 ± 0.016	14.601 ± 0.012	14.436 ± 0.011	14.311 ± 0.022	ARIES
2014-01-24.92	682.42	12.69	14.310 ± 0.028	14.860 ± 0.016	14.451 ± 0.011	—	14.064 ± 0.022	ARIES
2014-01-25.93	683.43	13.70	14.294 ± 0.019	14.867 ± 0.014	14.472 ± 0.010	14.213 ± 0.012	14.067 ± 0.020	ARIES
2014-01-27.91	685.41	15.68	14.441 ± 0.040	14.916 ± 0.023	14.465 ± 0.016	—	13.997 ± 0.030	ARIES
2014-01-28.89	686.39	16.66	14.534 ± 0.030	14.996 ± 0.016	14.561 ± 0.012	14.263 ± 0.011	14.023 ± 0.022	ARIES
2014-01-29.89	687.39	17.66	14.599 ± 0.040	15.007 ± 0.023	14.516 ± 0.016	14.206 ± 0.015	14.006 ± 0.030	ARIES
2014-01-30.91	688.41	18.68	14.689 ± 0.029	15.073 ± 0.016	14.609 ± 0.011	14.296 ± 0.011	14.044 ± 0.022	ARIES
2014-01-31.83	689.33	19.60	14.780 ± 0.029	15.143 ± 0.023	14.644 ± 0.016	14.308 ± 0.015	14.052 ± 0.030	ARIES
2014-02-01.84	690.34	20.61	14.859 ± 0.023	15.185 ± 0.016	14.676 ± 0.011	14.320 ± 0.011	14.062 ± 0.022	ARIES
2014-02-02.86	691.36	21.63	14.954 ± 0.025	15.245 ± 0.019	14.686 ± 0.014	14.344 ± 0.011	14.084 ± 0.022	ARIES
2014-02-08.94	697.44	27.71	—	—	—	—	—	ARIES
2014-02-09.82	698.32	28.59	15.662 ± 0.032	15.658 ± 0.017	14.962 ± 0.013	14.555 ± 0.012	14.270 ± 0.022	ARIES
2014-02-11.88	700.38	30.65	15.890 ± 0.049	15.816 ± 0.017	15.051 ± 0.013	14.624 ± 0.012	14.331 ± 0.022	ARIES
2014-02-12.91	701.41	31.68	16.013 ± 0.034	15.860 ± 0.024	15.064 ± 0.017	14.636 ± 0.015	14.333 ± 0.030	ARIES
2014-02-16.81	705.31	35.58	16.467 ± 0.045	16.087 ± 0.020	15.231 ± 0.014	14.751 ± 0.013	14.447 ± 0.023	ARIES
2014-02-17.80	706.30	36.57	16.516 ± 0.034	16.138 ± 0.019	15.232 ± 0.014	14.728 ± 0.012	14.423 ± 0.023	ARIES
2014-02-19.89	708.39	38.66	16.814 ± 0.046	16.263 ± 0.019	15.314 ± 0.019	14.818 ± 0.017	14.491 ± 0.031	ARIES
2014-02-21.74	710.24	40.51	16.910 ± 0.040	16.287 ± 0.020	15.365 ± 0.020	14.798 ± 0.017	14.498 ± 0.031	ARIES
2014-02-22.78	711.28	41.55	16.968 ± 0.042	16.331 ± 0.027	15.397 ± 0.019	14.817 ± 0.016	14.512 ± 0.031	ARIES
2014-02-25.84	714.34	44.61	17.399 ± 0.065	16.565 ± 0.022	15.469 ± 0.020	14.955 ± 0.017	14.601 ± 0.032	ARIES
2014-03-02.77	719.27	49.54	17.705 ± 0.060	16.722 ± 0.023	15.616 ± 0.017	15.078 ± 0.014	14.710 ± 0.023	ARIES
2014-03-07.76	724.26	54.53	17.957 ± 0.063	16.940 ± 0.025	15.768 ± 0.019	15.151 ± 0.015	14.804 ± 0.024	ARIES
2014-03-08.77	725.27	55.54	18.019 ± 0.075	16.985 ± 0.024	15.784 ± 0.022	15.173 ± 0.018	14.816 ± 0.032	ARIES
2014-03-12.79	729.29	59.56	18.301 ± 0.113	17.112 ± 0.036	15.879 ± 0.024	15.193 ± 0.018	14.884 ± 0.024	ARIES
2014-03-13.75	730.25	60.52	18.428 ± 0.113	17.160 ± 0.027	15.892 ± 0.021	15.247 ± 0.015	14.887 ± 0.024	ARIES
2014-03-14.87	731.37	61.64	18.596 ± 0.169	17.175 ± 0.039	15.914 ± 0.024	15.266 ± 0.019	14.916 ± 0.033	ARIES
2014-03-16.83	733.33	63.60	18.276 ± 0.167	17.243 ± 0.031	15.957 ± 0.026	15.294 ± 0.020	14.931 ± 0.033	ARIES

Table 7.A.3 - continued.

UT Date (yyyy-mm-dd)	JD 2456000+	Phase[a] (day)	U (mag)	B (mag)	V (mag)	R (mag)	I (mag)	Tel[b]
2014-03-18.72	735.22	65.49	18.426 ± 0.142	17.287 ± 0.033	15.997 ± 0.022	15.321 ± 0.017	14.962 ± 0.025	ARIES
2014-03-19.73	736.23	66.50	18.659 ± 0.156	17.306 ± 0.032	16.006 ± 0.023	15.335 ± 0.017	14.980 ± 0.026	ARIES
2014-03-20.71	737.21	67.48	18.931 ± 0.244	17.356 ± 0.042	16.045 ± 0.027	15.371 ± 0.020	15.013 ± 0.033	ARIES
2014-03-21.71	738.21	68.48	18.706 ± 0.132	17.373 ± 0.032	16.046 ± 0.027	15.375 ± 0.021	15.021 ± 0.034	ARIES
2014-03-22.82	739.32	69.59	18.712 ± 0.173	17.406 ± 0.041	16.096 ± 0.027	15.398 ± 0.020	15.046 ± 0.034	ARIES
2014-03-23.82	740.32	70.59	18.825 ± 0.175	17.505 ± 0.054	—	—	15.070 ± 0.034	ARIES
2014-03-29.87	746.37	76.64	—	—	16.350 ± 0.033	15.554 ± 0.022	15.181 ± 0.035	ARIES
2014-04-02.62	750.12	80.39	—	17.814 ± 0.048	16.532 ± 0.039	15.705 ± 0.025	15.291 ± 0.037	ARIES
2014-04-07.76	755.26	85.53	—	18.420 ± 0.100	17.025 ± 0.057	16.107 ± 0.033	15.648 ± 0.042	ARIES
2014-04-08.70	756.20	86.47	19.576 ± 0.295	18.437 ± 0.075	17.222 ± 0.061	16.227 ± 0.031	15.756 ± 0.035	ARIES
2014-04-09.84	757.34	87.61	20.295 ± 0.582	18.610 ± 0.091	17.436 ± 0.083	16.388 ± 0.041	15.902 ± 0.047	ARIES
2014-04-11.76	759.26	89.53	—	18.967 ± 0.104	17.586 ± 0.084	16.587 ± 0.043	16.080 ± 0.044	ARIES
2014-04-13.73	761.23	91.50	—	—	17.863 ± 0.124	—	—	ARIES
2014-04-14.69	762.19	92.46	—	19.200 ± 0.149	17.952 ± 0.117	16.824 ± 0.052	16.306 ± 0.052	ARIES
2014-04-19.72	767.22	97.49	20.076 ± 0.485	19.064 ± 0.133	18.032 ± 0.141	16.943 ± 0.067	16.451 ± 0.069	ARIES
2014-04-20.71	768.21	98.48	19.719 ± 0.302	18.988 ± 0.121	18.125 ± 0.133	16.958 ± 0.059	16.440 ± 0.057	ARIES
2014-04-21.71	769.21	99.48	19.580 ± 0.260	19.074 ± 0.126	18.123 ± 0.138	16.973 ± 0.060	16.482 ± 0.059	ARIES
2014-04-25.80	773.30	103.57	—	19.137 ± 0.131	18.106 ± 0.156	17.007 ± 0.073	16.516 ± 0.073	ARIES
2014-04-26.70	774.20	104.47	—	19.178 ± 0.128	18.148 ± 0.140	17.056 ± 0.064	16.555 ± 0.063	ARIES
2014-04-28.65	776.15	106.42	20.818 ± 1.294	19.074 ± 0.142	18.175 ± 0.163	17.040 ± 0.077	16.597 ± 0.080	ARIES
2014-05-04.69	782.19	112.46	20.558 ± 1.027	19.352 ± 0.175	18.311 ± 0.180	17.121 ± 0.081	16.638 ± 0.082	ARIES
2014-05-09.67	787.17	117.44	—	19.530 ± 0.176	18.429 ± 0.186	17.225 ± 0.077	16.754 ± 0.078	ARIES
2014-05-10.68	788.18	118.45	—	19.738 ± 0.238	18.399 ± 0.182	17.257 ± 0.080	16.796 ± 0.080	ARIES
2014-05-13.67	791.17	121.44	—	19.647 ± 0.221	18.433 ± 0.213	17.292 ± 0.092	16.869 ± 0.097	ARIES
2014-05-15.68	793.18	123.45	—	19.524 ± 0.215	18.516 ± 0.208	17.281 ± 0.083	16.840 ± 0.086	ARIES
2014-05-17.63	795.13	125.40	—	19.404 ± 0.151	18.458 ± 0.193	17.367 ± 0.100	16.910 ± 0.088	ARIES
2014-05-20.67	798.17	128.44	—	19.378 ± 0.158	18.660 ± 0.228	17.390 ± 0.087	17.014 ± 0.092	ARIES
2014-05-21.67	799.17	129.44	—	19.452 ± 0.163	18.693 ± 0.234	17.406 ± 0.089	17.014 ± 0.093	ARIES
2014-05-26.67	804.17	134.44	—	19.516 ± 0.203	18.606 ± 0.226	17.495 ± 0.117	17.122 ± 0.127	ARIES
2014-05-29.68	807.18	137.45	—	19.542 ± 0.235	18.678 ± 0.272	17.509 ± 0.102	17.118 ± 0.109	ARIES
2014-06-15.64	824.14	154.41	—	—	—	17.796 ± 0.156	17.417 ± 0.167	ARIES
2014-06-16.63	825.13	155.40	—	—	18.918 ± 0.293	17.772 ± 0.148	17.430 ± 0.161	ARIES

Table 7.A.3 - continued.

UT Date (yyyy-mm-dd)	JD 2456000+	Phase[a] (day)	U (mag)	B (mag)	V (mag)	R (mag)	I (mag)	Tel[b]
2014-06-27.65	836.15	166.42	—	20.092 ± 0.332	19.473 ± 0.501	18.014 ± 0.193	17.731 ± 0.225	ARIES
2014-11-26.95	988.45	318.72	—	—	—	19.883 ± 0.959	19.792 ± 1.411	ARIES

Swift UVOT photometry

UT Date (yyyy/mm/dd)	JD 2456000+	Phase[a] (day)	$uvw2$ (mag)	$uvm2$ (mag)	$uvw1$ (mag)	uvu (mag)	uvb (mag)	uvv (mag)	Tel[b] /Inst
2014-01-15.76	673.26	1.45	14.019 ± 0.048	14.007 ± 0.048	13.845 ± 0.048	13.851 ± 0.044	15.032 ± 0.050	15.054 ± 0.067	SWIFT
2014-01-16.79	674.29	2.47	14.084 ± 0.048	—	13.803 ± 0.044	—	—	—	SWIFT
2014-01-17.19	674.69	2.87	14.115 ± 0.049	14.060 ± 0.054	13.789 ± 0.046	13.651 ± 0.043	14.786 ± 0.047	14.756 ± 0.068	SWIFT
2014-01-18.88	676.38	4.56	14.535 ± 0.054	14.326 ± 0.056	13.975 ± 0.048	13.655 ± 0.043	14.799 ± 0.047	14.568 ± 0.061	SWIFT
2014-01-19.21	676.71	4.89	14.610 ± 0.054	14.368 ± 0.056	13.987 ± 0.047	13.715 ± 0.043	14.765 ± 0.047	14.729 ± 0.061	SWIFT
2014-01-19.47	676.97	5.15	14.662 ± 0.053	—	—	13.725 ± 0.042	—	—	SWIFT
2014-01-20.80	678.30	6.48	14.954 ± 0.061	14.768 ± 0.064	14.223 ± 0.050	13.779 ± 0.043	14.767 ± 0.047	14.535 ± 0.059	SWIFT
2014-01-21.91	679.41	7.59	15.193 ± 0.069	15.038 ± 0.064	14.347 ± 0.052	13.850 ± 0.044	14.757 ± 0.047	14.601 ± 0.060	SWIFT
2014-01-22.96	680.46	8.65	15.474 ± 0.081	15.172 ± 0.069	14.675 ± 0.067	13.858 ± 0.045	14.692 ± 0.048	14.332 ± 0.058	SWIFT
2014-01-23.70	681.20	9.38	15.658 ± 0.087	—	—	13.949 ± 0.043	—	—	SWIFT
2014-01-23.97	681.47	9.65	15.630 ± 0.088	15.463 ± 0.080	14.780 ± 0.073	13.969 ± 0.047	14.783 ± 0.050	14.356 ± 0.062	SWIFT
2014-01-24.87	682.37	10.55	15.829 ± 0.078	15.646 ± 0.066	14.855 ± 0.063	14.004 ± 0.044	14.786 ± 0.047	14.581 ± 0.058	SWIFT
2014-01-29.41	686.91	15.09	16.735 ± 0.087	16.591 ± 0.081	15.581 ± 0.066	14.470 ± 0.048	14.975 ± 0.048	14.596 ± 0.057	SWIFT
2014-02-07.85	696.35	24.53	18.389 ± 0.158	18.446 ± 0.157	17.035 ± 0.087	15.620 ± 0.068	15.520 ± 0.056	14.963 ± 0.059	SWIFT
2014-02-10.18	698.68	26.86	18.636 ± 0.175	18.946 ± 0.208	17.349 ± 0.097	15.884 ± 0.069	15.763 ± 0.060	15.030 ± 0.059	SWIFT

[a] with reference to the explosion epoch JD=2456669.7d

[b] ARIES: 104cm Sampurnanand telescope and 130cm Devasthal fast optical telescope at ARIES, Nainital, Inidia; SWIFT: *Swift* UVOT

Note: Data observed within 5 Hrs, are represented under single epoch observation.

7.B Tables of polarimetry

Table 7.B.1: Polarimetric evolution of SNe 2013hj and 2014G.

UT Date	JD	Phase[a]	Observed		ISP_{MW} subtracted	
(yyyy-mm-dd)	2456000+	(day)	P_R (%)	θ_R (°)	P_R (%)	θ_R (°)
SN 2013hj						
2014-01-02.96	660.46	23.46	0.56 ± 0.42	132.3 ± 21.8	0.63 ± 0.42	127.3 ± 21.8
2014-01-07.83	665.33	28.33	0.67 ± 0.50	127.1 ± 18.6	0.75 ± 0.50	123.4 ± 18.6
2014-01-24.85	682.35	45.35	0.44 ± 0.21	150.8 ± 10.4	0.44 ± 0.21	142.5 ± 10.4
2014-02-05.73	694.23	57.23	0.88 ± 0.29	151.2 ± 9.6	0.87 ± 0.29	147.0 ± 9.6
2014-03-06.69	723.19	86.19	0.98 ± 0.43	128.8 ± 12.8	1.07 ± 0.43	126.1 ± 12.8
SN 2014G						
2014-01-23.92	681.42	11.72	0.82 ± 0.65	131.9 ± 24.7	0.78 ± 0.65	134.0 ± 24.7
2014-01-26.93	684.43	14.73	1.59 ± 0.21	132.2 ± 4.2	1.54 ± 0.21	133.3 ± 4.2
2014-02-05.82	694.32	24.62	0.86 ± 0.20	134.3 ± 6.8	0.82 ± 0.20	136.4 ± 6.8

[a] with reference to the explosion epochs JD 2456637.0d and 2456669.7d for SNe 2013hj and 2014G respectively.

Table 7.B.2: Polarization measurements in R-band for field stars towards the direction of SNe 2013hj and 2014G.

Star ID	$\alpha_{\rm J2000}$ (h m s)	$\delta_{\rm J2000}$ ($^\circ\,'\,''$)	P_R (%)	θ_R ($^\circ$)
Stars towards SN 2013hj.				
HD 80083	09:17:36.04	-07:27:46.44	0.12 ± 0.10	5.3 ± 25.3
HD 79289	09:12:47.60	-16:47:58.57	0.16 ± 0.07	10.0 ± 15.1
HD 79308	09:12:57.26	-15:25:09.56	0.07 ± 0.09	36.4 ± 40.1
HD 82734	09:33:12.46	-21:06:56.60	0.25 ± 0.07	18.8 ± 8.0
HD 80749	09:21:09.59	-15:31:37.92	0.17 ± 0.10	15.1 ± 18.7
HD 78891	09:10:10.34	-16:51:45.40	0.03 ± 0.05	18.7 ± 42.9
HD 79914	09:16:27.54	-13:50:02.81	0.08 ± 0.06	17.6 ± 21.3
HD 78920	09:10:24.80	-14:54:00.65	0.05 ± 0.05	12.1 ± 35.3
HD 77935	09:05:02.23	-11:23:15.73	0.15 ± 0.09	19.1 ± 18.1
HD 78954	09:10:35.01	-16:58:20.89	0.05 ± 0.06	27.1 ± 30.7
HD 80990	09:22:34.28	-16:54:15.12	0.19 ± 0.09	16.3 ± 13.6
Stars towards SN 2014G.				
HD 91480	10:35:09.69	+57:04:57.49	0.32 ± 0.08	17.7 ± 8.7
HD 94247	10:53:34.45	+54:35:06.46	0.11 ± 0.06	117.1 ± 17.1
HD 102328	11:46:55.62	+55:37:41.48	0.22 ± 0.07	95.4 ± 8.9

Chapter 8

Summary, Conclusions and Future prospects

In this thesis we carried out multi-wavelength study of several core-collapse supernovae with collaborative observations from various national and international telescopes. We explored the excellent potential of using these energetic explosion as distance estimators at cosmic scale. We refined the existing formulation to extend this potential as a reliable distance estimator. We also revisited several issues regarding SNe like its energetics and properties of exploding progenitors. Hydrodynamical and semi-analytical models have been used to constrain these properties of the SNe events we studied. Detailed spectroscopic analysis and modeling has also been performed on these SNe, which revealed signatures of CSM-ejecta interaction in some of the events. Our study on SNe IIP and IIL events tried to answer existing queries on type II subtypes, as well as opened new queries on the association of Type IIL with interaction signatures found in H I features.

8.1 Summary and Conclusion

The conclusions of the work which we carried out in this thesis are summarized below.

Expanding photosphere method

Expanding photosphere method (EPM) being a redshift independent technique of distance estimation, has a great importance in astronomical and cosmological perspective. We applied EPM collectively on a sample of eight SNe and additionally on SN 2013ab as part of Chapter 5, to reliably estimate distances to their host galaxies. The comparative study of two dilution factors revealed that the corresponding EPM distances differ by 30 – 50% and Dessart & Hillier (2005a) prescription for dilution factor is significantly better suited than Hamuy et al. (2001) for EPM applications. In this study, we introduced the following two improvements in addition to existing EPM methodology – (1) using photospheric velocities estimated by SYNOW modeling observed spectra and (2) using the semi-deconvolution of filter response while fitting the observed broadband fluxes to estimate θ and T. Reddening or $E(B-V)$ being one of the quantity with most uncertainty, we examined its implication on EPM estimated results and showed that EPM is weakly dependent on $E(B-V)$. Our study not only revealed the potential of EPM as an excellent distance estimator, but also very useful in determination of explosion epoch of SNe. Among the SNe sample on which EPM has been implemented, four of them (SNe 2004et, 2005cs, 2012aw and 2013ab) have fairly precise determined explosion epoch from observational non-detection. The EPM estimated explosion epochs for all these SNe are found to be very consistent and within ~ 2 days of the observationally constrained values. This study also showed that dilution factor prescription are only applicable to data in early phases of SNe, i.e, when limited to < 50 days. We also note that SYNOW estimated photospheric velocities can be more reliable than velocities estimated by directly locating the absorption troughs, especially when spectra are of poor signal to noise ratio or contamination from neighboring spectral lines are dominant.

Optical study of SN 2012aw

SN 2012aw was one of the brights supernova of the year 2012, reaching a peak visual magnitude of 13.3 mag. The SN occurred in a solar metallicity region in the spiral arm of nearby galaxy M95 ($\sim$ 10 Mpc). The explosion epoch adopted is 2012 March

16.1 ± 0.8 UTC, based on observational detection and non detection. Systematic follow up observations have been carried out soon after its discovery. During a span of 270 days, 54 epoch of photometric data have been obtained from ARIES telescopes and 14 epoch of low resolution spectroscopic data from HCT and IGO telescopes. The total line of sight extinction is found to be $A_V = 0.23 \pm 0.03$ mag, using the $E(B-V)$ and Na I D equivalent width correlation (Barbon et al., 1990; Poznanski et al., 2012b; Turatto et al., 2003) to determine host galaxy reddening.

The photometric light curves shows a initial rising which peaks at $\sim$ 15d in V band, which is slower than typical IIP light curves. Following the initial peak, UB band light curves decline continuously, whereas VRI band light curve show a short decline and again rising and reaching a maximum at 52, 56 and 71d respectively. Due to well sampled data set of this bright SN we are able to locate light curve minima at 42, 39 and 31d in VRI bands respectively, which is the first observational detection of emergence of recombination phase in SNe IIP. This point in light curve marks the beginning of hydrogen recombination phase as temperature of outer layers drop below 6000K. The plateau phase extends up to $\sim$ 100 days and the mid plateau absolute visual magnitude is $M_V^p \sim -16.6$, which is consistent to normal IIP events. The absolute light curve shape and magnitude is remarkably identical to archetypal IIP SN 1999em. The amount of radioactive ^{56}Ni synthesized in the explosion is estimated from the tail bolometric light curve and is found to be $0.058 \pm 0.002 M_\odot$.

Spectral features of SN 2012aw shows features identical to normal IIP SNe. Detailed SYNOW modelling has been done on the spectra for line identification and to estimate line velocities for Hα, Hβ, He I and Fe II. Similar to SNe 1999em and 1999gi, SN 2012aw shows unusual high velocity (HV) features associated with Hβ and He I lines at 7 and 8d spectra, which are possible signature of CSM interaction. However these features may also be explained as N II lines using SYNOW model. A broadening of Hβ absorption trough start to appear from mid-plateau (55d) spectra which continues to broaden until last plateau spectra at 104d, where it turn out into two visually separable feature. Similar broadening has also been found in Hα troughs. While investigating these features, SYNOW could not fit the broadened troughs using single H I velocity. Only by invoking a HV component could reproduce

this feature, which is a signature of ejecta-CSM interaction. The nebular phase spectra at 270d shows characteristic emission features. The nebular Hα emission shows symmetric profile indicating no dust formation until 270d. Photospheric velocity profile estimated using Fe II lines are found similar to SN 2004et and about ~ 600 km s^{-1} higher than SNe 1999em and 1999gi. The explosion energy has been estimated to about 1–2 foe and the mass of progenitor lies in between 11 to 16 M$_{\odot}$.

Characterization of SN 2013ab

SN 2013ab is another a bright IIP SN exploded on 2013 February 16.5 ± 1.0 UTC, which was caught in observations soon after its explosion. In this work we presented six month of rigorous observation, both in spectroscopy as well as photometry, including optical and ultraviolet data. SN 2013ab is one of the most well studied SN with high cadence observation, typically few days in photometry and a week in spectroscopy. Follow up observations started immediately after the report of discovery, with 136 epoch of photometric observation and 25 epoch of spectroscopic observation. Additionally 25 epoch of data from *Swift* Ultraviotet Optical telescope (UVOT) have also been used in this work. Optical data were collected from 1m class ARIES telescopes, 1-2m class telescopes of LCOGT network, 1.22m Galileo telescope and 2m class Himalayan Chandra Telescope. The total line of sight extinction is estimated to be 0.14 ± 0.21 mag.

Spectroscopic and photometric comparison with other IIP SNe reveal that it is a normal SN IIP, with relatively steeper (0.92 mag (100 d)$^{-1}$) but shorter ($\sim$ 78d) plateau. The mass of synthesized radioactive nickel is estimated to be 0.064 ± 0.006M$_{\odot}$ from the tail bolometric luminosity. SN 2013ab is one of the best observed SN in UV wavelength with continued observation until 100 days. UV light curves shows fast declining during the first month, thereafter its settles onto a slow declining plateau phase which is rarely detected in SNe IIP in UV bands. This rare detection is possibly because of low extinction and distance of SN 2013ab which is not favored for most other SNe. The comparison of UV light curves with other SNe shows that SN 2013ab lie towards the brighter end of the sample. Detailed SYNOW modelling has been done on spectra to identify lines and estimate velocities for Hα, Hβ, He I

and Fe II lines. The photospheric velocity profile, estimated from Fe II lines, is found similar to that of SN 2012aw and 2004et.

The dense observational data of the SN provided us excellent opportunity to perform EPM and modelling. By applying EPM we could reliably constrain the distance to the host galaxy, which we estimated to be 24.26 ± 0.98 Mpc. To have an independent estimate of the radius of progenitor star, we followed the Rabinak & Waxman (2011) prescription and estimated a radius of $750 - 950$ $R_{\odot}$. A detailed general relativistic, radiation-hydrodynamical modelling has been performed on the SN, which yielded a progenitor mass of 9 $M_{\odot}$ and radius of 600 $R_{\odot}$ with an explosion energy of 0.35 foe.

Study of interacting IIL SN 2013ej

SN 2013ej is one of the brightest supernova discovered in the face-on galaxy M74 ($\sim$ 10 Mpc). From observational non detection the explosion epoch is determined to be 2013 July 23.8 ± 0.3 UTC. *UBVRI* photometric observations were done at 38 epochs and low resolution spectroscopic observation at 9 epochs using HCT and ARIES telescopes. One high resolution ($R \sim 31,500$) spectrum has been also obtained from ARC telescope at Apache point observatory. Data from *Swift* UVOT at 35 epochs have been also included in this work. The high resolution spectrum shows no sign of Na I D doublet due to the host galaxy, only impression for Milky Way is found, which implies negligible extinction due to host galaxy (Poznanski et al., 2012b). Thus only Galactic extinction (Schlafly & Finkbeiner, 2011) has been accounted for total line-of-sight extinction.

SN 2013ej exhibit a steep plateau decline rate of 1.74 mag $(100 \text{ d})^{-1}$, with a short plateau duration of $\sim$ 85 days. The light curve comparison shows that SN 2013ej suffers higher decline rate than all SNe IIP, but similar or lower than type IIL SNe 1980K, 2000dc and 2013by. The SN in not consistent with the very fundamental characteristics of SNe IIP, i.e. plateau or constant luminosity during first 9 – 100 days, rather it lies in a intermediate position in SNe II diversity (Anderson et al., 2014b). In fact, SN 2013ej is consistent and well within the range of SNe IIL light curve template (Faran et al., 2014), thus we reclassified this SN as type IIL,

instead of the initial classification as SN IIP based on early spectral matching. UV light curve of SN 2013ej shows extended plateau after reaching 30d and its shape and absolute magnitudes are remarkably identical to SN 2012aw. The plateau to nebular transition shows a drop of 2.4 mag in V band, which is higher than most other SNe II. Radioactive nickel mass estimated from tail bolometric luminosity is $0.020 \pm 0.002 M_{\odot}$, which lies towards the lower mass range for normal luminosity SNe II. The nebular phase decline rate is found to be significantly higher than that expected for $^{56}Co \rightarrow {}^{56}Fe$ decay rate, which is due to inefficient gamma ray trapping within the ejecta.

Spectroscopic features are identical to normal type II events. SYNOW modelling has been performed to identify spectral features and estimate velocities of various lines. Photospheric velocity profile are found to be similar to normal SNe IIP. However, Hα and Hβ velocity profile estimated by directly locating absorption minima, are found to be flatter as compared to other SNe IIP. Although, velocity profile starts off with values similar to that of normal SNe IIP, but it decline relatively slowly and continue to evolve at velocities higher than other SNe IIP. This particular feature has been also identified by Faran et al. (2014) for type IIL SNe. From detailed investigation of Hα and Hβ line profiles using SYNOW, we find absorption component of P-Cygni profile start to broaden from mid-plateau ($\sim$ 42d spectrum) onwards and can not be fitted with single H I velocity component. Invoking an additional HV H I component could only fit these broadened profile. This HV component can be traced through subsequent spectra in plateau phase, which is a possible indication of ejecta-CSM interaction. We also suggest that, this HV component is responsible for higher and flatter absorption-minima velocity profiles for Hα and Hβ. This may also be true for all SNe IIL, that ongoing interaction with stellar material from pre-SN mass loss is resulting into HV components in H I lines which is altering line velocity profile as we observed here and also for other IIL SNe. This led us to also conclude that ejecta-CSM interaction may not be uncommon for IIL SNe as they originate from massive progenitors (relative to normal SNe IIP) which has lost some fraction of its envelope during pre-SN evolution in form of stellar winds.

Nebular phase Hα emission shows an unusual notch which we explained as super-

imposition of two velocity components, one is blue-shifted and other is red-shifted with respect to rest position. This is a possible outcome of bipolar distribution of radioactive ^{56}Ni in the core.

Bolometric light curve of SN 2013ej has been modeled to estimate a progenitor mass of $\sim 14 M_{\odot}$ and radius of $\sim 450 R_{\odot}$ with explosion energy of ~ 2.3 foe. The steeper tail of bolometric light curve is modeled by incorporating leakage of gamma ray in the ejecta.

Photometric and polarimetric study of fast declining SNe 2013hj and 2014G

We presented photometric and polarimetric observations of two fast declining SNe 2013hj and 2014G. Our broadband photometric observations are extensive and of high cadence which covers all the essential phases of SNe light curves. The decline rate of SN 2013hj is 1.5 mag (100 d)$^{-1}$ (V-band) during the plateau phase with a duration of $\sim$ 98d. Unlike typical SNe IIP/L, SN 2013hj do not show sharp break in slope at the end of plateau. Rather a linear decline is visible only up to 80d, thereafter a gradual increase in slope is observed until end of plateau is reached. The plateau slope of SN 2013hj is found to be significantly higher than typical SNe IIP (e.g. SNe 1999em, 2012aw, 2013ab) while similar but marginally lower slope than SNe IIL template light curves (Faran et al., 2014). It falls at an intermediate position in broad SNe II continuum of properties (Anderson et al., 2014b). If at all it has to be classified as IIP or IIL, then it better qualify as a type IIL. On the other hand SN 2014G is a spectroscopically classified IIL SN, which we also confirm from characteristic light curve features it exhibit. The plateau slope is 2.55 mag (100 d)$^{-1}$ (V-band) with a sharp end of plateau at 77d. Our observational contribution is of significant importance considering the fact that only few SNe IIL have such high cadence observations which extends up to tail phase. Moreover, SN 2014G is also an excellent example demonstrating that IIL SNe does show a prominent break in light curve slope at the end of photospheric phase before settling onto tail phase, which is contrary to the historical notion that they continue to decline linearly until reaching the tail phase (Barbon et al., 1979). However it is now believed that all

SNe IIL does show photospheric to nebular transition if they are follow long enough with sufficient cadence (Anderson et al., 2014b).

The radioactive tail phase of SN 2014G is found to have a steeper decline rate than that expected from light curve powered from radioactive decay chain of ^{56}Ni$\rightarrow^{56}$Co$\rightarrow^{56}$Fe. Such steepening of tail light curve has also been observed for several other SNe IIL, e.g. SNe 1980K, 2013by, 2013ej. An important conclusion which we also derive based on this finding is that all type IIL SNe may exhibit such steepening of tail light curve, which is due to partial depletion of H envelope during pre-SN evolution, resulting into leakage of gamma rays from ejecta.

We estimated radioactive ^{56}Ni mass of 0.08M$_{\odot}$ and 0.05M$_{\odot}$ for SNe 2013hj and 2014G. On performing modelling of bolometric light curves we estimated explosion parameters. For SN 2013hj we estimate a progenitor mass of $\sim$ 11M$_{\odot}$ with a radius of $\sim$ 700R$_{\odot}$, whereas for SN 2014G progenitor mass is estimated to $\sim$ 9M$_{\odot}$ with radius $\sim$ 630M$_{\odot}$. The total explosion energy (kinetic + thermal) for both the SNe is approximately $\sim$ 2 foe.

The broadband polarimetric observations of SN 2013hj reveal some polarization after removal of interstellar polarization values, and it is also found to show subtle enhancement as SN evolves towards plateau end but with unchanged polarization angle. This indicate that, as the SN evolves and the envelope rarefy, deeper and more asymmetric core is revealed. Such enhancement of polarization toward plateau end was also found in type IIP SNe 1999em and 2004dj (Leonard et al., 2001, 2006). However due to less number of polarimetric observations for SN 2014G and uncertainty in interstellar polarization we could not detect any significant polarization for the SN.

8.2 Future scope

Supernovae being one of the most energetic cosmic events, it has attracted researchers as well as amateurs for long time. Despite of systematic study since last few decades, progress in supernova research is still in early stage when compared to the overall incomplete picture of its understanding. Collective work from numerous

researchers have been able to put together several key pieces of the puzzle, but have also opened our view towards the deeper unknowns. As newer and larger number of events start to accumulate in our pool of data, we start to realize the diverse nature of these events, which challenges some of the initial ideas drawn from limited sample of events. With progress in SNe research we could only realize that the diversity of CCSNe in luminosity, progenitor properties and nature of its environment are endless. Some of the important aspects which I came across in this thesis and would also like to pursue further work along this line in future are summarized below.

EPM application to distant supernovae

In this thesis we successfully applied EPM on number of relatively nearby SNe ($D < 25$ Mpc) whose host galaxies are well within the influence of local group of galaxy cluster. In our study we explored the excellent potential of EPM as reliable and independent distance estimator. Additionally we also refined existing EPM methodology to increase its reliability and accuracy. Along this line of work it would be a interesting to extend the study to distant high redshift SNe and also to construct an independent Hubble diagram. Apart from cosmological importance of the study, the estimated distance would also be useful in other astrophysical studies as well. However this extension of work would require extensive observational resources to obtain deep follow-up observations of the distant SNe in both spectroscopic and photometric mode. With modern telescopes and systematic follow-up programs like iPTF and ASAS-SN, number of distant supernovae are being discovered regularly which can be useful for this work.

Interacting supernovae

CCSNe exhibits ejecta-CSM interaction signatures in optical, radio or X-ray wavebands. Type IIn SNe are thought to originate from massive WR type progenitors or LBVs. Pre-supernova mass loss from these massive progenitors form extended dense shell of materials which are responsible to produce narrow emission lines in spectra and also produce complex interaction signatures while ejecta interacts with the shell. The study of these interactions give information about the environment

and progenitor when the mass loss of the shell happened back in time. However in type IIP/L SNe, the pre-SN mass loss in form of low density stellar wind are insufficient to produce emission lines but sufficient enough to produce X-rays at the shock interaction front when ejecta meets the wind. The emitted X-ray excites the ejecta to produce H I absorption line which are detected in spectra. These HV absorption features are direct indicator of interaction interface. Density of stellar wind and mass loss rate can be estimated from these absorption features (Chugai et al., 2007). In IIP/L SNe, HV signatures start to appear from mid-plateau onwards and continues to grow, however those being weak in strength it often becomes difficult to identify due to blending with other metallic lines.

In Chapters 4 and 6 we discussed the interaction signatures detected in H I absorption profiles which were very weak and subtle features submerged in strong P-Cygni and other metallic lines. Spectral modelling like SYNOW is useful to analyze these features. Interactions in SNe have interesting implications on observed parameters. SN 2013ej (Bose et al., 2015b) and PTF11iqb (Smith et al., 2015) are two such examples where interaction has altered the observable parameters exhibiting different characteristics altogether.

Fast declining or type IIL supernovae

Fast declining or type IIL SNe does not constitute entirely different class of SNe, rather they form a continuum of physical properties with SNe IIP and they belong to the broad type II diversity Anderson et al. (2014b). However SNe IIL originate from relatively heavier progenitors which may have lost some mass in form of stellar winds during pre-SN evolution, which may give rise to ejecta-CSM interaction signature in SN observation. Study of few recent type IIL SNe 2008fq (Faran et al., 2014), 2013by (Valenti et al., 2015) and our studied SN 2013ej (Bose et al., 2015b), all showed CSM interaction signatures. Due to low detection rate and rapid decline in brightness, very few type IIL SNe have prolonged observation to cover mid to end-plateau where interaction signature is most prominent. Thus with limited sample of SNe IIL, it is still not clear whether interaction is a common phenomenon in type IIL or fast declining SNe. In context of SN 2013ej (see Chapter 6) we proposed

that, the slow decline of Hα and Hβ line velocities and overall higher values in comparison to normal SNe IIP is a consequence of blending of HV absorption lines originating from CSM interaction. It has been also observed that this flatter and higher H I velocity profile is common to all SNe IIL (Faran et al., 2014), which led us to ask one step further – whether CSM interaction is common to SNe IIL, and if so, whether the characteristic H I velocity profile is a consequence of CSM interaction only. In order to address these questions one need to observe newer and more of these fast declining events with sufficient coverage and their detailed study has to be done to identify subtle interaction signatures.

Asymmetry in supernovae

CCSNe shows significant amount of polarization during various stages of evolution which are direct indicator of asymmetry in explosion. Since polarimetric observation are difficult and not much beneficial unless the SN is moderately bright. Often strong assumptions are made that explosion, envelope and core are all spherically symmetric merely because of the lack of information and it also simplifies our analysis. There are ample examples of asymmetry in SN which have interesting implications in parameter estimation through modeling and other derived properties. It is generally expected a polarization of 1% is equivalent up to $\sim$ 20% asymmetry in explosion (Leonard & Filippenko, 2005). For instance, Leonard et al. (2001) estimated that a asymmetry of 10% would overestimate EPM distance by $\sim$ 5% if the oblate SN is viewed edge-on, while results may also be underestimated by $\sim$ 10% if it is viewed face-on, and this error naturally increases with higher degree of asymmetry. Therefore, polarimetric observation and study from case to case basis would be useful to firmly characterize events and constrain their various parameters. Time evolution of polarization parameters can reveals asymmetry of internal layers and can also tell us about the variation of geometrical orientation among those layers. For example, in SN 2005af (Pereyra et al., 2006) a large rotation in polarization angle is observed over the photospheric phase which is not fully explained. Spectropolarimetry of bright SNe can also reveal information about the dust properties of host galaxies. Handful of evidences have been found showing that host galaxy dust properties

significantly differ from Milky way (e.g. SN 1986G; Hough et al. 1987 and SN 2001el; Wang et al. 2003a), which need to explored further for other SNe as well.

Some of the other important aspects of SNe research which would be interesting to peruse as future studies are:

- *Dust formation from supernovae*: SNe II are primary of source of Si and Fe group heavy elements as well as p-, r- and s-process elements, which are responsible for dust formation (Todini & Ferrara, 2001) and heavy element enrichment in the universe. The synthesized material ejected in the CSM which cools down to from dust can be studied from late time observation of SNe. The asymmetry in Hα emission due to differential extinction is the prime indicator of dust formation.

- *Over- or under-luminous SNe II*: There are number of SNe whose intrinsic luminosity are found to deviate significantly by few order of magnitude from typical normal-luminosity SNe. The nature of progenitors and the remnants for these objects are often disputed and undergoing physical mechanisms to relate the observed parameters are not fully explained. More such events are needed to be observed in detail to establish theoretical model explaining these phenomena.

- *Light echoes from SNe*: Light echoes are elusive phenomenon caused by scattering of SN light from distant dust environment. It is essentially the observed reflection of the SN itself after some period of time, depending on the distance of reflecting dust environment. Study of light echoes can provide critical information about morphology of CSM and ISM, composition of dust grains and pre-burst history of the event. Light echoes are generally observed after couple of years after the explosion when the SN light has gone faint and echoed light is above significance level of detection. Such observation require extremely powerful observing resources to detect the faint reflected light. SN 1987A is one of the famous SN whose spatially resolved light echo has been extensively

observed over several years (Suntzeff et al., 1988; Xu et al., 1995). In a recent study with observations from *HST* revealed light echoes from SN 2012aw (Van Dyk et al., 2015), which is one of the event we extensively studies in the thesis (see Chapter 4). Bases on distance extinction and apparent brightness, SN 2013ej is also a probable candidate among our observed events (see Chapter 6) which we may expect to show light echoes when SN light will be faint enough.

Bibliography

Alard, C. 2000, A&AS, 144, 363 63, 253

Alard, C., & Lupton, R. H. 1998, ApJ, 503, 325 63, 253

Anderson, J. P., Dessart, L., Gutierrez, C. P., et al. 2014a, MNRAS, 441, 671 20, 179, 231

Anderson, J. P., González-Gaitán, S., Hamuy, M., et al. 2014b, ApJ, 786, 67 xxxiii, xlii, xlvi, 18, 19, 39, 166, 201, 215, 216, 220, 238, 247, 248, 265, 267, 279, 280, 297, 299, 300, 302

Antezana, R., Hamuy, M., Gonzalez, L., et al. 2013, Central Bureau Electronic Telegrams, 3757, 1 250, 252

Arcavi, I., Gal-Yam, A., Kasliwal, M. M., et al. 2010, ApJ, 721, 777 79

Arcavi, I., Gal-Yam, A., Cenko, S. B., et al. 2012, ApJL, 756, L30 18, 201

Arnett, D. 1996, Supernovae and Nucleosynthesis: An Investigation of the History of Matter from the Big Bang to the Present 130, 171, 221

Arnett, W. D. 1980, ApJ, 237, 541 29, 31, 130, 152, 171, 241, 270, 271

—. 1982, ApJ, 253, 785 29, 30, 241, 271

Arnett, W. D., & Fu, A. 1989, ApJ, 340, 396 29, 30, 241, 242, 248, 271, 272

Asplund, M., Grevesse, N., Sauval, A. J., & Scott, P. 2009, ARA&A, 47, 481 109

Baade, W., & Zwicky, F. 1934, Proceedings of the National Academy of Science, 20, 259 3

Barbon, R., Benetti, S., Rosino, L., Cappellaro, E., & Turatto, M. 1990, A&A, 237, 79 23, 101, 119, 139, 161, 212, 257, 295

Barbon, R., Ciatti, F., & Rosino, L. 1979, A&A, 72, 287 19, 39, 201, 247, 299

—. 1982, A&A, 116, 35 xlii, xlvi, 216, 260, 265

Baron, E., Branch, D., & Hauschildt, P. H. 2007, ApJ, 662, 1148 84

Baron, E., Nugent, P. E., Branch, D., & Hauschildt, P. H. 2004, ApJL, 616, L91 24, 35, 80, 136

Baron, E., Hauschildt, P. H., Branch, D., et al. 1995, ApJ, 441, 170 35

Baron, E., Branch, D., Hauschildt, P. H., et al. 2000, ApJ, 545, 444 132, 135

Barrett, P. 1988, MNRAS, 234, 937 xlvii, 28, 249, 278

Bayless, A. J., Pritchard, T. A., Roming, P. W. A., et al. 2013, ApJL, 764, L13 xxxix, xlii, xlvi, 108, 117, 121, 126, 128, 163, 167, 217, 218, 267

Becker, A. 2015, HOTPANTS: High Order Transform of PSF ANd Template Subtraction, Astrophysics Source Code Library, ascl:1504.004 63

Bersten, M. C., Benvenuto, O., & Hamuy, M. 2011, ApJ, 729, 61 28, 108, 119, 151, 152, 161, 241, 271

Bersten, M. C., & Hamuy, M. 2009, ApJ, 701, 200 242

Bessell, M. S. 1990, PASP, 102, 1181 85

Bessell, M. S., Castelli, F., & Plez, B. 1998, A&A, 333, 231 50

Blanchard, P., Zheng, W., Cenko, S. B., et al. 2013, Central Bureau Electronic Telegrams, 3422, 1 157

Blinnikov, S. I., & Bartunov, O. S. 1993, A&A, 273, 106 220

Blondin, S., & Tonry, J. L. 2007, ApJ, 666, 1024 17, 250

Bose, S., & Kumar, B. 2014a, ApJ, 782, 98 37, 175, 181, 184, 227, 257

Bose, S., & Kumar, B. 2014b, in IAU Symposium, Vol. 296, IAU Symposium, ed. A. Ray & R. A. McCray, 90–94 109

Bose, S., Kumar, B., Sutaria, F., et al. 2013, MNRAS, 433, 1871 xxxix, xl, xlii, xliii, xlvi, 22, 79, 84, 90, 104, 159, 163, 165, 167, 169, 172, 175, 179, 181, 203, 215, 216, 218, 219, 223, 225, 227, 231, 237, 245, 251, 259, 260, 265, 267, 268

Bose, S., Valenti, S., Misra, K., et al. 2015a, MNRAS, 450, 2373 xlii, xliii, xlvi, 215, 216, 218, 219, 225, 231, 250, 259, 260, 265

Bose, S., Sutaria, F., Kumar, B., et al. 2015b, ApJ, 806, 160 xlvi, 21, 22, 31, 260, 262, 265, 266, 267, 271, 272, 302

Branch, D., Benetti, S., Kasen, D., et al. 2002, ApJ, 566, 1005 24, 83, 136, 173, 181, 226

Breeveld, A. A., Landsman, W., Holland, S. T., et al. 2011, in American Institute of Physics Conference Series, Vol. 1358, American Institute of Physics Conference Series, ed. J. E. McEnery, J. L. Racusin, & N. Gehrels, 373–376 65, 192, 210, 255

Brown, P. J., Breeveld, A. A., Holland, S., Kuin, P., & Pritchard, T. 2014, Ap&SS, 354, 89 xlii, 210, 218, 255

Brown, P. J., Holland, S. T., Immler, S., et al. 2009, AJ, 137, 4517 xxxix, xlii, xlvi, 65, 167, 191, 210, 218, 255, 267

Brown, T. M., Baliber, N., Bianco, F. B., et al. 2013, PASP, 125, 1031 159

Burnham, Jr., R. 1978, Burnham's celestial handbook, Vols._1,_2,_and_3. 2

Burrows, A. 2000, Nature, 403, 727 xxxiii, 7

Cardelli, J. A., Clayton, G. C., & Mathis, J. S. 1989, ApJ, 345, 245 117

Chakraborty, P., Das1, H. K., & Tandon, S. N. 2005, Bulletin of the Astronomical Society of India, 33, 513 116, 117

Chatzopoulos, E., Wheeler, J. C., & Vinko, J. 2012, ApJ, 746, 121 29, 31, 241, 242, 271, 272

Chugai, N. N. 1988, Soviet Astronomy Letters, 14, 334 142, 179

—. 1994, ApJL, 428, L17 151

—. 2006, Astronomy Letters, 32, 739 21, 28, 232, 249

Chugai, N. N., Chevalier, R. A., & Utrobin, V. P. 2007, ApJ, 662, 1136 xxxiii, 22, 237, 302

Chugai, N. N., Fabrika, S. N., Sholukhova, O. N., et al. 2005, Astronomy Letters, 31, 792 21, 232

Clocchiatti, A., & Wheeler, J. C. 1997, ApJ, 491, 375 31, 242, 272

Colgate, S. A., & Johnson, M. H. 1960, Phys. Rev. Lett., 5, 235 8

Colgate, S. A., & White, R. H. 1966, ApJ, 143, 626 9

Cowen, D. F., Franckowiak, A., & Kowalski, M. 2010, Astroparticle Physics, 33, 19 123

Dall'Ora, M., Botticella, M. T., Pumo, M. L., et al. 2014, ApJ, 787, 139 186

Denisenko, D., Lipunov, V., Gorbovskoy, E., et al. 2014, Central Bureau Electronic Telegrams, 3787, 2 250, 252

Dessart, L., & Hillier, D. J. 2005a, A&A, 439, 671 xiv, 37, 82, 85, 105, 167, 184, 189, 294

—. 2005b, A&A, 437, 667 xl, 145, 180, 184, 233

Dessart, L., & Hillier, D. J. 2005c, in Astronomical Society of the Pacific Conference Series, Vol. 332, The Fate of the Most Massive Stars, ed. R. Humphreys & K. Stanek, 415 24, 136, 179, 231

—. 2006, A&A, 447, 691 35, 37, 80, 119, 126, 161

Dessart, L., Livne, E., & Waldman, R. 2010, MNRAS, 408, 827 148, 149, 154

Dessart, L., Blondin, S., Brown, P. J., et al. 2008, ApJ, 675, 644 xxxix, xlii, xlvi, 84, 102, 167, 218, 267

Eastman, R. G., Schmidt, B. P., & Kirshner, R. 1996, ApJ, 466, 911 37, 80, 85, 183

Eenmae, T., Martin, J. C., Grammer, S., & Humphreys, R. 2014, The Astronomer's Telegram, 5935, 1 251

Eldridge, J. J., & Tout, C. A. 2004, MNRAS, 353, 87 10, 32

Elmhamdi, A., Chugai, N. N., & Danziger, I. J. 2003a, A&A, 404, 1077 172

Elmhamdi, A., Danziger, I. J., Chugai, N., et al. 2003b, MNRAS, 338, 939 xxxvi, xxxix, xlii, xlvi, 24, 80, 125, 142, 150, 165, 179, 216, 231, 265

Eswaraiah, C., Maheswar, G., Pandey, A. K., et al. 2013, A&A, 556, A65 256

Fagotti, P., Dimai, A., Quadri, U., et al. 2012, Central Bureau Electronic Telegrams, 3054, 1 108

Falk, S. W., & Arnett, W. D. 1977, ApJS, 33, 515 28, 241, 271

Faran, T., Poznanski, D., Filippenko, A. V., et al. 2014, MNRAS, 445, 554 xlii, xlvi, 18, 19, 201, 216, 238, 240, 248, 262, 263, 265, 279, 297, 298, 299, 302, 303

Fassia, A., Meikle, W. P. S., Chugai, N., et al. 2001, MNRAS, 325, 907 173

Fesen, R. A., & Becker, R. H. 1991, ApJ, 371, 621 34

Filippenko, A. V. 1997, ARA&A, 35, 309 xxxiii, 13, 14, 21, 39, 79

Filippenko, A. V., & Foley, R. J. 2005, IAU Circ., 8484, 2 xlvii, 278

Fisher, A., Branch, D., Hatano, K., & Baron, E. 1999, MNRAS, 304, 67 24, 83, 136, 173, 226

Fisher, A., Branch, D., Nugent, P., & Baron, E. 1997, ApJL, 481, L89 24, 83, 136, 173, 226

Fraser, M., Ergon, M., Eldridge, J. J., et al. 2011, MNRAS, 417, 1417 84, 104, 107, 141

Fraser, M., Maund, J. R., Smartt, S. J., et al. 2012, ApJL, 759, L13 108

—. 2014, MNRAS, 439, L56 202, 244, 245

Freedman, W. L., Madore, B. F., Gibson, B. K., et al. 2001, ApJ, 553, 47 104, 109

Fukugita, M., Ichikawa, T., Gunn, J. E., et al. 1996, AJ, 111, 1748 50

Fukugita, M., Shimasaku, K., & Ichikawa, T. 1995, PASP, 107, 945 50, 127

Gaensler, B. M., & Wallace, B. J. 2003, ApJ, 594, 326 34

Gandhi, P., Yamanaka, M., Tanaka, M., et al. 2013, ApJ, 767, 166 81, 107

Garcia-Segura, G., Langer, N., & Mac Low, M.-M. 1996, A&A, 316, 133 34

Gehrels, N., Chincarini, G., Giommi, P., et al. 2004, ApJ, 611, 1005 63, 210, 255

Gupta, R., Burse, B., Das, H. K., et al. 2002, Bulletin of the Astronomical Society of India, 30, 745 116

Gutiérrez, C. P., Anderson, J. P., Hamuy, M., et al. 2014, ApJL, 786, L15 225, 226

Hamuy, M. 2003, ApJ, 582, 905 xliii, 81, 107, 130, 131, 152, 172, 221, 222, 248, 270

Hamuy, M., & Pinto, P. A. 2002, ApJL, 566, L63 35, 80, 257

Hamuy, M., & Suntzeff, N. B. 1990, AJ, 99, 1146 xxxvi, xxxix, xlii, xlvi, 125, 128, 165, 216, 265

Hamuy, M., Suntzeff, N. B., Heathcote, S. R., et al. 1994, PASP, 106, 566 70, 117, 198

Hamuy, M., Walker, A. R., Suntzeff, N. B., et al. 1992, PASP, 104, 533 70

Hamuy, M., Pinto, P. A., Maza, J., et al. 2001, ApJ, 558, 615 xiv, 80, 85, 105, 184, 294

Han, J. 2009, in IAU Symposium, Vol. 259, IAU Symposium, ed. K. G. Strassmeier, A. G. Kosovichev, & J. E. Beckman, 455–466 276

Hanuschik, R. W., & Dachs, J. 1987, A&A, 182, L29 142, 179, 231

Hardie, R. H., & Ballard, C. M. 1962, PASP, 74, 242 61

Harutyunyan, A. H., Pfahler, P., Pastorello, A., et al. 2008, A&A, 488, 383 17, 250

Hayes, D. S., & Philip, A. G. D. 1985, in IAU Symposium, Vol. 111, Calibration of Fundamental Stellar Quantities, ed. D. S. Hayes, L. E. Pasinetti, & A. G. D. Philip, 469–472 70

Heger, A., Fryer, C. L., Woosley, S. E., Langer, N., & Hartmann, D. H. 2003, ApJ, 591, 288 xxxiv, 10, 32, 33, 108, 248

Heiles, C. 2000, AJ, 119, 923 257, 275

Henden, A., Krajci, T., & Munari, U. 2012, Information Bulletin on Variable Stars, 6024, 1 112

Hendry, M. A., Smartt, S. J., Maund, J. R., et al. 2005, MNRAS, 359, 906 212

Herrmann, K. A., Ciardullo, R., Feldmeier, J. J., & Vinciguerra, M. 2008, ApJ, 683, 630 212

Hirata, K., Kajita, T., Koshiba, M., Nakahata, M., & Oyama, Y. 1987, Physical Review Letters, 58, 1490 11

Hopkins, A. M., & Beacom, J. F. 2006, ApJ, 651, 142 35, 80

Horne, K. 1986, PASP, 98, 609 116, 198

Hough, J. H., Bailey, J. A., Rouse, M. F., & Whittet, D. C. B. 1987, MNRAS, 227, 1P 276, 304

Hoyle, F., & Fowler, W. A. 1960, ApJ, 132, 565 3

Iben, Jr., I., & Tutukov, A. V. 1984, ApJS, 54, 335 4

Immler, S., & Brown, P. J. 2012, The Astronomer's Telegram, 3995, 1 108, 154

Immler, S., Brown, P. J., Milne, P., et al. 2007, ApJ, 664, 435 84

Inserra, C., Baron, E., & Turatto, M. 2012a, MNRAS, 422, 1178 132, 139, 175, 227

Inserra, C., Turatto, M., Pastorello, A., et al. 2011, MNRAS, 417, 261 81, 132, 186, 202

—. 2012b, MNRAS, 422, 1122 xlii, xlvi, 22, 81, 84, 104, 141, 143, 162, 202, 216, 237, 245, 259, 260, 265

Inserra, C., Pastorello, A., Turatto, M., et al. 2013, A&A, 555, A142 173, 189

Itoh, R., Ui, T., & Yamanaka, M. 2012, Central Bureau Electronic Telegrams, 3054, 2 108

Janka, H.-T. 2012, Annual Review of Nuclear and Particle Science, 62, 407 32, 107

Janka, H.-T., Langanke, K., Marek, A., Martínez-Pinedo, G., & Müller, B. 2007, Phys. Rep., 442, 38 11

Jeffery, D. J., & Branch, D. 1990, in Supernovae, Jerusalem Winter School for Theoretical Physics, ed. J. C. Wheeler, T. Piran, & S. Weinberg, 149 24, 142

Jerkstrand, A., Fransson, C., Maguire, K., et al. 2012, A&A, 546, A28 150

Jones, M. I., Hamuy, M., Lira, P., et al. 2009, ApJ, 696, 1176 36, 37, 80, 99, 100, 184, 257

Jordi, K., Grebel, E. K., & Ammon, K. 2006, A&A, 460, 339 120

Kasen, D., & Woosley, S. E. 2009, ApJ, 703, 2205 80, 123

Kim, M., Zheng, W., Li, W., et al. 2013, Central Bureau Electronic Telegrams, 3606, 1 204

Kirshner, R. P., & Kwan, J. 1974, ApJ, 193, 27 35, 79, 81, 183, 257

Kochanek, C. S., Khan, R., & Dai, X. 2012, ApJ, 759, 20 108, 149

Kozma, C., & Fransson, C. 1998, ApJ, 497, 431 151

Krisciunas, K., Hamuy, M., Suntzeff, N. B., et al. 2009, AJ, 137, 34 xlii, xlvi, 216, 265

Kumar, B., Pandey, S. B., Eswaraiah, C., & Gorosabel, J. 2014, MNRAS, 442, 2 xlvii, 276, 278

Landolt, A. U. 2009, AJ, 137, 4186 59, 61, 111, 191, 253

Lee, M., Li, K. L., Wang, J.-W., et al. 2013, The Astronomer's Telegram, 5466, 1 202

Leonard, D. C. 2007, ArXiv e-prints, arXiv:0712.4035 xxxiv, 27

Leonard, D. C., & Filippenko, A. V. 2001, PASP, 113, 920 27, 248

Leonard, D. C., & Filippenko, A. V. 2005, in Astronomical Society of the Pacific Conference Series, Vol. 342, 1604-2004: Supernovae as Cosmological Lighthouses, ed. M. Turatto, S. Benetti, L. Zampieri, & W. Shea, 330 27, 28, 249, 278, 281, 303

Leonard, D. C., Filippenko, A. V., Ardila, D. R., & Brotherton, M. S. 2001, ApJ, 553, 861 xlvii, 27, 28, 248, 249, 276, 278, 281, 300, 303

Leonard, D. C., Kanbur, S. M., Ngeow, C. C., & Tanvir, N. R. 2002a, in Bulletin of the American Astronomical Society, Vol. 34, American Astronomical Society Meeting Abstracts, 1143 215

Leonard, D. C., Kanbur, S. M., Ngeow, C. C., & Tanvir, N. R. 2003, ApJ, 594, 247 80

Leonard, D. C., Pignata, G., Dessart, L., et al. 2012, The Astronomer's Telegram, 4033, 1 108

Leonard, D. C., Filippenko, A. V., Li, W., et al. 2002b, AJ, 124, 2490 xxxvi, xxxvii, xxxix, xl, xlii, xliii, xlvi, 36, 37, 84, 100, 122, 123, 125, 132, 134, 135, 163, 165, 175, 215, 216, 225, 259, 260, 265

Leonard, D. C., Filippenko, A. V., Gates, E. L., et al. 2002c, PASP, 114, 35 xxxvi, xxxvii, xxxviii, xxxix, xl, xlii, xliii, xlvi, xlvii, 21, 80, 120, 122, 125, 128, 131, 132, 134, 135, 139, 141, 144, 146, 163, 165, 172, 175, 216, 223, 225, 232, 259, 260, 265, 278

Leonard, D. C., Filippenko, A. V., Ganeshalingam, M., et al. 2006, Nature, 440, 505 28, 249, 278, 281, 300

Leonard, P. b. D. C., Pignata, G., Dessart, L., et al. 2013, The Astronomer's Telegram, 5275, 1 202, 223, 245

Levesque, E. M., Massey, P., Olsen, K. A. G., et al. 2005, ApJ, 628, 973 152

Li, H., & McCray, R. 1992, ApJ, 387, 309 151

Litvinova, I. I., & Nadezhin, D. K. 1983, Ap&SS, 89, 89 152

Litvinova, I. Y., & Nadezhin, D. K. 1985, Soviet Astronomy Letters, 11, 145 152, 248

Liu, W., & Dalgarno, A. 1995, ApJ, 454, 472 151

Maguire, K., Di Carlo, E., Smartt, S. J., et al. 2010, MNRAS, 404, 981 xxxvii, xl, xliii, 24, 134, 142, 147, 153, 175, 225

Maguire, K., Jerkstrand, A., Smartt, S. J., et al. 2012, MNRAS, 420, 3451 149

Makarov, D., Prugniel, P., Terekhova, N., Courtois, H., & Vauglin, I. 2014, A&A, 570, A13 158, 252, 257

Margutti, R., Chakraborti, S., Brown, P. J., & Sokolovsky, K. 2013, The Astronomer's Telegram, 5243, 1 203, 237, 240, 245

Marion, G. H., Vinko, J., Kirshner, R. P., et al. 2014, ApJ, 781, 69 175, 227

Maund, J. R., Wheeler, J. C., Patat, F., et al. 2007, ApJ, 671, 1944 276

Menzies, J. W., Catchpole, R. M., van Vuuren, G., et al. 1987, MNRAS, 227, 39P xli, 186

Milisavljevic, D., Margutti, R., Soderberg, A. M., et al. 2013, ApJ, 767, 71 175, 227

Minkowski, R. 1941, PASP, 53, 224 12

Misra, K., Pooley, D., Chandra, P., et al. 2007, MNRAS, 381, 280 127

Munari, U., Vagnozzi, A., & Castellani, F. 2012, Central Bureau Electronic Telegrams, 3054, 3 108

Nadyozhin, D. K. 2003, MNRAS, 346, 97 152

Nagy, A. P., Ordasi, A., Vinkó, J., & Wheeler, J. C. 2014, A&A, 571, A77 241, 242, 271, 272

Ochner, P., Siviero, A., Tomasella, L., et al. 2014, The Astronomer's Telegram, 5767, 1 250

Oke, J. B. 1990, AJ, 99, 1621 70, 117, 198

Olivares, E. F., Hamuy, M., Pignata, G., et al. 2010, ApJ, 715, 833 35, 81, 161, 212, 257, 258

Pastorello, A., Zampieri, L., Turatto, M., et al. 2004, MNRAS, 347, 74 107

Pastorello, A., Baron, E., Branch, D., et al. 2005, MNRAS, 360, 950 179, 231

Pastorello, A., Sauer, D., Taubenberger, S., et al. 2006, MNRAS, 370, 1752 84, 102

Pastorello, A., Valenti, S., Zampieri, L., et al. 2009, MNRAS, 394, 2266 xxxvi, xxxviii, xxxix, xlii, xlvi, 84, 102, 107, 123, 125, 128, 141, 144, 162, 165, 166, 167, 216, 218, 259, 265, 267

Pastorello, A., Pumo, M. L., Navasardyan, H., et al. 2012, A&A, 537, A141 186

Pastorello, A., Benetti, S., Brown, P. J., et al. 2015, MNRAS, 449, 1921 173

Patat, F., Barbon, R., Cappellaro, E., & Turatto, M. 1994, A&A, 282, 731 123, 166

Pereyra, A., Magalhães, A. M., Rodrigues, C. V., et al. 2006, A&A, 454, 827 xlvii, 27, 248, 278, 303

Perlmutter, S., Aldering, G., Goldhaber, G., et al. 1999, ApJ, 517, 565 35

Pilyugin, L. S., Thuan, T. X., & Vílchez, J. M. 2006, MNRAS, 367, 1139 109

Poole, T. S., Breeveld, A. A., Page, M. J., et al. 2008, MNRAS, 383, 627 64, 191

Popov, D. V. 1993, ApJ, 414, 712 29, 241, 271

Poznanski, D. 2013, ArXiv e-prints, arXiv:1304.4967 79

Poznanski, D., Ganeshalingam, M., Silverman, J. M., & Filippenko, A. V. 2011, MNRAS, 415, L81 119, 212

Poznanski, D., Nugent, P. E., Ofek, E. O., Gal-Yam, A., & Kasliwal, M. M. 2012a, The Astronomer's Telegram, 3996, 1 108

Poznanski, D., Prochaska, J. X., & Bloom, J. S. 2012b, MNRAS, 426, 1465 23, 119, 212, 257, 295, 297

Pumo, M. L., & Zampieri, L. 2011, ApJ, 741, 41 28, 187, 188, 190, 241, 271

—. 2013, MNRAS, 434, 3445 188

Pumo, M. L., Zampieri, L., & Turatto, M. 2010, Memorie della Societa Astronomica Italiana Supplementi, 14, 123 187

Pun, C. S. J., Kirshner, R. P., Sonneborn, G., et al. 1995, ApJS, 99, 223 xxxviii, 144, 150

Quimby, R. M., Wheeler, J. C., Höflich, P., et al. 2007, ApJ, 666, 1093 xxxviii, 24, 84, 102, 144, 162, 173, 259, 260

Rabinak, I., & Waxman, E. 2011, ApJ, 728, 63 xv, xli, 185, 186, 297

Ramaprakash, A. N., Gupta, R., Sen, A. K., & Tandon, S. N. 1998, A&AS, 128, 369 75, 256

Rautela, B. S., Joshi, G. C., & Pandey, J. C. 2004, Bulletin of the Astronomical Society of India, 32, 159 xxxv, 72, 255, 256

Richmond, M. W. 2014, Journal of the American Association of Variable Star Observers (JAAVSO), 42, 333 205, 212

Riess, A. G., Filippenko, A. V., Challis, P., et al. 1998, AJ, 116, 1009 35

Roming, P. W., Townsley, L. K., Nousek, J. A., et al. 2000, in Society of Photo-Optical Instrumentation Engineers (SPIE) Conference Series, Vol. 4140, X-Ray and Gamma-Ray Instrumentation for Astronomy XI, ed. K. A. Flanagan & O. H. Siegmund, 76–86 64

Roming, P. W. A., Hunsberger, S. D., Mason, K. O., et al. 2004, in Society of Photo-Optical Instrumentation Engineers (SPIE) Conference Series, Vol. 5165, X-Ray and Gamma-Ray Instrumentation for Astronomy XIII, ed. K. A. Flanagan & O. H. W. Siegmund, 262–276 64

Roming, P. W. A., Kennedy, T. E., Mason, K. O., et al. 2005, Space Sci. Rev., 120, 95 210, 255

Roy, R., Kumar, B., Benetti, S., et al. 2011, ApJ, 736, 76 81, 84, 103, 107, 123, 141

Russell, D. G. 2002, ApJ, 565, 681 104, 109

Sagar, R., Kumar, B., & Omar, A. 2013, ArXiv e-prints, arXiv:1304.0235 109

Sagar, R., Kumar, B., Omar, A., & Joshi, Y. C. 2012, in Astronomical Society of India Conference Series, Vol. 4, Astronomical Society of India Conference Series, 173 111, 159

Sahu, D. K., Anupama, G. C., Srividya, S., & Muneer, S. 2006, MNRAS, 372, 1315 xxxvi, xxxvii, xxxviii, xxxix, xl, xlii, xliii, xlvi, 24, 84, 101, 122, 125, 128, 134, 135, 142, 144, 150, 163, 165, 175, 179, 216, 225, 231, 259, 265

Sanders, N. E., Soderberg, A. M., Gezari, S., et al. 2015, ApJ, 799, 208 201, 247

Scarrott, S. M., Rolph, C. D., & Semple, D. P. 1990, in IAU Symposium, Vol. 140, Galactic and Intergalactic Magnetic Fields, ed. R. Beck, R. Wielebinski, & P. P. Kronberg, 245–251 276

Scarrott, S. M., Rolph, C. D., Wolstencroft, R. W., & Tadhunter, C. N. 1991, MNRAS, 249, 16P 276

Schlafly, E. F., & Finkbeiner, D. P. 2011, ApJ, 737, 103 xxxix, xlii, xlvi, 102, 160, 167, 212, 218, 258, 267, 297

Schlegel, D. J., Finkbeiner, D. P., & Davis, M. 1998, ApJ, 500, 525 117

Schmidt, B. P., Kirshner, R. P., & Eastman, R. G. 1992a, ApJ, 395, 366 35, 37, 80, 81

Schmidt, B. P., Kirshner, R. P., Eastman, R. G., et al. 1994, ApJ, 432, 42 80

Schmidt, G. D., Elston, R., & Lupie, O. L. 1992b, AJ, 104, 1563 73, 77, 256

Serkowski, K., Mathewson, D. S., & Ford, V. L. 1975, ApJ, 196, 261 275, 276

Shapiro, P. R., & Sutherland, P. G. 1982, ApJ, 263, 902 26

Shappee, B. J., Kochanek, C. S., Stanek, K. Z., et al. 2013, The Astronomer's Telegram, 5237, 1 202

Shivvers, I., Mauerhan, J. C., Leonard, D. C., Filippenko, A. V., & Fox, O. D. 2014, ArXiv e-prints, arXiv:1408.1404 173

Siviero, A., Tomasella, L., Pastorello, A., et al. 2012, Central Bureau Electronic Telegrams, 3054, 4 108

Smartt, S. J. 2009, ARA&A, 47, 63 38, 248

—. 2015, PASA, 32, 16 12, 38

Smartt, S. J., Eldridge, J. J., Crockett, R. M., & Maund, J. R. 2009, MNRAS, 395, 1409 12, 38, 79, 107, 108, 152, 153, 248

Smartt, S. J., Maund, J. R., Hendry, M. A., et al. 2004, Science, 303, 499 12

Smith, N., Li, W., Filippenko, A. V., & Chornock, R. 2011, MNRAS, 412, 1522 79

Smith, N., Mauerhan, J. C., Cenko, S. B., et al. 2015, MNRAS, 449, 1876 240, 302

Sobolev, V. V. 1957, SvA, 1, 678 24

Spiro, S., Pastorello, A., Pumo, M. L., et al. 2014, MNRAS, 439, 2873 xliii, 222, 223

Stalin, C. S., Hegde, M., Sahu, D. K., et al. 2008, Bulletin of the Astronomical Society of India, 36, 111 117

Stetson, P. B. 1987, PASP, 99, 191 54, 111, 191

—. 1992, J. R. Astron. Soc. Canada, 86, 71 111

Stockdale, C. J., Ryder, S. D., Van Dyk, S. D., et al. 2012, The Astronomer's Telegram, 4012, 1 108, 154

Suntzeff, N. B., Heathcote, S., Weller, W. G., Caldwell, N., & Huchra, J. P. 1988, Nature, 334, 135 305

Taddia, F., Stritzinger, M. D., Sollerman, J., et al. 2013, A&A, 555, A10 240

Takáts, K., & Vinkó, J. 2006, MNRAS, 372, 1735 82, 102

—. 2012, MNRAS, 419, 2783 80, 82, 83, 84, 90, 101, 131, 181, 233

Takáts, K., Pumo, M. L., Elias-Rosa, N., et al. 2014, MNRAS, 438, 368 xlii, xlvi, 175, 186, 216, 227, 265

Theureau, G., Hanski, M. O., Coudreau, N., Hallet, N., & Martin, J.-M. 2007, A&A, 465, 71 162

Todini, P., & Ferrara, A. 2001, MNRAS, 325, 726 304

Tomasella, L., Cappellaro, E., Fraser, M., et al. 2013, MNRAS, 434, 1636 xlii, xlvi, 186, 216, 265

Trammell, S. R., Hines, D. C., & Wheeler, J. C. 1993, ApJL, 414, L21 274

Tran, H. D., Filippenko, A. V., Schmidt, G. D., et al. 1997, PASP, 109, 489 274

Tsvetkov, D. Y., Goranskij, V., & Pavlyuk, N. 2008, Peremennye Zvezdy, 28, 8 xxxvi, xxxix, 125, 165

Tully, R. B., & Fisher, J. R. 1988, Catalog of Nearby Galaxies 252, 258

Tully, R. B., Rizzi, L., Shaya, E. J., et al. 2009, AJ, 138, 323 104, 162

Turatto, M. 2003, in Lecture Notes in Physics, Berlin Springer Verlag, Vol. 598, Supernovae and Gamma-Ray Bursters, ed. K. Weiler, 21–36 xxxiii, 15, 21

Turatto, M., Benetti, S., & Cappellaro, E. 2003, in From Twilight to Highlight: The Physics of Supernovae, ed. W. Hillebrandt & B. Leibundgut, 200 21, 23, 102, 119, 161, 212, 257, 295

Uomoto, A. 1986, ApJL, 310, L35 151

Utrobin, V. P. 2007, A&A, 461, 233 28, 149, 241, 271

Utrobin, V. P., & Chugai, N. N. 2009, A&A, 506, 829 108, 149

—. 2013, ArXiv e-prints, arXiv:1306.5122 103

Valenti, S., Sand, D., Howell, D. A., et al. 2013, The Astronomer's Telegram, 5228, 1 238

Valenti, S., Sand, D., Pastorello, A., et al. 2014, MNRAS, 438, L101 202, 205, 210, 212, 244, 245, 250

Valenti, S., Sand, D., Stritzinger, M., et al. 2015, MNRAS, 448, 2608 xxxix, xlii, xlvi, 167, 202, 216, 218, 240, 260, 262, 265, 267, 302

van Dokkum, P. G. 2001, PASP, 113, 1420 54, 68, 116, 198, 210

Van Dyk, S. D. 1992, AJ, 103, 1788 12

Van Dyk, S. D., Hamuy, M., & Filippenko, A. V. 1996, AJ, 111, 2017 12

Van Dyk, S. D., Li, W., & Filippenko, A. V. 2003, PASP, 115, 1289 12

Van Dyk, S. D., Peng, C. Y., Barth, A. J., & Filippenko, A. V. 1999, AJ, 118, 2331 12

Van Dyk, S. D., Cenko, S. B., Poznanski, D., et al. 2012, ApJ, 756, 131 xxxiv, 23, 108, 110, 119

Van Dyk, S. D., Lee, J. C., Anderson, J., et al. 2015, ApJ, 806, 195 305

Vinkó, J., & Takáts, K. 2007, in American Institute of Physics Conference Series, Vol. 937, Supernova 1987A: 20 Years After: Supernovae and Gamma-Ray Bursters, ed. S. Immler, K. Weiler, & R. McCray, 394–398 82

Vinkó, J., Takáts, K., Szalai, T., et al. 2012, A&A, 540, A93 80, 102

Vollmann, K., & Eversberg, T. 2006, Astronomische Nachrichten, 327, 862 119

Wagoner, R. V. 1981, ApJL, 250, L65 37, 84

Wang, L., Baade, D., Höflich, P., & Wheeler, J. C. 2002a, The Messenger, 109, 47 27, 248

Wang, L., Howell, D. A., Höflich, P., & Wheeler, J. C. 2001, ApJ, 550, 1030 274

Wang, L., & Wheeler, J. C. 1996, ApJL, 462, L27 27, 28, 248, 249

—. 2008, ARA&A, 46, 433 274

Wang, L., Wheeler, J. C., Höflich, P., et al. 2002b, ApJ, 579, 671 28, 249

Wang, L., Baade, D., Höflich, P., et al. 2003a, ApJ, 591, 1110 276, 304

Wang, S.-i., Hildebrand, R. H., Hobbs, L. M., et al. 2003b, in Society of Photo-Optical Instrumentation Engineers (SPIE) Conference Series, Vol. 4841, Instrument Design and Performance for Optical/Infrared Ground-based Telescopes, ed. M. Iye & A. F. M. Moorwood, 1145–1156 210

Webbink, R. F. 1984, ApJ, 277, 355 4

Whelan, J., & Iben, Jr., I. 1973, ApJ, 186, 1007 4

Wilson, J. R. 1982, Proc. Univ. Illinois Meeting on Numerical Astrophysics 10

Winkler, P. F., Gupta, G., & Long, K. S. 2003, ApJ, 585, 324 2

Woosley, S. E. 1988, in Lecture Notes in Physics, Berlin Springer Verlag, Vol. 305, IAU Colloq. 108: Atmospheric Diagnostics of Stellar Evolution, ed. K. Nomoto, 361 5

Woosley, S. E. 1993, ApJ, 405, 273 32

Woosley, S. E., Heger, A., & Weaver, T. A. 2002, Reviews of Modern Physics, 74, 1015 5, 10

Woosley, S. E., & Weaver, T. A. 1986, ARA&A, 24, 205 11

—. 1995, ApJS, 101, 181 149, 150, 151

Xu, J., Crotts, A. P. S., & Kunkel, W. E. 1995, ApJ, 451, 806 305

Yadav, N., Chakraborti, S., & Ray, A. 2012, The Astronomer's Telegram, 4010, 1 108, 154

Young, P. A., Fryer, C. L., Hungerford, A., et al. 2006, ApJ, 640, 891 34

Zampieri, L., Pastorello, A., Turatto, M., et al. 2003, MNRAS, 338, 711 29, 187, 241, 271

Zhao, F.-Y., Strom, R. G., & Jiang, S.-Y. 2006, Chinese J. Astron. Astrophys., 6, 635 2

Zheng, W., Blanchard, P., Cenko, S. B., Filippenko, A. V., & Cucchiara, A. 2013, The Astronomer's Telegram, 4823, 1 157, 158

Zwitter, T., Munari, U., & Moretti, S. 2004, IAU Circ., 8413, 1 102